université
PARIS-SACLAY

Digital and analog quantum algorithms for the nuclear many-body problem

Algorithmes quantiques digitaux et analogiques pour le problème à N corps nucléaire

Thèse de doctorat de l'Université Paris-Saclay

École doctorale n°576 : Particules hadrons énergie et noyau : instrumentation, imagerie, cosmos et simulation (PHENIICS)
Spécialité de doctorat : Physique nucléaire
Graduate School : Physique. Référent : Faculté des sciences d'Orsay

Thèse préparée dans les unités de recherche
Département de Physique Nucléaire (Université Paris-Saclay, CEA)
et **IJCLab (Université Paris-Saclay, CNRS)**,
sous la direction de **Denis Lacroix**, Directeur de recherche,
et le co-encadrement de **Vittorio Somà**, Directeur de recherche.

Thèse soutenue à Paris-Saclay, le 1 octobre 2026, par

Samuel AYCHET-CLAISSE

Composition du jury

Membres du jury avec voix délibérative

Thomas Ayral Professeur, CPHT, École Polytechnique	Président
Morten Hjorth-Jensen Professeur, Université d'Oslo	Rapporteur & Examinateur
Arnau Rios Professeur, Université de Barcelone	Rapporteur & Examinateur
Mariane Mangin-Brinet Directrice de recherche, LPSC, Grenoble	Examinatrice
Bruno Senjean Chargé de recherche, Institut Charles Gerhardt, Montpellier	Examinateur

THESE DE DOCTORAT

NNT : 2026UPASP089

université PARIS-SACLAY

ÉCOLE DOCTORALE
Particules, hadrons, énergie et noyau : instrumentation, imagerie, cosmos et simulation (PHENIICS)

Titre : Algorithmes quantiques digitaux et analogiques pour le problème à N corps nucléaire
Mots clés : Calcul quantique, Problème à N corps, Physique Nucléaire

Résumé : La description de particules en interaction, soumises aux effets quantiques, est connue sous le nom de problème à N corps. Sa résolution exacte se heurte à la croissance exponentielle des ressources de calcul nécessaires avec le nombre de degrés de liberté considérés. Parmi les développements menés pour aborder ce problème et repousser les limites actuelles, le calcul quantique représente une piste prometteuse. Notamment, les algorithmes quantiques variationnels, des algorithmes hybrides classique-quantique plus résilients face aux erreurs que leurs homologues purement quantiques, sont particulièrement intéressants pour aborder le problème à N corps avec les plateformes quantiques actuellement disponible.

Cette thèse explore l'application des tels algorithmes au problème à N corps nucléaire. Les notions de physique nucléaire et de calcul quantique nécessaires à la compréhension du présent travail, de son contexte, et de ses objectifs, sont d'abord introduites. Ensuite, plusieurs généralisations de l'algorithme hybride ADAPT-VQE sont présentées pour approcher l'état fondamental d'un système quantique à N corps. Leurs performances sont testées et comparées en simulation avec une application sur le modèle de pairing, qui permet d'étudier les systèmes superfluides comme les noyaux d'atomes. Les approximations obtenues pour l'état fondamental constituent le point de départ d'une autre procédure de calcul hybride permettant d'évaluer les fonctions de Green de tels systèmes. Celle-ci a été simulée et validée pour ce cas modèle, et les ressources quantiques nécessaires ont été quantitativement estimées.

Ces résultats ont été obtenus sur des émulateurs d'ordinateurs quantiques digitaux supposés parfaits. Cependant, les ordinateurs quantiques actuels restent limités par le bruit, et pour envisager leur utilisation à court terme il est nécessaire de prendre en compte leurs contraintes techniques. Pour cela, le calcul quantique analogique est plus adapté que le calcul quantique digital. C'est pourquoi, dans la seconde partie de cette thèse, l'intérêt s'est porté sur les ordinateurs quantiques à atomes neutres, qui se prêtent naturellement au calcul quantique analogique. Leur utilisation avec des procédures variationnelles soulève différents obstacles et limitations. Plusieurs méthodes sont présentées ici pour lever ces difficultés, aboutissant à un protocole destiné à calculer l'état fondamental d'un modèle simple du deutéron sur ces machines. Une méthodologie complète est élaborée et pourra être testée sur des ordinateurs quantiques à atomes neutres actuels et futurs.

Title: Digital and analog quantum algorithms for the nuclear many-body problem
Keywords: Quantum computing, Many-Body problem, Nuclear Physics

Abstract: The description of interacting particles, subject to quantum effects, is known as the many-body problem. Its exact resolution faces the exponential growth of the required computational resources with the number of degrees of freedom considered. Among the developments aimed at tackling this problem and pushing beyond current limits, quantum computing represents a promising approach. Notably, the variational quantum algorithms, hybrid quantum-classical algorithms that are more resilient to errors than their purely quantum counterparts, are particularly interesting to tackle the many-body problem with currently available quantum platforms.

This thesis investigates the application of such algorithms to the nuclear many-body problem. The notions of nuclear physics and quantum computing required to understand the present work, its context, and its objectives, are first introduced. Then, several generalisations of the ADAPT-VQE hybrid algorithm are presented to approximate the ground state of a quantum many-body system. Their performances are benchmarked and compared in a simulation, with an application to the pairing model, which allows to study superfluid systems such as atomic nuclei. The resulting ground state approximations constitute the starting point of another hybrid computing procedure designed to evaluate Green's functions of such systems. This procedure has been simulated and validated within this test model, and the required quantum resources have been quantitatively estimated.

These results have been obtained with emulators of ideal digital quantum computers. However, current quantum computers remain limited by noise, and to consider their short-term use, it is necessary to take into account their technical constraints. To this purpose, analog quantum computing is more adapted than digital quantum computing. Hence, in the second part of this thesis, the focus has been on neutral atom quantum computers, which are naturally adapted to analog quantum computing. Their use with variational procedures raises different obstacles and limitations. Several methods are presented here to lift these difficulties, resulting in a protocol intended for the computation, on these machines, of the ground state of a simple model of the deuteron. A complete methodology has been developed with the goal of testing it on current and future neutral atom quantum computers.

Remerciements

Je tiens à exprimer ici ma gratitude envers toutes les personnes qui m'ont apporté leur soutien durant ces trois années de thèse.

Tout d'abord, je remercie chaleureusement les membres de mon jury pour le temps qu'ils ont consacré à ma soutenance et à la lecture de mon manuscrit. Je suis honoré que des chercheurs à la pointe de la physique nucléaire et du calcul quantique aient pu apprécier mon travail. Les mots que vous avez eu pour l'exprimer m'ont particulièrement touché.

Ce travail a largement bénéficié de l'implication de Denis et Vittorio. Avec vos deux styles à la fois différents et complémentaires, il y a dans votre duo tout ce dont un doctorant peut rêver pour son encadrement. Votre expertise, vos idées, vos intuitions, qui m'ont guidé et débloqué à de nombreuses reprises, ont été déterminantes dans l'aboutissement de cette thèse. Pour tout le temps que vous m'avez consacré, pour tout ce que vous m'avez enseigné, pour votre confiance, votre patience, votre bienveillance, merci !

Je suis également reconnaissant envers toutes les personnes que j'ai eu le plaisir de côtoyer au DPhN et à l'IJCLab. Chers collègues et amis, ma vie au labo n'aurait pas été aussi chouette et stimulante sans vous. Merci pour ces supers moments aux restaurants, bar à jeu, karaoké, laser game, escalade, ... Et merci encore pour avoir partagé toutes ces délicieuses spécialités culinaires de vos pays respectifs, tout autour du monde.

Un grand merci également à Nicolas pour avoir pris soin de mon ordinateur quand celui-ci en avait besoin, à Isabelle et Élodie pour mes missions et démarches au CEA, et à Balsama pour m'avoir aiguillé avec l'école doctorale. Si je vous ai si souvent sollicités, c'est parce que votre aide est précieuse.

Pendant ma thèse j'ai eu le plaisir d'enseigner à l'université en dirigeant des TDs de maths et de physique. Merci aux équipes pédagogiques qui m'ont accueilli, et en particulier aux responsables d'UE qui m'ont fait confiance.

Entrer dans le monde fascinant de la physique quantique nécessite un long apprentissage préalable, qu'on ne peut pas effectuer seul. Si j'ai pu y accéder, c'est aussi grâce au travail de mes professeurs successifs. En maternelle, primaire, collège, lycée, prépa, école d'ingénieur, licence, master, vous m'avez inspiré et donné le goût d'apprendre. Merci à vous tous.

Enfin, je remercie tout particulièrement mes proches, amis et famille, sans qui je ne serais pas arrivé jusque-là. Notamment mes parents, mon frère, et Doriane. Merci !

Contents

General introduction **11**

1 The nuclear many-body problem **15**
1.1 Elements of quantum many-body physics . . . 15
1.1.1 From one-body to many-body . . . 15
1.1.2 Indistinguishable particles . . . 15
1.1.3 Second quantized formulation . . . 17
1.2 An overview of nuclear theory . . . 18
1.2.1 What is nuclear physics? . . . 18
1.2.2 Theoretical models . . . 20
1.2.3 Self-consistent Green's functions . . . 22
1.3 Two models relevant for nuclear theory . . . 24
1.3.1 The pairing model . . . 24
1.3.2 A model for the deuteron . . . 27
1.4 Conclusion . . . 28

2 Digital quantum computing **29**
2.1 Algebraic preliminaries . . . 29
2.1.1 Pauli strings . . . 29
2.1.2 Hermitian operators . . . 30
2.1.3 Unitary operators . . . 30
2.2 The qubit . . . 31
2.2.1 Description . . . 31
2.2.2 Operations . . . 32
2.2.3 Measurement . . . 33
2.3 States and operations on several qubits . . . 34
2.3.1 States of N qubits . . . 34
2.3.2 Operations on N qubits . . . 35
2.3.3 A graphical representation of qubit operations: the quantum circuit 36
2.3.4 Comparison with classical computing . . . 38
2.4 Measuring qubits . . . 39
2.4.1 Direct measurement . . . 39
2.4.2 Measurement with a basis rotation . . . 40
2.4.3 Finite number of measurements: statistical uncertainty . . . 40
2.5 Some examples of quantum algorithms . . . 41
2.5.1 Quantum Fourier Transform . . . 42
2.5.2 Quantum Phase Estimation . . . 43

2.6 Many-body problems on a quantum computer . . . 47
2.6.1 From many-body states to qubit states . . . 47
2.6.2 Mapping fermions to qubits: the observables . . . 48
2.6.3 Application to Hamiltonians of section 1.3 . . . 49
2.6.4 Number of Pauli strings versus number of measurements . . . 52
2.7 Conclusion . . . 52

3 In search of the ground state - application to pairing 53
3.1 Some variational quantum algorithms . . . 53
3.1.1 The Variational Quantum Eigensolver . . . 53
3.1.2 ADAPT-VQE-based algorithms: general description . . . 55
3.2 ADAPT-VQE-based algorithms: four different versions . . . 56
3.2.1 The original ADAPT-VQE . . . 56
3.2.2 Selection of the "best" operator . . . 57
3.2.3 An alternative set of operators . . . 58
3.2.4 Summary of the 4 versions . . . 60
3.2.5 Estimation of the number of quantum evaluations . . . 60
3.3 Application to pairing Hamiltonian . . . 61
3.3.1 Convergence of the four versions . . . 61
3.3.2 Comparison with fixed number of operators . . . 63
3.3.3 Necessity of the re-optimisation . . . 65
3.4 Conclusion . . . 65

4 Quantum simulation of Green's functions 67
4.1 General methodology . . . 67
4.1.1 Quantum calculation in time domain . . . 67
4.1.2 Quantum calculation in energy domain . . . 69
4.2 Application to pairing - simplifications . . . 70
4.2.1 Simplifications due to symmetries . . . 71
4.2.2 Expansion into Pauli operators . . . 72
4.2.3 Pauli grouping . . . 73
4.3 Application to pairing - results . . . 75
4.3.1 Results for the Green's function . . . 75
4.3.2 Odd systems . . . 77
4.3.3 Evaluation of statistical error and required number of measurements 79
4.4 Conclusion . . . 80

5 Analog quantum computing with neutral atoms 83
5.1 Analog quantum computing . . . 84
5.2 Neutral atom quantum computer . . . 85
5.2.1 Why neutral atoms . . . 85
5.2.2 Register preparation and measurement . . . 85
5.2.3 Quantum computation . . . 86
5.3 Analog variational algorithm with neutral atoms - challenges . . . 88
5.3.1 Impossibility to stop the interaction . . . 89
5.3.2 A complex evolution . . . 89
5.3.3 Relative phases in the amplitudes of the evolved state . . . 91

5.3.4 Constraints on the atom relative distances . . . 91
5.3.5 Ruby's hardware limitations . . . 91
5.4 Conclusion . . . 93

6 Analog variational ground-state energy estimation with a constrained atom-based quantum computer 95
6.1 XY mode and local detunings . . . 95
6.1.1 General method . . . 95
6.1.2 Justification of the procedure for two qubits . . . 97
6.1.3 Application to the deuteron . . . 98
6.1.4 Application to the pairing Hamiltonian . . . 101
6.1.5 Limitations of the method . . . 104
6.2 Ising mode and alternative encoding . . . 105
6.2.1 Benefits of an alternative encoding . . . 105
6.2.2 A convenient pulse . . . 108
6.2.3 Reducing the effect of interaction for measurements . . . 110
6.2.4 Application to the AnalogDevice . . . 112
6.2.5 Influence of the duration and the choice of basis rotations . . . 115
6.3 Conclusion . . . 116

General conclusion 117

Appendices 120

A Some extra elements of many-body physics 121
A.1 Slater determinants form an orthonormal basis . . . 121
A.2 The Fock space as a Hilbert space . . . 122
A.3 On the annihilation operator . . . 122

B General expression of a unitary mapping Z to X or Y 125

C Some derivations required for the algorithms presented in section 3.2 127
C.1 Decomposition into Pauli strings of the commutators in Eq. (3.5) . . . 127
C.2 Justification of Eq. (3.6) . . . 128
C.3 Determination of the parameters in Eq. (3.6) . . . 129

D A procedure for the exact preparation of a given state 131

E Calculation of the energy curve derivatives (6.13) 135

F Some other derivations required in chapter 6 139
F.1 Effect of qubit-qubit interaction during the state preparation with SLM mask in the 2-qubit case . . . 139
F.2 Impossibility to evaluate some observables with global basis rotations . . . 141

G Synthèse en français 143

Bibliography 145

General introduction

A wide variety of physical systems can be described as made of interacting particles subject to quantum effects. This is the case, for instance, of spins in a magnetic system, electrons in solids, in atoms, or in molecules, nucleons in atomic nuclei... Their description is known as the many-body problem. Many-body problems are challenging because their exact resolution faces the exponential growth of the required computational resources with the number of considered degrees of freedom, limiting our knowledge on these systems.

For instance, atomic nuclei are made of two to a few hundreds nucleons. As a consequence, they are in general mesoscopic system, *i.e.* systems containing most often too many particles for an exact treatment, but too few for statistical methods. This gives rise to a rich phenomenology, but makes their theoretical description demanding. Moreover, nuclear systems are subject to Coulomb, weak, and strong interactions, with the latter intervening in a non-perturbative regime. This involves a complicated Hamiltonian, and a quick growth of the required Hilbert space. Therefore, for more than ≈ 20 nucleons, for which the truncation of the Hilbert space and diagonalization of the Hamiltonian still give meaningful results, approximate methods are needed. However, the latter remain costly and are in general limited in accuracy or in tractability.

Among the developments aimed at tackling the many-body problem and pushing beyond current limits, quantum computing represents a promising approach. Using the properties of quantum systems to perform specific computing tasks, it has the potential to overcome classical computers for various applications, such as factorisation, data search, optimisation, or simulation of many-body systems. The latter application is, somewhat, "natural". Indeed, a quantum computer, as a controllable system of interacting qubits, is itself a many-body system, hence a natural candidate to simulate another many-body system. If the latter is a real system that is difficult to manipulate and measure (*e.g.* an atomic nucleus), encoding it on qubits, which are easier to control, ideally leads to accurate evaluations of the expectation value of observables. Moreover, quantum computers can realize models of many-body systems that do not naturally exist, in order to study a simplified system or a specific interaction isolated from other effects (*e.g.* pairing correlations in nuclei).

Several strategies exist to access relevant properties of many-body systems with a quantum computer. Among them, variational quantum algorithms are particularly interesting to tackle the many-body problem with currently available quantum platforms. Combining a classical optimisation algorithm to the ability of a quantum computer for efficiently encoding a many-body state and evaluating the corresponding energy (or the expectation value of another operator), these hybrid quantum-classical algorithms are more resilient to errors than their purely quantum counterparts.

Current quantum computing technologies are indeed subject to noise. Qubit state decoherence and imperfect operations deteriorate the results. Various technologies are de-

veloped to tackle this issue, resulting in the use of a wide diversity of quantum systems to realize qubits, such as photons, ions, neutral atoms, quantum dots, Josephson junctions, ... In particular, two paradigms can be identified for the realization of quantum computers. The digital approach consists in defining a small set of elementary operations (gates) on qubits, so that this set is universal, *i.e.* its gates can be combined in order to build every possible operation. This allows to build quantum algorithms as an assembly of such gates irrespectively of the hardware details. The analog approach is instead closer to the hardware. In this approach, the qubit state is evolved according to the Schrödinger equation, with a tunable Hamiltonian determined by the hardware. While less universal than the digital mode, this allows to more efficiently take into account the hardware constraints, in order to reduce the noise and the accumulation of errors.

Neutral atoms are particularly suited for analog quantum computing. Within the French project *Hybrid HPC Quantum Initiative* (HQI) [1], the company Pasqal [2] has developed and delivered such a neutral atom quantum computer, called Ruby, to the French research center *Commissariat à l'énergie atomique et aux énergies alternatives* (CEA). This device has been recently installed at the *Très Grand Centre de Calcul* (TGCC) [3], a high-performance computing center of CEA. The HQI project and the possibility of using the neutral atom machine have motivated physics applications within several research communities. In this context, the present thesis addresses the application of quantum variational methods to the nuclear many-body problem, with both digital and analog approaches. The former is followed in chapters 2, 3, and 4, while the latter is addressed in chapters 5 and 6, with a specific focus on the Ruby device and its constraints.

In chapter 1, the nuclear many-body problem is presented. Notions of many-body physics formalism are given, followed by a quick overview of nuclear theory, in order to understand the context of this thesis. One-body Green's functions, which will be used in the fourth chapter, are introduced as defined in the context of the self-consistent Green's function *ab-initio* method. This chapter ends with the presentation of two models relevant for nuclear theory, the pairing model and a simple model for the deuteron, which will serve as test models for the methods developed in the following chapters.

In chapter 2, the building blocks of digital quantum computing are introduced: qubits, unitary operations, quantum circuit representation, measurement. Two examples of quantum algorithms are described to illustrate the potential advantage of quantum computers over classical ones, for specific tasks. Then, a strategy to encode a many-body problem on qubits is given and applied on the two models presented in the previous chapter.

In chapter 3, variational quantum algorithms are addressed. Several procedures, based on the Adaptive Derivative-Assembled Pseudo-Trotter ansatz Variational Quantum Eigensolver (ADAPT-VQE) scheme introduced in [4], are defined for the approximate preparation of the ground state of many-body systems. Their performances are benchmarked with the pairing Hamiltonian in a noiseless simulation of digital quantum computer.

In chapter 4, the approximate ground states encoded on qubits, obtained in the previous chapter, are used as an input for a procedure dedicated to the computation of the Green's functions introduced in chapter 1. Here again, this strategy is simulated and benchmarked with the pairing Hamiltonian. A quantitative analysis of the required number of quantum measurements is detailed.

In chapter 5, the focus is made on analog quantum computing and the neutral atom technology. Details are given on the analog paradigm, followed by a description of the main

elements of neutral atom quantum computers. Several challenges, raised by the use of this technology for variational quantum algorithms, are identified.

In chapter 6, several methods are developed to address these challenges. Two approaches are reported. The first one explores the use of a potential future neutral atom device to perform variational optimisations restricted to a subspace of the qubit space with a given Hamming weight. The pairing and deuteron Hamiltonians introduced in chapter 1 are used to test the method. The second approach focuses on the existing Ruby device and introduces an alternative to the usual Jordan-Wigner fermion-to-qubit encoding to leverage several obstacles raised by the constraints of this machine. This is applied to the deuteron Hamiltonian truncated in a 3-dimensional space, resulting in a complete protocol adapted to Ruby's hardware, and ready to be tested on this device.

Chapter 1

The nuclear many-body problem

This chapter presents some notions of quantum many-body physics with a focus on nuclear theory. Specifically, it concentrates on aspects that are useful for the next chapters where many-body problems are mapped to quantum computing systems. The many-body formalism that will be required in the following chapters is first introduced in section 1.1. Then, a brief overview of nuclear theory, with a focus on static properties, is given in section 1.2 to precise the context of this thesis. Finally, the section 1.3 describes two models relevant for nuclear theory that will be used as test models in the following chapters.

1.1 Elements of quantum many-body physics

Here are introduced some elements of quantum many-body physics. The fermionic Fock space is built from a one-body Hilbert space. The second-quantized formulation of states and operators, widely used in the following, is defined.

1.1.1 From one-body to many-body

Let us consider a particle in a quantum system. Its state is an element $|\psi\rangle$ of a Hilbert space $\mathcal{H}_1$. To avoid some technicalities, and because it will be sufficient in the following, let us suppose here that $\mathcal{H}_1$ is finite-dimensional. The notions presented here can be extended for an infinite-dimensional Hilbert space, while it could require some carefulness. Let $\{|\alpha\rangle\}_\alpha$ be an orthonormal basis of $\mathcal{H}_1$.

Let us consider now a quantum system of N such particles, labelled $1, 2, ..., N$. If these particles are distinguishable one from another, they can be described together by an element $|\Psi\rangle$ of the Hilbert space $\mathcal{H}_N = \mathcal{H}_1^{\otimes N}$, which can be equipped with the basis $\mathcal{B}_N = \{|\alpha_1\rangle \otimes |\alpha_2\rangle \otimes ... \otimes |\alpha_N\rangle\}_{\alpha_1,\alpha_2,...,\alpha_N}$. A given state $|\alpha_1\rangle \otimes |\alpha_2\rangle \otimes ... \otimes |\alpha_N\rangle$ of this basis describes the situation where particle 1 is in state $|\alpha_1\rangle$, particle 2 in state $|\alpha_2\rangle$, ... , and particle N in state $|\alpha_N\rangle$. It will be convenient in the following to use the more explicit notation

$$|\alpha_1\rangle \otimes |\alpha_2\rangle \otimes ... \otimes |\alpha_N\rangle = |1 : \alpha_1,\ 2 : \alpha_2,\ ...\ ,\ N : \alpha_N\rangle. \tag{1.1}$$

1.1.2 Indistinguishable particles

The situation is different if the particles are indistinguishable one from another (like, for example, a system of electrons). In this case, a normalized vector $|\Psi\rangle$ describes the

same state that the vector $P_\sigma|\Psi\rangle$ obtained with a permutation σ of the particles. Here the permutation operator P_σ is defined by its action on the basis $\mathcal{B}_N$ as

$$P_\sigma|1:\alpha_1,\ 2:\alpha_2,\ \dots,\ N:\alpha_N\rangle = |1:\alpha_{\sigma(1)},\ 2:\alpha_{\sigma(2)},\ \dots,\ N:\alpha_{\sigma(N)}\rangle. \tag{1.2}$$

In quantum physics, a state is described by a normalized element of a Hilbert space, defined up to a global phase. Since $|\Psi\rangle$ and $P_\sigma|\Psi\rangle$ are both normalized and represent the same state, they should be equal, up to a global phase. However, this is not the case in general with $|\Psi\rangle \in \mathcal{H}_N$. So $\mathcal{H}_N$ cannot be the Hilbert space describing a system of N indistinguishable particles.

Actually, there exist elements $|\Psi\rangle \in \mathcal{H}_N$ that satisfy this requirement. For example, this is the case for the totally symmetric states, *i.e.* states in $\mathcal{S}_N(\mathcal{H}_N)$ where $\mathcal{S}_N$ is the symmetrization operator, defined as

$$\mathcal{S}_N = \frac{1}{\sqrt{N!}} \sum_{\sigma\in\mathscr{S}_N} P_\sigma. \tag{1.3}$$

For any normalized $|\Psi\rangle \in \mathcal{S}_N(\mathcal{H}_N)$ and any permutation σ in the symmetric group $\mathscr{S}_N$, $P_\sigma|\Psi\rangle = |\Psi\rangle$ so $|\Psi\rangle$ can represent the state of N indistinguishable particles. Conversely, for each choice of N one-body state labels $\alpha_1, ..., \alpha_N$ there is a state $\mathcal{S}_N|1:\alpha_1,\ 2:\alpha_2,\ \dots,\ N:\alpha_N\rangle$[1] in $\mathcal{S}_N(\mathcal{H}_N)$ to describe it. Particles that can be described by such states are called bosons.

The previous requirement can also be fulfilled by the totally antisymmetric states, *i.e.* states in $\mathcal{A}_N(\mathcal{H}_N)$ where $\mathcal{A}_N$ is the antisymmetrization operator, defined as

$$\mathcal{A}_N = \frac{1}{\sqrt{N!}} \sum_{\sigma\in\mathscr{S}_N} \varepsilon(\sigma) P_\sigma, \tag{1.4}$$

where $\varepsilon(\sigma) = \pm 1$ denotes the signature of the permutation σ. Here again, for any normalized $|\Psi\rangle \in \mathcal{A}_N(\mathcal{H}_N)$ and any permutation $\sigma \in \mathscr{S}_N$, $P_\sigma|\Psi\rangle = \varepsilon(\sigma)|\Psi\rangle = \pm|\Psi\rangle$ so $|\Psi\rangle$ can represent the state of N indistinguishable particles. Particles that can be described by such states are called fermions.

Bosons are symmetric under any exchange of 2 particles, while fermions are antisymmetric under these operations. This difference has drastic physical consequences. In particular, if the one-body state labels $\alpha_1, ..., \alpha_N$ are not pairwise distinct, there exists a corresponding bosonic state but there is no such fermionic state since $\mathcal{A}_N|1:\alpha_1,\ 2:\alpha_2,\ \dots,\ N:\alpha_N\rangle = 0$ (the zero element of $\mathcal{H}_N$). Said differently, a one-body state can be occupied by several bosons while it cannot have more than one fermion (Pauli exclusion principle).

Here and in the following, we will consider fermionic particles. To describe them in the corresponding many-body space $\mathcal{A}_N(\mathcal{H}_N)$, it is convenient to consider the states obtained by antisymmetrizing the states in $\mathcal{B}_N$ as

$$\begin{aligned}
|\alpha_1, \alpha_2, ..., \alpha_N\rangle &= \mathcal{A}_N|1:\alpha_1,\ 2:\alpha_2,\ \dots,\ N:\alpha_N\rangle \\
&= \frac{1}{\sqrt{N!}} \sum_{\sigma\in\mathscr{S}_N} \varepsilon(\sigma)|1:\alpha_{\sigma(1)},\ 2:\alpha_{\sigma(2)},\ \dots,\ N:\alpha_{\sigma(N)}\rangle \\
&= \frac{1}{\sqrt{N!}} \sum_{\sigma\in\mathscr{S}_N} \varepsilon(\sigma)|\alpha_{\sigma(1)}\rangle \otimes |\alpha_{\sigma(2)}\rangle \otimes ... \otimes |\alpha_{\sigma(N)}\rangle.
\end{aligned} \tag{1.5}$$

[1] If $\alpha_1, ..., \alpha_N$ are not pairwise distinct, $\mathcal{S}_N|1:\alpha_1,\ 2:\alpha_2,\ \dots,\ N:\alpha_N\rangle$ has to be normalized.

Due to the similarity of this expression with determinants, these states are called Slater determinants [5]. They have common properties with usual determinants that naturally encode the behaviour of fermions. Indeed, given two one-body state labels α_i, α_j one has

- $|\alpha_1, ..., \alpha_i, ..., \alpha_j, ..., \alpha_N\rangle = -|\alpha_1, ..., \alpha_j, ..., \alpha_i, ..., \alpha_N\rangle$ (antisymmetry with respect to the exchange of two particles),
- $|\alpha_1, ..., \alpha_i, ..., \alpha_i, ..., \alpha_N\rangle = 0$ (Pauli exclusion principle).

Importantly, if one denotes the one-body states in $\mathcal{H}_1$ as $\beta_1, ..., \beta_M$, the $\binom{M}{N}$ Slater determinants $|\beta_{k_1}, \beta_{k_2}, ..., \beta_{k_N}\rangle$ satisfying $k_1 < k_2 < ... < k_N$ form an orthonormal basis of $\mathcal{A}_N(\mathcal{H}_N)$ (see justification in appendix A).

1.1.3 Second quantized formulation

In order to consider states with different number of particles, one needs to define the so-called Fock space

$$F(\mathcal{H}_1) = \mathbb{C} \oplus \mathcal{H}_1 \oplus \mathcal{A}_2(\mathcal{H}_2) \oplus ... \oplus \mathcal{A}_M(\mathcal{H}_M), \tag{1.6}$$

where M is the number of independent one-body states (*i.e.* the dimension of $\mathcal{H}_1$)[2]. Note that a state in $F(\mathcal{H}_1)$ can be a linear combination of states with different numbers of particles. With the scalar product inherited from the $\mathcal{H}_N$'s (see appendix A), this is a Hilbert space.

On this space one can define $2M$ linear maps $F(\mathcal{H}_1) \to F(\mathcal{H}_1)$, which will be widely used in the following: the (fermionic) creation and annihilation operators $\{a^\dagger_\beta, a_\beta\}_\beta$. The creation operator associated to a one-body state β can be defined by the following action on Slater determinants

$$a^\dagger_\beta |\alpha_1, ..., \alpha_N\rangle = |\beta, \alpha_1, ..., \alpha_N\rangle. \tag{1.7}$$

As a consequence of Pauli exclusion principle, when $a^\dagger_\beta$ applies on a Slater determinant for which the one-body state labelled β is already populated by a particle, the result is 0. The corresponding annihilation operator a_β is its Hermitian conjugate, which behaves when applied to a Slater determinant as (see justification in appendix A)

$$a_\beta |\alpha_1, \alpha_2, ..., \alpha_N\rangle = \begin{cases} |\alpha_2, \alpha_3, ..., \alpha_N\rangle & \text{if } \beta = \alpha_1 \\ -|\alpha_1, \alpha_3, ..., \alpha_N\rangle & \text{if } \beta = \alpha_2 \\ \vdots & \vdots \\ (-1)^{N-1}|\alpha_1, \alpha_2, ..., \alpha_{N-1}\rangle & \text{if } \beta = \alpha_N \\ 0 & \text{if } \beta \notin \{\alpha_1, ..., \alpha_N\} \end{cases}. \tag{1.8}$$

One can deduce the following commutation relations

$$\forall \alpha, \beta, \quad \begin{aligned} a_\alpha a_\beta + a_\beta a_\alpha &= 0\,, \\ a^\dagger_\alpha a^\dagger_\beta + a^\dagger_\beta a^\dagger_\alpha &= 0\,, \\ a_\alpha a^\dagger_\beta + a^\dagger_\beta a_\alpha &= \delta_{\alpha\beta}\mathbb{1}\,. \end{aligned} \tag{1.9}$$

[2] As a consequence of the Pauli exclusion principle, the total number of particles N in a fermionic system cannot be higher than M. Moreover, if the dimension of $\mathcal{H}_1$ is not finite, neither is the dimension of $F(\mathcal{H}_1)$.

There exists a state $|\text{vac}\rangle$, called "vacuum state", such that $\forall\alpha,\ a_\alpha|\text{vac}\rangle = 0$. This is the state with no particles. It can be obtained from a Slater determinant $|\alpha_1, ..., \alpha_N\rangle$ by applying $a_{\alpha_N}...a_{\alpha_1}$ on it. Any N-body Slater determinant can be expressed as

$$|\alpha_1, ..., \alpha_N\rangle = a^\dagger_{\alpha_1}...a^\dagger_{\alpha_N}|\text{vac}\rangle. \tag{1.10}$$

This can be interpreted as the creation of N particles in states $\alpha_1, ..., \alpha_N$ on top of the vacuum. Since N-particle Slater determinants generate $\mathcal{A}_N(\mathcal{H}_N)$, any N-body state $|\Psi\rangle$ can be written with creation operators applied on the vacuum as

$$|\Psi\rangle = \sum_{1\leq\alpha_1<...<\alpha_N\leq M} c_{\alpha_1,...,\alpha_N} a^\dagger_{\alpha_1}...a^\dagger_{\alpha_N}|\text{vac}\rangle. \tag{1.11}$$

Also, any N-body operator O_N can be written as a combination of creation and annihilation operators as

$$O_N = \sum_{\substack{1\leq\alpha_1<...<\alpha_N\leq M\\ 1\leq\beta_1<...<\beta_N\leq M}} c_{\alpha_1,...,\alpha_N,\beta_N,...,\beta_1} a^\dagger_{\alpha_1}...a^\dagger_{\alpha_N} a_{\beta_N}...a_{\beta_1}. \tag{1.12}$$

This form, where in every term the creation operators are on the left and the annihilation operators are on the right, is called "normal ordered". Any given product of creation and annihilation operators can be normal ordered using commutation relations 1.9. While this can produce a lot of terms, this can be performed in an efficient way using Wick's theorem [6].

Finally, any operator O on the Fock space can be expressed as a combination of identity, 1-body, 2-body, ... operators, *i.e.*

$$O \;=\; c_0\,\mathbb{1} \;+\; \sum_{\alpha,\beta} c_{\alpha,\beta}\, a^\dagger_\alpha a_\beta \;+\; \sum_{\alpha_1,\alpha_2,\beta_1,\beta_2} c_{\alpha_1,\alpha_2,\beta_2,\beta_1}\, a^\dagger_{\alpha_1} a^\dagger_{\alpha_2} a_{\beta_2} a_{\beta_1} \;+\; \ldots\ . \tag{1.13}$$

This formulation of many-body states and operators will be the starting point for their encoding into qubits in section 2.6.

1.2 An overview of nuclear theory

This section gives an overview of nuclear theory, its scope, and the main methods used to model nuclei. A focus is made on the Green's function approach in anticipation of chapter 4.

1.2.1 What is nuclear physics?

Nuclear physics is the study of systems made of nucleons (neutrons and protons). It concerns especially atomic nuclei, but also bigger objects such as neutron stars. In these systems, nucleons are bound together by their interactions: the strong force, weak force, Coulomb repulsion and even gravity in neutron stars are combining together to produce at least a bound state. These interactions result in a difference between the mass of the system and the mass of its constituents when they are isolated. In particular, the mass of a nucleus made of N neutrons and Z protons can be decomposed as

$$m = Zm_p + Nm_n - \frac{E(N,Z)}{c^2} \tag{1.14}$$

where $E(N,Z)$ is the binding energy.

Nuclei can be classified according to their number of protons and neutrons, as in the Segrè chart in Fig. 1.1. Their number of nucleons ranges from two to a few hundreds, making their theoretical description challenging: most of the nuclei have too many nucleons for an exact treatment, and too few for statistical methods. This also implies a wide variety of phenomena.

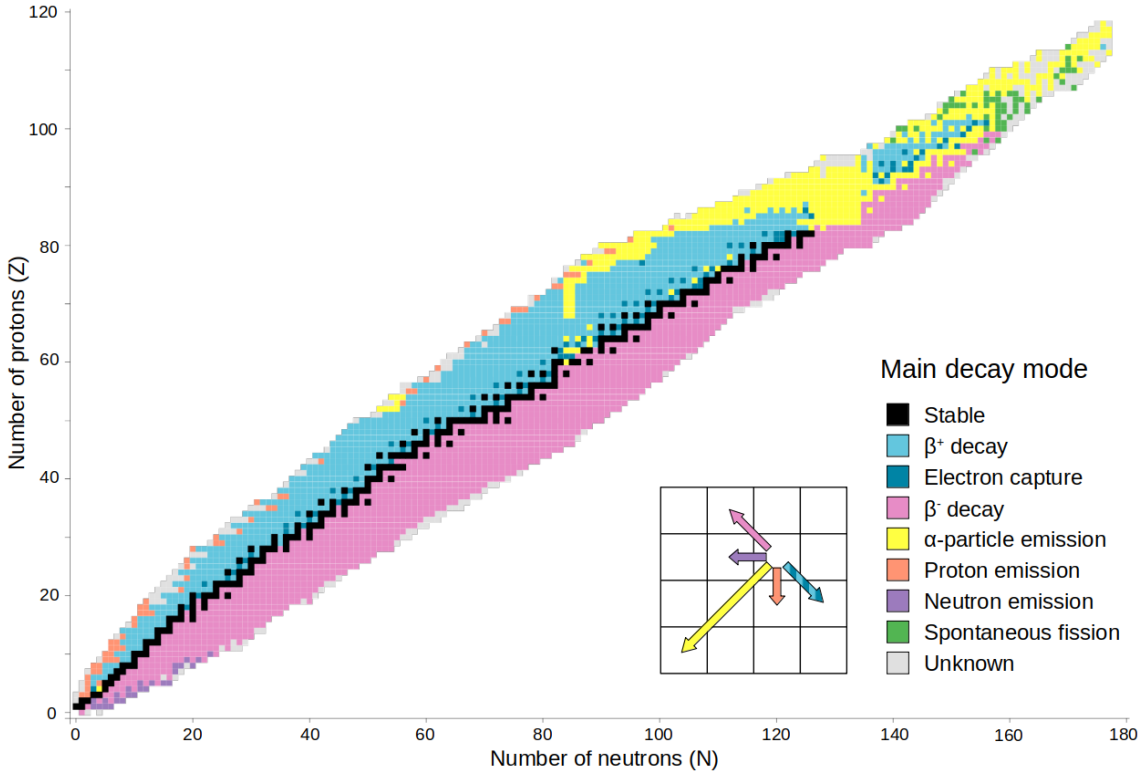


Figure 1.1: *Segrè chart, i.e. classification of the nuclei according to their number of neutrons and protons. The stable nuclei are represented in black. For the other ones, the colors indicate the main decay modes, as indicated in the legend. Decay modes result in a movement on the chart, as indicated next to the legend. Adapted from [7].*

Since nuclei have different binding energies, they can transform into each other via several types of processes (see Fig. 1.1). This decay defines a half-life duration for each nucleus, except for stable ones. Knowing their binding energies, half-life durations, or favourite types of decay are typical objectives of nuclear physics research. Many related questions remain open. For example, some models predict that some superheavy nuclei should exist beyond the heavier one ever observed (oganesson ^{294}Og, with 118 protons and 176 neutrons) with an increased half-life duration compared to other nuclei in this region of the Segrè chart, forming an "island of stability". Finding a process to build such nuclei is a challenge that has not been achieved yet. Intensive experimental and theoretical research also concerns exotic nuclei, *i.e.* nuclei that locates away from the stability valley (the "diagonal" region with stable isotopes). Nuclear physics is also concerned about nuclear reactions via collisions (in laboratory or in stars), excited states, deformation, ... with applications to other fields, *e.g.* research on nuclear astrophysics or applications to energy production. In order to understand and predict these phenomena, a wide variety of theoretical methods has been developed for a century.

1.2.2 Theoretical models

Here is a quick overview of some methods classically used to model atomic nuclei. A more complete review can be found in [8] or [9].

Early models

One of the first models of the atomic nucleus is the liquid drop model suggested by Gamov in 1929 [10]. Following this idea, Weizsäcker and Bethe proposed in 1935 a semi-empirical formula [11] for the binding energy of nuclei in their ground states as a function of N and Z

$$E(Z,N) = a_v A - a_s A^{2/3} - a_c \frac{Z}{A^{1/3}} - a_a \frac{(N-Z)^2}{A} - a_p \frac{\delta_0}{A^{k_p}}, \tag{1.15}$$

where the parameters $a_v, a_s, a_c, a_a, a_p, k_p$ are fitted on the data, and δ_0 takes the values $0, -1, 1$ respectively for $A = Z+N$ odd, Z and N odd, Z and N even. This formula describes the ground state binding energy due to the nuclear strong force. Limited in range, this force is considered to be exerted between neighbouring nucleons: each of the A nucleon feels the attraction of surrounding neighbours (hence the first term) except the nucleons on the surface (hence the second term). To be substracted, the repulsion due to Coulomb interaction between protons (third term) and an effect due to asymmetry between protons and neutrons (fourth term). The fifth term accounts for the pairing, due to spin coupling between nucleons in the same states up to spin projection. It reproduces the odd-even staggering observed in nuclear isotopic and isotonic chains.

This formula reproduces broadly the binding energies across the nuclear chart but is not sufficient. Difference with experimental data reveals some excess of stability for specific numbers of neutrons and protons, called "magic numbers" : $8, 20, 28, 50, 82, 126$. This can be put in parallel with the atomic model for which interaction between electrons is neglected so that they fill energy levels determined by the one-body potential created by the nucleus. These energy levels are grouped into shells (sets of close energy levels), and number of electrons corresponding to complete shells give particularly stable atoms. This inspired the non-interacting nuclear shell model which succeeded in reproducing the magic numbers after the contribution of Goeppert-Mayer and Jensen in 1949 [12, 13]. As a major difference with the atomic model, in the nucleus there is no such one-body potential created by an external element in which the nucleons can be placed in. The one considered in nuclear shell model comes from a mean field, *i.e.* an average on the interactions due to the nucleon themselves. Despite this difference, this model has revealed fruitful in modelling the properties of nuclei [14].

The era of QCD

Nucleons are not elementary particles. They are made of quarks and gluons, so nucleons interactions comes from the strong interaction between quarks and gluons, fundamentally described by Quantum Chromodynamics (QCD). Hence, a precise modelling of nuclei should account for this theory. But at energy scales relevant for nuclear physics, QCD is not perturbative, making exact calculations impossible in practice.

To overcome this issue, one can remark that at nuclear physics energy scales, quarks and gluons are confined into hadronic particles such as nucleons and pions. Therefore one can work with them as fundamental degrees of freedom, with an effective interaction between

them derived from QCD. To this extent, Effective Field Theories (EFT) [15] provide methods to build an effective Hamiltonian describing nucleon interactions from the Lagrangian of QCD. In particular, one can distinguish chiral EFTs from pionless EFTs. The former include the pions (the meson with the lowest energy) in the degrees of freedom, while the latter do not. Therefore, pionless EFTs provides easier calculations, but its range of application is limited to energy scales lower than the pion mass (around ~ 100 MeV), while chiral EFTs are valid until the second-lowest meson mass (the rho meson at ~ 800 MeV is one consider only up and down quarks).

The resulting Hamiltonian, together with the formalism introduced in section 1.1 allow to conveniently model a nucleus as a many-body problem. The Hamiltonian may depend on time (*e.g.* for reaction processes), but here and in the following one considers isolated nuclei, for which this is not the case. The states $|\Psi_k^A\rangle$ and energies E_k^A of a nucleus made of A nucleons are then solutions of the time-independent Schrödinger equation

$$H|\Psi_k^A\rangle = E_k^A|\Psi_k^A\rangle. \tag{1.16}$$

Ab initio approaches

This is the starting point for nuclear *ab initio* methods [16]. The meaning of *ab initio* ("from first principles") in this context might seem misleading since one starts with an effective Hamiltonian. Actually, starting with nucleon degrees of freedom appears to be sufficient at energy scales of nuclear physics to provide accurate predictions. Hence methods that consider these degrees of freedom together with an effective Hamiltonian derived from QCD, are said to be *ab initio* when they provide systematically improvable predictions with controlled uncertainties [17].

The computational cost of solving Eq. (1.16) with an exact diagonalisation[3] scales exponentially with the number of nucleons A. This currently limits the applicability of direct diagonalisation to $A \lesssim 20$. To consider heavier nuclei, *ab initio* methods approximate exact solutions by performing suitable truncations. First, the one-body Hilbert space has to be reduced to some finite-dimensional subspace in order to get a tractable A-body space. This can be done by truncating a suitable one-body basis *e.g.* harmonic oscillator basis. Then the exact solution is expanded on top of a reference state and this expansion is truncated to make the computation feasible. For instance, in Many-Body Perturbation Theory (MBPT), the Hamiltonian is split as $H = H_0 + H_1$ into an "easy" part H_0 and a "small" part H_1. This means that the ground state $|\Phi^{(0)}\rangle$ and energy $E^{(0)}$ of H_0 are easy to get, and the exact ground state $|\Phi\rangle$ and energy E of H are close to $|\Phi^{(0)}\rangle$ and $E^{(0)}$. MBPT describes how $|\Phi\rangle$ and E can be expanded on top of $|\Phi^{(0)}\rangle$ and $E^{(0)}$ [18].

This expansion implies the computation of terms with increasing complexity, up to the chosen truncation order. More sophisticated methods have been developed to include infinite subsets of such terms in the calculation via iterative processes, increasing the precision of the results with a limited impact on computational resources. They include in particular In-Medium Similarity Renormalisation Group [19, 20], Coupled Cluster [21, 22], and Self-Consistent Green's Functions [23–25] (see section 1.2.3). Importantly, these methods provide systematically improvable solutions, allowing to check that the result converges when

[3] To perform such a diagonalisation, the infinite-dimensional Hilbert space has to be truncated in a suitable way. To be valid, the results must converge with respect to this truncation.

increasing the truncation order. Moreover, their polynomial scaling with A has allowed progresses across the nuclear chart in the past two decades [16].

Effective approaches

Despite this significative improvement in terms of computational scaling, the range of applicability of *ab initio* methods is still currently limited to medium-mass nuclei [8, 16], or closed-shell nuclei up to lead [26, 27]. Alternative methods exist to deal with heavier nuclei in a more approximate way. They provide nicer computational scaling at the cost of a loss in predictive power.

A first type of approximations consists in neglecting some interactions, *i.e.* simplifying the Hamiltonian in order to reduce the active Hilbert space. The more drastic option is to suppose that the A nucleons do not interact (except via Pauli exclusion). This reduces the A-body problem (1.16) into A one-body problems $h_i|\phi_k^{(i)}\rangle = \varepsilon_k^{(i)}|\phi_k^{(i)}\rangle$. Their solutions define energy levels in which nucleons can be placed using Pauli exclusion principle, leading to the Non-Interacting Shell Model already evoked. While being a significant approximation, this model succeed in predicting large energy gaps between major shells.

This feature can be used as a starting point to include interactions while keeping some reduction of the computational effort *e.g.* by neglecting the interactions between the different major shells. This is the way followed by the Interacting Shell Model. It consists in defining a valence space, *i.e.* a Hilbert space describing only the nucleons in the incomplete shell(s), while keeping the other nucleons in a "frozen core" (closed shells). Then the problem can be solved exactly in the valence space, whose dimension is smaller than the full Hilbert space, saving computational resources. To build the Hamiltonian in the valence space, a first approach is to fit its parameters to experimental data. This phenomenological approach provides precise predictions in the regions of the nuclear chart where data is available, but becomes less accurate in other regions. Another way consists in deriving the valence space Hamiltonian from the full A-body Hamiltonian using many-body techniques, which grants more predictive power [28, 29]. For both strategies, one eventually faces limitations related to the size of the valence space when going to heavy nuclei.

A second type of approximations for the problem (1.16) consists in simplifying the wavefunction by using practical ansätze such as the ones given by Hartree-Fock theory. As a consequence, the interactions are encoded into an effective potential. This potential defines a functional giving the energy as a function of the density matrix (the state), which has to be minimised to find the ground state. The Energy Density Functional methods [30] are based on this functional rather than the Hamiltonian. Such functional is built from physical considerations and its parameters fitted on experimental data. The computational complexity of Energy Density Functional methods scales gently with A, allowing to reproduce many features of nuclei across the whole nuclear chart.

1.2.3 Self-consistent Green's functions

The Self-Consistent Green's Function (SCGF) method, an *ab-initio* technique evoked in previous subsection, uses as a key ingredient the Green's function. Since the chapter 4 describes a quantum computing method to calculate this object, a description is given here.

Initially introduced by Green in 1828 [31] for electromagnetism, the Green's function has revealed to be a powerful tool to solve differential equations. It can be defined as the solu-

tion G of the equation $\mathcal{D}G = \delta$, where $\mathcal{D}$ is a linear differential operator, and δ is the Dirac distribution. When $\mathcal{D}$ corresponds to Schrödinger or Klein-Gordon equations, G is called "propagator" or "two-point correlation functions". Green's function methods constitutes an alternative way to solve the many-body Schrödinger equation. In the SCGF context, the one body Green's function is defined as follows [32]

$$ig_{\alpha\beta}(t,t') := \langle\Psi_0^A|\mathcal{T}[a_\alpha(t)a_\beta^\dagger(t')]|\Psi_0^A\rangle, \tag{1.17}$$

where $|\Psi_0^A\rangle$ is the A-body ground state, $\mathcal{T}[.]$ is the time-ordering operator, and $a_\alpha(t), a_\beta^\dagger(t')$ are the annihilation and creation operators corresponding to one-body states α, β in Heisenberg picture.

One usually considers systems that are invariant under time translation. In this case, the Green's function $g_{\alpha\beta}(t,t')$ depends only on $t'-t$. The resulting single-variable function can be Fourier transformed, and written in the so-called Lehman's representation

$$g_{\alpha\beta}(\omega) = \sum_\nu \frac{\langle\Psi_0^A|\hat{a}_\alpha|\Psi_\nu^{A+1}\rangle\langle\Psi_\nu^{A+1}|\hat{a}_\beta^\dagger|\Psi_0^A\rangle}{\omega-(E_\nu^{A+1}-E_0)+i\eta} + \sum_\mu \frac{\langle\Psi_0^A|\hat{a}_\beta^\dagger|\Psi_\mu^{A-1}\rangle\langle\Psi_\mu^{A-1}|\hat{a}_\alpha|\Psi_0^A\rangle}{\omega-(E_0-E_\mu^{A-1})-i\eta}\,, \tag{1.18}$$

where the parameter $\eta > 0$ has to be considered in the limit $\eta \to 0^+$ after $g_{\alpha\beta}(\omega)$ has been used to compute quantities that do not diverge in this limit. E_0 is the ground-state energy (associated with the A-body ground state $|\Psi_0^A\rangle$), and $\{E_\nu^{A\pm1}, |\Psi_\nu^{A\pm1}\rangle\}_\nu$ are the ground and excited states and energies of the systems with $A\pm1$ particles, making explicit the fact that A-body Green's functions contain information about $(A\pm1)$-body systems. In the numerators, the spectroscopic amplitudes $\langle\Psi_\nu^{A+1}|\hat{a}_\beta^\dagger|\Psi_0^A\rangle$ and $\langle\Psi_\mu^{A-1}|\hat{a}_\alpha|\Psi_0^A\rangle$ correspond, once modulus-squared, to the probabilities of reaching the eigenstates ν and μ of the $(A\pm1)$-body systems by adding or removing a particle to/from the A-body system. In the denominators, the poles are the corresponding separation energies.

Green's functions are typically obtained using an equation of motion. Starting from the equation of motion for creation and annihilation operators $i\frac{d}{dt}a_\alpha^{(\dagger)}(t) = [a_\alpha^{(\dagger)}(t), H]$ and moving to the Fourier domain, one eventually derives the so-called Dyson equation

$$g_{\alpha\beta}(\omega) = g_{0\,\alpha\beta}(\omega) + \sum_{\gamma\delta} g_{0\,\alpha\gamma}(\omega)\Sigma^*_{\gamma\delta}(\omega)g_{\delta\beta}(\omega). \tag{1.19}$$

In this equation, $g_{0\,\alpha\beta}$ is the uncorrelated Green's function, defined in the same way as $g_{\alpha\beta}$ in Eq. (1.17) but with an uncorrelated state instead of the exact $|\Psi_0^A\rangle$. $\Sigma^*_{\gamma\delta}$ is the irreducible self-energy, encoding the interactions in the system (and depending also on $g_{\alpha\beta}$, which makes this approach self-consistent). Dyson's equation can be solved self-consistently, *i.e.* injecting an initial guess for $g_{\alpha\beta}$ on the right-hand side of the equation to get a resulting $g_{\alpha\beta}$ closer to the exact value, and iterating until convergence. Approximations are made into the self-energy, using algebraic or diagrammatic methods. Once the Green's function is computed, the density matrix and any one-body operator $O = \sum_{\alpha\beta} o_{\alpha\beta}a_\alpha^\dagger a_\beta$ expectation values can be obtained via

$$\rho_{\alpha\beta} := \langle\Psi_0^A|a_\alpha^\dagger a_\beta|\Psi_0^A\rangle = \lim_{t'\to t^+} g_{\alpha\beta}(t,t'), \tag{1.20}$$

and

$$\langle\Psi_0^A|O|\Psi_0^A\rangle = \sum_{\alpha\beta} o_{\alpha\beta}\rho_{\alpha\beta}. \tag{1.21}$$

This can be generalised to higher-body operators as explained in [32].

In the following chapters, results of Green's function calculations will be presented using their trace, which can be expressed as

$$F(\omega) := \sum_{\alpha} g_{\alpha\alpha}(\omega) = \sum_{\nu} \frac{SF_{\nu}^{+}}{\omega - (E_{\nu}^{A+1} - E_0) + i\eta} + \sum_{\mu} \frac{SF_{\mu}^{-}}{\omega - (E_0 - E_{\mu}^{A-1}) - i\eta}, \tag{1.22}$$

where

$$SF_{\nu}^{+} := \sum_{\alpha} |\langle \Psi_0^A | \hat{a}_{\alpha} | \Psi_{\nu}^{A+1} \rangle|^2 \quad \text{and} \quad SF_{\mu}^{-} := \sum_{\alpha} |\langle \Psi_0^A | \hat{a}_{\beta}^{\dagger} | \Psi_{\mu}^{A-1} \rangle|^2 \tag{1.23}$$

are the spectroscopic factors. To give an example, the real and imaginary parts of this function are plotted in Fig. 1.2, exactly computed for the pairing Hamiltonian defined in section 1.3.1. They present peaks at the separation energies, with a height determined by the spectroscopic factors. The width of the peaks is fixed by the parameter η. In chapter 4, this function will be used to gauge the quality of the computed Green's function.

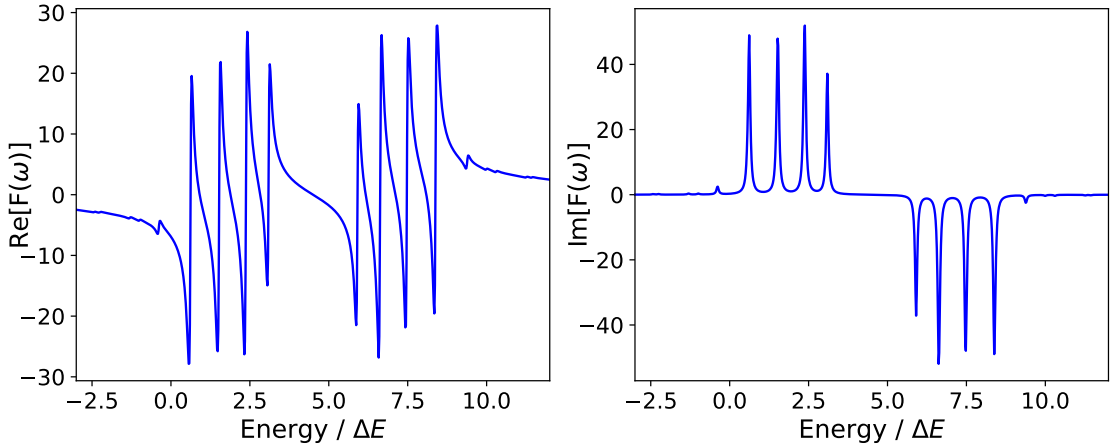


Figure 1.2: *Real (left) and imaginary (right) part of the function (1.22) computed exactly for a system of $A = 8$ particles on $D = 8$ doubly-degenerated levels governed by the pairing Hamiltonian (see section 1.3.1) with coupling strength $g = 0.6$. The width of the peaks has been set to $\eta = 0.04$.*

1.3 Two models relevant for nuclear theory

Quantum computing is a promising approach to push forward the current limits of nuclear theory. However, the complexity of realistic nuclei models is beyond today's capabilities of quantum computers. At this point in time, to explore the potential of quantum computing for nuclear theory, one needs simple models to start with. This section presents two such models that will be used as test models in the following chapters.

1.3.1 The pairing model

When considering the binding energies of an isotopic chain of nuclei, one realizes that systems with an even number of neutrons N are more bound than their odd-N neighbours. This can also be observed with protons in isotonic chains. This phenomenon, called "odd-even staggering", is caused by nucleon pairing: when two of them occupy time-reversed

single-particle states *i.e.* one-body states that are equal up to the spin projections, they interact in such a way that they can form a correlated pair. This effect is similar to the pairing of electrons in superconducting materials, or the pairing of ^{3}He atoms in the superfluid phase. Bardeen, Cooper, and Schrieffer proposed in late 1950's a theory to describe it, therefore called "BCS theory" [33]. Developed in the context of superconductivity, it has then been adapted to nuclear theory where it is frequently used to model pairing effects in nuclei [30, 34–36].

The pairing Hamiltonian

The pairing correlations in nuclei are difficult to treat. However, simple models of pairing exist, isolating this effect from other ones. In particular, the BCS theory provides the pairing Hamiltonian, for which one considers the following form here and in next chapters

$$H_P = \sum_{k=1}^{D} \varepsilon_k (a_k^\dagger a_k + a_{\bar{k}}^\dagger a_{\bar{k}}) - g \sum_{k \neq l} \sum a_k^\dagger a_{\bar{k}}^\dagger a_{\bar{l}} a_l \, . \tag{1.24}$$

It describes a system made of particles that can occupy $2D$ single-particle states. The latter are organized into D levels associated with energies $\varepsilon_1, ..., \varepsilon_D$. For $k \in \{1, ..., D\}$, the k^{th} level contains two degenerate single-particle states labelled k and $\bar{k}$ (time-reversed states). The parameter g corresponds to the strength of the pairing interaction. The higher it is, the lower is the energy of configurations where the particles are organized in pairs, *i.e.* where the levels contain either 0 or 2 particles. For simplicity in the following, let us consider the case of equally spaced levels, *i.e.* $\forall k, \varepsilon_k = k\Delta E$. Since the only relevant parameter left is $g/\Delta E$, one can set ΔE to 1, meaning that g is expressed in units of ΔE.

This Hamiltonian has a block-diagonal structure in Fock space, where each block is defined by the total number of particles A, the number of unpaired particles (*i.e.* the number of levels occupied by 1 particle in one of its two degenerate single-particle states), and the single-particle states occupied by these unpaired particles. One can show that when A is even, the A-body ground state belongs to the subspace with no unpaired particles (the seniority-0 subspace). Since it is preserved by Hamiltonian (1.24), one can work in this subspace, whose dimension is $\binom{D}{A/2}$, instead of the full A-body space, whose dimension is $\binom{2D}{A}$. For instance, if we consider 8 particles on 8 (doubly degenerated) levels, the full 8-body space has a dimension $\binom{16}{8} = 12870$ while the fully-paired subspace has a dimension $\binom{8}{4} = 70$. In this subspace, the problem can be simplified by introducing the pair creation and annihilation operators $P_k^\dagger = a_k^\dagger a_{\bar{k}}^\dagger$ and $P_k = a_{\bar{k}} a_k$ for $k \in \{1, ..., D\}$ and rewriting the pairing Hamiltonian (1.24) as

$$H'_P = \sum_{k=1}^{D} 2\varepsilon_k P_k^\dagger P_k - g \sum_{k \neq l} \sum P_k^\dagger P_l \, . \tag{1.25}$$

Indeed, in the fully-paired subspace, $a_k^\dagger a_k + a_{\bar{k}}^\dagger a_{\bar{k}} = 2P_k^\dagger P_k$ (which is not true in the full space). This form in terms of pair operators will be exploited in the following chapters.

The BCS ansatz

BCS theory also provides an ansatz wavefunction that can be optimised to approximate the ground state of (1.24), namely

$$|\Psi_{BCS}\rangle = \prod_{k=1}^{D}(U_k + V_k a_k^\dagger a_{\bar{k}}^\dagger)|\text{vac}\rangle, \tag{1.26}$$

where $\{U_k, V_k\}_k$ are the parameters to optimise with the constraint $\forall k, |U_k|^2+|V_k|^2 = 1$ (due to normalization). Actually, one can show that for the ground state of (1.24) these amplitudes are real and positive in the basis of Slater determinants[4]. So one can write $\forall k, U_k = \sin(\theta_k)$ and $V_k = \cos(\theta_k)$ with $0 \leq \theta_k \leq \frac{\pi}{2}$, and consequently get rid of the normalization condition.

This ansatz is a combination of states with different number of particles. Since the physical system has a fixed number of particles A, one should in principle, at the end of the computation, project the result into the A-particle subspace. However, the optimisation might result in a wavefunction with a small amplitude in this subspace, making such projection difficult due to amplification of errors. To prevent this issue, one has to force the system to stay close to the A-particle subspace during the optimisation. This can be achieved using the particle-number operator $\hat{N}$ with a Lagrange multiplier λ, to obtain a state with the right number of particles in average, after the minimisation of

$$\langle\Psi_{BCS}|\Big(H - \lambda(\hat{N} - A)\Big)|\Psi_{BCS}\rangle. \tag{1.28}$$

This is an example of a method using symmetry breaking to solve a problem. Symmetry breaking (usually on the number of particles or the rotational symmetry in the context of nuclear physics) is a powerful tool for many-body methods, allowing to avoid divergences due to degeneracies [37, 38] and to build product state ansätze containing more correlations that the symmetry-preserving product states, *i.e.* Slater determinants. It is a key ingredient in state-of-the-art methods for nuclear Density Functional Theory [9, 30] and ab-initio calculations [39–41].

For the BCS wavefunction, an optimisation on only two parameters is required. Indeed, minimising the quantity (1.28) implies to cancel its derivatives with respect to parameters $\theta_1, ..., \theta_D$ and λ. As derived in [35], the resulting equations can be rearranged into

$$\begin{aligned} |U_k|^2 &= \frac{1}{2}\Big(1 + \frac{k\Delta E - \lambda}{\sqrt{(k\Delta E - \lambda)^2 + \Delta^2}}\Big), \\ |V_k|^2 &= \frac{1}{2}\Big(1 - \frac{k\Delta E - \lambda}{\sqrt{(k\Delta E - \lambda)^2 + \Delta^2}}\Big), \end{aligned} \tag{1.29a}$$

[4] Given a state $|\Psi_{GS}\rangle = \sum_i c_i|\phi_i\rangle$ expressed in the basis of Slater determinants $\{|\phi_i\rangle\}_i$, its energy (with Hamiltonian (1.24)) can be written as

$$\langle\Psi_{GS}|H_P|\Psi_{GS}\rangle = \sum_{k=1}^{D}\sum_i |c_i|^2\varepsilon_k\langle\phi_i|(a_k^\dagger a_k + a_{\bar{k}}^\dagger a_{\bar{k}})|\phi_i\rangle - g\sum_{k\neq l}\sum_i\sum_j c_i^* c_j\langle\phi_i|a_k^\dagger a_{\bar{k}}^\dagger a_{\bar{l}} a_l|\phi_j\rangle\ . \tag{1.27}$$

For any set of indices i, j, k, l, $\langle\phi_i|a_k^\dagger a_{\bar{k}}^\dagger a_{\bar{l}} a_l|\phi_j\rangle = (0 \text{ or } 1) \geq 0$, so replacing the coefficients c_i by their modulus $|c_i|$ increases (in absolute value) the interaction term while not affecting the first term. As a result, the ground state (which minimises the energy) necessarily have positive real amplitudes in its decomposition into Slater determinants.

$$\sum_{k=1}^{D}\left(1-\frac{k\Delta E-\lambda}{\sqrt{(k\Delta E-\lambda)^2+\Delta^2}}\right)=A, \tag{1.29b}$$

$$\sum_{k=1}^{D}\frac{1}{\sqrt{(k\Delta E-\lambda)^2+\Delta^2}}=\frac{2}{g}. \tag{1.29c}$$

The Fermi energy λ and the gap Δ are determined by Eq. (1.29b) and Eq. (1.29c), reflecting respectively the average particle number, and the minimisation of the energy. The two equations have to be solved simultaneously (this can be easily done numerically) to get λ and Δ. When $g/\Delta E$ is smaller than a critical value (obtained with $\Delta = 0$ in Eq. (1.29c)), these equations cannot be solved and this approach fails. This identifies the phase transition between normal and superfluid states. Above the critical value, λ and Δ are well-defined and can be injected into Eqs. (1.29a) to obtain the values of $\{U_k, V_k\}_k$, resulting in the optimised BCS state $|\Psi_{BCS}\rangle$.

Once this optimisation is achieved, one might want to project this symmetry-breaking state into the subspace with the right number of particles. This can be realized at polynomial cost using projection techniques [9, 42]. Quantum computing methods have also been developed to perform this projection [43]. The projection can also be carried out before the optimisation, *i.e.* the optimisation can be performed with the projected state. These two schemes will be denoted PAV (Projection After Variation) and VAP (Variation After Projection) in the following.

In chapters 3 and 4, the pairing Hamiltonian will be used to test quantum computing methods. In particular, the ground energy of the system and the corresponding Green's function will be addressed. The BCS approximation presented in this subsection will serve as a benchmark.

1.3.2 A model for the deuteron

Pairing is an important piece for the modelling of nuclei, but other effects are present. However encoding the full, realistic nuclear Hamiltonian on quantum computers is currently very challenging. Actually, an EFT provides a relatively simple Hamiltonian that can be used in quantum computing applications. This is the pionless EFT, corresponding to the low-energy limit of QCD, with only nucleons as degrees of freedom. Applicable at energy scales below the pion mass, it has been successfully used for light nuclei in classical calculations. Let us start with the simplest nucleus: the deuteron. This nucleus formed by a neutron and a proton has been simulated on a quantum computer in [44]. In this paper, the authors used pionless EFT at leading order to get a Hamiltonian expressed in the harmonic oscillator basis with a single operator (in addition to the kinetic terms): a contact operator in the ${}^3S_1$ partial wave. When the basis is truncated to the M first basis states, the resulting deuteron Hamiltonian reads as (see [44])

$$H_D = \sum_{k,k'=0}^{M-1} \langle k'|(T+V)|k\rangle a^\dagger_{k'} a_k \ , \tag{1.30}$$

where the kinetic energy and potential matrix elements read as

$$\langle k'|T|k\rangle = \frac{\hbar\omega}{2}\left[(2k+3/2)\delta_k^{k'} - \sqrt{k(k+1/2)}\delta_k^{k'+1} - \sqrt{(k+1)(k+3/2)}\delta_k^{k'-1}\right],$$
$$\langle k'|V|k\rangle = V_0\delta_k^0\delta_k^{k'}.$$

with $V_0 = -5.68658111$ MeV and $\hbar\omega = 7$ MeV. It can be written in a more synthetic way as

$$\frac{1}{\hbar\omega}H_D = \left(\frac{3}{4} - \frac{|V_0|}{\hbar\omega}\right)a_0^\dagger a_0 + \sum_{k=1}^{M-1}\left(k+\frac{3}{4}\right)a_k^\dagger a_k - \frac{1}{2}\sum_{k=1}^{M-1}\sqrt{k\left(k+\frac{1}{2}\right)}\left(a_{k-1}^\dagger a_k + a_k^\dagger a_{k-1}\right). \quad (1.31)$$

The ground energy E of the Deuteron (within this simple effective model) in the full (infinite-dimensional) Hilbert space can be obtained by computing the ground energy E_M of Hamiltonian (1.31) for increasing values of the truncation order M until convergence, as illustrated in Fig. 1.3, using[5] $E_2 \geq E_3 \geq ... \geq E$. This model will be used as a test model in chapter 6.

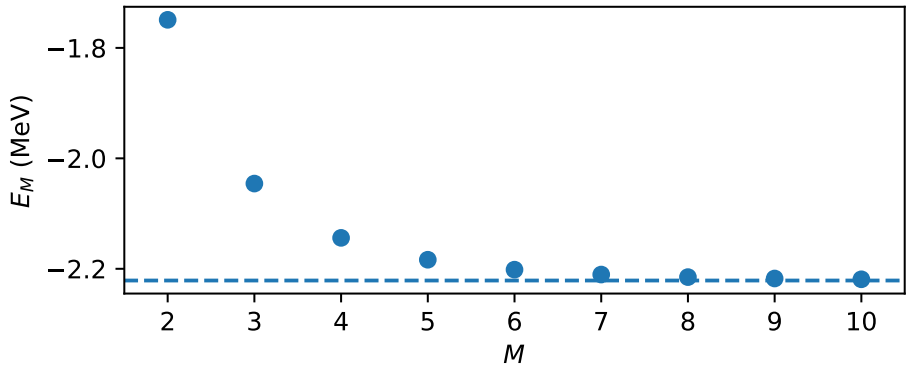


Figure 1.3: *Deuteron energy computed from exact diagonalisation of Hamiltonian (1.31) for several values of the truncation order M. One observes a convergence, as M increases, towards the ground state energy in the non-truncated space, indicated by the dashed line.*

1.4 Conclusion

This chapter has presented some elements of many-body physics and nuclear theory. Some methods used and developed in order to model nuclei have been evoked. This is not an easy task, but past and current research makes progresses across the nuclear chart. In parallel, quantum computing is also developing. While it also faces its own challenges, its potential for the modelling of many-body systems makes it promising for nuclear theory.

The next chapter introduces quantum computing and explains how a many-body problem can be encoded into qubits in order to compute expectation values of observables. The pairing model will be used to benchmark digital quantum computing methods designed to approximate a ground state in chapter 3 and to compute in chapter 4 the Green's functions introduced in section 1.2.3. The deuteron model will be used to test analog quantum computing techniques in chapter 6.

[5]Indeed, given two subspaces $A \subset B$, the state with minimal energy in B has an energy lower or equal to the energy of every state in B, including the states in A and in particular the state with minimal energy in A.

Chapter 2

Digital quantum computing

This chapter is a quick introduction to digital quantum computing. It follows two objectives. The first one is to provide some elements of understanding to a reader who is familiar with quantum mechanics but not with quantum computing. The second one is to establish some details which will be used in the following chapters. After some preliminaries in section 2.1 on Pauli strings, Hermitian operators and unitaries, a first description of the qubit is given in section 2.2, with some details on operations and measurement. The generalisation to several qubits is used in section 2.3 to introduce quantum computing, with an emphasis on measurement in section 2.4. Applications are evoked through some examples of quantum algorithms explained in section 2.5. In section 2.6, a specific focus is made on the encoding of the quantum many-body problem, which is the scope of the thesis. For a more complete view on quantum computing, see [45, 46].

2.1 Algebraic preliminaries

Some algebraic notions used in the following are introduced here. Let us consider an n-dimensional Hilbert space $\mathcal{H}$ and the space of its endomorphisms $\mathcal{L}(\mathcal{H})$. The identity of $\mathcal{L}(\mathcal{H})$ will be written $\mathbb{1}$. For $A \in \mathcal{L}(\mathcal{H})$, its Hermitian conjugate is denoted $A^\dagger$.

2.1.1 Pauli strings

The Pauli operators X, Y, Z are the elements of $\mathcal{L}(\mathbb{C}^2)$ whose matrices in the canonical basis write as

$$X = \begin{pmatrix} 0 & 1 \\ 1 & 0 \end{pmatrix}, \quad Y = \begin{pmatrix} 0 & -i \\ i & 0 \end{pmatrix}, \quad Z = \begin{pmatrix} 1 & 0 \\ 0 & -1 \end{pmatrix}. \tag{2.1}$$

It is usually convenient to keep in mind their products and commutators, *i.e.*

$$X^2 = Y^2 = Z^2 = \mathbb{1}, \qquad XY = iZ, \qquad YX = -iZ, \qquad [X, Y] = 2iZ, \tag{2.2}$$

and similarly with circular permutations of X, Y, Z.

$\mathbb{1}, X, Y, Z$ can be assembled using the Kronecker product "$\otimes$" to build operators on bigger spaces. Indeed, for some $N \in \mathbb{N}^*$ and $\sigma_1, ..., \sigma_N \in \{\mathbb{1}, X, Y, Z\}$, $\sigma_1 \otimes ... \otimes \sigma_N$ is an operator acting on a 2^N Hilbert space, usually called a Pauli string. In the following, the notation $\mathcal{P}_N := \{\sigma_1 \otimes ... \otimes \sigma_N \ / \ \sigma_1, ..., \sigma_N \in \{\mathbb{1}, X, Y, Z\}\}$ is adopted for the set of all Pauli strings of length N. For $i \in \{1, ..., N\}$, it is common to denote $Z_i = \mathbb{1} \otimes ... \otimes Z \otimes ... \otimes \mathbb{1}$ the Pauli string made only of $\mathbb{1}$'s except in position i where there is a Z. Similarly with X and Y.

2.1.2 Hermitian operators

An operator $A \in \mathcal{L}(\mathcal{H})$ is said to be Hermitian-symmetric or just Hermitian when $A^\dagger = A$. The set of all Hermitian operators on $\mathcal{H}$, denoted here $\mathcal{L}_H$, forms a vector subspace of $\mathcal{L}(\mathcal{H})$. Consider the case $n = 2$. In the canonical basis of $\mathcal{H}$, a Hermitian operator $A \in \mathcal{L}_H$ can be written as

$$A = \begin{pmatrix} \alpha + \delta & \beta - i\gamma \\ \beta + i\gamma & \alpha - \delta \end{pmatrix} = \alpha \mathbb{1} + \beta X + \gamma Y + \delta Z, \tag{2.3}$$

where $\alpha, \beta, \gamma, \delta \in \mathbb{R}$. Moreover, this decomposition is unique, meaning that $\mathcal{P}_1 = \{\mathbb{1}, X, Y, Z\}$ is a basis of $\mathcal{L}_H$ as a real vector space.

Consider now the case $n = 2^N$ for some $N \in \mathbb{N}^*$. Similarly to the case $N = 1$, $\mathcal{P}_N$ is a basis of $\mathcal{L}_H$ as a real vector space. Indeed,

- Since $\mathcal{H}$ is a 2^N-dimensional Hilbert space, an operator $A \in \mathcal{L}(\mathcal{H})$ is determined by *a priori* 2^{2N} complex parameters, *i.e.* 2^{4N} real parameters. However, the condition $A^\dagger = A$ reduces the number of free parameters by a factor 2. Then, $\mathcal{L}_H$ is a 2^{2N}-dimensional $\mathbb{R}$-vector space.
- $\mathcal{P}_N$ contains 2^{2N} elements (4 possibilities for each of the N factors) and they all belong to $\mathcal{L}_H$ since for $\sigma_1, ..., \sigma_N \in \{\mathbb{1}, X, Y, Z\}$, $(\sigma_1 \otimes ... \otimes \sigma_N)^\dagger = \sigma_1^\dagger \otimes ... \otimes \sigma_N^\dagger = \sigma_1 \otimes ... \otimes \sigma_N$.
- Let $\hat{0}$ be the null operator on $\mathcal{L}_H$, and $\{\lambda_{\sigma_1,...,\sigma_N}\}_{\sigma_1,...,\sigma_N \in \{\mathbb{1},X,Y,Z\}}$ a set of 2^{2N} real numbers such that

$$\sum_{\sigma_1,...,\sigma_N \in \{\mathbb{1},X,Y,Z\}} \lambda_{\sigma_1,...,\sigma_N} \sigma_1 \otimes ... \otimes \sigma_N = \hat{0}\,. \tag{2.4}$$

  Tracing out this equality gives[1] $2^N \lambda_{\mathbb{1},...,\mathbb{1}} = 0$, so $\lambda_{\mathbb{1},...,\mathbb{1}} = 0$. For any other Pauli string $P = \rho_1 \otimes ... \otimes \rho_N$, one can multiply Eq. (2.4) by P before tracing out, to show in the same way[2] that its coefficient $\lambda_{\rho_1,...,\rho_N}$ is zero. Thereby $\mathcal{P}_N$ is linearly independent.

Then, any Hermitian operator on $\mathcal{H}_{2^N}$ writes (in a unique way) as a linear combination of Pauli strings, with real coefficients.

2.1.3 Unitary operators

An operator $U \in \mathcal{L}(\mathcal{H})$ is said to be unitary when $UU^\dagger = U^\dagger U = \mathbb{1}$, *i.e.* U is invertible and its inverse is its Hermitian conjugate. For example, Pauli strings are unitary since they are Hermitian and square to $\mathbb{1}$. The set of all unitary operators acting on the n-dimensional space $\mathcal{H}$, together with the composition of operators, forms a group called the unitary group, and denoted $U(n)$.

Importantly, unitary operators are isometries. In particular they preserve the norm. Another important property: any unitary operator can be written $U = e^{iA}$ where $A \in \mathcal{L}_H$ (and conversely for any $A \in \mathcal{L}_H$, e^{iA} is unitary). Indeed, $U(n)$ is a Lie group associated to the Lie algebra $\mathfrak{u}(n)$ consisting of all anti-Hermitian operators of $\mathcal{L}(\mathcal{H})$ (B anti-Hermitian means $B^\dagger = -B$), and any anti-Hermitian operator B can be written $B = iA$ where A is a Hermitian operator.

[1] Indeed, $\mathrm{Tr}(X) = \mathrm{Tr}(Y) = \mathrm{Tr}(Z) = 0$, and $\mathrm{Tr}(\mathbb{1}) = 2$. Moreover for any operators $A_1, ..., A_N$, $\mathrm{Tr}(A_1 \otimes ... \otimes A_N) = \mathrm{Tr}(A_1)...\mathrm{Tr}(A_N)$. So the trace of any Pauli string is 0 except for the identity.

[2] Using properties of Eq. (2.2) one can see this multiplication by P realizes, up to some factors $\pm i$, a permutation of the Pauli strings where P is mapped to $P^2 = \mathbb{1} \otimes ... \otimes \mathbb{1}$.

2.2 The qubit

This section presents the qubit, the operations one can perform on it, and how information can be accessed via measurements.

2.2.1 Description

A qubit is a two-level quantum system. In practice, it can be realised in many different ways: the spin of a particle, two well-isolated energy levels of an atom or an ion, the polarisation or the path of a photon, the direction of the current in a superconducting electronic circuit... Its state is described by an element of $\mathbb{C}^2$, so it can be written as $|\Psi\rangle = a|0\rangle + b|1\rangle$ with $a, b \in \mathbb{C}$. As any quantum state, it is normalized ($|a|^2 + |b|^2 = 1$) and defined up to a global phase, so it is common to write it as

$$|\Psi\rangle = \cos\left(\frac{\rho}{2}\right)|0\rangle + e^{i\phi}\sin\left(\frac{\rho}{2}\right)|1\rangle\,, \tag{2.5}$$

with two angles $\rho \in [0, \pi]$ and $\phi \in [0, 2\pi[$. This defines also a point on a sphere, leading to the Bloch sphere representation of a qubit state, as illustrated in Fig. 2.1.

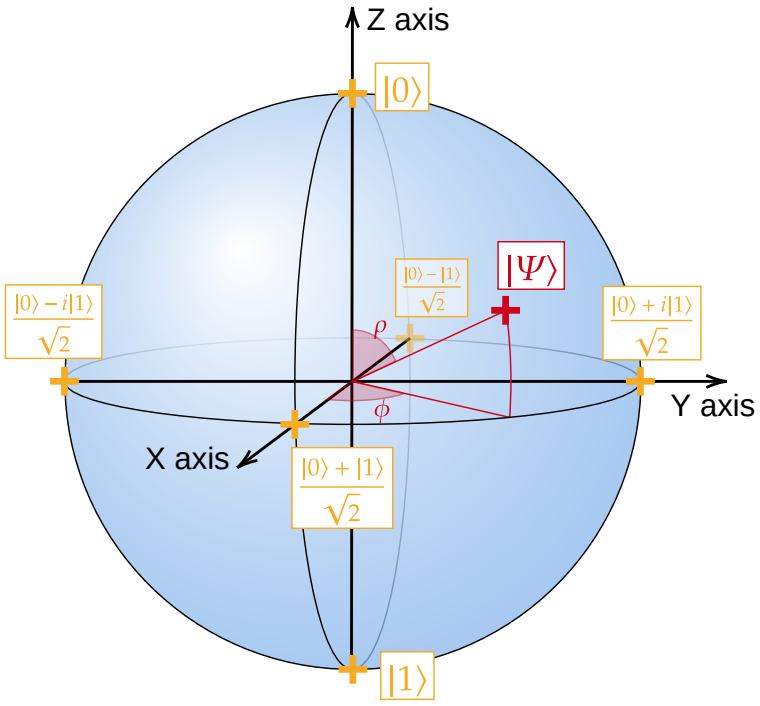


Figure 2.1: *Bloch sphere, whose points correspond to qubit states. The generic state* $|\Psi\rangle = \cos(\frac{\rho}{2})|0\rangle + e^{i\phi}\sin(\frac{\rho}{2})|1\rangle$ *is represented in red as the point on the sphere whose polar coordinates are* (ρ, ϕ)*. Some other states are represented in orange. The axis labels '*X *axis', '*Y *axis', '*Z *axis' are justified by the fact that the operators* $R_x(\theta) = e^{-i\frac{\theta}{2}X}$, $R_y(\theta) = e^{-i\frac{\theta}{2}Y}$, $R_z(\theta) = e^{-i\frac{\theta}{2}Z}$ *correspond to rotations with an angle* θ *around these three axes, respectively. More generally, given* $\vec{\sigma} = (X, Y, Z)$ *and a normalized vector* $\vec{v} \in \mathbb{R}$*, the operator* $R_{\vec{v}}(\theta) = e^{-i\frac{\theta}{2}\vec{v}\cdot\vec{\sigma}}$ *corresponds to a rotation with an angle* θ *around the axis defined by* $\vec{v}$*.*

2.2.2 Operations

Operations acting on a qubit are unitary maps on $\mathbb{C}^2$, *i.e.* elements the group $U(2)$. Combining the results established in section 2.1, any $U \in U(2)$ can be written using Pauli operators as

$$U = e^{i(\alpha\mathbb{1}+\beta X+\gamma Y+\delta Z)} = e^{i\alpha}e^{i(\beta X+\gamma Y+\delta Z)}, \tag{2.6}$$

where $\alpha, \beta, \gamma, \delta \in \mathbb{R}$. For example, $X = e^{-i\frac{\pi}{2}}e^{i\frac{\pi}{2}X}$, $Y = e^{-i\frac{\pi}{2}}e^{i\frac{\pi}{2}Y}$, and $Z = e^{-i\frac{\pi}{2}}e^{i\frac{\pi}{2}Z}$. To explicit unitaries further, let us denote $\theta^2 = \beta^2 + \gamma^2 + \delta^2$ so that $(\beta, \gamma, \delta) = (\theta v_x, \theta v_y, \theta v_z)$ where $\vec{v} = (v_x, v_y, v_z)$ is normalized, and $\vec{\sigma} = (X, Y, Z)$, leading to $U = e^{i\alpha}e^{i\theta\vec{v}\cdot\vec{\sigma}}$. One can check that $(\vec{v}\cdot\vec{\sigma})^2 = \mathbb{1}$, so $e^{i\theta\vec{v}\cdot\vec{\sigma}}$ can be expanded as

$$\begin{aligned} U &= e^{i\alpha}\Big(\sum_{k \text{ even}}\frac{(i\theta)^k}{k!}\mathbb{1} + \sum_{k \text{ odd}}\frac{(i\theta)^k}{k!}\vec{v}\cdot\vec{\sigma}\Big) = e^{i\alpha}\Big(\cos(\theta)\mathbb{1} + i\sin(\theta)\vec{v}\cdot\vec{\sigma}\Big) \\ &= e^{i\alpha}\begin{pmatrix}\cos(\theta)+iv_z\sin(\theta) & \sin(\theta)(iv_x+v_y)\\ \sin(\theta)(iv_x-v_y) & \cos(\theta)-iv_z\sin(\theta)\end{pmatrix}. \end{aligned} \tag{2.7}$$

Some common examples, which will be useful in the following, are defined on table 2.1.

Name	Operator
Rotation of 2θ around X axis	$R_x(2\theta) = e^{-i\theta X} = \begin{pmatrix}\cos(\theta) & -i\sin(\theta)\\ -i\sin(\theta) & \cos(\theta)\end{pmatrix}$
Rotation of 2θ around Y axis	$R_y(2\theta) = e^{-i\theta Y} = \begin{pmatrix}\cos(\theta) & -\sin(\theta)\\ \sin(\theta) & \cos(\theta)\end{pmatrix}$
Rotation of 2θ around Z axis	$R_z(2\theta) = e^{-i\theta Z} = \begin{pmatrix}e^{-i\theta} & 0\\ 0 & e^{i\theta}\end{pmatrix}$
Hadamard gate	$H = \frac{1}{\sqrt{2}}\begin{pmatrix}1 & 1\\ 1 & -1\end{pmatrix}$
Phase gate	$P(\theta) = e^{i\frac{\theta}{2}(\mathbb{1}-Z)} = \begin{pmatrix}1 & 0\\ 0 & e^{i\theta}\end{pmatrix}$
S gate	$S = P(\frac{\pi}{2}) = \begin{pmatrix}1 & 0\\ 0 & i\end{pmatrix}$
T gate	$T = P(\frac{\pi}{4}) = \begin{pmatrix}1 & 0\\ 0 & e^{i\frac{\pi}{4}}\end{pmatrix}$

Table 2.1: *Some common examples of one-qubit operators.*

$e^{-i\alpha}U = e^{i\theta\vec{v}\cdot\vec{\sigma}}$ can be interpreted as a rotation in the Bloch sphere around the axis defined by the normalized vector $\vec{v}$, with an angle 2θ. In particular, the rotations $R_x(2\theta)$, $R_y(2\theta)$, $R_z(2\theta)$ as defined in table 2.1 are obtained respectively with $\vec{v} = (1, 0, 0)$, $\vec{v} = (0, 1, 0)$, $\vec{v} = (0, 0, 1)$. Two such rotation axes are sufficient to generate any unitary in $U(2)$ (up to the global phase $e^{i\alpha}$). For example, given $U \in U(2)$, there exist angles α, η, μ, ν such that[3]

$$U = e^{i\alpha}R_z(\eta)R_y(\mu)R_z(\nu). \tag{2.8}$$

2.2.3 Measurement

While a classical bit of information has only two possible states (0 or 1), the possible states of a qubit are infinitely many. This can be understood with the correspondence between the qubit states and the points on a sphere, established with Eq. (2.5). However, a qubit does not contain more *accessible* information that a classical bit. Indeed, to access information, one has to measure it, *i.e.* project it in $|0\rangle$ or $|1\rangle$. This measurement has only two possible outcomes, which are usually labeled 0 and 1. They come with probabilities p_0 and p_1, which depend on the state $|\Psi\rangle$ of the qubit according to the Born rule

$$p_0 = |\langle 0|\Psi\rangle|^2, \qquad p_1 = |\langle 1|\Psi\rangle|^2. \tag{2.11}$$

If one knows how to prepare $|\Psi\rangle$, one can repeat the preparation and the measurement to approximate these probabilities. From these probabilities the expectation value of the Pauli operator Z can be reconstructed as

$$\langle\Psi|Z|\Psi\rangle = \langle\Psi|\Big(|0\rangle\langle 0| - |1\rangle\langle 1|\Big)|\Psi\rangle = |\langle 0|\Psi\rangle|^2 - |\langle 1|\Psi\rangle|^2 = p_0 - p_1. \tag{2.12}$$

Moreover, if one performs an operation U before the measurement, one measures the state $|\Psi'\rangle = U|\Psi\rangle$, giving access to the expectation value of Z on the state $|\Psi'\rangle$. This is also the expectation value of $U^\dagger ZU$ on the state $|\Psi\rangle$ since $\langle\Psi'|Z|\Psi'\rangle = \langle\Psi|U^\dagger ZU|\Psi\rangle$. For example, using $U = e^{i\frac{\pi}{4}Y}$ gives the expectation value of $e^{-i\frac{\pi}{4}Y}Ze^{i\frac{\pi}{4}Y} = X$. There are several ways to do it. As established in appendix B, the general expression of a unitary transformation U_x satisfying $X = U_x^\dagger Z U_x$ reads as (up to a global phase)

$$U_x = e^{i\theta G(\theta)} \quad \text{with} \quad G(\theta) = \text{cotan}(\theta)Y \pm \sqrt{\frac{1-\text{cotan}(\theta)^2}{2}}(X+Z), \tag{2.13}$$

where θ is an angle such that $\cos(2\theta) \leq 0$. These transformations correspond to a rotation of the Bloch sphere mapping the Z axis to the X axis, as illustrated in Fig. 2.2. It is quite common to use $U_x = H$ (Hadamard gate, defined on table 2.1) for that, which corresponds (up to a global phase) to $\theta = \frac{\pi}{2}$ in Eq. (2.13) and to the red circle in Fig. 2.2. Similarly, one can evaluate the expectation value of Y using a unitary U_y satisfying $Y = U_y^\dagger Z U_y$, *i.e.* a unitary U_y of the form (see appendix B):

$$U_y = e^{i\theta G(\theta)} \quad \text{with} \quad G(\theta) = -\text{cotan}(\theta)X \pm \sqrt{\frac{1-\text{cotan}(\theta)^2}{2}}(Y+Z), \tag{2.14}$$

for some angle θ such that $\cos(2\theta) \leq 0$. It is quite common to use $U_y = HS^\dagger$ (S is defined in table 2.1), which corresponds to $\theta = \frac{\pi}{3}$ in Eq. (2.14).

[3] Indeed, in Eq. (2.7), the diagonal coefficients of $e^{-i\alpha}U$ are conjugated, and similarly with the anti-diagonal coefficients. So one can rewrite them:

$$\begin{cases} \cos(\theta) \pm iv_z \sin(\theta) = Ce^{\pm i\varphi} \\ \sin(\theta)(iv_x \pm v_y) = \pm Se^{\pm i\varphi'} \end{cases}. \tag{2.9}$$

Since $C^2 + S^2 = \cos(\theta)^2 + (v_x^2 + v_y^2 + v_z^2)\sin(\theta)^2 = 1$, there is an angle θ' such that $C = \cos(\theta')$ and $S = \sin(\theta')$. This allows to write:

$$e^{-i\alpha}U = \begin{pmatrix} \cos(\theta')e^{i\varphi} & \sin(\theta')e^{i\varphi'} \\ -\sin(\theta')e^{-i\varphi'} & \cos(\theta')e^{-i\varphi} \end{pmatrix}. \tag{2.10}$$

Defining $\theta' = -\frac{\mu}{2}$, $\varphi = \frac{-\eta-\nu}{2}$, $\varphi' = \frac{-\eta+\nu}{2}$, this is the same as $R_z(\eta)R_y(\mu)R_z(\nu)$, as one can check if one performs the matrix product.

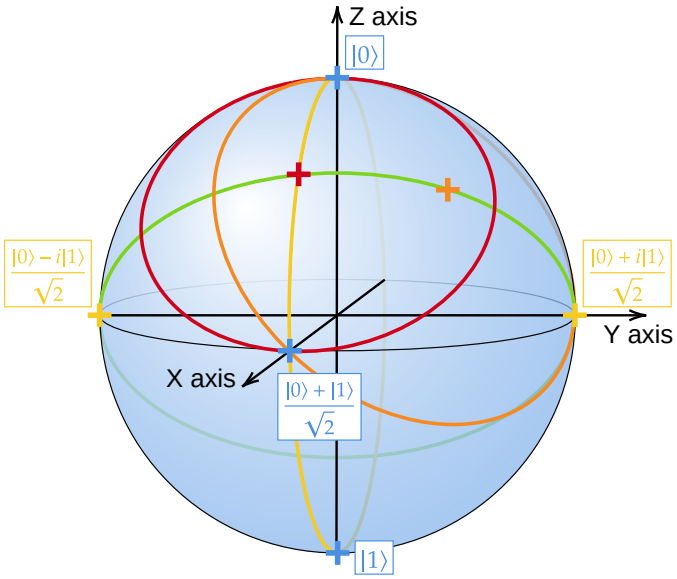


Figure 2.2: *Bloch sphere with a representation of some of the unitaries $U_x = e^{i\theta G(\theta)}$ defined in Eq. (2.13), mapping Z axis to X axis. In red: $\theta = \pi/2$. In orange: $\theta = \pi/3$. In yellow: $\theta = \pm\pi/4$. For each of them are represented, in the same color, the center of the corresponding rotation i.e. the point $(v_x, v_y, v_z) \in \mathbb{R}^3$ such that $G(\theta) = v_x X + v_y Y + v_z Z$, and the set of states $\{e^{itG(\theta)}|0\rangle / 0 \leq t \leq 2\pi\}$, forming a circle on the sphere. The green circle is the set of all possible such centers of rotation. Some other points are represented in blue with their related state.*

As established in section 2.1, any Hermitian operator on $\mathbb{C}^2$ can be written as a linear combination of $\mathbb{1}, X, Y, Z$ with real coefficients. So from repeated measurements on a qubit one can approximate expectation values of any 1-qubit observable. We will see in section 2.4 that this result holds with more qubits.

2.3 States and operations on several qubits

This section generalises the notions of section 2.2 to more than one qubit in order to introduce quantum computing. Some key results on qubits operations are evoked, and in particular how they can be built from operations on 1 and 2 qubits. This motivates the use of a convenient graphical representation: the quantum circuits which are presented here. Some elements of comparison between classical and quantum computing are given at the end of the section to guide the intuition.

2.3.1 States of *N* qubits

A state of N qubits is an element of $\mathcal{H}_N := \mathbb{C}^2 \otimes \mathbb{C}^2 \otimes ... \otimes \mathbb{C}^2$, *i.e.* the 2^N-dimensional Hilbert space generated by all bitstring states of length N. For example,

$$\begin{aligned} \mathcal{H}_2 &= \text{span}(\{|00\rangle, |01\rangle, |10\rangle, |11\rangle\}) \\ \mathcal{H}_3 &= \text{span}(\{|000\rangle, |001\rangle, |010\rangle, |011\rangle, |100\rangle, |101\rangle, |110\rangle, |111\rangle\}) \\ &... \end{aligned} \tag{2.15}$$

where the shorter notation $|b_1 b_2 ... b_N\rangle = |b_1\rangle \otimes |b_2\rangle \otimes ... \otimes |b_N\rangle$ is used.

Among all these states, one can distinguish the separable ones from the entangled ones. An N-qubit state $|\Psi\rangle$ is called separable when it can be written as a tensor product of 1-qubit states as $|\Psi\rangle = |\psi_1\rangle \otimes ... \otimes |\psi_N\rangle$. In this case, the states of its components are well-defined and can be considered individually. Otherwise, it is called entangled, and it is not possible to define its component individually in such a way that one can predict the correlations between the measurements performed on the components. An important example of entangled state is the Bell pair $\frac{|00\rangle+|11\rangle}{\sqrt{2}}$[4]. Entanglement is a quantum effect that is necessary [47] (but not sufficient [48]) for a quantum algorithm to surpass a classical one.

2.3.2 Operations on *N* qubits

The operations on (an isolated system of) N qubits are the elements of $U(2^N)$, *i.e.* the unitaries acting on $\mathcal{H}_N$. Importantly, this implies that these operations are reversible: no information is lost during the computation (until measurement). Another important consequence is the no-cloning theorem, stating that it is impossible to copy an N-qubit state. More precisely, there is no $2N$-qubit unitary U and N-qubit state $|s\rangle$ such that for any N-qubit state $|\psi\rangle$, $U(|s\rangle \otimes |\psi\rangle) = |\psi\rangle \otimes |\psi\rangle$[5].

Unitaries on several qubits can be built from 1-qubit unitaries using the following rules:

1. Given two m-qubit unitaries U and V, their composition $V.U$ is an m-qubit unitary. Indeed, $(V.U)^\dagger.(V.U) = U^\dagger.V^\dagger.V.U = \mathbb{1}$.

2. Given an m-qubit unitary U and k-qubit unitary V, their Kronecker product $U \otimes V$ is an $(m+k)$-qubit unitary. Indeed, $(U \otimes V)^\dagger.(U \otimes V) = (U^\dagger \otimes V^\dagger).(U \otimes V) = (U^\dagger.U) \otimes (V^\dagger.V) = \mathbb{1}$.

3. Given an m-qubit unitary U, m qubits labelled $t_1, ..., t_m$ called "target qubits", and k qubits labelled $c_1, ..., c_k$ called "control qubits", the application C_U which applies U on the target qubits "when the control qubits are all in '1'" is an $(m+k)$-qubit unitary called "controlled U". To be more precise, let us consider a generic state of control and target qubits that can be written as

$$|\Psi\rangle = a|1...1\rangle^{\perp}_{c_1,...,c_k} \otimes |\phi_0\rangle_{t_1,...,t_m} + b|1...1\rangle_{c_1,...,c_k} \otimes |\phi_1\rangle_{t_1,...,t_m} \tag{2.17}$$

   where $|1...1\rangle_{c_1,...,c_k} = |1\rangle_{c_1} \otimes ... \otimes |1\rangle_{c_k}$, $|1...1\rangle^{\perp}_{c_1,...,c_k}$ is its orthogonal in the Hilbert space describing qubits $c_1, ..., c_k$, and $|\phi_0\rangle_{t_1,...,t_m}$ and $|\phi_1\rangle_{t_1,...,t_m}$ are states of the target qubits. C_U can then be defined by

$$C_U|\Psi\rangle = a|1...1\rangle^{\perp}_{c_1,...,c_k} \otimes |\phi_0\rangle_{t_1,...,t_m} + bU|1...1\rangle_{c_1,...,c_k} \otimes |\phi_1\rangle_{t_1,...,t_m}. \tag{2.18}$$

[4] To be convinced that it cannot be written as a separable state, let us suppose it can. This gives $a, b, c, d \in \mathbb{C}$ such that $\frac{|00\rangle+|11\rangle}{\sqrt{2}} = (a|0\rangle + b|1\rangle) \otimes (c|0\rangle + d|1\rangle) = ac|00\rangle + ad|01\rangle + bc|10\rangle + bd|11\rangle$. Identifying the coefficients, one gets $ad = bc = 0$ and $ac = bd = \frac{1}{\sqrt{2}}$, leading to a contradiction ($ad = 0 \implies (a = 0$ or $d = 0) \implies (ac = 0$ or $bd = 0)$, so with $ac = bd = \frac{1}{\sqrt{2}}$ this leads to $\frac{1}{\sqrt{2}} = 0$).

[5] If such U and $|s\rangle$ existed, we could apply it to any two states $|\phi\rangle$ and $|\varphi\rangle$:

$$\begin{aligned} U(|s\rangle \otimes |\phi\rangle) &= |\phi\rangle \otimes |\phi\rangle \\ U(|s\rangle \otimes |\varphi\rangle) &= |\varphi\rangle \otimes |\varphi\rangle \end{aligned} \tag{2.16}$$

The inner product of these two equations gives $(\langle s| \otimes \langle\varphi|)U^\dagger U(|s\rangle \otimes |\phi\rangle) = (\langle\varphi \otimes \langle\varphi|)(|\phi\rangle \otimes |\phi\rangle)$, *i.e.* $\langle\varphi|\phi\rangle^2 = \langle\varphi|\phi\rangle$. Since $x^2 = x$ has only two solutions 0 and 1, this means that $|\phi\rangle$ and $|\varphi\rangle$ are either equal or orthogonal, contradicting the fact that U should apply to any N-qubit state.

One can apply the † of this definition to prove that $C_U^\dagger = C_{U^\dagger}$, and then check that $C_U^\dagger . C_{U^\dagger} = \mathbb{1}$, showing that C_U is indeed unitary.

Using above rules 1 and 2, one can build many N-qubit unitaries from 1-qubit ones. For example, given N Pauli operators $\sigma_1, ..., \sigma_N \in \{\mathbb{1}, X, Y, Z\}$, the Pauli string $\sigma_1 \otimes ... \otimes \sigma_N$ is an N-qubit unitary. However, this is limited as such unitaries act independently on each qubits (they map separable state to separable states). To generate entanglement, rules 3 is required. In particular, the operator C_{NOT} obtained with 1 control qubit, 1 target qubit, and $U = X$, is commonly used for this. Its matrix representation in the basis $\{|00\rangle, |01\rangle\, |10\rangle, |11\rangle\}$ reads as

$$C_{NOT} = \begin{pmatrix} 1 & 0 & 0 & 0 \\ 0 & 1 & 0 & 0 \\ 0 & 0 & 0 & 1 \\ 0 & 0 & 1 & 0 \end{pmatrix}. \tag{2.19}$$

Restricting its action on the basis states ($|00\rangle \mapsto |00\rangle, |01\rangle \mapsto |01\rangle, |10\rangle \mapsto |01\rangle, |11\rangle \mapsto |10\rangle$), this operator can be described as a logical NOT gate applied on the second qubit (the "target qubit") when the first one (the "control qubit") is in state $|1\rangle$. This justifies its name, a contraction of "Controlled NOT".

This 2-qubit unitary, composed with 1-qubit unitaries using composition and Kronecker product, is sufficient to generate all N-qubit unitaries [45, 49]. The set $\{C_{NOT}\} \cup U(2)$ can then be considered as "universal" in a similar way than when a set of logical operations *e.g.* $\{\text{NAND}, \text{COPY}\}$ is called "universal" because it generates all boolean functions with compositions in a series and in parallel. However, this universal set of quantum operators is infinite, and one can wonder if there exist a finite such universal set. Actually, since the set $U(2)$ of all 1-qubit unitaries is uncountable, this is impossible. However, there exist finite sets $\mathcal{S}$ of them, e.g. $\mathcal{S} = \{H, S, T\}$ (see table 2.1), such that any 1-qubit unitary can be approximated, up to an arbitrary precision ϵ by the composition of unitaries from $\mathcal{S}$. Moreover, the Solovay-Kitaev theorem [45, 50, 51] shows that only $O(\log^c(1/\epsilon))$ of them are required for that, where c is a constant close to 2 (its best possible value remains unknown [45] !). Then, given such a set $\mathcal{S} \subset U(2)$, $\mathcal{S} \cup C_{NOT}$ is said to be "universal" in this asymptotic meaning.

In the digital computing paradigm, where a quantum computation is thought as a sequence of given unitaries applied to the qubits, it is quite usual to describe an N-qubit unitary as a combination of 1- and 2-qubit unitaries using "." and "$\otimes$". However, this can lead to heavy expressions: consider for example the 3-qubit operator $U = (R_x(\theta) \otimes C_{NOT}).(C_{NOT} \otimes \mathbb{1}).(H \otimes H \otimes H)$. Hopefully, there is a convenient graphical way to represent such operators: the quantum circuits.

2.3.3 A graphical representation of qubit operations: the quantum circuit

A quantum circuit consists of horizontal lines, each representing a qubit, with blocks on them representing operators, usually called gates. A gate put across k lines represents a k-qubit operator applied on the corresponding qubits. Two conventions are typically used for the representation of gates:

- A k-qubit operator U can be represented by its name inside a rectangle: $\boxed{U}$. This rectangle covers the k qubits on which U applies.

- A k-qubit operator U controlled by l qubits (as defined in Eq. (2.18)) is represented by the same rectangle, but linked by a vertical line to the control qubits on which a "•" is put.

As an exception to this controlled operator convention, if U is the 1-qubit operator X, the box $\boxed{X}$ is replaced by a $\oplus$. This is in particular the case for the C_{NOT} operator defined in Eq. (2.19). The resulting diagram can be thought as a deformation of the logical circuit representing a copy of the first bit followed by a XOR between one copy and the second bit (see table 2.3 in section 2.3.4).

Time goes from left to right, meaning that operators on the right are applied after operators on the left (notice that this is opposite to matrix product). One usually indicates the initialization of the qubits on the left. Sometimes, final measurement is represented with a dedicated icon on the right. An example is given on Fig. 2.3 (a).

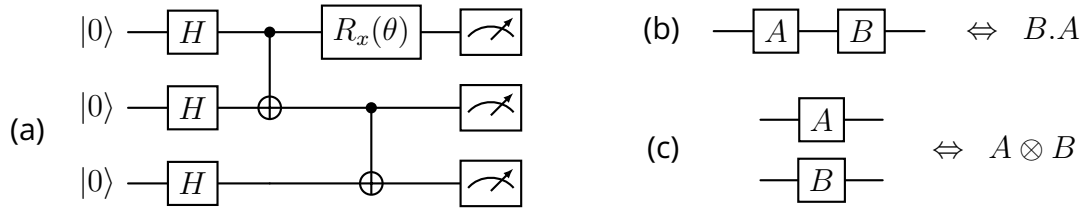
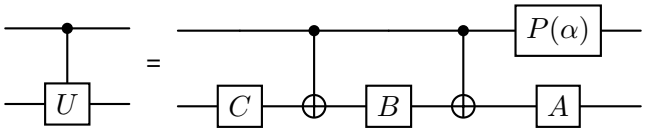


Figure 2.3: *(a) Quantum circuit on 3 qubits corresponding to their initialisation in the state* $|0\rangle$*, the application on them of the operator* $U = (R_x(\theta) \otimes C_{NOT}).(C_{NOT} \otimes \mathbb{1}).(H \otimes H \otimes H)$*, and their measurement. (b) Equivalence between the sequential composition of gates and the product of their corresponding operators. (c) Equivalence between the parallel composition of gates and the Kronecker product of their corresponding operators.*

This representation is convenient because it behaves nicely with composition and Kronecker product. The composition of gates in a series translates composition of corresponding operators (see Fig. 2.3 (b)), while the composition of gates in parallel translates Kronecker product of corresponding operators (see Fig. 2.3 (c)).

Let us see how quantum circuits are convenient to visualize unitaries with an example: the proof that for any 1-qubit unitary U, the corresponding 2-qubit unitary C_U can be made from C_{NOT}'s and 1-qubit unitaries. First, let us consider the decomposition $U = e^{i\alpha}AXBXC$ where $A, B, C \in U(2)$ such that[6] $ABC = \mathbb{1}$. Then C_U can be built as follows [45, 49]



The 2-qubit state on which it applies can be written (without any loss of generality) as $|\Psi\rangle = a|0\rangle \otimes |\phi_1\rangle + b|1\rangle \otimes |\phi_2\rangle$, so using linearity one can describe C_U by its action on $|0\rangle \otimes |\phi_1\rangle$ and $|1\rangle \otimes |\phi_2\rangle$, by reading the previous circuit in the two cases:

- If the first qubit is in state $|0\rangle$, the C_{NOT}'s are not activated *i.e.* $ABC = \mathbb{1}$ is applied on the second qubit. Moreover, the phase $e^{i\alpha}$ from the phase gate $P(\alpha)$ (defined in table 2.1) is not applied. To sum up, nothing happens to the qubits (U is not applied).

- If the first qubit is in state $|1\rangle$, the phase $e^{i\alpha}$ is applied and the C_{NOT}'s are activated: the transformation applied on the second qubit is $AXBXC$. Since the phase $e^{i\alpha}$ is global ($e^{i\alpha}|1\rangle \otimes |\phi_2\rangle = |1\rangle \otimes e^{i\alpha}|\phi_2\rangle$), $U = e^{i\alpha}AXBXC$ is applied on second qubit.

The quantum circuits will be used in the following to represent operations on qubits and in particular to describe quantum algorithms.

2.3.4 Comparison with classical computing

To have a better intuition on quantum computing, it can be interesting to compare it with classical computing. Table 2.2 sums up a parallel between the two computing paradigms, comparing the corresponding units of information and operations.

	Classical computing	Quantum computing
Unit of information	bit: $b \in \{0,1\}$	qubit: $\|\psi\rangle = a\|0\rangle + b\|1\rangle$
Operations on this unit	$\mathsf{I}_d : \begin{matrix} 0 \mapsto 0 \\ 1 \mapsto 1 \end{matrix}$, NOT : $\begin{matrix} 0 \mapsto 1 \\ 1 \mapsto 0 \end{matrix}$	All unitaries $U \in U(2)$
State of N units	bitstring $\vec{b} \in \{0,1\}^N$	$\|\Psi\rangle = \sum_{\vec{b}\in\{0,1\}^N} c_{\vec{b}}\|\vec{b}\rangle$
Operations on N units	All boolean functions $f : \{0,1\}^N \to \{0,1\}^N$	All unitaries $U \in U(2^N)$
Graphical representation of these operations	Logical circuits	Quantum circuits

Table 2.2: *Some elements of comparison between classical and quantum computing.*

Some N-qubit unitaries are represented in canonical basis by matrices whose coefficients are either 0 or 1. When restricted to the bitstring states, they can be regarded as boolean functions, *i.e.* classical bit operations. Two examples are given in table 2.3.

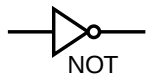
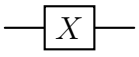
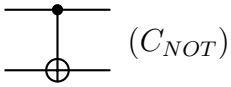
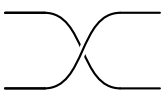
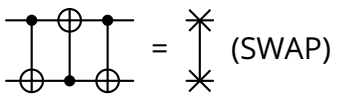
Logical operation	Unitary
	
	
	

Table 2.3: *A parallel between some logical operations and their unitary analogue. Note that the C_{NOT} diagram takes inspiration from its classical counterpart.*

2.4 Measuring qubits

An important aspect of quantum computing is that the only way to retrieve information from the calculation is to measure the qubits, resulting in their projection onto one of the bitstrings. This section explains how repeating the preparation of N qubits in a given state and their subsequent measurement allows to evaluate the associated expectation value of any N-qubit observable. The last subsection discusses the statistical uncertainty due to the finite number of measurements.

2.4.1 Direct measurement

Similarly to the 1-qubit case, the measurement of a system of N qubits gives a bitstring $\vec{b} = (b_1, ..., b_N)$ where for $i \in \{1, ..., N\}$, $b_i \in \{0, 1\}$ represents the value obtained when measuring the qubit i. If the same procedure (operations on qubits to prepare a state $|\Psi\rangle$ and measurement) is repeated sufficiently many times, one can evaluate the probabilities associated to the measurement of each bitstring as

$$\forall \vec{b} \in \{0,1\}^N, \quad p_{\vec{b}} = |\langle \vec{b}|\Psi\rangle|^2. \tag{2.21}$$

One can also write it $p_{\vec{b}} = \langle\Psi|\vec{b}\rangle\langle\vec{b}|\Psi\rangle$ to underline the fact that this probability is the expectation value of the observable $|\vec{b}\rangle\langle\vec{b}|$. Thus, from measurements one can determine the expectation value of any observable that writes as a linear combination of such $|\vec{b}\rangle\langle\vec{b}|$, *i.e.* that is diagonal in the basis $\{|\vec{b}\rangle\}_{\vec{b}\in\{0,1\}^N}$. This is the case, for example, of observables of the form $Z^{a_1} \otimes ... \otimes Z^{a_N}$ where $\vec{a} = (a_1, ..., a_N) \in \{0,1\}^N$ (so that $\forall i, Z^{a_i}$ is $\mathbb{1}$ or Z). Indeed, for $\vec{b} = (b_1, ...b_N) \in \{0,1\}^N$ one has

$$\begin{aligned}
\langle\vec{b}|Z^{a_1} \otimes ... \otimes Z^{a_N}|\vec{b}\rangle &= \langle b_1|Z^{a_1}|b_1\rangle \times ... \times \langle b_N|Z^{a_N}|b_N\rangle \\
&= (-1)^{a_1 b_1} \times ... \times (-1)^{a_N b_N} \\
&= (-1)^{\vec{a}\cdot\vec{b}}, \\
\text{so} \quad Z^{a_1} \otimes ... \otimes Z^{a_N} &= \sum_{\vec{b}\in\{0,1\}^N} (-1)^{\vec{a}\cdot\vec{b}} |\vec{b}\rangle\langle\vec{b}|, \\
\text{then} \quad \langle\Psi|Z^{a_1} \otimes ... \otimes Z^{a_N}|\Psi\rangle &= \sum_{\vec{b}\in\{0,1\}^N} (-1)^{\vec{a}\cdot\vec{b}}\, p_{\vec{b}}\,.
\end{aligned} \tag{2.22}$$

Actually, the sets $\{Z_1^{a_1} \otimes ... \otimes Z_N^{a_N}\}_{a_1,...a_N\in\{0,1\}}$ and $\{|\vec{b}\rangle\langle\vec{b}|\}_{\vec{b}\in\{0,1\}^N}$ represent two bases of the subspace containing observables whose expectation values can be obtained from direct measurements. For other observables, an extra operation is required.

[6] This can be obtained from Eq. (2.8) by writing

$$\begin{aligned}
U &= e^{i\alpha} R_z(\eta) R_y(\mu) R_z(\nu) \\
&= e^{i\alpha} R_z(\eta) R_y(\tfrac{\mu}{2}) R_y(\tfrac{\mu}{2}) R_z(\tfrac{\nu+\eta}{2}) R_z(\tfrac{\nu-\eta}{2}) \\
&= e^{i\alpha} R_z(\eta) R_y(\tfrac{\mu}{2}) X X R_y(\tfrac{\mu}{2}) X X R_z(\tfrac{\nu+\eta}{2}) X X R_z(\tfrac{\nu-\eta}{2}) \quad \text{(since } XX = \mathbb{1}\text{)} \\
&= e^{i\alpha} A X B X C
\end{aligned} \tag{2.20}$$

where $A = R_z(\eta)R_y(\frac{\mu}{2})$, $B = XR_y(\frac{\mu}{2})XXR_z(\frac{\nu+\eta}{2})X$, and $C = R_z(\frac{\nu-\eta}{2})$ are unitaries.
Since $XYX = -Y$, $XR_y(\frac{\mu}{2})X = \cos(\frac{\mu}{2})X\mathbb{1}X + i\sin(\frac{\mu}{2})XYX = \cos(\frac{\mu}{2})\mathbb{1} - i\sin(\frac{\mu}{2})Y = R_y(\frac{-\mu}{2})$.
Similarly $XZX = -Z$ so $XR_z(\frac{\nu+\eta}{2})X = R_z(\frac{-\nu-\eta}{2})$. Then $B = R_y(\frac{-\mu}{2})R_z(\frac{-\nu-\eta}{2})$, so $ABC = \mathbb{1}$.

2.4.2 Measurement with a basis rotation

Expectation values of other observables can be obtained by applying a unitary transformation before the measurement to perform a basis change, in the same way than for the 1-qubit case discussed previously in section 2.2.3.

In particular, one can use 1-qubit unitaries U_x and U_y as defined in Eqs. (2.13) and (2.14) (*e.g.* $U_x = H$ and $U_y = HS^\dagger$) to locally change the Z basis into X basis or Y basis. Given a Pauli string $\sigma_1 \otimes ... \otimes \sigma_N$ where $\forall i \in \{1, ..., N\}, \sigma_i \in \{\mathbb{1}, X, Y, Z\}$, one can build the following N-qubit unitary

$$U_{\sigma_1 ... \sigma_N} = U_{\sigma_1} \otimes ... \otimes U_{\sigma_N} \quad \text{where} \quad \forall i, U_{\sigma_i} = \begin{cases} \mathbb{1} & \text{if } \sigma_i \in \{\mathbb{1}, Z\} \\ U_x & \text{if } \sigma_i = X \\ U_y & \text{if } \sigma_i = Y \end{cases}. \tag{2.23}$$

This unitary satisfies $\sigma_1 \otimes ... \otimes \sigma_N = U^\dagger_{\sigma_1 ... \sigma_N} Z^{a_1} \otimes ... \otimes Z^{a_N} U_{\sigma_1 ... \sigma_N}$ where $(a_1, ..., a_N)$ is some bitstring of length N. So $\langle \Psi | \sigma_1 \otimes ... \otimes \sigma_N | \Psi \rangle = \langle \Psi | U^\dagger_{\sigma_1 ... \sigma_N} Z^{a_1} \otimes ... \otimes Z^{a_N} U_{\sigma_1 ... \sigma_N} | \Psi \rangle$ can be obtained by repeating the following steps

- prepare $|\Psi\rangle$,
- apply $U_{\sigma_1 ... \sigma_N}$,
- perform a measurement and collect the resulting bitstring.

As explained in the previous subsection, once one has accumulated enough statistics, one can evaluate the Pauli string expectation value. Moreover, since the set of all Pauli strings on N qubits forms a basis of the $\mathbb{R}$-vector space of N-qubit observables, as established in section 2.1, any observable expectation value can be obtained from qubits measurements.

2.4.3 Finite number of measurements: statistical uncertainty

It has been argued previously that repeating preparation and measurement allows to approximate the probabilities associated to each bitstring. In practice, the number of repetitions N_{shots} is often limited, and one wishes to minimise it in order to lower the computation time. A finite number of repetitions introduces errors on the estimation of the probabilities, and consequently on the result of the computation. So it is important to quantify the error induced by a given choice of N_{shots}.

For each bitstring $\vec{b} = (b_1, ...b_N) \in \{0, 1\}^N$, one denotes $X_{\vec{b}}$ the random variable counting the number of measurements leading to the outcome $\vec{b}$ among the N_{shots} measurements, so that $\frac{1}{N_{shots}} X_{\vec{b}}$ is an estimate of the probability $p_{\vec{b}}$. In this way, the random variables $\{X_{\vec{b}}\}_{\vec{b} \in \{0,1\}^N}$ taken together follow the multinomial law associated to N_{shots} and probabilities $\{p_{\vec{b}}\}_{\vec{b} \in \{0,1\}^N}$. Their corresponding variances and covariances are well-defined and read as

$$\text{Var}(X_{\vec{b}}) = N_{shots} \times p_{\vec{b}} \times (1 - p_{\vec{b}}), \tag{2.24a}$$

$$\text{Cov}(X_{\vec{b}}, X_{\vec{b}'}) = -N_{shots} \times p_{\vec{b}} \times p_{\vec{b}'} \quad (\text{if } \vec{b} \neq \vec{b}'). \tag{2.24b}$$

This implies that the standard deviation on the estimation of the probability $p_{\vec{b}}$ reads as

$$\sqrt{\text{Var}\left(\frac{1}{N_{shots}} X_{\vec{b}}\right)} = \sqrt{\frac{p_{\vec{b}} \times (1 - p_{\vec{b}})}{N_{shots}}}. \tag{2.25}$$

Eqs. (2.24) also enables us to evaluate the variance on the estimation of every observable that is diagonal in the basis $\{|\vec{b}\rangle\}_{\vec{b}\in\{0,1\}^N}$, and in particular Pauli strings that contain only $\mathbb{1}$ and Z. To show it, let us consider such an observable O. Without loss of generality, it can be written as

$$O = \sum_{\vec{b}\in\{0,1\}^N} c_{\vec{b}} |\vec{b}\rangle\langle\vec{b}|, \tag{2.26}$$

where the $c_{\vec{b}}$ are real coefficients (because $O^\dagger = O$). Then the estimator o of $\langle\Psi|O|\Psi\rangle$ is the corresponding linear combination of estimators $\frac{1}{N_{shots}} X_{\vec{b}}$. Using the bilinearity of the covariance, its variance reads as

$$\begin{aligned}
\mathrm{Var}(o) &= \sum_{\vec{b}} \frac{c_{\vec{b}^2}}{N_{shots}^2} \mathrm{Var}(X_{\vec{b}}) - \sum_{\vec{b}\neq\vec{b}'} \sum \frac{c_{\vec{b}} c_{\vec{b}'}}{N_{shots}^2} \mathrm{Cov}(X_{\vec{b}}, X_{\vec{b}'}) \\
&= \frac{1}{N_{shots}} \Big(\sum_{\vec{b}} c_{\vec{b}}^2 p_{\vec{b}} (1 - p_{\vec{b}}) - \sum_{\vec{b}\neq\vec{b}'} \sum c_{\vec{b}} c_{\vec{b}'} p_{\vec{b}} p_{\vec{b}'} \Big) \\
&= \frac{1}{N_{shots}} \sum_{\vec{b}\neq\vec{b}'} \sum c_{\vec{b}} (c_{\vec{b}} - c_{\vec{b}'}) p_{\vec{b}} p_{\vec{b}'}.
\end{aligned} \tag{2.27}$$

This can be generalised in the case of an observable O' which is not diagonal in the basis $\{|\vec{b}\rangle\}_{\vec{b}\in\{0,1\}^N}$. Indeed, one can decompose this observable as $O' = \sum_k O_k$ where each O_k can be evaluated from measurements after having applied the convenient unitary U_k as explained below. Then, O' can be evaluated from N_{shots} measurements for each k. Due to the required basis rotations, the set of measurement outcomes used to evaluate O_k is disjoint from the one used to evaluate $O_{k'}$, for $k \neq k'$. Therefore, the estimator o_k of $\langle\Psi|O_k|\Psi\rangle$ is independent of the estimator $o_{k'}$ of $\langle\Psi|O_{k'}|\Psi\rangle$. Hence, the variance on the estimator o' of O' is

$$\mathrm{Var}(o') = \sum_k \mathrm{Var}(o_k), \tag{2.28}$$

where each $\mathrm{Var}(o_k)$ can be obtained from Eq. (2.27). As a result, with N_{shots} measurements for each k, the variance of O' takes the form $\frac{V_0}{N_{shots}}$.

This allows to estimate the number N_{shots} needed to reach a target accuracy ϵ with a given probability using the Bienaymé-Tchebychev inequality

$$\mathbb{P}\Big(|o - \langle\Psi|O|\Psi\rangle| \geq \epsilon \Big) \leq \frac{V_0}{N_{shots}\epsilon^2} \,. \tag{2.29}$$

However, in practice this inequality can lead to an overestimation of the required number of shots. Better estimations can be obtained by using more advanced techniques [52, 53].

2.5 Some examples of quantum algorithms

To understand quantum computing, it is important to dissect some quantum algorithms. This section explains two of them: the quantum Fourier transform, and the quantum phase estimation for which an application is presented.

2.5.1 Quantum Fourier Transform

The discrete Fourier transform is a linear map whose computation is crucial for many problems (signal processing, differential equations, ...). It maps a vector $(x_0, ..., x_{n-1}) \in \mathbb{C}^n$ to another one $(y_0, ..., y_{n-1}) \in \mathbb{C}^n$ defined as

$$\forall k \in \{0, ..., n-1\}, \quad y_k = \frac{1}{\sqrt{n}} \sum_{j=0}^{n-1} x_j e^{2\pi i jk/n}. \tag{2.30}$$

The corresponding matrix in the canonical basis of $\mathbb{C}^n$ writes $\Omega = (\frac{1}{\sqrt{n}}\omega^{jk})_{jk}$, where $\omega = e^{i\frac{2\pi}{n}}$. Since $\omega^* = \omega^{-1}$,

$$\Omega^\dagger \Omega = \left(\frac{1}{n} \sum_{k=0}^{n-1} \omega^{k(j-l)} \right)_{jl} = (\delta_{j,l})_{jl} = I_n. \tag{2.31}$$

So the discrete Fourier transform is a unitary map, which implies it can implement an operation on qubits. The best known classical algorithm (Fast Fourier transform) performing this task requires $O(n \log(n))$ operations. Here is presented the Quantum Fourier Transform (QFT), a quantum algorithm which requires instead $O(\log(n)^2)$ operations in $O(\log(n))$ qubits.

The QFT on N qubits (implementing the Fourier transform of size $n = 2^N$) is described by the quantum circuit of Fig. 2.4. Let us see how it transforms a bitstring state $|a_1 a_2 ... a_N\rangle$, by computing the resulting state $|\Psi_{\text{out}}\rangle$.

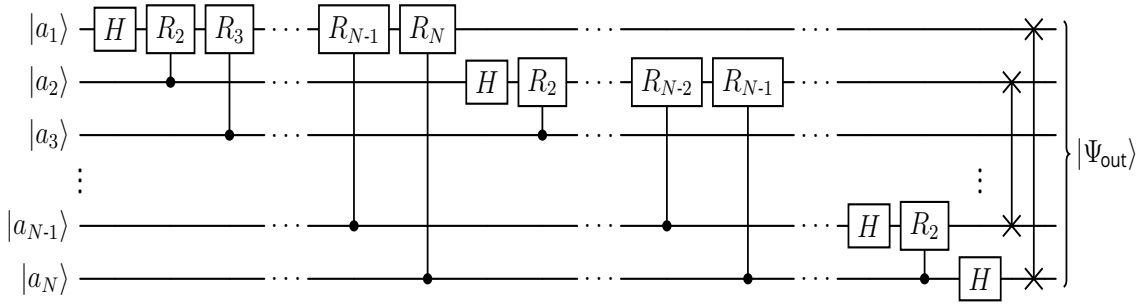


Figure 2.4: *Quantum circuit of the QFT on N qubits. H is the Hadamard gate, R_k is the phase gate $P(2\pi/2^k)$ (see table 2.1), and the vertical lines ending with crosses on the right represent SWAP gates, i.e. the 2-qubit gates whose effect is to swap the states of the qubits on which it applies (see table 2.3).*

The computation starts with a Hadamard gate transforming the state of the first qubit, initially $|a_1\rangle$ (where a_1 is 0 or 1), into

$$H|a_1\rangle = \frac{1}{\sqrt{2}}\Big(|0\rangle + (-1)^{a_1}|1\rangle\Big) = \frac{1}{\sqrt{2}}\Big(|0\rangle + e^{i\frac{2\pi}{2}a_1}|1\rangle\Big). \tag{2.32}$$

Then the R_2 gate, controlled by the second qubit, applies a phase $e^{i\frac{2\pi}{2^2}}$ on the $|1\rangle$ component if and only if $a_2 = 1$. Said differently, qubit 1 takes a phase $e^{i\frac{2\pi}{2^2}a_2}$ on its $|1\rangle$ component. Similarly with the controlled $R_3, ..., R_N$ gates. The full state can then be written as

$$\frac{1}{\sqrt{2}}\Big(|0\rangle + e^{i2\pi\left(\frac{a_1}{2}+\frac{a_2}{2^2}+...+\frac{a_N}{2^N}\right)}|1\rangle\Big) \otimes |a_2...a_N\rangle = \frac{1}{\sqrt{2}}\Big(|0\rangle + e^{i\frac{2\pi}{2^N}\overline{a_1...a_N}}|1\rangle\Big) \otimes |a_2...a_N\rangle \tag{2.33}$$

where $\overline{a_1...a_N} = a_1 2^{N-1} + ... + 2^0 a_N$ is the integer whose binary decomposition is the bitstring $a_1...a_n$.

A similar treatment is made on qubits $2, ..., N$, resulting in the state

$$\frac{1}{\sqrt{2^N}} \bigotimes_{k=1}^{N} \left(|0\rangle + e^{i2\pi \left(\frac{a_k}{2} + \frac{a_{k+1}}{2^2} + ... + \frac{a_N}{2^{N+1-k}} \right)} |1\rangle \right) = \frac{1}{\sqrt{2^N}} \bigotimes_{k=1}^{N} \left(|0\rangle + e^{i \frac{2\pi}{2^N} 2^{k-1} \overline{a_1...a_N}} |1\rangle \right). \quad (2.34)$$

Note that for each qubit k, the phases $e^{i2\pi 2^{k-2} a_1}, ..., e^{i2\pi a_{k-1}}$ have been added without any effect since they are all equal to 1. Using again the notation $\omega = e^{i \frac{2\pi}{2^N}}$, and denoting the final SWAP gates with an operator S, the output state finally writes as

$$\begin{aligned} |\Psi_{\text{out}}\rangle &= \frac{1}{\sqrt{2^N}} S \bigotimes_{k=1}^{N} \left(|0\rangle + \omega^{2^{k-1} \overline{a_1...a_N}} |1\rangle \right) \\ &= \frac{1}{\sqrt{2^N}} \sum_{b_1,...,b_N \in \{0,1\}} \omega^{\overline{a_1...a_N} \sum_{k=1}^{N} 2^{N-k} b_k} S|b_N...b_1\rangle \\ &= \frac{1}{\sqrt{2^N}} \sum_{b_1,...,b_N \in \{0,1\}} \omega^{\overline{a_1...a_N} \times \overline{b_1...b_N}} |b_1...b_N\rangle. \end{aligned} \quad (2.35)$$

The tensor product has been developed to write the result as a combination of all the bitstring states. The SWAP gates allow to have the right correspondence between the bitstring states $|b_1...b_N\rangle$ and the integer $\overline{b_1...b_N}$ in the exponent of their associated coefficient. Finally, if one denotes the bitstring states by their corresponding integers as $|j\rangle = |b_1...b_N\rangle$ where $j = \overline{b_1...b_N}$, one can conclude that the quantum circuit shown in Fig. 2.4 implements the linear map acting on a bitstring state $|k\rangle = |a_1...a_N\rangle$ as

$$|k\rangle \rightarrow \frac{1}{\sqrt{2^N}} \sum_{j=1}^{2^N - 1} \omega^{kj} |j\rangle \, , \quad (2.36)$$

which indeed corresponds to the discrete Fourier transform as defined in Eq. (2.30).

QFT is an important component of several other quantum or hybrid algorithms, such as the famous Shor algorithm that can theoretically factorize integers faster than any known classical algorithms [54], or the Quantum Phase Estimation (QPE) [55] explained in the next section.

2.5.2 Quantum Phase Estimation

Presentation

The QPE is a quantum algorithm that estimates the eigenelements of a given unitary operator U. In the following these eigenelements are written $\{e^{2i\pi\lambda}, |\phi_\lambda\rangle\}_\lambda$[7], where all the λ's, called "eigenphases" in the following, are in $[0, 1[$. The quantum circuit representing the QPE is depicted on Fig. 2.5.

It is organized with two registers. The first register contains d qubits, initialized in $|0...0\rangle$, where d is the number of desired precision digits on the eigenvalues. The second register

[7] Indeed, a unitary operator has its eigenvalues on the unit circle since $U^\dagger U = \mathbb{1}$.

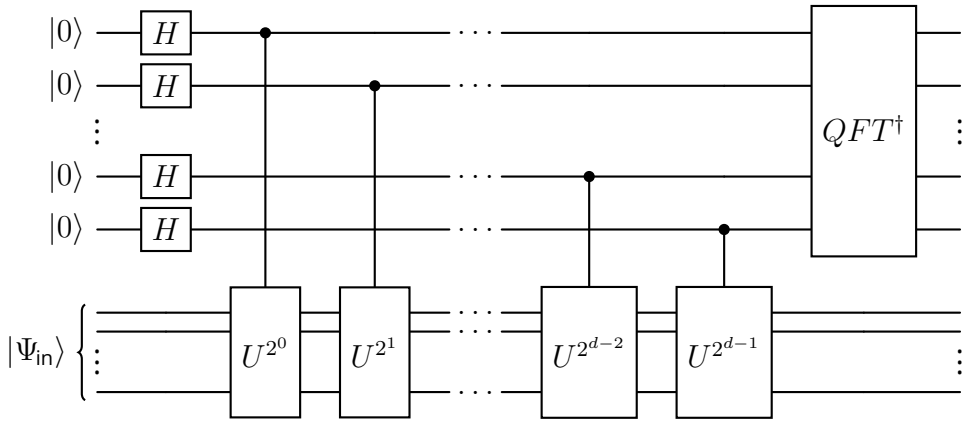


Figure 2.5: *Quantum circuit of the QPE, evaluating the eigenvalues of a unitary operator U with d precision digits on their phase.*

contains m qubits where 2^m is the dimension of U. It is initialized in a state $|\Psi_{\text{in}}\rangle$ that can be decomposed in the eigenbasis of U as $|\Psi_{\text{in}}\rangle = \sum_\lambda c_\lambda |\phi_\lambda\rangle$ so that

$$\forall p \in \mathbb{N}, \quad U^p |\Psi_{\text{in}}\rangle = \sum_\lambda c_\lambda e^{2i\pi p\lambda} |\phi_\lambda\rangle. \tag{2.37}$$

The algorithm can be decomposed in three steps:

1. The layer of Hadamard gates transforms the input state $|0...0\rangle \otimes |\Psi_{\text{in}}\rangle$ into

$$\Big(\bigotimes_{k=1}^{d} H|0\rangle\Big) \otimes |\Psi_{\text{in}}\rangle = \frac{1}{\sqrt{2^d}} \bigotimes_{k=1}^{d} \Big(|0\rangle + |1\rangle\Big) \otimes |\Psi_{\text{in}}\rangle. \tag{2.38}$$

2. For each qubit k in the first register, a $U^{2^{k-1}}$ controlled by qubit k is applied on the second register. Using Eq. (2.37) and moving adequately the phases, the result can be written as

$$\begin{aligned}\sum_\lambda \frac{c_\lambda}{\sqrt{2^d}} \bigotimes_{k=1}^{d} \Big(|0\rangle + e^{2i\pi 2^{k-1}\lambda}|1\rangle\Big) \otimes |\phi_\lambda\rangle &= \sum_\lambda \frac{c_\lambda}{\sqrt{2^d}} \sum_{b_1,...,b_d \in \{0,1\}} e^{2i\pi\lambda\overline{b_1...b_d}} |b_1...b_d\rangle \otimes |\phi_\lambda\rangle \\ &= \sum_\lambda \frac{c_\lambda}{\sqrt{2^d}} \sum_{j=0}^{2^d-1} \omega^{2^d\lambda j} |j\rangle \otimes |\phi_\lambda\rangle, \end{aligned} \tag{2.39}$$

   where the notations of the previous section have been used in last line.

3. Finally, the inverse QFT is applied. From Eq. (2.36) one can see that if for any eigenphase λ, $2^d\lambda$ is an integer (between 0 and $2^d - 1$ since $\lambda \in [0, 1[$), the result is

$$\sum_\lambda c_\lambda |2^d\lambda\rangle \otimes |\phi_\lambda\rangle \tag{2.40}$$

In the general case, it can be written as

$$\sum_{\lambda} c_\lambda \sum_{k=0}^{2^d-1} x_k(\lambda)|k\rangle \otimes |\phi_\lambda\rangle \ , \tag{2.41}$$

$$\text{where } x_k(\lambda) = \frac{1}{2^d}\sum_{j=0}^{2^d-1} \omega^{(2^d\lambda-k)j} = \frac{1}{2^d}\frac{1-\omega^{(2^d\lambda-k)2^d}}{1-\omega^{(2^d\lambda-k)}} (\text{or } 1) = e^{i\pi(1-\frac{1}{2^d})(2^d\lambda-k)} f(2^d\lambda - k)$$

$$\text{and} \quad f : x \mapsto \begin{cases} \frac{\sin(x\pi)}{2^d \sin(\frac{x\pi}{2^d})} & \text{if } x \neq 0, \pm 2^d, ... \\ 1 \quad \text{else} \end{cases} \ . \tag{2.42}$$

When the measurement of the first register is performed, one gets the bitstring corresponding to k with probability

$$p_k = \sum_{\lambda} |c_\lambda|^2 |x_k(\lambda)|^2 = \sum_{\lambda} |c_\lambda|^2 |f(2^d\lambda - k)|^2. \tag{2.43}$$

Since the function f is peaked around 0, this probability is maximal when $k/2^d$ is close to one of the eigenphases λ, especially those for which the corresponding eigenstate $|\phi_\lambda\rangle$ has a sizeable overlap with the input state $|\Psi_{\text{in}}\rangle$. Moreover, the output state of the second register, if not measured, is projected into the state

$$|\Psi_{\text{out}}\rangle = \frac{1}{\sqrt{p_k}} \sum_{\lambda} c_\lambda x_k(\lambda)|\phi_\lambda\rangle. \tag{2.44}$$

If k is close to $2^d\lambda$ for a given λ_0, $|x_k(\lambda_0)|^2 \approx 1$ while $\forall \lambda \neq \lambda_0, |x_k(\lambda)|^2 \approx 0$, meaning that $|\Psi_{\text{out}}\rangle$ is close to $|\phi_{\lambda_0}\rangle$ in terms of fidelity. Thereby, repeating measurements after the QPE allows to evaluate the eigenelements of U.

This algorithm can be used to find the eigenelements $\{E_i, |\varphi_i\rangle\}_i$ of a Hermitian operator H. Indeed, one can use the QPE with $U = e^{i(H-E_{ref})t}$ where the parameters t and E_{ref} are chosen so that every eigenvalue E_i of H satisfies $0 \leq (E_i - E_{ref})t < 2\pi$. The latter condition is needed to avoid confusion between eigenvalues $E_i \neq E_j$ for which $e^{iE_it} \approx e^{iE_jt}$ due to periodicity of the complex exponential.

Thereby, the QPE allows to evaluate eigenelements of an operator of dimension 2^m using m qubits to encode it and d qubits to encode the result. Here again, an exponential speedup compared to classical algorithms can be achieved, provided that one can build the U^{2^k} unitaries from a number of elementary quantum operations that is polynomial with k (without a significant loss on precision). This is not a big requirement: since U is unitary, it can always be written as $U = e^{iHt}$ where H is Hermitian, so $U^{2^k} = e^{iH2^kt}$ can be built in a similar way as U. An example is given below.

Example of application

Here is presented an application of the QPE with the following Hamiltonian

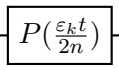
$$H_P = \sum_{k=1}^{m} \varepsilon_k(\mathbb{1} - Z_k) - \frac{g}{2}\sum_{k<l}(X_kX_l + Y_kY_l). \tag{2.45}$$

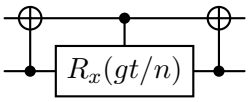
This is the pairing Hamiltonian (1.25) expressed with qubit operators using pair encoding as detailed in section 2.6.3. In general it is difficult to implement $e^{2i\pi(H-E_{ref})t}$ as a set of

qubit operations. At the price of introducing an approximation, this becomes much easier when decomposing the exponential using the Trotter formula $e^{A+B} = \lim_{n\to\infty}(e^{A/n}e^{B/n})^n$ [56] truncated at some order n, *i.e.*

$$U(t) = e^{i(H_p - E_{ref})t} \approx e^{-iE_{ref}t}\Big(\prod_{k=1}^{m} e^{i\varepsilon_k(\mathbb{1}-Z_k)t/n}\prod_{k<l} e^{-i\frac{g}{2}(X_kX_l+Y_kY_l)t/n}\Big)^n. \tag{2.46}$$

This leads to considering the building blocks

$e^{i\varepsilon_k(\mathbb{1}-Z_k)t/n} =$ 

and $e^{-i\frac{g}{2}(X_kX_l+Y_kY_l)t/n} =$ 

. (2.47)

These blocks are assembled to construct the unitary $U(t)$ of Eq. (2.46) and similarly $U(t)^{2^k} = U(2^k t)$ for $k \in \{1, ..., d-1\}$. They are then used in a simulated QPE to determine the eigenvalues of Hamiltonian (2.45), whose parameters have been set to $m = 4$, $g = 0.6$ and $\forall k, \varepsilon_k = k$. With $d = 6$ qubits to encode the result, $n = 4$ Trotter steps, parameters $t = 0.5$ and $E_{ref} = 3.0$ adjusted to get a precise and unambiguous result, and an input state $|\Psi_{\text{in}}\rangle = |1100\rangle$, the resulting distribution is plotted on Fig. 2.6. This can be compared with the eigenvalues obtained from direct diagonalisation, corresponding to the peaks of the red curve. The heights of the peaks correspond to the fidelities $|\langle\phi_\lambda|\Psi_{\text{in}}\rangle|^2$ between the input state and the eigenstates.

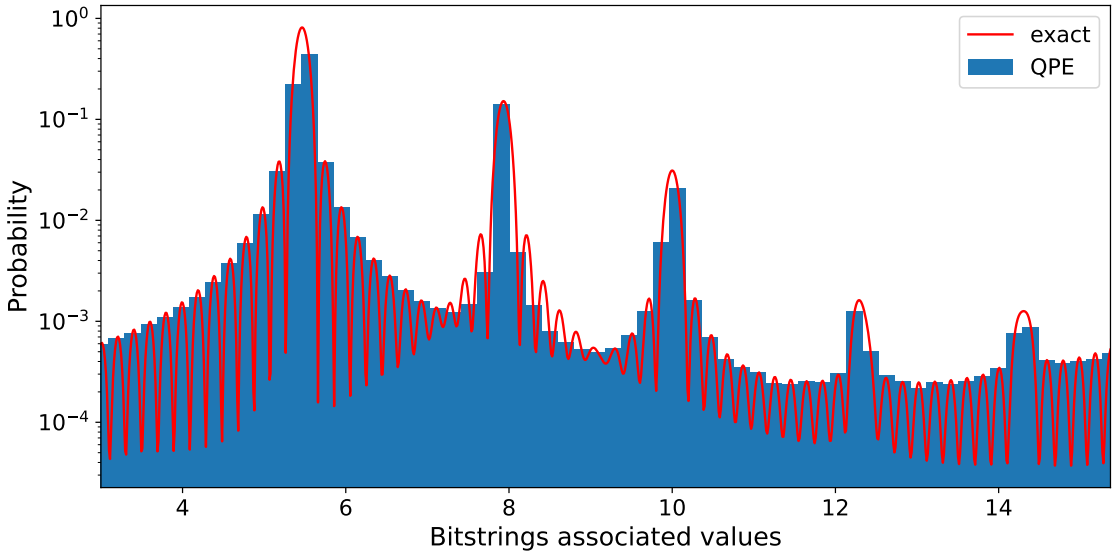


Figure 2.6: *Result of a simulated QPE. The blue bars represent the probability distribution (in log scale) on the measured bitstrings. The bitstrings are labelled by their corresponding integer multiplied by $\frac{2\pi}{2^d t}$, in order to compare them with the eigenvalues of the Hamiltonian (2.45). The red curve corresponds to the function $x \to \sum_\lambda |c_i|^2 |f(\frac{2^d t}{2\pi}(E_i - x))|^2$ where f is the function defined in Eq. (2.42), $\{E_i\}_i$ are the exact eigenvalues of Hamiltonian (2.45) and c_i are the coefficients of the input state $|\Psi_{in}\rangle$ in the exact eigenbasis. The exact eigenelements have been computed with exact diagonalisation.*

2.6 Many-body problems on a quantum computer

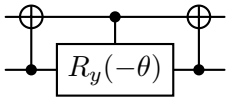
Another important class of quantum algorithms is the one of quantum simulations. Indeed, quantum computers are particularly suitable to simulate quantum systems [57]. Systems of qubits, as controllable many-body systems, can be used to simulate other many-body systems. This section explains a straightforward way to encode fermionic many-body systems into qubits, and fermionic many-body observables into qubit observables. This will be used in following chapters to tackle some quantum simulation algorithms.

2.6.1 From many-body states to qubit states

As presented in section 1.1, a fermionic many-body product state can be seen as a set of 1-particle states that can be occupied or not. To each of them on can assign a qubit whose state $|1\rangle$ correspond to its occupancy and state $|0\rangle$ to its emptiness. In this way, the qubit state $|00...0\rangle$ encodes the vacuum state $|\text{vac}\rangle$, and more generally any bitstring state $|b_1 b_2 ... b_M\rangle$ encodes the $(b_1 + ... + b_M)$-body Slater determinant $(a_1^\dagger)^{b_1}...(a_M^\dagger)^{b_M}|\text{vac}\rangle$ where each single-particle state i is occupied if and only if $b_i = 1$. The Hamming weight of the bitstring corresponds to the number of particles in the system. Finally, a generic N-body state can be written as a linear combination of Slater determinants: its corresponding qubits state is defined as the same combination of the associated bitstring states.

Operators applied on the qubits can be interpreted in the many-body physics framework. For example, if a qubit i is in state $|0\rangle$ and one applies an X operator, giving state $|1\rangle$, this corresponds to a particle creation in single-particle state i (see Fig 2.7 (b)). However, this does not mean that X corresponds to a creation operator since it only works when the input state is $|0\rangle$. Actually, a creation operator is not unitary so it cannot correspond to an operation on qubits. A more relevant example is the following. A particle excitation/desexcitation between two distinct single-particle states i and j corresponds (in the 2-qubit subspace describing qubits i and j) to an exchange between qubit states $|10\rangle_{ij}$ and $|01\rangle_{ij}$. This can be performed in a continuous way with the rotation (in the subspace spanned by these two states) generated by $G_{ij} = \frac{1}{2}(X_i Y_j - Y_i X_j)$ as follows[8]

$$e^{i\theta G_{ij}} = \begin{pmatrix} 1 & 0 & 0 & 0 \\ 0 & \cos(\theta) & -\sin(\theta) & 0 \\ 0 & \sin(\theta) & \cos(\theta) & 0 \\ 0 & 0 & 0 & 1 \end{pmatrix}_{ij} = \quad .$$



(2.48)

The use of this operation is illustrated below in Fig 2.7 (c).

The interest of this method resides in the ability of qubits to efficiently represent a highly entangled many-body state. Indeed, a many-body state defined on M single-particle states can be represented on M qubits, while with a classical computer it would require *a priori* to store 2^M amplitudes. The next section explains how observable expectation values can be obtained from qubit measurements.

[8] Indeed, $e^{i\theta G_{ij}}$ can be developed using $G_{ij}^3 = G_{ij}$ as done in appendix C.2, leading to this matrix form. To understand the corresponding quantum circuit, one can first consider the matrix associated to the controlled-$R_y(-\theta)$, and then realize that the effect of the two surrounding C_{NOT} gates is to exchange the components $|01\rangle$ and $|11\rangle$ (exchange second and last columns of the matrix, and same with the lines).

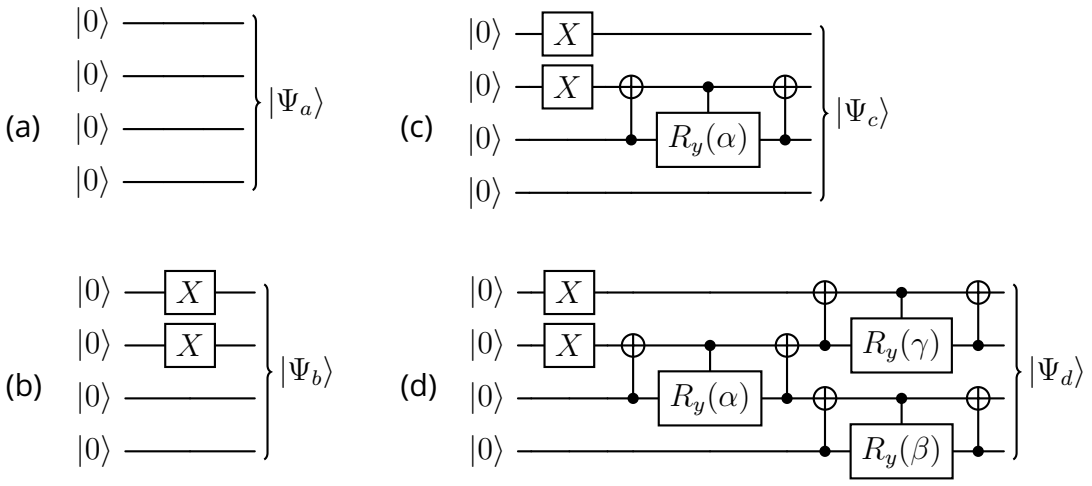


Figure 2.7: *Quantum circuits representing* 4*-qubit operations applied to the vacuum state to prepare a many-body state* $|\Psi\rangle$*. (a) Vacuum state* $|\Psi_a\rangle = |0000\rangle$*. (b) Slater determinant* $|\Psi_b\rangle = |1100\rangle$*. (c) A combination of Stater determinants* $|\Psi_c\rangle = \cos(\alpha)|1100\rangle + \sin(\alpha)|1010\rangle$*. (d) A more complicated state* $|\Psi_d\rangle = \cos(\alpha)|1100\rangle + \sin(\alpha)\cos(\beta)\big(\cos(\gamma)|1010\rangle + \sin(\gamma)|0110\rangle\big) + \sin(\alpha)\sin(\beta)\big(\cos(\gamma)|1001\rangle + \sin(\gamma)|0101\rangle\big)$.

Here and in the following, we consider systems of fermions. The mapping presented here is not adapted for bosons because the occupancy of a single-particle state can take more values than 0 or 1 particle. Other strategies have to be considered, for example using qudits (d-level quantum systems) instead of qubits, or encoding the occupancy of each single-particle state with several qubits [58].

2.6.2 Mapping fermions to qubits: the observables

Now that one can represent a many-body state with qubits, one may want to measure its energy or any many-body observable. As seen in section 2.4, all qubits observables can be (approximately) retrieved from measurements. But how to translate a many-body observable, written as a combination of creation and annihilation operators $\{a_i, a_i^\dagger\}_{1\leq i\leq M}$, into a qubit observable, written as a combination of Pauli strings? Regarding the actions of creation and annihilation operators on the occupancy of a single-particle state, one can expect the following behaviours from their analogue in the qubits world

$$\begin{cases} |0\rangle \mapsto |1\rangle \\ |1\rangle \mapsto 0 \end{cases} \text{ for creation, and } \begin{cases} |0\rangle \mapsto 0 \\ |1\rangle \mapsto |0\rangle \end{cases} \text{ for annihilation.} \tag{2.49}$$

So it would be natural to associate them with the following Pauli operators combinations

$$\begin{aligned} a_i^\dagger \to \sigma_i^- &= |1\rangle\langle 0| = \frac{1}{2}(X_i - iY_i) = \begin{pmatrix} 0 & 0 \\ 1 & 0 \end{pmatrix}_i, \\ a_i \to \sigma_i^+ &= |0\rangle\langle 1| = \frac{1}{2}(X_i + iY_i) = \begin{pmatrix} 0 & 1 \\ 0 & 0 \end{pmatrix}_i. \end{aligned} \tag{2.50}$$

To define the qubit analogue of a generic N-body observable O, one can replace each a_i by σ_i^+ and each $a_i^\dagger$ by σ_i^-, for all i from 1 to N. Unfortunately, such a definition depends on the

order of the creation and annihilation operators. For example, if one defines $a_1 a_2^\dagger \to \sigma_1^+ \sigma_2^-$, this imposes $a_2^\dagger a_1 \to -\sigma_2^- \sigma_1^+$ since $a_1, a_2^\dagger$ anti-commute (recall that we deal with fermions here) but σ_1^+, σ_2^- commute. This potential minus sign can be encoded with an extra factor $\prod_{0\leq p<i}(-Z_p)$, leading to

$$a_i^\dagger \to \Big(\prod_{0\leq p<i}(-Z_p)\Big)\sigma_i^- \quad \text{and} \quad a_i \to \Big(\prod_{0\leq p<i}(-Z_p)\Big)\sigma_i^+. \tag{2.51}$$

These are the building blocks of the so-called Jordan-Wigner mapping [59] $\mathrm{JW}[.]$, defined for any many-body operator (written as a combination of creation and annihilation operators as in Eq.(1.13)) by imposing linearity $\mathrm{JW}[O+\lambda O'] = \mathrm{JW}[O] + \lambda \mathrm{JW}[O']$ and preservation of product $\mathrm{JW}[O.O'] = \mathrm{JW}[O].\mathrm{JW}[O']$. This defines a morphism from the algebra generated by $\{a_i, a_i^\dagger\}_{1\leq i\leq M}$, to the algebra generated by $\{\mathbb{1}, X_i, Y_i, Z_i\}_{1\leq i\leq M}$. Moreover, $\mathrm{JW}[O^\dagger] = \mathrm{JW}[O]^\dagger$ since $\mathrm{JW}[a_i]^\dagger = \mathrm{JW}[a_i^\dagger]$ (and $\dagger$ behaves well on both sides so $\mathrm{JW}[.]$ is a morphism of *-algebra). In particular, this mapping conserves the fermionic commutation relations (1.9)

$$\begin{aligned}
&\mathrm{JW}[a_i]\mathrm{JW}[a_j] + \mathrm{JW}[a_j]\mathrm{JW}[a_i] = 0\,,\\
&\mathrm{JW}[a_i^\dagger]\mathrm{JW}[a_j^\dagger] + \mathrm{JW}[a_j^\dagger]\mathrm{JW}[a_i^\dagger] = 0\,,\\
&\mathrm{JW}[a_i]\mathrm{JW}[a_j^\dagger] + \mathrm{JW}[a_j^\dagger]\mathrm{JW}[a_i] = \delta_{ij}\mathbb{1}.
\end{aligned} \tag{2.52}$$

Importantly, one can also affirm that this mapping "conserves the physics". More precisely, there is a compatibility between the N-body states $|\Psi_{MB}\rangle$ and observables O with their qubits analogues $|\Psi\rangle$ and $\mathrm{JW}[O]$ since the resulting expectation values are the same: $\langle\Psi|\mathrm{JW}[O]|\Psi\rangle = \langle\Psi_{MB}|O|\Psi_{MB}\rangle$[9].

2.6.3 Application to Hamiltonians of section 1.3

In this subsection, the Jordan-Wigner mapping is used to transform Hamiltonians of section 1.3 into qubit observables, in order to measure their expectation values, *i.e.* the energy of the state encoded into qubits.

[9] First, realize that $\langle 0...0|\mathbb{1}|0...0\rangle = 1 = \langle \mathrm{vac}|\mathbb{1}|\mathrm{vac}\rangle$, while for $N \in \mathbb{N}^*$ and $2N$ one-body state labels $\alpha_1, ..., \alpha_N, \beta_1, ..., \beta_N$,

$$\begin{aligned}
\langle 0...0|\mathrm{JW}[a_{\alpha_1}^\dagger ... a_{\alpha_N}^\dagger a_{\beta_N} ... a_{\beta_1}]|0...0\rangle &= \pm\langle 0...0|\sigma_{\alpha_1}^- ... \sigma_{\alpha_N}^- \sigma_{\beta_N}^+ ... \sigma_{\beta_1}^+|0...0\rangle\\
&= 0\\
&= \langle \mathrm{vac}|a_{\alpha_1}^\dagger ... a_{\alpha_N}^\dagger a_{\beta_N} ... a_{\beta_1}|\mathrm{vac}\rangle
\end{aligned} \tag{2.53}$$

Note that in the first line, the $-Z_i$'s produced by the JW mapping have been absorbed by the $|0...0\rangle$, resulting in the $\pm$ sign. One then have used $\sigma^+|0\rangle = 0$.

Then, given a many-body observable O, one can express it in its normal-ordered form (1.13) and deduce from Eq. (2.53) that $\langle 0...0|\mathrm{JW}[O]|0...0\rangle = \langle \mathrm{vac}|O|\mathrm{vac}\rangle$. Finally, this can be extended to expectation values on an arbitrary many-body state $|\Psi_{MB}\rangle$ encoded on qubits by $|\Psi\rangle$, using Eq. (1.11) to write $\langle\Psi_{MB}|O|\Psi_{MB}\rangle$ as a combination of other observables expectation values on the vacuum state.

Preliminaries

To facilitate the calculation, let us first realize that when one transform a pair of creation/annihilation operators with the same index, the Z's cancel:

$$\mathrm{JW}[a_k^\dagger a_k] = \mathrm{JW}[a_k^\dagger]\mathrm{JW}[a_k] = \sigma_k^-\Big(\prod_{0\leq p<k}(-Z_p)\Big)\Big(\prod_{0\leq p<k}(-Z_p)\Big)\sigma_k^+ = \sigma_k^-\sigma_k^+ \tag{2.54}$$

where $Z^2 = \mathbb{1}$ and the commutation of σ_k^- with $\prod_{0\leq p<k}(-Z_p)$ have been used. The result can be explicited further with the Pauli operator relations as

$$\mathrm{JW}[a_k^\dagger a_k] = \frac{1}{4}(X_k - iY_k)(X_k + iY_k) = \frac{1}{2}(\mathbb{1} - Z_k). \tag{2.55}$$

Similarly (or more directly using the commutation relation $a_k^\dagger a_k + a_k a_k^\dagger = \mathbb{1}$),

$$\mathrm{JW}[a_k a_k^\dagger] = \frac{1}{2}(\mathbb{1} + Z_k). \tag{2.56}$$

Pairing Hamiltonian (1.24)

In the context of the Pairing Hamiltonian, the indices of single-particle states has been labelled with their corresponding levels and a bar to distinguish the two time-reversed states as $\{k, \bar{k}\}_{1\leq k\leq D}$. Since the order of indices matter when applying the Jordan-Wigner transformation, one needs to fix it. In the following, the indices will be ordered as $1, \bar{1}, 2, \bar{2}, ..., D, \bar{D}$. In a similar way than in Eq. (2.54), when transforming pairs of creation/annihilation operators with neighbouring indices k and $\bar{k}$, all the Z's cancel because they appear twice, except $Z_{\bar{k}}$ which can be absorbed using the relations $Z\sigma^\pm = \pm\sigma^\pm$ and $\sigma^\pm Z = \mp\sigma^\pm$. For instance, the pair operators $P_k^\dagger = a_k^\dagger a_{\bar{k}}^\dagger$ and $P_l = a_{\bar{l}} a_l$ are mapped to

$$\begin{aligned}\mathrm{JW}[P_k^\dagger] = \mathrm{JW}[a_k^\dagger a_{\bar{k}}^\dagger] &= \sigma_k^-(-Z_{\bar{k}})\sigma_{\bar{k}}^- = \sigma_k^-\sigma_{\bar{k}}^- \\ \mathrm{JW}[P_l] = \mathrm{JW}[a_{\bar{l}} a_l] &= \sigma_{\bar{l}}^+(-Z_{\bar{l}})\sigma_l^+ = \sigma_{\bar{l}}^+\sigma_l^+\end{aligned} \tag{2.57}$$

One has now all the material to transform the pairing Hamiltonian (1.24):

$$\begin{aligned}\mathrm{JW}[H_P] &= \mathrm{JW}\Big[\sum_{k=1}^{D}\varepsilon_k(a_k^\dagger a_k + a_{\bar{k}}^\dagger a_{\bar{k}}) - g\sum_{k\neq l}\sum a_k^\dagger a_{\bar{k}}^\dagger a_{\bar{l}} a_l\Big] \\ &= \sum_{k=1}^{D}\varepsilon_k\Big(\mathrm{JW}[a_k^\dagger a_k] + \mathrm{JW}[a_{\bar{k}}^\dagger a_{\bar{k}}]\Big) - g\sum_{k\neq l}\sum \mathrm{JW}[a_k^\dagger a_{\bar{k}}^\dagger]\mathrm{JW}[a_{\bar{l}} a_l] \\ &= \sum_{k=1}^{D}\varepsilon_k\Big(\mathbb{1} - \frac{1}{2}Z_k - \frac{1}{2}Z_{\bar{k}}\Big) - g\sum_{k\neq l}\sum \sigma_k^-\sigma_{\bar{k}}^-\sigma_{\bar{l}}^+\sigma_l^+ \\ &= \Big(\sum_{k=1}^{D}\varepsilon_k\Big)\mathbb{1} - \frac{1}{2}\sum_{k=1}^{D}(Z_k + Z_{\bar{k}}) - g\Gamma\end{aligned} \tag{2.58}$$

$$\begin{aligned}\text{where } \Gamma = \sum_{k\neq l}\sigma_k^-\sigma_{\bar{k}}^-\sigma_{\bar{l}}^+\sigma_l^+ = \frac{1}{8}\sum_{k<l}\Big[&X_kX_{\bar{k}}X_{\bar{l}}X_l + Y_kY_{\bar{k}}Y_{\bar{l}}Y_l - X_kX_{\bar{k}}Y_{\bar{l}}Y_l - Y_kY_{\bar{k}}X_{\bar{l}}X_l \\ &+ X_kY_{\bar{k}}X_{\bar{l}}Y_l + Y_kX_{\bar{k}}Y_{\bar{l}}X_l + X_kY_{\bar{k}}Y_{\bar{l}}X_l + Y_kX_{\bar{k}}X_{\bar{l}}Y_l\Big].\end{aligned} \tag{2.59}$$

Note that, when developing $\sigma_k^-\sigma_{\bar{k}}^-\sigma_{\bar{l}}^+\sigma_l^+ + \sigma_l^-\sigma_{\bar{l}}^-\sigma_{\bar{k}}^+\sigma_k^+$, all terms with an imaginary coefficient cancel.

Pairing Hamiltonian (1.25) in pair encoding

If one restricts to the fully-paired subspace, the pairing Hamiltonian can be written using pair operators as in Eq. (1.25). The pair operators can be themselves encoded into qubits, similarly to as JW transformation. This means directly encoding each pair occupation/non-occupation on a single qubit, reducing the number of qubits by a factor 2 [60].

To understand how this simplification can be justified from the particle-to-qubit encoding, let us first develop Eq. (2.57) to explicit the qubit operators on which the pair operators are mapped by the Jordan-Wigner mapping:

$$\mathrm{JW}[P_k^\dagger] = \frac{1}{2}(X_k - iY_k)\frac{1}{2}(X_{\bar{k}} - iY_{\bar{k}}) = \frac{1}{2}\Big[\widetilde{X}_k - i\widetilde{Y}_k\Big] \tag{2.60}$$
$$(\text{and consequently} \quad \mathrm{JW}[P_k] = \frac{1}{2}\Big[\widetilde{X}_k + i\widetilde{Y}_k\Big])$$

where, in the two-qubit basis $\{|00\rangle_{k\bar{k}}, |01\rangle_{k\bar{k}}, |10\rangle_{k\bar{k}}, |11\rangle_{k\bar{k}}\}$,

$$\begin{aligned}\widetilde{X}_k &:= \tfrac{1}{2}(X_kX_{\bar{k}} - Y_kY_{\bar{k}}) = \begin{pmatrix}0&0&0&1\\0&0&0&0\\0&0&0&0\\1&0&0&0\end{pmatrix}_{k\bar{k}},\\ \widetilde{Y}_k &:= \tfrac{1}{2}(X_kY_{\bar{k}} + Y_kX_{\bar{k}}) = \begin{pmatrix}0&0&0&-i\\0&0&0&0\\0&0&0&0\\i&0&0&0\end{pmatrix}_{k\bar{k}}.\end{aligned} \tag{2.61}$$

These operators can be seen as effectively acting only on span($|00\rangle_{k\bar{k}}, |11\rangle_{k\bar{k}}$), *i.e.* on the fully paired subspace. Moreover, one realizes that in this subspace, which can be naturally mapped to a single qubit, $\widetilde{X}$ and $\widetilde{Y}$ read precisely as X and Y Pauli matrices. It follows that P_k and $P_k^\dagger$ can be utilized when considering pairs, exactly like a_k and $a_k^\dagger$ are employed when considering particles, and one can drop the "$\widetilde{\ }$" in Eq. (2.60) to consider the transformation

$$\begin{aligned}P_k^\dagger &\to \frac{1}{2}(X_k - iY_k)\\ P_k &\to \frac{1}{2}(X_k + iY_k)\end{aligned} \tag{2.62}$$

which is denoted $\mathrm{JW}'[.]$ in the following. In this way, the pairing Hamiltonian (1.25) is mapped to

$$\begin{aligned}\mathrm{JW}'[H'_P] &= \mathrm{JW}'\Big[\sum_{k=1}^{D} 2\varepsilon_k P_k^\dagger P_k - g\sum_{k\neq l}\sum P_k^\dagger P_l\Big]\\ &= \sum_{k=1}^{D}\varepsilon_k(\mathbb{1} - Z_k) - \frac{g}{2}\sum_{k<l}\sum(X_kX_l + Y_kY_l)\,,\end{aligned} \tag{2.63}$$

Deuteron Hamiltonian (1.31)

One can also apply the Jordan-Wigner mapping to the deuteron Hamiltonian (1.31), leading to

$$\begin{aligned}\mathrm{JW}\Big[\frac{1}{\hbar\omega}H_D\Big] &= \mathrm{JW}\Bigg[\Big(\frac{3}{4} - \frac{|V_0|}{\hbar\omega}\Big)a_0^\dagger a_0 + \sum_{k=1}^{M-1}\Big(k+\frac{3}{4}\Big)a_k^\dagger a_k - \frac{1}{2}\sum_{k=1}^{M-1}\sqrt{k\Big(k+\frac{1}{2}\Big)}\Big(a_{k-1}^\dagger a_k + a_k^\dagger a_{k-1}\Big)\Bigg]\\ &= \Big(\frac{3}{4} - \frac{|V_0|}{\hbar\omega}\Big)\hat{n}_0 + \sum_{k=1}^{M-1}\Big(k+\frac{3}{4}\Big)\hat{n}_k - \frac{1}{4}\sum_{k=1}^{M-1}\sqrt{k\Big(k+\frac{1}{2}\Big)}\Big(X_{k-1}X_k + Y_{k-1}Y_k\Big)\end{aligned} \tag{2.64}$$

where $\forall k, \hat{n}_k = \frac{1}{2}(\mathbb{1} - Z_k)$.

2.6.4 Number of Pauli strings versus number of measurements

Jordan-Wigner mapping transforms a many-body observable into a linear combination of Pauli strings. While this can lead to a lot of strings, there is no need to measure each of them independently and precisely. First, some Pauli strings, associated with very low coefficients, can be neglected with a limited impact on the result. Then, they can be grouped into fully commuting sets in which all Pauli string expectation values can be retrieved from the same series of measurements associated with a suitable basis rotation. Indeed, if two Pauli strings commute, they can be diagonalized using the same basis rotation U, which can be performed before the measurements to get their expectation values as explained in section 2.4.2. Therefore, if N_{sets} is the number of such fully commuting sets, and N_{shots} is the number of measurements required to accumulate enough statistics to get (with the desired precision) the expectation values of the Pauli strings in a given set, the total number of measurements N_{meas} required to evaluate any Pauli strings one need to evaluate can be expressed as

$$N_{meas} = N_{sets} \times N_{shots} \ . \tag{2.65}$$

Actually, more advanced techniques allow to optimise this number of measurements without changing the target precision [52, 53]. However, for simplicity in the following chapters Eq. (2.65) will be considered to evaluate the required number of measurements.

To reduce N_{sets}, it is preferable to have low-weight Pauli strings, *i.e.* strings made with many $\mathbb{1}$'s (indeed, they are more likely to commute). However, the extra Z_p's in the prefactor required for Jordan-Wigner mapping favour high-weight Pauli strings, rising the required number of measurements. That's why other mappings, associated to other encodings, might be more suitable in some situations. In particular, Bravyi-Kitaev method [61] allows to reduce the weight of Pauli strings.

2.7 Conclusion

This chapter has introduced the elementary concepts of quantum computing: qubits, unitary operations, quantum circuit representation, measurement,... Some notions that will be used in the following chapters have been discussed in more details. Concrete examples of quantum algorithms have been explained. The encoding of the many-body problem on qubits presented here will be the starting point of the next chapter, where it will be applied to the nuclear many-body problem. The application of quantum computing to this field is quite recent, and have led to several developments in the last years (see *e.g.* [62–66]).

Importantly, quantum computers have been presented here as ideal, theoretical objects. In practice, quantum computers are build using various quantum systems. Every physical implementation faces numerous challenges which limit the current number of qubits and operations that can be performed. This is why a universal fault-tolerant quantum computer with enough qubits and operations capabilities to clearly surpass classical computers remains, in 2026, a theoretical object. The research is active and explores many ways to push forward the current limits, with frequent successes. Among the various approaches, analog quantum computing appears to be a promising one to tackle specific problems such as the simulation of quantum systems. This approach will be described in chapter 5, with an emphasis on a Rydberg atoms platform [67].

Chapter 3

In search of the ground state - application to pairing

This chapter addresses variational quantum algorithms in the context of the search for the ground state of a many-body system. Specifically, it presents algorithms based on the Adaptive Derivative-Assembled Pseudo-Trotter ansatz Variational Quantum Eigensolver (ADAPT-VQE) scheme introduced in [4]. The first section describes two types of variational algorithms: the Variational Quantum Eigensolver (VQE), and a generalisation of the ADAPT-VQE. Then section 3.2 focuses on four versions of the latter. These variants are applied in section 3.3 to approximate the ground state and corresponding energy of the pairing Hamiltonian (2.63), with the goal of comparing and benchmarking them. Some results presented in this chapter have been published in [68].

3.1 Some variational quantum algorithms

This section explains how the ground state of a quantum many-body system can be approximated by an ansatz wavefunction encoded on a quantum computer using the VQE procedure. It also presents an improved version of this algorithm, the ADAPT-VQE, which allows to build a more compact ansatz.

3.1.1 The Variational Quantum Eigensolver

Section 2.6 has explained how a quantum computer can efficiently encode a many-body state $|\Psi\rangle$ and measure its energy $\langle\Psi|H|\Psi\rangle$, where H is the Hamiltonian of this system. This can be used to find or approximate its ground state $|\Psi_{GS}\rangle$ and the associated energy E_{GS}. More precisely, given an ansatz wavefunction $|\Psi(\vec{\theta})\rangle$ parametrised by $\vec{\theta}$, one can optimise $\langle\Psi(\vec{\theta})|H|\Psi(\vec{\theta})\rangle$ over the values of $\vec{\theta}$ to find a minimum. To do so, one can start with an input set of parameters $\vec{\theta}_0$, use the quantum computer to build $|\Psi(\vec{\theta}_0)\rangle$ and compute the corresponding energy $E_0 = \langle\Psi(\vec{\theta}_0)|H|\Psi(\vec{\theta}_0)\rangle$. Then one can choose a new set of parameters $\vec{\theta}_1$, compute again the corresponding energy $E_1 = \langle\Psi(\vec{\theta}_1)|H|\Psi(\vec{\theta}_1)\rangle$, and so on. The inputs $\vec{\theta}_0, \vec{\theta}_1, ...$ can be determined by a classical optimiser which minimises the energy until convergence. This results in a hybrid quantum-classical algorithm, called Variational Quantum Eigensolver (VQE), and schematically depicted in Fig. 3.1.

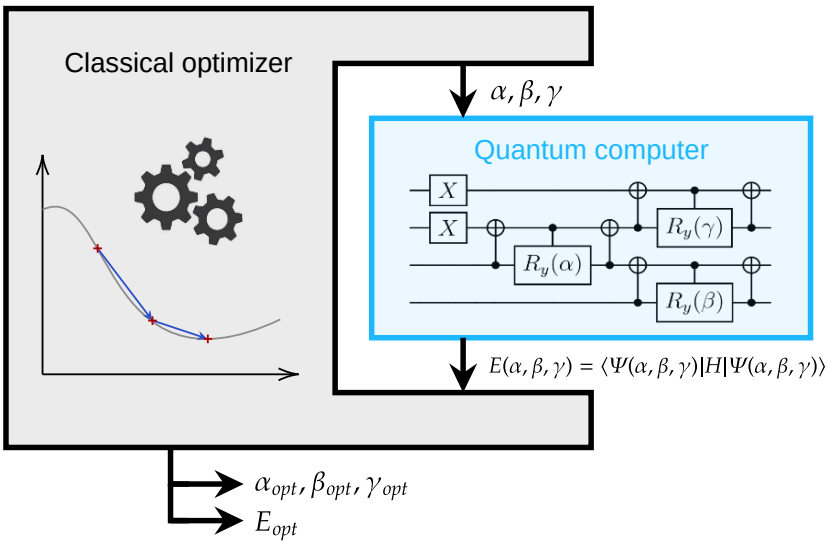


Figure 3.1: *Schematic description of a VQE algorithm based on a wavefunction ansatz* $|\Psi(\alpha, \beta, \gamma)\rangle$ *depending on* 3 *parameters* α, β, γ*. The classical optimiser (in grey) uses evaluations of the function* $(\alpha, \beta, \gamma) \to E(\alpha, \beta, \gamma) = \langle\Psi(\alpha, \beta, \gamma)|H|\Psi(\alpha, \beta, \gamma)\rangle$ *with several inputs in order to get the optimised input* $(\alpha_{opt}, \beta_{opt}, \gamma_{opt})$ *and output* E_{opt}*. These evaluations are performed with a quantum computer (in blue) which encodes* $|\Psi(\alpha, \beta, \gamma)\rangle$ *on qubits and performs measurements in order to build the corresponding energy* $E(\alpha, \beta, \gamma)$ *as explained in sections 2.4 and 2.6.*

As a remark, some applications of this algorithm do not require full convergence towards the ground state. For instance, this algorithm was originally designed [69] to build a state reaching a good overlap with $|\Psi_{GS}\rangle$ in order to serve as an input for a QPE (see section 2.5.2). Moreover, any energy (exactly) computed from an ansatz wavefunction provides an upper bound on the ground state energy[1].

The advantage of this method, compared to classical optimisation, resides in the possibility to efficiently manage ansatz wavefunctions that could be impossible to handle on a classical computer due to a prohibitive resource requirement. However, it shares with its classical counterpart many reasons to fail, namely:

- For some wrong choices of ansätze, the distance between $|\Psi_{GS}\rangle$ and the ansatz space $\{|\Psi(\vec{\theta})\rangle\}_{\vec{\theta}}$ can be too big, resulting in an optimised state too far from the ground state. This issue cannot in general be solved by just using a big ansatz space with a lot of parameters (see following point). So one has to carefully chose the ansatz. Common suitable choices [70] include hardware-efficient ansätze to efficiently explore the Hilbert space with a given number of parameters, physically-inspired ones such as the Unitary Coupled Cluster ansatz [71], or Hamiltonian variational ansatz [72] inspired by the Trotterization of adiabatic state preparation.

- If the number of parameters to optimise is too high, the gradients vanish and the optimisation becomes intractable. This is the so-called Barren plateau phenomenon [73].

[1] Actually, if the ansatz wavefunction is not restricted to the physical Hilbert space (*e.g.* if one allows for some symmetries to be broken), the corresponding energy might be lower than the exact ground state energy.

- The presence of local minima in the energy landscape is also an issue. It requires either to exploit some knowledge on the shape of this landscape (if available), or to try different starting points, which is not efficient if there are too many local minima. This issue will be discussed in chapter 6.

When considering realistic implementations of current quantum computers, one has to add an extra issue: the noise. This can affect in particular gradient-based algorithms. Indeed, to compute the derivative of the energy $\langle\Psi(\vec{\theta})|H|\Psi(\vec{\theta})\rangle$ with respect to a parameter θ_i, one needs *a priori* to evaluate it at $\theta_i + s$ and $\theta_i - s$, where s is small, and perform the difference of the resulting energies. Since these energies are likely to be close to each other, the noise can significantly affect the difference. However, due to the specific analytic form of some quantum operations, it is often possible to compute this gradient using a value of s which is not small (typically $\pi/2$), thus limiting the impact of noise. This is called the parameter shift rule [74].

3.1.2 ADAPT-VQE-based algorithms: general description

On the one hand, the VQE algorithm is quite general since many ansatz wavefunctions and classical optimisations methods can be considered and adapted to a given problem. On the other hand, it is quite restrictive since the number of parameters to optimise (and quantum operations performed on qubits) is fixed from the beginning with the choice of the ansatz. Too few parameters: the ansatz is restricted and remains far from the ground state. Too many: the optimisation is either slow or stuck in a Barren plateau. Hence, as an alternative, it can be convenient to add parameters one by one and optimise them at each step, resulting in a progressive convergence which could be stopped when the number of parameters is sufficient. This is the main idea behind the ADAPT-VQE algorithm introduced in 2019 [4].

Here, a generalised version of this algorithm will be considered, defined by

1. an initial wavefunction $|\Psi_0\rangle$, usually the Hartree-Fock state,
2. a set of parametrized operators $\mathcal{R} = \{R_i(\theta)\}_i$ suitably chosen to build an ansatz wavefunction of the form $|\Psi_n\rangle = R_{i_n}(\theta_n)...R_{i_1}(\theta_1)|\Psi_0\rangle$,
3. a criterion to select an operator at each step.

An iteration $n \geq 1$ of this algorithm, which is schematically depicted in Fig. 3.2, decomposes as follows. First, knowing the state $|\Psi_{n-1}\rangle = R_{i_{n-1}}(\theta_{n-1})...R_{i_1}(\theta_1)|\Psi_0\rangle$, the criterion has to select an operator R_{i_n} in the set $\mathcal{R}$ for which there is a parameter θ such that $R_{i_n}(\theta)|\Psi_{n-1}\rangle$ has a lower energy than $|\Psi_{n-1}\rangle$. Then, a one-parameter VQE is applied to find the best value θ_n of this parameter, leading to the state $R_{i_n}(\theta_n)R_{i_{n-1}}(\theta_{n-1})...R_{i_1}(\theta_1)|\Psi_0\rangle$. Finally, all the parameters $\theta_1, ..., \theta_n$ are re-optimised using a VQE , resulting in the state $|\Psi_n\rangle = R_{i_n}(\theta'_n)R_{i_{n-1}}(\theta'_{n-1})...R_{i_1}(\theta'_1)|\Psi_0\rangle$, starting point of the next iteration. This re-optimisation may be removed since it induces extra quantum evaluations, but it appears that the algorithm is much more efficient with it, as illustrated in section 3.3.3. The procedure is typically stopped when the selection criterion does not find an operator in $\mathcal{R}$ susceptible to reduce the energy[2].

[2]The stopping criterion depends on the selection criterion, which can complicate the comparison of several versions of ADAPT-VQE. For the application to pairing in next section, the procedures will be stopped according to a fixed number of iterations or a limitation on the computation time.

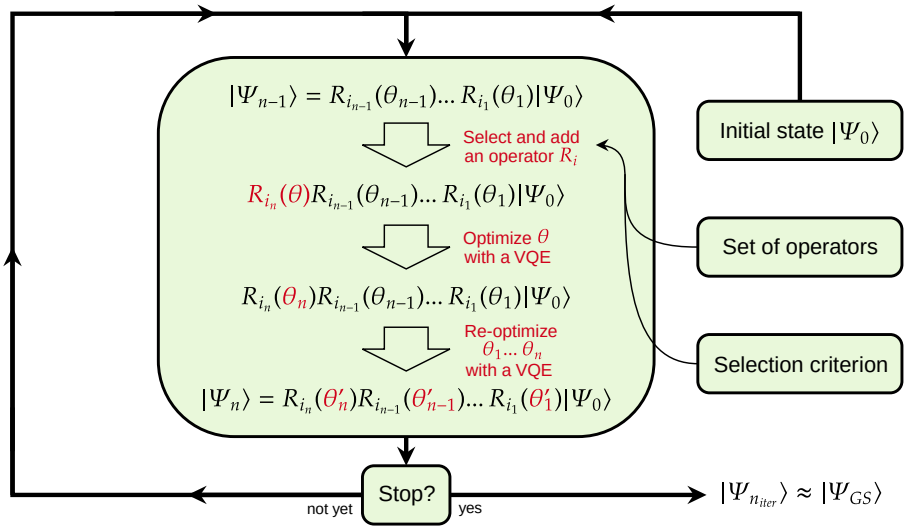


Figure 3.2: *Schematic description of a generalisation of the ADAPT-VQE algorithm as described in section 3.1.2. Elements that change at each step of the n^{th} iteration are written in red.*

Depending on the chosen set of operators and the selection criterion, one can consider several versions of this procedure. Four such versions are described in the next section and applied to the pairing Hamiltonian in section 3.3. All of them will start with the Slater determinant $|\Psi_0\rangle = |1\cdots10\cdots0\rangle$, which corresponds to the Hartree-Fock state. To encode this state on qubits (all initialized in state $|0\rangle$), X-gates are applied on the ones corresponding to occupied levels.

3.2 ADAPT-VQE-based algorithms: four different versions

This section presents four versions of the algorithm defined in section 3.1.2. The original ADAPT-VQE is first described, followed by alternative procedures obtained by changing the selection criterion and the set of operators.

3.2.1 The original ADAPT-VQE

To build a convenient ansatz, the original ADAPT-VQE algorithm [4] took inspiration from a Trotterized unitary coupled cluster ansatz (with single and double particle excitations), resulting in operators of the form

$$e^{i\frac{\theta}{2}(a_\alpha^\dagger a_\beta - a_\beta^\dagger a_\alpha)}, \quad e^{i\frac{\theta}{2}(a_\alpha^\dagger a_\gamma^\dagger a_\delta a_\beta - a_\beta^\dagger a_\delta^\dagger a_\gamma a_\alpha)}. \tag{3.1}$$

For the following application to pairing, one can restrict to the fully paired subspace as explained in section 1.3.1. So one keeps only the operators that do not break pairs, which can be written as

$$e^{i\frac{\theta}{2}(P_\alpha^\dagger P_\beta - P_\beta^\dagger P_\alpha)} \tag{3.2}$$

where $P_\alpha^\dagger = a_\alpha^\dagger a_{\bar{\alpha}}^\dagger$ and $P_\beta^\dagger = a_{\bar{\beta}} a_\beta$ are the pair operators introduced in section 1.3.1. Operators in Eq. (3.2) physically represent pair excitation/desexcitation. To apply them on qubits

encoding pairs, one makes use of the mapping (2.62), resulting in the set

$$\mathcal{R} = \{e^{i\theta G_{\alpha\beta}}\}_{\alpha\neq\beta}\,, \quad \text{where} \quad \forall\alpha\neq\beta, \quad G_{\alpha\beta} = \frac{1}{2}(X_\alpha Y_\beta - Y_\alpha X_\beta). \tag{3.3}$$

These operators have already been presented in Eq. (2.48).

At each iteration n, the algorithm adds an operator $G_{\alpha\beta}$ to the ansatz $|\Psi_{n-1}\rangle$ obtained at previous iteration, in order to get a new ansatz $|\Psi_n\rangle = e^{i\theta G_{\alpha\beta}}|\Psi_{n-1}\rangle$. Each possible choice of operator $G_{\alpha\beta}$ corresponds to an energy curve

$$E_n^{\alpha\beta}(\theta) := \langle\Psi_{n-1}|e^{-i\theta G_{\alpha\beta}} H e^{i\theta G_{\alpha\beta}}|\Psi_{n-1}\rangle, \tag{3.4}$$

whose derivative at $\theta = 0$ writes as

$$\left(\frac{dE_n^{\alpha\beta}(\theta)}{d\theta}\right)_{\theta=0} = i\langle\Psi_{n-1}|[H, G_{\alpha\beta}]|\Psi_{n-1}\rangle. \tag{3.5}$$

This expectation value can be evaluated by measuring the qubits encoding $|\Psi_{n-1}\rangle$, with basis rotations corresponding to the Pauli strings in which $[H, G_{\alpha\beta}]$ decomposes (this decomposition is detailed in appendix C.1). The first step of iteration n is to evaluate this expectation value for any operator in the set. Since a large energy derivative (in absolute value) is likely to produce a high drop in energy, the selected operator is the one with the largest value of $\left|\left(\frac{dE_n^{\alpha\beta}(\theta)}{d\theta}\right)_{\theta=0}\right|$. The resulting algorithm will be referred in the following as ADAPT-St (standard version).

3.2.2 Selection of the "best" operator

Actually, the selection of the operator based on the evaluation of (3.5) does not always provide the "best" operator, *i.e.* the operator $G_{\alpha\beta}$ for which $\min_\theta E_n^{\alpha\beta}(\theta)$ is minimal, as pointed out in Ref. [75] and illustrated in Fig. 3.3. Moreover, it is possible here to com-

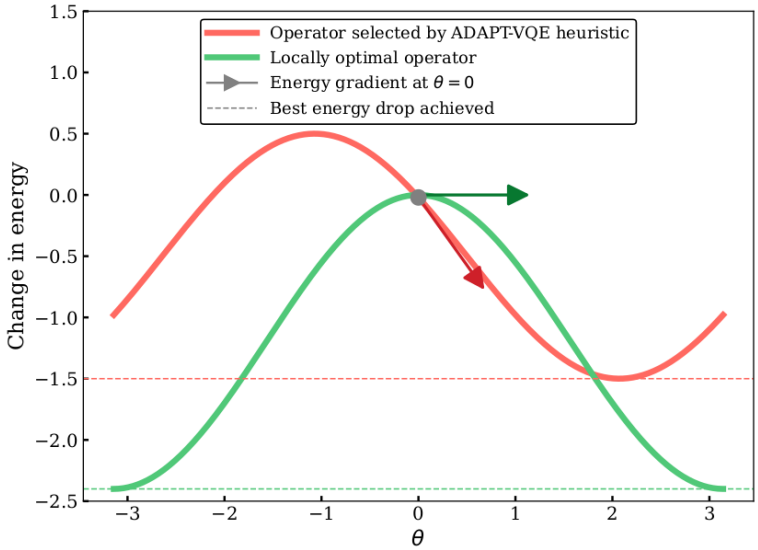


Figure 3.3: *Illustration of a case where the criterion based on the highest energy derivative does not select the operator allowing the best energy drop. Figure taken from [75].*

pute for each operator $G_{\alpha\beta}$ the corresponding quantity $\min_\theta E_n^{\alpha\beta}(\theta)$ and select the one for which this minimal energy is the lowest. Indeed, one can take advantage of the fact that the energy curves (3.4) can often be expressed in an analytical form. Specifically, with the operators considered here, one can always write (see appendix C.2)

$$E_n^{\alpha\beta}(\theta) = C_0 + C_1\cos(\theta+\gamma_1) + C_2\cos(2\theta+\gamma_2), \tag{3.6}$$

with only five parameters $C_0, C_1, C_2, \gamma_1, \gamma_2$ that depend on the wavefunction and the operators themselves. Therefore, in practice, the evaluation of $E_n^{\alpha\beta}(\theta)$ at five different values of θ is sufficient[3] to infer the whole energy curve (see appendix C.3) and in particular its minimum. This allows us to replace the previous selection criterion with the one that selects the operator leading to the energy curve with the lowest minimum. The algorithm obtained using this alternative criterion will be referred in the following as ADAPT-Min.

3.2.3 An alternative set of operators

Finally, this work considers an alternative set of operators to (3.2), namely

$$\mathcal{R}' = \{B_{i,i+1}(\theta)\}_i \quad \text{where} \quad \forall i, B_{i,i+1}(\theta) = \begin{pmatrix} 1 & 0 & 0 & 0 \\ 0 & \cos(\theta) & \sin(\theta) & 0 \\ 0 & \sin(\theta) & -\cos(\theta) & 0 \\ 0 & 0 & 0 & 1 \end{pmatrix}_{i,i+1}. \tag{3.7}$$

These operators are a simplified version of the more general class of operators proposed in Ref. [76] to efficiently prepare symmetry-preserving states. As depicted on the quantum circuit of Fig. 3.4 (a), operators (3.7) can be realized from 1-qubit gates and 3 C_{NOT} gates, which is optimal[4]. This is interesting for implementation on real hardware, because C_{NOT} gates have a highest error rate than 1-qubit gates in current quantum computer. Moreover, these operators apply only between neighbouring qubits i and $i+1$. This may save a lot of SWAP operations when the qubit connectivity is limited.

Contrary to the previous set $\mathcal{R}$ defined in Eq. (3.3), these operators are not rotations (their determinant is -1). So there is no θ_0 such that $B_{i,i+1}(\theta_0) = \mathbb{1}$. As a consequence, the state $|\Psi_{n-1}\rangle$ obtained at the end of the $(n-1)^{\text{th}}$ iteration does not belong to the set of states $\mathcal{K} = \{R(\theta)|\Psi_{n-1}\rangle \mid R \in \mathcal{R}', \theta \in [0, 2\pi[\}$ on which $|\Psi_{n-1}\rangle$ can be mapped by operators in $\mathcal{R}'$. This raises two issues:

- The selection criterion used for the ADAPT-St version is not adapted to the set $\mathcal{R}'$. Indeed, the derivative of the energy at a given state $R_i(\theta_0)|\Psi_{n-1}\rangle$ tells us about the ability to reduce the energy from this state. But at iteration n, one needs to reduce the energy from the ansatz $|\Psi_{n-1}\rangle$, so if $R_i(\theta_0)|\Psi_{n-1}\rangle \neq |\Psi_{n-1}\rangle$, there is no reason to evaluate the operator R_i with the energy derivative at this state.

- There is no guarantee that the ansatz $|\Psi_n\rangle = B_{i_n,i_n+1}(\theta_n)|\Psi_{n-1}\rangle$ will have a lower energy than $|\Psi_{n-1}\rangle$ at the end of the n^{th} iteration. More precisely, there can be a

[3] This applies in an ideal case where these evaluations are noiseless. If this is not the case, it might be useful to fit the energy curve from more evaluations.

[4] Ref. [77] shows that 3 C_{NOT} gates together with 1-qubit gates are sufficient, and in general necessary, to implement any 2-qubit operations. This number can be reduced to 2 in the particular case of real 2-qubit operations with determinant 1, *i.e.* elements of $SO(4)$. This is instead not possible in general for the $B_{i,i+1}(\theta)$ operators. For example $B_{i,i+1}(\frac{\pi}{2})$ is a SWAP gate, which cannot be built from less than 3 C_{NOT}'s (even when adding 1-qubit gates) as also shown in Ref. [77].

situation where the energy of every state in $\mathcal{K}$ is strictly higher that the energy of $|\Psi_{n-1}\rangle$. In section 3.3.1, it will be shown that this can occur in practical situations and can lead to a breakdown of the convergence if the ADAPT-Min selection criterion is adopted.

To overcome these issues, one can select the operators according to a predefined order. The order chosen here is similar (but not identical) to the one suggested in Ref. [76]. Starting from the Slater determinant $|\Psi_0\rangle = |1\cdots10\cdots0\rangle$, the first $B_{i,i+1}(\theta)$ operator is applied on the two qubits i and $i+1$ corresponding respectively to the highest occupied level and the lowest unoccupied one. Then the operators are placed one after the other in successive columns to add more and more correlations, as illustrated on Fig. 3.4 (b). This order is motivated by the observation that the selection criterion of the ADAPT-Min version effectively place the operators of $\mathcal{R}'$ in a similar order before the occurrence of the convergence breakdown evoked in previous paragraph.

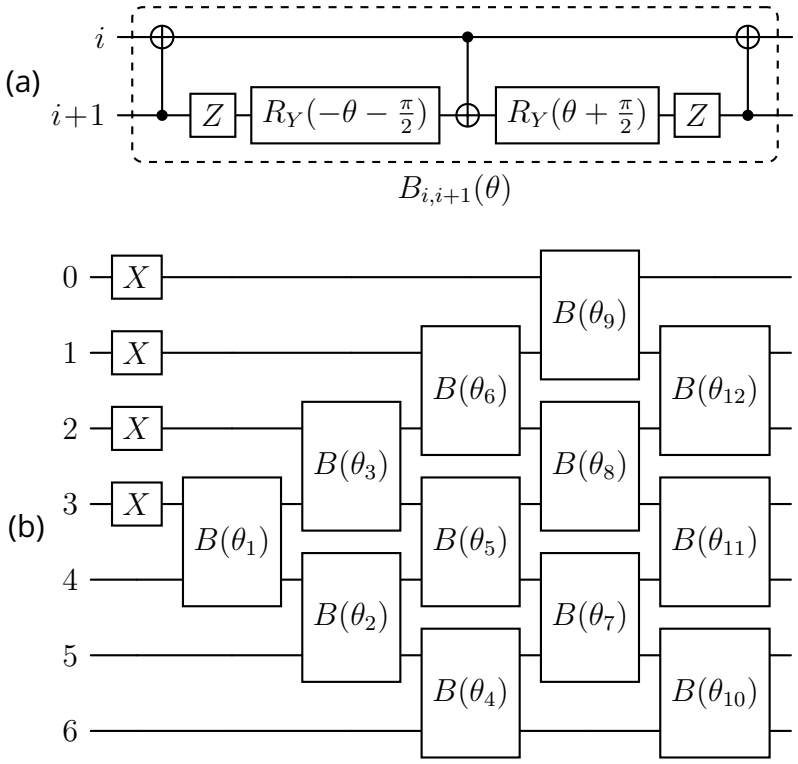


Figure 3.4: *Circuit corresponding to the operator $B_{i,i+1}(\theta)$ used in the ADAPT-Fix approach (a), and example of circuit using these blocks (b). In the latter, the angle indices indicate the order in which the operator are placed in this approach (other indices have been dropped here for clarity).*

The version of the algorithm depicted in section 3.1.2 with the set of operators (3.7) and the selection criterion based on the minimum of the energy curve will be referred as ADAPT-Min2 in the following, while the version obtained with the operators (3.7) selected according to the predefined order described in previous paragraph will be denoted ADAPT-Fix. Nevertheless, one should keep in mind that the choice of a predefined order takes us away from the original spirit of ADAPT-VQE where the operators are selected in a way dictated by the simulated system itself.

3.2.4 Summary of the 4 versions

The four algorithms described in this section are summarized in the following table.

Version	Operators	Selection process
ADAPT-St	$e^{i\theta G_{\alpha\beta}} = \begin{pmatrix} 1 & 0 & 0 & 0 \\ 0 & \cos(\theta) & -\sin(\theta) & 0 \\ 0 & \sin(\theta) & \cos(\theta) & 0 \\ 0 & 0 & 0 & 1 \end{pmatrix}_{\alpha\beta}$	For each $G_{\alpha\beta}$, compute $\lvert\langle\Psi_{n-1}\rvert[H, G_{\alpha\beta}]\rvert\Psi_{n-1}\rangle\rvert$ and select the $G_{\alpha\beta}$ with the highest value.
ADAPT-Min	$e^{i\theta G_{\alpha\beta}} = \begin{pmatrix} 1 & 0 & 0 & 0 \\ 0 & \cos(\theta) & -\sin(\theta) & 0 \\ 0 & \sin(\theta) & \cos(\theta) & 0 \\ 0 & 0 & 0 & 1 \end{pmatrix}_{\alpha\beta}$	For each $G_{\alpha\beta}$, retrieve the energy curve $E_n^{\alpha\beta}(\theta)$ from 5 measurements and select the $G_{\alpha\beta}$ with the lowest energy minimum.
ADAPT-Min2	$B_{i,i+1}(\theta) = \begin{pmatrix} 1 & 0 & 0 & 0 \\ 0 & \cos(\theta) & \sin(\theta) & 0 \\ 0 & \sin(\theta) & -\cos(\theta) & 0 \\ 0 & 0 & 0 & 1 \end{pmatrix}_{i,i+1}$	For each $G_{\alpha\beta}$, retrieve the energy curve $E_n^{\alpha\beta}(\theta)$ from 5 measurements and select the $G_{\alpha\beta}$ with the lowest energy minimum.
ADAPT-Fix	$B_{i,i+1}(\theta) = \begin{pmatrix} 1 & 0 & 0 & 0 \\ 0 & \cos(\theta) & \sin(\theta) & 0 \\ 0 & \sin(\theta) & -\cos(\theta) & 0 \\ 0 & 0 & 0 & 1 \end{pmatrix}_{i,i+1}$	Predefined order.

3.2.5 Estimation of the number of quantum evaluations

The performance of these algorithms depends on their ability to build an ansatz wave-function which quickly approximates the ground state, but also on the number N_{ev} of required quantum evaluations[5]. This number can be decomposed as

$$N_{ev} = \sum_{n=1}^{N_{iter}} (s_n + o_n + r_n), \tag{3.8}$$

where N_{iter} is the number of iterations, and s_n, o_n, r_n are the number of quantum evaluations required at iteration n respectively for the operator selection, the optimisation of the parameter θ_n, and the re-optimisation of $\theta_1, ..., \theta_n$. With ADAPT-St, the selection step evaluates the expectation value of $[H, G_{\alpha\beta}]$ for $1 \leq \alpha < \beta \leq D$, with D the size of the system (within the pairing model, this is the number of levels *i.e.* pairs of doubly degenerated one-body states). Therefore $\frac{1}{2}D(D-1)$ expectation values need to be evaluated at the selection step of a given iteration. As shown in appendix C.1, the Pauli strings in which $[H, G_{\alpha\beta}]$ decomposes can be grouped into 5 fully-commuting sets, hence $s_n = \frac{5}{2}D(D-1)$. With ADAPT-Min, the selection step computes $E_n^{\alpha\beta}(\theta)$ for $1 \leq \alpha < \beta \leq D$ and 5 values of θ. Moreover, the Pauli strings composing the Hamiltonian (2.63) can be grouped into 3 fully-commuting sets, so $s_n = \frac{15}{2}D(D-1)$. This is similar with ADAPT-Min, except for the number of operators which is $D-1$ instead of $\frac{1}{2}D(D-1)$, leading to $s_n = 15(D-1)$. With ADAPT-Fix, the selection step does not require any quantum evaluations: $s_n = 0$.

The number of quantum evaluations required for the 1-parameter optimisation can be considered as independent of the iteration. This step evaluates the energy approximately a

[5]Here, a quantum evaluation refers to a series of N_{shots} measurements in a given measurement basis, from which one can approximate the expectation value of any observable that is diagonal in this basis, as explained in section 2.4.

constant number of times c and each of these evaluations requires 3 quantum evaluations due to the expression of Hamiltonian (2.63) as already mentioned, hence $o_n \approx 3c$. This part does not concern the ADAPT-Min and ADAPT-Min2 versions since the optimised θ is obtained when the energy curve is built for the operator selection.

Finally, r_n usually increases with n since the re-optimisation at iteration n is an optimisation on n parameters. The optimisation algorithm used in this work is the Broyden–Fletcher–Goldfarb–Shanno (BFGS) algorithm, for which the number of required evaluations scales as $O(n^2)$.

The resulting numbers of quantum evaluations required by each of the four algorithms are summarized in table 3.1. To know how N_{ev} evolves with the size D of the system, one needs to clarify how N_{iter} depends on D, within a given target precision. This key question is actually difficult to answer, and no clear conclusion on this aspect were obtained during this application[6].

Version	N_{ev}
ADAPT-St	$(\frac{5}{2}D(D-1)+3c)N_{iter}+O(N_{iter}^3)$
ADAPT-Min	$\frac{15}{2}D(D-1)N_{iter}+O(N_{iter}^3)$
ADAPT-Min2	$N_{ev}=15(D-1)N_{iter}+O(N_{iter}^3)$
ADAPT-Fix	$3cN_{iter}+O(N_{iter}^3)$

Table 3.1: *Number of quantum evaluations N_{ev} required by each of the four algorithms described in the text.*

3.3 Application to pairing Hamiltonian

This section presents results of numerical simulations made in the context of the pairing model presented in section 1.3.1, with the goal of testing the ADAPT-VQE-based methods introduced in previous section. While several system sizes have been tested, here and in the following the results are reported in the case of $A = 8$ particles in $D = 8$ doubly-degenerated energy levels, which corresponds to half-filling, unless otherwise specified. This choice is a compromise between a system not too small, and sufficient convergence (as reported in Fig. 3.5) within an arbitrary limit of 24h of CPU calculations (quantum simulation is heavy on a classical computer). These calculations have been performed using the quantum emulation software QISKIT [79] and the High Performance Computing (HPC) resources from the French computing center TGCC [3].

3.3.1 Convergence of the four versions

Figure 3.5 shows the resulting ground-state energies for the case $A = D = 8$ (*i.e.*, half filling) and for three values of g as a function of the iterations in the ADAPT-VQE algorithm. In addition to total energies (top panels), in the bottom panels are displayed relative errors defined as

$$\delta E \quad = \quad \frac{E - E_{\text{exact}}}{E_{\text{HF}} - E_{\text{exact}}} \,, \tag{3.9}$$

[6]The recent work [78] suggests that this scaling is exponential.

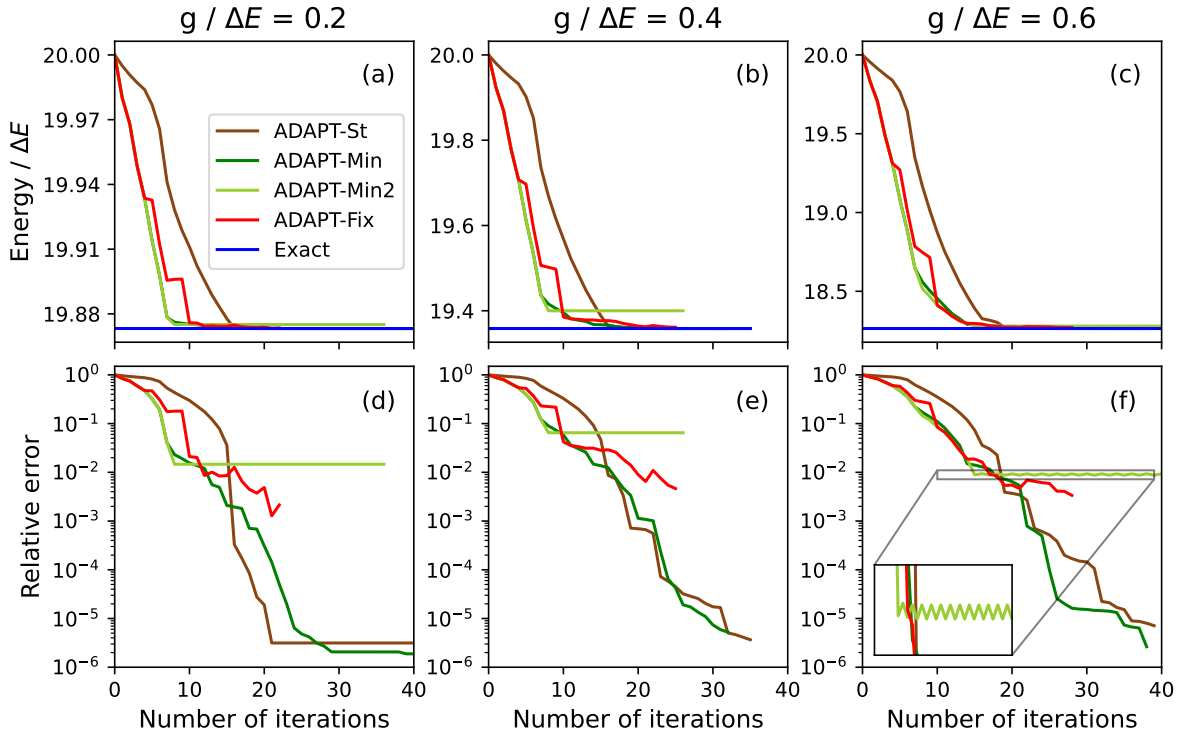


Figure 3.5: *Ground-state energy as a function of the number of iterations computed with the adaptative methods described in the text, for $A = 8$ particles in $D = 8$ levels and for $g/\Delta E = 0.2$ (a), 0.4 (b) and 0.6 (c). Note that, in the top panels, the range covered by the vertical axis varies to help visualize the convergence to the exact ground-state energy (represented by a blue horizontal line). The corresponding relative errors defined in Eq.* (3.9) *are shown in panels (d), (e), and (f), respectively. The computations were performed on a classical HPC machine simulating a quantum device, with a maximum allowed wall time of 24 hours. In the present figure, all iterations completed within this wall time are shown. As a consequence of this practical constraint, it might happen that the curves have not all reached full convergence.*

where E_{HF} and E_{exact} are respectively the Hartree-Fock and the exact ground state energies.

While the ADAPT-St and ADAPT-Min algorithms yield a quick convergence towards the exact value, one notices that the latter version outperforms the former in the first iterations. This is coherent with the fact that ADAPT-Min selects at each step the best operator to reduce the energy, while this is not the case with the ADAPT-St criterion. However, as it can be seen in the relative errors, the ADAPT-St convergence eventually accelerates and becomes equivalent to ADAPT-Min around 15 iterations. This shows that selecting the operator yielding the deeper energy drops at each steps does not necessarily gives the deeper energy drop in total after N_{iter} iterations, for N_{iter} high enough (higher than $15 - 20$ in the applications reported in Fig. 3.5). In other words, the path in the Hilbert space defined by the algorithm can be non-optimal at each step but optimal in the long run.

While reducing the energy as fast as ADAPT-Min at the beginning, ADAPT-Min2 stops the convergence at some point. With the applications reported in Fig. 3.5, it cannot go beyond $\approx 10^{-2}$ in relative error. The oscillations put in evidence by the inset in the case $g = 0.6$, together with the order of the operators recorded in the corresponding simulation suggest the following interpretation. As already mentioned in section 3.2.3, with the set of operators $\mathcal{R}'$ defined in Eq. (3.7) one can reach an iteration n where for every $B \in \mathcal{R}'$ and

every θ, $B(\theta)|\Psi_{n-1}\rangle$ has an energy strictly higher than $|\Psi_{n-1}\rangle$. When this happens, an operator $B_{i_n,i_n+1} \in \mathcal{R}'$ is selected anyway, resulting in an ansatz $|\Psi_n\rangle = B_{i_n,i_n+1}(\theta_n)|\Psi_{n-1}\rangle$ of higher energy than $|\Psi_{n-1}\rangle$. The algorithm can cancel this wrong move at iteration $n+1$ with $|\Psi_{n+1}\rangle = B_{i_n,i_n+1}(\theta_n)B_{i_n,i_n+1}(\theta_n)|\Psi_{n-1}\rangle = |\Psi_{n-1}\rangle$ (because $B_{i_n,i_n+1}(\theta_n)^2 = \mathbb{1}$). So it starts at the same point than two iterations before: it is stuck in a loop. This explains the energy oscillations observed in the case $g = 0.6$ reported in Fig. 3.5 (however, in the cases $g = 0.2$ and $g = 0.4$ the recorded order of operators is not fully compatible with this interpretation, indicating that the cause of the convergence interruption might be more complex). To overcome these oscillations, a restriction of the set of operators at given iterations (such as removing for iteration n the operator that has been used at iteration $n-1$) can be considered, but this has not been tested within this work.

The ADAPT-Fix converges a bit slower in the first iterations, but it avoids being stuck. Although, as expected, the corresponding energy does not decrease monotonically, it is globally decreasing (at least up to the computed iterations). Within the cases reported in Fig. 3.5, it appears to be less efficient than ADAPT-St and ADAPT-Min, but this is not a generality since it outperforms them in the high-coupling case ($g \leq 0.7$) of a bigger system tested ($N = 5$ pairs in $D = 10$ levels), at least up to the ≈ 30 iterations that have been computed.

Let us remark that except ADAPT-Min2, the algorithms presented here reach an excellent accuracy on the total energy by spanning only a fraction of the full Hilbert space. Indeed, in the present case, taking into account normalization and time-reversal symmetry, one needs *a priori* $\binom{8}{4} - 1 = 69$ real coefficients, hence 69 iterations, to exactly expand the many-body wave function. Figure 3.5 shows instead that 20 iterations are sufficient to get less than 1% relative error on the correlation energy. As evoked in section 3.2.5, an important point concerns the scaling of this required number of iterations with respect to the system size.

3.3.2 Comparison with fixed number of operators

In Fig. 3.6 are reported the ground-state energies, relative errors, and fidelities obtained after 20 iterations for the same system with g ranging from 0.1 to 1.0. The accuracy of the methods ADAPT-St, ADAPT-Min, ADAPT-Min2 and ADAPT-Fix is compared with energies and fidelities obtained using the BCS-based ansätze projected within the PAV and VAP schemes evoked in section 1.3.1[7]. Focusing on the latter, one notices that the VAP, as expected, always outperforms the PAV[8]. In particular, the VAP succeeds in smoothly interpolating between the normal ($g < g_c$) and superfluid ($g > g_c$) phases (in the present example $g_c \simeq 0.298$), while the PAV collapses to the Hartree-Fock limit around and below g_c. In general, all methods except PAV are able to provide a good approximation to the energy for all values of the coupling strength.

Fig. 3.6 (a) and (b) shows that 20 iterations allows the ADAPT-St, ADAPT-Min, ADAPT-Fix algorithms to outperform the BCS ansätze in approximating the ground energy of the tested pairing system, except at high coupling where the latter are known to be particularly effi-

[7] While polynomial scaling methods have been evoked in section 1.3.1 to perform these projections, the PAV and VAP results presented in Fig. 3.6 have been obtained via a brute-force projection for simplicity, by selecting the components of the wavefunction with the adequate number of particles and normalizing the resulting projected state. This is possible because the system simulated here is small enough.

[8] Indeed, the VAP is the optimised projected BCS state, so one can expect it to have a lower energy than other projected BCS states, including the PAV.

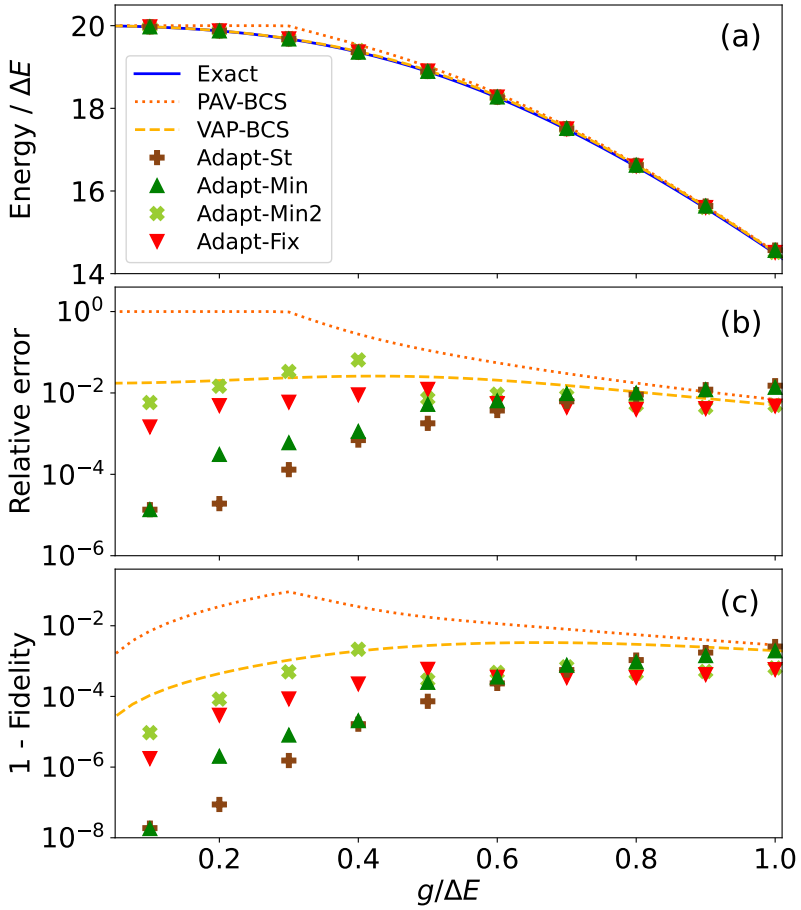


Figure 3.6: *Total ground-state energy (a), relative energy error (b), and infidelity (i.e. $1 - fidelity$) (c) as a function of the coupling strength $g/\Delta E$ for the different ansätze considered in this work, including the VAP and PAV (the latter collapses to the Hartree-Fock limit around and below $g_c \simeq 0.298$). As in Fig. 3.5, results are shown for $A = 8$ particles in $D = 8$ doubly-degenerated levels (half filling). Values from the ADAPT-VQE-based ansätze correspond to results obtained at the 20^{th} iteration.*

cient. Moreover, the pannel (c) shows that that the ground state is also well-approximated by the compact wavefunction built by these algorithms. The present success of the ADAPT-VQE-based methods confirms the findings of Ref. [80] and makes them in particular a promising alternative to symmetry-breaking/restoration approaches for quantum computations of strongly correlated systems.

It should be noted that the VAP approach is still rather competitive, taking into account that only D parameters are optimised to minimise the energy, while in the ADAPT-VQE-based methods the number of parameters grows as the number of iterations. This raises again the crucial question evoked at the end of section 3.2.5: how does the number of iterations required to reach a target accuracy scales with the system size? Actually, this may depend on the operators used in the procedure and their ability to include significative parts of the wavefunction with a limited number of them. Maybe more relevant operators than the ones defined in Eqs. (3.3) and (3.7) can be used to improve the algorithms presented here.

3.3.3 Necessity of the re-optimisation

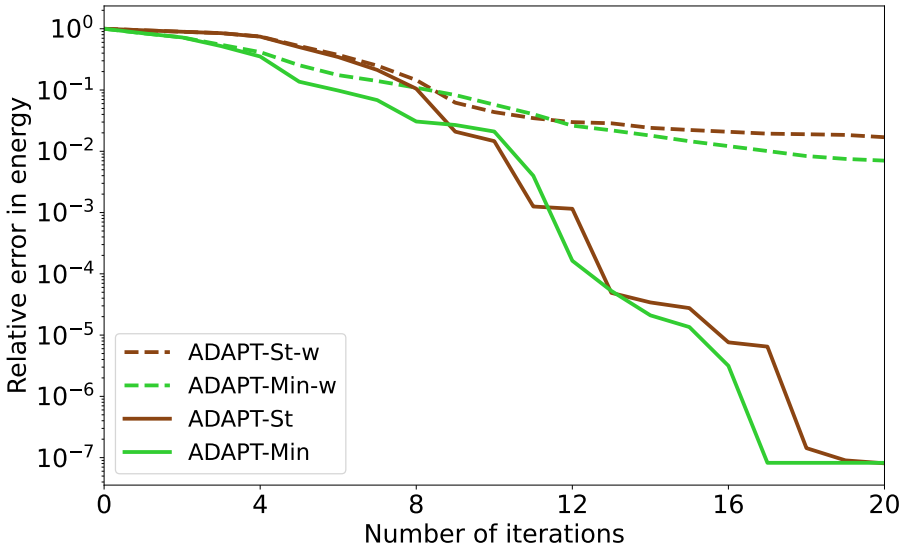


Figure 3.7: *Application of the algorithms ADAPT-St, ADAPT-Min, and their counterparts without this re-optimisation step called ADAPT-St-w and ADAPT-Min-w respectively, to a pairing system with $A = 6$ particles in $D = 6$ levels and a coupling constant $g = 0.6$. The curves represent the relative error in energy (3.9) with respect to the iteration.*

The re-optimisation performed at the end of each iteration requires extra quantum evaluations. This is the price to pay to obtain a compact and accurate ansatz wavefunction, as illustrated in fig. 3.7. This figure presents a comparison of ADAPT-St and ADAPT-Min with their counterparts without this re-optimisation step, denoted as ADAPT-St-w and ADAPT-Min-w respectively. While, for the first iterations, the re-optimisation matters less than the selection criterion, it becomes decisive around the 10^{th} iteration to reach a precision below 1% of the relative error in energy. It allows to improve the ansatz wavefunction by several orders of magnitude in the energy error without adding any extra operator.

3.4 Conclusion

This chapter has presented variational algorithms allowing to efficiently combine excitation operators in order to build a compact ansatz wavefunction approximating the ground state of a system. Several ADAPT-VQE-inspired algorithms have been described and benchmarked with an application to the pairing Hamiltonian. They have proven very efficient in providing an accurate approximation of the N-body ground state, with high fidelities ($> 99\%$) reached after $15 - 20$ iterations (for the considered system whose Hilbert space is 70-dimensional), even when the system is close to the normal-to-superfluid transition. In particular, the resulting ansätze obtained here after 20 iterations have revealed closer to the exact ground state than the standard projected BCS ansätze (PAV and VAP).

These methods will be used in the following chapter to compute the one-body Green's function of the same pairing system. To simplify the discussion, the application will focus on the ADAPT-Min approach, which seems to be the best approach for $g/\Delta E < 1$, *i.e.* for the regime of interest of nuclear physics applications.

Chapter 4

Quantum simulation of Green's functions

This chapter describes and benchmarks a procedure first introduced in [81] to approximate Green's functions from quantum evaluations. The general method, based on Lehmann representation (1.18), *i.e.* the Green's function in energy domain, is explained in section 4.1 after a brief aside about direct quantum calculation in time domain. The algorithm is then applied to the pairing model (1.24). Section 4.2 details the simplifications induced by this model, and the decomposition into Pauli strings of the operators that have to be evaluated with a quantum computer. In particular, the number of quantum evaluations required to evaluate all these Pauli strings is discussed.

The results, simulated on a noiseless quantum emulator in the limit of infinite number of measurements, are presented in section 4.3. A quantitative evaluation of the difference with the exact Green's function is provided. It is shown that the method also yields approximate energies of systems with an odd number of particles, which are usually more difficult to describe on classical computers. Finally, the limit of infinite number of measurements is relaxed and numerical estimates are given on the number of measurements required to reach a given target accuracy. Some results presented in this chapter have been published in [68].

4.1 General methodology

A short discussion about the quantum calculation of Green's function in time domain is first made below. Then the procedure used in the following to compute it in energy domain is described.

4.1.1 Quantum calculation in time domain

The direct calculation of the Green's function from its definition Eq. (1.17) is in principle possible on a quantum computer. To understand how, let us rewrite this definition and consider the case $t' < t$ (the case $t < t'$ yields a similar calculation with $a^\dagger_\beta(t')a_\alpha(t)$ instead of $a_\alpha(t)a^\dagger_\beta(t')$ due to the time ordering). Using Jordan-Wigner mapping in this case, the Green's

function can be expressed as

$$\begin{aligned} ig_{\alpha\beta}(t,t') &= \langle\Psi_0^A|a_\alpha(t)a_\beta^\dagger(t')|\Psi_0^A\rangle \\ &= \langle\Psi_0^A|U^\dagger(t)a_\alpha U(t)U^\dagger(t')a_\beta^\dagger U(t')|\Psi_0^A\rangle \\ &= (-1)^{\beta-\alpha}\langle\Psi_{q,0}^A|U_q^\dagger(t)Z_1...Z_{\alpha-1}(X_\alpha+iY_\alpha)U_q(t)U_q^\dagger(t')Z_1...Z_{\beta-1}(X_\beta-iY_\beta)U_q(t')|\Psi_{q,0}^A\rangle \\ &= (-1)^{\beta-\alpha}\Big(F(X_\alpha,X_\beta)+iF(Y_\alpha,X_\beta)-iF(X_\alpha,Y_\beta)+F(Y_\alpha,Y_\beta)\Big), \end{aligned} \tag{4.1}$$

where, for $\sigma,\sigma'\in\{X,Y\}$,

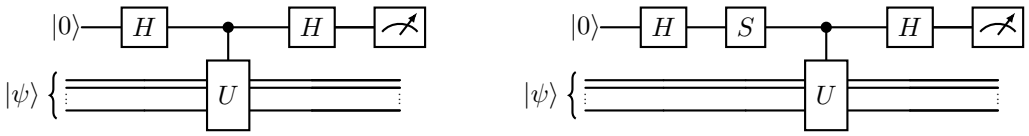
$$F(\sigma_\alpha,\sigma'_\beta) := \langle\Psi_{q,0}^A|U_q^\dagger(t)Z_1...Z_{\alpha-1}\sigma_\alpha U_q(t)U_q^\dagger(t')Z_1...Z_{\beta-1}\sigma'_\beta U_q(t')|\Psi_{q,0}^A\rangle.$$

Here $|\Psi_0^A\rangle$ is the A-particle ground state, $|\Psi_{q,0}^A\rangle$ is the corresponding state encoded on qubits, $U(t)$ is the evolution operator, and $U_q(t)=\mathrm{JW}\big[U(t)\big]$ is its transformation under the Jordan-Wigner mapping defined in section 2.6.2.

Since the terms $F(\sigma_\alpha,\sigma'_\beta)$ are not *a priori* expectation values of hermitian operators, they cannot be decomposed into expectation values of Pauli strings in order to be evaluated by measuring $|\Psi_{q,0}^A\rangle$ in several bases. However, each of them is the expectation value of a unitary operator. Therefore, they can be evaluated on a quantum computer with a Hadamard test[1] (non-destructive measurement), where the evolution operators can be implemented using standard quantum operations and Trotter decomposition [56, 70].

However, long time evolutions are needed to resolve accurately the corresponding spectrum[2]. That is why such a procedure requires significant improvements to the quantum hardware (especially in terms of noise reduction) [82]. A more viable path for implementation on current quantum devices exploits the Lehmann representation of Green's functions (1.18). One can take advantage of the explicit presence of the exact eigenstates and eigenenergies in different particle-number sectors to devise suitable approximations for G_{ij}. This strategy is followed here for the calculation of the one-body Green's function from expectation values evaluated with a quantum computer.

[1]The Hadamard test is a method to get the expectation value of a given unitary U on a state $|\psi\rangle$ from repeated measurements on a single qubit. It can be represented with the following circuits.



Let us consider the first circuit. The state just before measurement writes as

$$\frac{1}{2}|0\rangle\otimes(\mathbb{1}+U)|\psi\rangle+\frac{1}{2}|1\rangle\otimes(\mathbb{1}-U)|\psi\rangle. \tag{4.2}$$

Therefore the probability to measure $|0\rangle$ and $|1\rangle$ are respectively

$$\begin{aligned} p_0 &= \langle\psi|(\mathbb{1}+U^\dagger)(\mathbb{1}+U)|\psi\rangle, \\ p_1 &= \langle\psi|(\mathbb{1}-U^\dagger)(\mathbb{1}-U)|\psi\rangle. \end{aligned} \tag{4.3}$$

Their difference gives $p_0-p_1=\frac{1}{2}\langle\psi|(U+U^\dagger)|\psi\rangle=\mathrm{Re}(\langle\psi|U|\psi\rangle)$. Similarly, with the second circuit one gets $p_0-p_1=\mathrm{Im}(\langle\psi|U|\psi\rangle)$.

[2]Indeed, the accuracy ΔE on the spectrum is related to the time evolution ΔT via the uncertainty relation $\Delta E.\Delta T\sim 1$, which follows from the Fourier transform.

4.1.2 Quantum calculation in energy domain

A procedure to obtain the Green's function of a system described by a Hamiltonian H, based on the Lehmann representation, has been recently highlighted in Ref. [81]. Following the hybrid quantum-classical paradigm, this method distributes the numerical effort between the Quantum Processing Unit (QPU) and the classical one (CPU), as follows.

1. A quantum algorithm (such that the ones described in chapter 3) is used to build a qubit wavefunction encoding an approximation of the A-particle ground-state wavefunction. This approximate ground state is denoted by $|\widetilde{\Psi}_0^A\rangle$ below[3].

2. Two sets of operators $\{\Lambda_\alpha^+\}_{1\leq\alpha\leq\Omega}$ and $\{\Lambda_\alpha^-\}_{1\leq\alpha\leq\Omega}$ are chosen to build states with $A\pm1$ particles. Each operator in the former (latter) has the effect of increasing (reducing) particle number by one unit when applied to the reference state $|\widetilde{\Psi}_0^A\rangle$, which results in two new sets of (eventually non-orthogonal) states

$$\left\{|\phi_1^{A+1}\rangle,\cdots,|\phi_\Omega^{A+1}\rangle\right\} := \left\{\Lambda_1^+,\cdots,\Lambda_\Omega^+\right\}|\widetilde{\Psi}_0^A\rangle\,, \tag{4.4a}$$

$$\left\{|\phi_1^{A-1}\rangle,\cdots,|\phi_\Omega^{A-1}\rangle\right\} := \left\{\Lambda_1^-,\cdots,\Lambda_\Omega^-\right\}|\widetilde{\Psi}_0^A\rangle\,. \tag{4.4b}$$

   Such states span reduced subspaces of the $(A+1)$- and $(A-1)$-body Hilbert spaces, respectively. They define the following overlaps and Hamiltonian matrix elements

$$\mathcal{O}_{\alpha\beta}^{A\pm1} := \langle\phi_\alpha^{A\pm1}|\phi_\beta^{A\pm1}\rangle = \langle\widetilde{\Psi}_0^A|\Lambda_\alpha^\mp\Lambda_\beta^\pm|\widetilde{\Psi}_0^A\rangle\,, \tag{4.5a}$$

$$\mathcal{H}_{\alpha\beta}^{A\pm1} := \langle\phi_\alpha^{A\pm1}|H|\phi_\beta^{A\pm1}\rangle = \langle\widetilde{\Psi}_0^A|\Lambda_\alpha^\mp H\Lambda_\beta^\pm|\widetilde{\Psi}_0^A\rangle\,. \tag{4.5b}$$

   These $4\Omega^2$ expectation values are computed by the QPU: the operators $\Lambda_\alpha^\mp\Lambda_\beta^\pm$ and $\Lambda_\alpha^\mp H\Lambda_\beta^\pm$ are decomposed into combinations of Pauli strings, which are evaluated by measuring, after the suitable basis rotations, qubits prepared in a state encoding $|\widetilde{\Psi}_0^A\rangle$. These decompositions and evaluations are detailed in section 4.2.

3. Approximate eigenstates of the Hamiltonian with $A\pm1$ particles

$$|\widetilde{\Psi}_\nu^{A\pm1}\rangle = \sum_\alpha c_{\alpha,\nu}^{A\pm1}|\phi_\alpha^{A\pm1}\rangle\,, \tag{4.6}$$

   together with their corresponding eigenvalues $\widetilde{E}_\nu^{A\pm1}$, can be obtained by solving, in the two reduced subspaces defined by Eqs. (4.4), the generalised eigenvalue problem

$$\sum_\beta \mathcal{H}_{\alpha\beta}^{A\pm1}c_{\beta,\nu}^{A\pm1} = \widetilde{E}_\nu^{A\pm1}\sum_\beta \mathcal{O}_{\alpha\beta}^{A\pm1}c_{\beta,\nu}^{A\pm1}. \tag{4.7}$$

   The expectation values computed in the previous step are substituted into this equation, that is solved on the CPU[4]. This provides approximations for Ω eigenstates and

[3] To simplify the notations, $|\widetilde{\Psi}_0^A\rangle$ will denote both the approximate A-particle ground state and the qubit state encoding it.

[4] The solution of the generalised eigenvalue problem is rather standard on classical computers and is made in two steps. First, the overlap matrix is diagonalized to obtain an orthogonal basis for the reduced subspace of interest. Then, this orthogonal basis is employed to diagonalize the Hamiltonian matrix. Noteworthy, the diagonalization might lead to fewer states than in the set $\{|\phi_\alpha^{A\pm1}\rangle\}$ if these states are not linearly independent. In practice, this situation does not lead to any specific difficulty.

eigenvalues of H with $A \pm 1$ particles, $\{|\widetilde{\Psi}_\nu^{A\pm1}\rangle, \widetilde{E}_\nu^{A\pm1}\}_{0\leq\nu\leq\Omega-1}$. While this resembles what is standardly referred to as configuration mixing in nuclear physics, in the quantum computing context it has been put forward as an efficient way to mitigate hardware noise and has been termed Quantum Subspace Expansion (QSE) [83–89]. Notably, the QSE method has also been developed for nuclear physics model Hamiltonians such as the pairing model using the quantum Krylov technique [90] or in the Lipkin model using either the quantum computing extension of the generator coordinate method [91] or the so-called quantum equation of motion technique [92, 93].

4. Finally, an approximate Green's function is built using these eigenelements as

$$g_{\alpha\beta}(\omega) = \sum_\nu \frac{\langle\widetilde{\Psi}_0^A|a_\alpha|\widetilde{\Psi}_\nu^{A+1}\rangle\langle\widetilde{\Psi}_\nu^{A+1}|a_\beta^\dagger|\widetilde{\Psi}_0^A\rangle}{\omega-(\widetilde{E}_\nu^{A+1}-\widetilde{E}_0)+i\eta} + \sum_\mu \frac{\langle\widetilde{\Psi}_0^A|a_\beta^\dagger|\widetilde{\Psi}_\mu^{A-1}\rangle\langle\widetilde{\Psi}_\mu^{A-1}|a_\alpha|\widetilde{\Psi}_0^A\rangle}{\omega-(\widetilde{E}_0-\widetilde{E}_\mu^{A-1})-i\eta} \,. \tag{4.8}$$

   The spectroscopic amplitudes appearing in the numerators of Eq. (4.8) can be obtained by combining expectation values $\langle\widetilde{\Psi}_0^A|a_\alpha\Lambda_\gamma^+|\widetilde{\Psi}_0^A\rangle$ (which can be computed on the QPU) with the coefficients $c_{\beta,\nu}^{A\pm1}$ (obtained by solving Eq. (4.7)) as one can see by inserting Eq. (4.6) as

$$\langle\widetilde{\Psi}_0^A|a_\alpha|\widetilde{\Psi}_\nu^{A+1}\rangle = \sum_\gamma c_{\gamma,\nu}^{A+1}\langle\widetilde{\Psi}_0^A|a_\alpha|\phi_\gamma^{A+1}\rangle = \sum_\gamma c_{\gamma,\nu}^{A+1}\langle\widetilde{\Psi}_0^A|a_\alpha\Lambda_\gamma^+|\widetilde{\Psi}_0^A\rangle \,, \tag{4.9}$$

   and similarly with $\langle\widetilde{\Psi}_0^A|a_\beta^\dagger|\widetilde{\Psi}_\mu^{A-1}\rangle$.

Until now, the operators $\{\Lambda_\alpha^\pm\}_\alpha$ have not been specified. A natural choice would be, for Λ_α^+, to combine $m+1$ creation and m annihilation operators to build $(m+1)$-particle–m-hole excitations as $\{a_\alpha^\dagger\}_\alpha$, $\{a_\alpha^\dagger a_\beta^\dagger a_\gamma\}_{\alpha,\beta,\gamma}$, …, with $0 \leq m \leq A-1$ (and similarly for Λ_α^-). In the present study, we simply consider $\{\Lambda_\alpha^+\}_\alpha = \{a_\alpha^\dagger\}_\alpha$ and $\{\Lambda_\alpha^-\}_\alpha = \{a_\alpha\}_\alpha$, so that the expectation values entering Eq. (4.9) read as

$$\langle\widetilde{\Psi}_0^A|a_\alpha\Lambda_\beta^+|\widetilde{\Psi}_0^A\rangle = \langle\widetilde{\Psi}_0^A|\Lambda_\alpha^- a_\beta^\dagger|\widetilde{\Psi}_0^A\rangle = \mathcal{O}_{\alpha\beta}^{A+1} \,, \tag{4.10a}$$

$$\langle\widetilde{\Psi}_0^A|a_\alpha^\dagger\Lambda_\beta^-|\widetilde{\Psi}_0^A\rangle = \langle\widetilde{\Psi}_0^A|\Lambda_\alpha^+ a_\beta|\widetilde{\Psi}_0^A\rangle = \mathcal{O}_{\alpha\beta}^{A-1} \,. \tag{4.10b}$$

This choice leads to the benefit that the overlaps (4.5a) can be used again, and the QPU evaluation of the amplitudes in step 4 can be skipped, which results in a significant computational gain. The whole procedure obtained with this specific choice is schematically summarized in Fig. 4.1.

In summary, in the strategy depicted here, the manipulation of the complicated many-body states in Fock space is assigned to the QPU. This manipulation includes the circuit used to build the ansatz for the many-body wave function, and the calculation of expectation values of operators. All other tasks are performed on a classical machine, including the ansatz optimisation, the subspace diagonalization, and the calculation of the one-body Green's function from the expectation values. Below, this approach is applied to compute the one-body Green's functions associated to the pairing Hamiltonian (1.24). Its performance is evaluated using a noiseless emulation of a quantum computer.

4.2 Application to pairing - simplifications

After the general description, in the previous section, of a method approximating the Green's function from quantum evaluations, this section focuses on the application to the

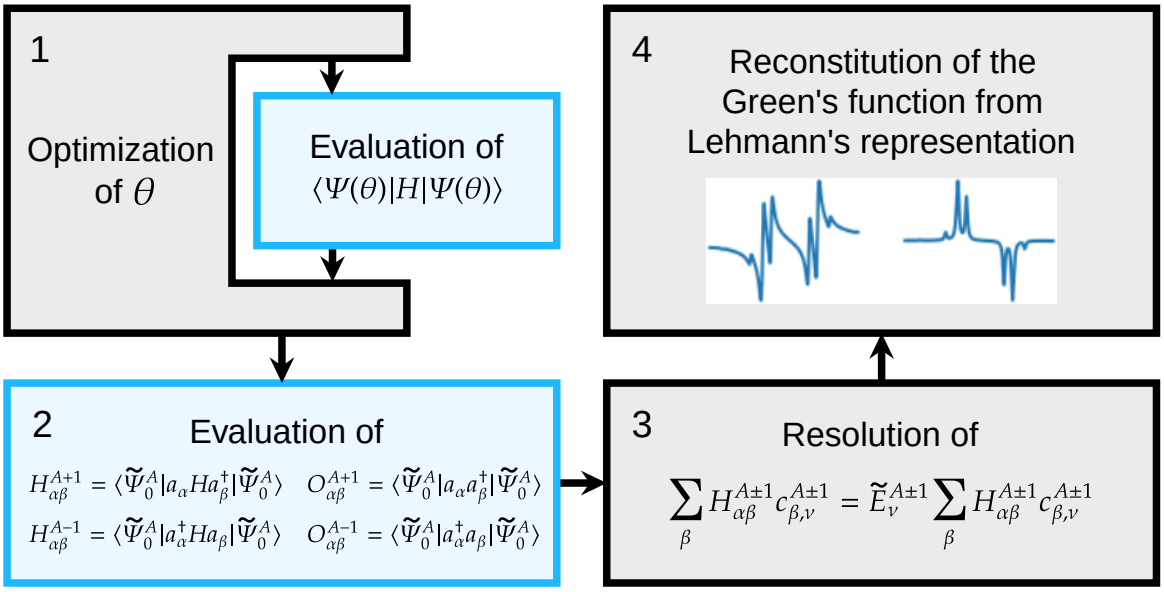


Figure 4.1: *Schematic representation of the procedure described in section 4.1.2 with* $\{\Lambda^+_\alpha\}_\alpha = \{a^\dagger_\alpha\}_\alpha$ *and* $\{\Lambda^-_\alpha\}_\alpha = \{a_\alpha\}_\alpha$*. The blue boxes indicates the steps where a quantum processor is used to evaluate expectation values. The first step, in the left upper part, represents the preparation of an ansatz wavefunction approximating the ground state as described in section 3.1 while the three other boxes represent the evaluation of expectation values defined in Eqs. (4.5), the resolution of the two generalised eigenvalue problems of Eq. (4.7) and the reconstitution of the Green's function from Lehmann's representation. These four steps correspond to ones described in the text.*

pairing Hamiltonian (1.24) with an even number of particles. Using the specificity of this Hamiltonian, further simplifications, discussed below, can be made, leading to a reduction of the number of operators (4.5) that have to be evaluated. These operators are then decomposed into Pauli strings, which are finally grouped together in order to reduce the number of required quantum evaluations.

4.2.1 Simplifications due to symmetries

Starting from the ground-state approximation $|\widetilde{\Psi}^A_0\rangle$, one needs to evaluate the $4\Omega^2$ expectation values introduced in Eqs. (4.5). As a consequence of the choice $\{\Lambda^+_\alpha\}_{1\leq\alpha\leq\Omega} = \{a^\dagger_\alpha\}_{\alpha\in\{1,\bar{1},\ldots,D,\bar{D}\}}$ (and similarly for $\{\Lambda^-_\alpha\}_{1\leq\alpha\leq\Omega}$), $\Omega = 2D$ so that one has *a priori* $16D^2$ expectation values to compute on the QPU. However, due to the fact that Hamiltonian (1.24) has a block-diagonal structure (it does not couple Slater determinants with distinct configurations of unpaired particles) and $|\widetilde{\Psi}^A_0\rangle$ does not contain unpaired particle, one has

$$\mathcal{O}^{A+1}_{\beta\alpha} = \langle\widetilde{\Psi}^A_0|a_\beta a^\dagger_\alpha|\widetilde{\Psi}^A_0\rangle = 0 \quad \text{and} \quad \mathcal{H}^{A+1}_{\beta\alpha} = \langle\widetilde{\Psi}^A_0|a_\beta H a^\dagger_\alpha|\widetilde{\Psi}^A_0\rangle = 0 \quad \text{for } \alpha \neq \beta, \tag{4.11}$$

and similarly in the subspace with $A-1$ particles. This implies that one needs to evaluate only 4Ω expectation values instead of $4\Omega^2$. In addition, because of the symmetry between barred and non-barred levels in the test model in Eq. (1.24), one can show that for any $k \in \{1,\ldots,D\}$, $\mathcal{H}^{A\pm1}_{kk} = \mathcal{H}^{A\pm1}_{\bar{k}\bar{k}}$ and $\mathcal{O}^{A\pm1}_{kk} = \mathcal{O}^{A\pm1}_{\bar{k}\bar{k}}$. This divides the number of required evaluations by a factor 2, leading ultimately to $2\Omega = 4D$ expectation values to evaluate. While this reduces

the numerical effort required for the results presented below, one should keep in mind that, for a more general model (*e.g.* a realistic nuclear system), one would have to evaluate the $4\Omega^2$ expectation values of Eqs. (4.5).

As a result, within the test model used here and the choice of operators $\{\Lambda_\alpha^\pm\}_\alpha$, one simply needs to evaluate

$$\mathcal{O}_{ii}^{A+1} = \langle \widetilde{\Psi}_0^A | a_i a_i^\dagger | \widetilde{\Psi}_0^A \rangle \,, \qquad \mathcal{O}_{ii}^{A-1} = \langle \widetilde{\Psi}_0^A | a_i^\dagger a_i | \widetilde{\Psi}_0^A \rangle \,, \tag{4.12a}$$

$$\mathcal{H}_{ii}^{A+1} = \langle \widetilde{\Psi}_0^A | a_i H a_i^\dagger | \widetilde{\Psi}_0^A \rangle \,, \qquad \mathcal{H}_{ii}^{A-1} = \langle \widetilde{\Psi}_0^A | a_i^\dagger H a_i | \widetilde{\Psi}_0^A \rangle \,, \tag{4.12b}$$

for $i \in \{1, ..., D\}$. To do so, one has to express operators $a_i a_i^\dagger$, $a_i^\dagger a_i$, $a_i H a_i^\dagger$, $a_i^\dagger H a_i$ into qubit observables, which is the purpose of the following section. Since the matrices $\mathcal{H}^{A\pm1}, \mathcal{O}^{A\pm1}$ are now diagonal, the generalised eigenvalue problem (4.7) becomes trivial to solve. Its solution writes as

$$\widetilde{E}_\nu^{A\pm1} = \mathcal{H}_{\nu\nu}^{A\pm1} / \mathcal{O}_{\nu\nu}^{A\pm1}, \qquad c_{\beta,\nu}^{A\pm1} = \delta_{\beta,\nu} \,. \tag{4.13}$$

4.2.2 Expansion into Pauli operators

By means of the Jordan-Wigner mapping described in section 2.6.2, expressions (4.12) are decomposed into expectation values of Pauli terms. After expressing $a_i a_i^\dagger$ and $a_i^\dagger a_i$ as

$$\mathrm{JW}[a_i a_i^\dagger] = \frac{1}{2}(\mathbb{1} + Z_i) \,, \tag{4.14a}$$

$$\mathrm{JW}[a_i^\dagger a_i] = \frac{1}{2}(\mathbb{1} - Z_i) \,, \tag{4.14b}$$

the overlaps can be written as

$$\mathcal{O}_{ii}^{A+1} = \frac{1}{2} + \frac{1}{2}\langle \widetilde{\Psi}_0^A | Z_i | \widetilde{\Psi}_0^A \rangle \,, \tag{4.15a}$$

$$\mathcal{O}_{ii}^{A-1} = \frac{1}{2} - \frac{1}{2}\langle \widetilde{\Psi}_0^A | Z_i | \widetilde{\Psi}_0^A \rangle \,. \tag{4.15b}$$

It follows that only one Pauli string has to be evaluated both for $\mathcal{O}_{ii}^{A+1}$ and $\mathcal{O}_{ii}^{A-1}$.

The derivation of the Hamiltonian kernels $\mathcal{H}_{ii}^{A+1}$ and $\mathcal{H}_{ii}^{A-1}$ is less straightforward. Using the expression of Hamiltonian (1.24), one has

$$\mathrm{JW}[a_i H a_i^\dagger] = \sum_{k=1}^{D} \varepsilon_k \Big(\mathrm{JW}[a_i a_k^\dagger a_k a_i^\dagger] + \mathrm{JW}[a_i a_{\bar{k}}^\dagger a_{\bar{k}} a_i^\dagger] \Big) - g \sum_{k \neq l} \mathrm{JW}[a_i a_k^\dagger a_{\bar{k}}^\dagger a_{\bar{l}} a_l a_i^\dagger] \,, \tag{4.16}$$

for $i \in \mathcal{I} := \{1, \bar{1}, \ \dots \ , D, \bar{D}\}$. To compute the terms $\mathrm{JW}[a_i a_j^\dagger a_j a_i^\dagger]$ for $j \in \mathcal{I}$, one has to distinguish the case $j \neq i$, for which

$$\mathrm{JW}[a_i a_j^\dagger a_j a_i^\dagger] \ = \mathrm{JW}[a_i a_i^\dagger] \mathrm{JW}[a_j^\dagger a_j] = \frac{1}{4}(\mathbb{1} + Z_i)(\mathbb{1} - Z_j) \,, \tag{4.17}$$

from the case $j = i$, for which

$$\mathrm{JW}[a_i a_j^\dagger a_j a_i^\dagger] = \mathrm{JW}[a_i a_i^\dagger] = \frac{1}{2}(\mathbb{1} + Z_i) \,. \tag{4.18}$$

Then, for $k, l \in \{1, \ \dots \ , D\}$,

$$\mathrm{JW}[a_i a_k^\dagger a_{\bar{k}}^\dagger a_{\bar{l}} a_l a_i^\dagger] = \mathrm{JW}[a_i a_i^\dagger] \mathrm{JW}[a_k^\dagger a_{\bar{k}}^\dagger a_{\bar{l}} a_l] \tag{4.19}$$

if $i \notin \{k, \bar{k}, l, \bar{l}\}$, while it is 0 otherwise. Using the fact that $\mathrm{JW}[a_k^\dagger a_{\bar{k}}^\dagger a_{\bar{l}} a_l] = \sigma_k^- \sigma_{\bar{k}}^- \sigma_{\bar{l}}^+ \sigma_l^+$ with $\sigma_\alpha^\pm := \frac{1}{2}(X_\alpha \pm iY_\alpha)$, one finally obtains

$$\begin{aligned}\mathrm{JW}[a_i H a_i^\dagger] &= (\mathbb{1} + Z_i)\Big(\frac{\varepsilon_i}{2}\mathbb{1} + \sum_{j\in I\setminus\{i\}} \frac{\varepsilon_j}{4}(\mathbb{1} - Z_j) - \frac{g}{2}\Gamma_i\Big) \\ &= (\mathbb{1} + Z_i)\left[\left(\frac{\varepsilon_i}{4} + \sum_{k=1}^{D}\frac{\varepsilon_k}{2}\right)\mathbb{1} - \sum_{j\in\mathcal{I}\setminus\{i\}}\frac{\varepsilon_j}{4}Z_j - \frac{g}{2}\Gamma_i\right], \end{aligned} \tag{4.20}$$

where

$$\Gamma_i = \sum_{\substack{k\neq l\\ k,l\neq i}} \sigma_k^-\sigma_{\bar{k}}^-\sigma_{\bar{l}}^+\sigma_l^+ = \frac{1}{8}\sum_{\substack{k<l\\ k,l\neq i}} \Big[X_k X_{\bar{k}} X_{\bar{l}} X_l + Y_k Y_{\bar{k}} Y_{\bar{l}} Y_l - X_k X_{\bar{k}} Y_{\bar{l}} Y_l - Y_k Y_{\bar{k}} X_{\bar{l}} X_l \\ + X_k Y_{\bar{k}} X_{\bar{l}} Y_l + Y_k X_{\bar{k}} Y_{\bar{l}} X_l + X_k Y_{\bar{k}} Y_{\bar{l}} X_l + Y_k X_{\bar{k}} X_{\bar{l}} Y_l\Big].$$

Note that, when developing $\sigma_k^-\sigma_{\bar{k}}^-\sigma_{\bar{l}}^+\sigma_l^+ + \sigma_l^-\sigma_{\bar{l}}^-\sigma_{\bar{k}}^+\sigma_k^+$, all terms with an imaginary coefficient cancel. Similarly, one has

$$\mathrm{JW}[a_i^\dagger H a_i] = (\mathbb{1} - Z_i)\left[\left(-\frac{\varepsilon_i}{4} + \sum_{k=1}^{D}\frac{\varepsilon_k}{2}\right)\mathbb{1} - \sum_{j\in\mathcal{I}\setminus\{i\}}\frac{\varepsilon_j}{4}Z_j - \frac{g}{2}\Gamma_i\right]. \tag{4.21}$$

From these expressions, we see that there are $O(D^2)$ Pauli strings to evaluate in order to get $\mathcal{H}_{ii}^{A+1}$ and $\mathcal{H}_{ii}^{A-1}$, mainly coming from Γ_i. This has to be done for all $i \in \{1, ..., D\}$, leading to a total of $O(D^3)$ Pauli strings needed to build the Green's function of Hamiltonian (1.24).

4.2.3 Pauli grouping

As explained in section 2.6.4, Pauli strings can be grouped together into N_{sets} fully commuting sets so that all the Pauli strings in a given set can be evaluated all at once from N_{shots} measurements. This allows reducing the total number of measurements to $N_{meas} = N_{sets} \times N_{shots}$. While the scaling of N_{shots} with the target precision is addressed in section 4.3.3, the present section discusses the evaluation of N_{sets}.

Pauli strings coming from $\mathcal{O}_{ii}^{N+1}$, $\mathcal{O}_{ii}^{N-1}$ and from one-body terms of $\mathcal{H}_{ii}^{N+1}$ and $\mathcal{H}_{ii}^{N-1}$ contain only $\mathbb{1}$'s and Z's, such that they can all (for all values of i) be evaluated together without the need to rotate the qubit basis prior to the measurement. The remaining contributions, coming from Γ_i and $Z_i\Gamma_i$ terms in Eqs. (4.20)-(4.21), take the forms $P_{kl}^{(u)}$ and $Z_i P_{kl}^{(u)}$, where $P_{kl}^{(1)}, ..., P_{kl}^{(8)}$ are the Pauli strings, acting on qubits $k, \bar{k}, l, \bar{l}$, reading respectively as

$$\begin{aligned} &XXXX, \quad YYYY, \quad XYXY, \quad YXYX, \\ &XXYY, \quad YYXX, \quad XYYX, \quad YXXY. \end{aligned} \tag{4.22}$$

In order to group them, let us define the $8D$ sets $E_i^{(u)} := \{P_{kl}^{(u)}, Z_i P_{kl}^{(u)}\}_{1\leq k<l\leq D,\ k,l\neq i}$. Each of them is a fully commuting set, so one can find a basis transformation allowing to evaluate all its Pauli strings. Let us consider two 1-qubit operations U_x and U_y mapping respectively X to Z and Y to Z as obtained from the general expressions (2.13) and (2.14). For $E_i^{(1)}$, $E_i^{(2)}$, $E_i^{(3)}$, $E_i^{(4)}$, one can use the basis transformations composed of $\mathbb{1}\otimes\mathbb{1}$ on qubits i and $\bar{i}$, and respectively $U_x \otimes U_x$, $U_y \otimes U_y$, $U_x \otimes U_y$, $U_y \otimes U_x$ on qubits k and $\bar{k}$ for all $k \neq i$. Examples of 1- and 2-qubit unitaries that can be used to build the required $2D$-basis transformations are given in table 4.1.

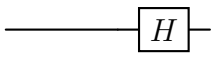
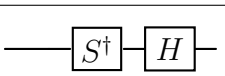
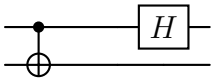
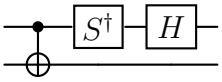
Pauli strings	Basis in which they can be measured	Basis transformation
$\mathbb{1},\ Z$	$\{\|0\rangle, \|1\rangle\}$	$\mathbb{1} =$
$\mathbb{1},\ X$	$\{\frac{\|0\rangle+\|1\rangle}{2}, \frac{\|0\rangle-\|1\rangle}{2}\}$	$U_x =$ 
$\mathbb{1},\ Y$	$\{\frac{\|0\rangle+i\|1\rangle}{2}, \frac{\|0\rangle-i\|1\rangle}{2}\}$	$U_y =$ 
$\mathbb{11},\ ZZ,\ XX,\ YY$	$\{\frac{\|00\rangle+\|11\rangle}{2}, \frac{\|00\rangle-\|11\rangle}{2}, \frac{\|01\rangle+\|10\rangle}{2}, \frac{\|01\rangle-\|10\rangle}{2}\}$	$U_v =$ 
$\mathbb{11},\ ZZ,\ XY,\ YX$	$\{\frac{\|00\rangle+i\|11\rangle}{2}, \frac{\|00\rangle-i\|11\rangle}{2}, \frac{\|01\rangle+i\|10\rangle}{2}, \frac{\|01\rangle-i\|10\rangle}{2}\}$	$U_w =$ 

Table 4.1: *Some fully commuting sets of 1- and 2-qubit Pauli strings (first column) with corresponding bases in which they are all diagonal so that they can be simultaneously evaluated from measurement statistics (second column). The third column indicates examples of unitaries (represented by quantum circuits) that can be used to performed the required basis rotation.*

Sets $E_i^{(5)}$, $E_i^{(6)}$, $E_i^{(7)}$, $E_i^{(8)}$ require different basis transformations since they contain strings acting differently (some with a X, some with a Y) on the same qubit ν, for some ν (*e.g.* in $E_i^{(5)}$, the string $X_1 X_{\bar{1}} Y_2 Y_{\bar{2}}$ acts with a Y on qubits 2 and $\bar{2}$ while the string $X_2 X_{\bar{2}} Y_3 Y_{\bar{3}}$ acts on them with a X). The corresponding basis transformations require the use of an extra CNOT gate for each qubit pair $(k, \bar{k})$ with $k \neq i$. They can be obtained from the previous ones, by replacing the 2-qubit transformations $U_x \otimes U_x$, $U_y \otimes U_y$, $U_x \otimes U_y$, $U_y \otimes U_x$ respectively by U_v, U_v, U_w, U_w, which are represented in table 4.1. For example, all strings of the set $E_i^{(5)}$ can be measured using a unitary made of U_v in each pair $(k, \bar{k})$ with $k \neq i$.

For this specific system, one thus obtains $N_{sets} = 8D + 1$ (*i.e.* the $8 \times D$ sets $E_i^{(u)}$ plus the set with all strings containing only $\mathbb{1}$'s and Z's). This can be further reduced by noticing that the reunion of $E_i^{(1)}$, $E_i^{(2)}$, $E_i^{(5)}$, $E_i^{(6)}$ is also fully commuting, and its strings can all be measured using a basis transformation made of U_v in every pair of qubits $k, \bar{k}$, except the pair $i, \bar{i}$ on which the identity is applied. Similarly the strings of $E_i^{(3)}$, $E_i^{(4)}$, $E_i^{(7)}$, $E_i^{(8)}$ can all be measured using U_w instead of U_v. The number of fully-commuting sets can then be reduced to

$$N_{sets} = 2D + 1. \tag{4.23}$$

Alternatively, if one wants to avoid the use of extra CNOT gates for measurements, one can divide $E_i^{(5)}$, $E_i^{(6)}$, $E_i^{(7)}$, $E_i^{(8)}$ in sets with fixed k, whose corresponding basis measurement does not require C_{NOT} gates, but instead transformations obtained as a tensor product of U_x, U_y, and $\mathbb{1}$. This choice leads to $N_{sets} = O(D^2)$ to compute the whole Green's function.

While simulations presented in the following have been performed in the limit of an infinite number of measurements, numerical estimates for the number of measurements required in practice to achieve a given precision on the Green's functions are discussed in section 4.3.3. Finally, let us note that the cost of the classical part of the calculation, *i.e.* the resolution of the generalised eigenvalue problem (4.7) and the assembly of the building blocks of the Green's function in Lehmann representation (4.8), is negligible compared to the QPU computation.

4.3 Application to pairing - results

Let us now present the results of the application of the procedure described in section 4.1 to the pairing model. The quality of the resulting Green's functions is quantified using the first moments of the associated spectral strength distribution. Moreover, the procedure used here is shown to also provide approximations to the energies of neighbouring odd-particle systems.

The quantum calculations have been simulated using the quantum emulation software QISKIT [79] and the HPC resources from the TGCC [3]. Calculations were performed without noise, and in the limit of infinite number of measurements. The last part of this section goes beyond the latter limit to estimate numerically the number of measurements required to reach a target precision.

4.3.1 Results for the Green's function

The method described in section 4.1.2 requires an approximation of the ground state $|\widetilde{\Psi}_0^A\rangle$ to start with. The results obtained using the ADAPT-Min ansatz of chapter 3 are compared here to the results obtained using the PAV-BCS and VAP-BCS ansätze introduced in section 1.3.1. While the ADAPT-Min ansatz is, by construction, encoded in qubits, the PAV-BCS and VAP-BCS need to be realized with a unitary operation applied on the initial qubit state $|0...0\rangle$.

The BCS state $|\Psi_{BCS}\rangle = \prod_{k=1}^{D}(U_k + V_k a_k^\dagger a_{\bar{k}}^\dagger)|\text{vac}\rangle$ is easy to implement since it is a product state. It can be realized with a rotation $R_y(\theta_k)$ (with $U_k = \cos(\theta_k)$ and $V_k = \sin(\theta_k)$) performed on every qubit k followed by a C_{NOT} gate with control qubit k and target qubit $\bar{k}$, resulting in

$$\bigotimes_{k=1}^{D}\left(\begin{array}{c} k \\ \bar{k} \end{array}\right.\!\!\!

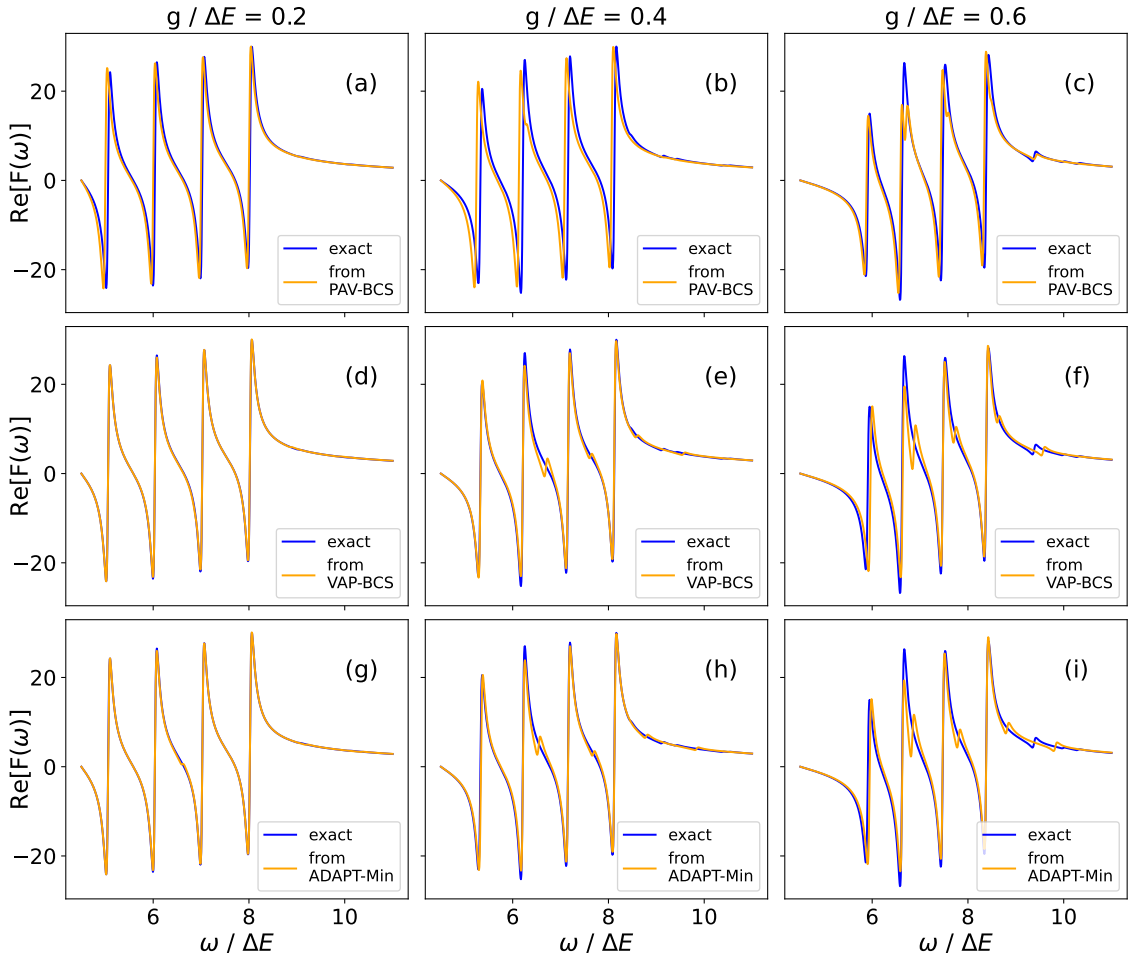


Figure 4.2: *Real part of the function $F(\omega)$ defined in Eq. (1.22), where the regularizing parameter η has been set to 0.04. Taking advantage of the symmetry of $F(\omega)$ (see Fig. 1.2), the focus is made here for simplicity on the forward (i.e. one-particle addition) part. Exact results for $A = 8$ particles in $D = 8$ doubly-degenerated levels with coupling $g \in \{0.2, 0.4, 0.6\}$ (from left to right) are shown in blue and compared with approximate ones obtained with the PAV-BCS [panels (a), (b), (c)], VAP-BCS [panels (d), (e), (f)], and ADAPT-Min (stopped at 20 iterations) [panels (g), (h), (i)] techniques.*

In all cases, a fairly good reproduction of the exact Green's function is obtained independently of the coupling strength. Even in the PAV-BCS case, the Green's function appears rather close to the exact solution. At weak coupling, this is mainly due to the fact that the total energy is largely dominated by the Hartree-Fock component, and even a significant error on the correlation energies does not degrade substantially the Green's function. In the intermediate regime, even if absolute correlation energies are not well reproduced by the PAV-BCS (see panel (b) of Fig. 4.4), such an error cancels out to a good extent when considering the energy differences that enter the denominator of Eq. (4.8). Eventually, the PAV-BCS generally improves compared to the other techniques as the coupling strength increases. While the VAP-BCS and the ADAPT-Min are practically indistinguishable from the exact results at small coupling, some small discrepancies become visible in the superfluid regime.

In order to gauge the performance of the various methods in a more quantitative way,

let us consider the first few moments of the spectral strength distribution, defined as (see *e.g.* Ref. [94])

$$M_p := \sum_\nu SF_\nu^+ (E_\nu^{A+1} - E_0^A)^p + \sum_\mu SF_\mu^- (E_0^A - E_\mu^{A-1})^p \,, \tag{4.25}$$

where SF_ν^+ and SF_μ^- are the spectroscopic factors

$$SF_\nu^+ := \sum_\alpha |\langle \Psi_\nu^{A+1} | a_\alpha^\dagger | \Psi_0^A \rangle|^2 \,, \tag{4.26a}$$

$$SF_\mu^- := \sum_\alpha |\langle \Psi_\mu^{A-1} | a_\alpha | \Psi_0^A \rangle|^2 \,. \tag{4.26b}$$

Relative errors with respect to exact moments (with $p = 1, 2, 3, 4$) for the different approaches are reported in Fig. 4.3. A clear hierarchy between the three methods emerges, with the PAV-BCS involving the bigger errors on each of the computed moments. VAP-BCS and ADAPT-Min perform generally very well, with errors of at most a few percent for the stronger coupling. The Green's function involved by ADAPT-Min is slightly more accurate than the one involved by VAP-BCS. This provides an additional quantitative criterion to affirm that 20 iterations of ADAPT-Min are sufficient to carry a more accurate approximation of the ground state than the VAP-BCS and PAV-BCS.

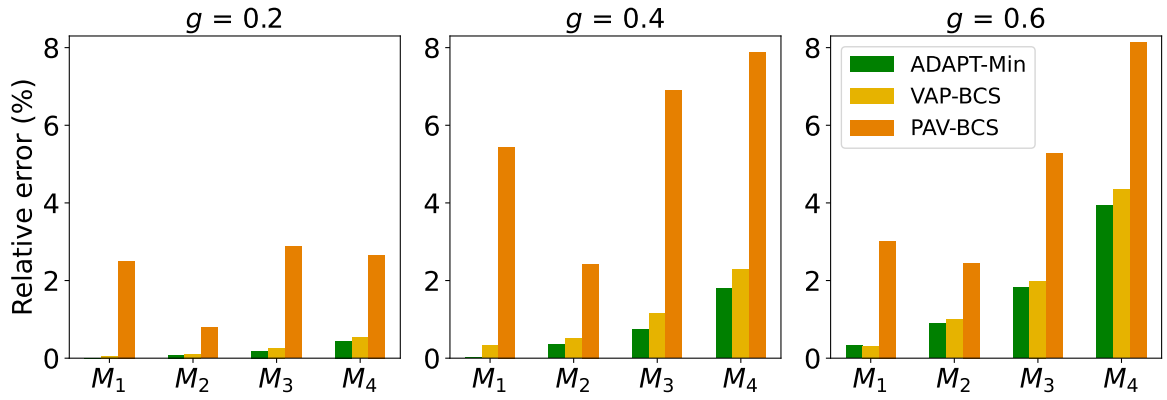


Figure 4.3: *Relative error (in %) on the first four moments of the spectral strength distribution* (4.25)*, obtained for a pairing system with $A = 8$ particles in $D = 8$ doubly-degenerated levels, from the PAV-BCS, VAP-BCS, and ADAPT-Min (stopped after 20 iterations) ground-state ansätze. Values for the three coupling strengths $g = 0.2, 0.4, 0.6$ are reported respectively in the left, middle, and right panels. This comparison allows to quantitatively characterize the Green's functions calculations reported in Fig. 4.2 and to establish a clear hierarchy between the efficacy of the three ansätze: 20 iterations of ADAPT-Min are sufficient to carry more accurate results than the VAP-BCS, which is itself more precise than PAV-BCS.*

4.3.2 Odd systems

An interesting byproduct of the use of the QSE approach is that one has access to approximate eigenenergies of the neighbouring odd systems with $A \pm 1$ particles. Figure 4.4 shows the approximate correlation energies obtained for odd and even systems in the case of $D = 8$ doubly-degenerated levels and for the same three different values of the interaction strength as in the computation reported in Fig. 4.2. For even systems, the energies

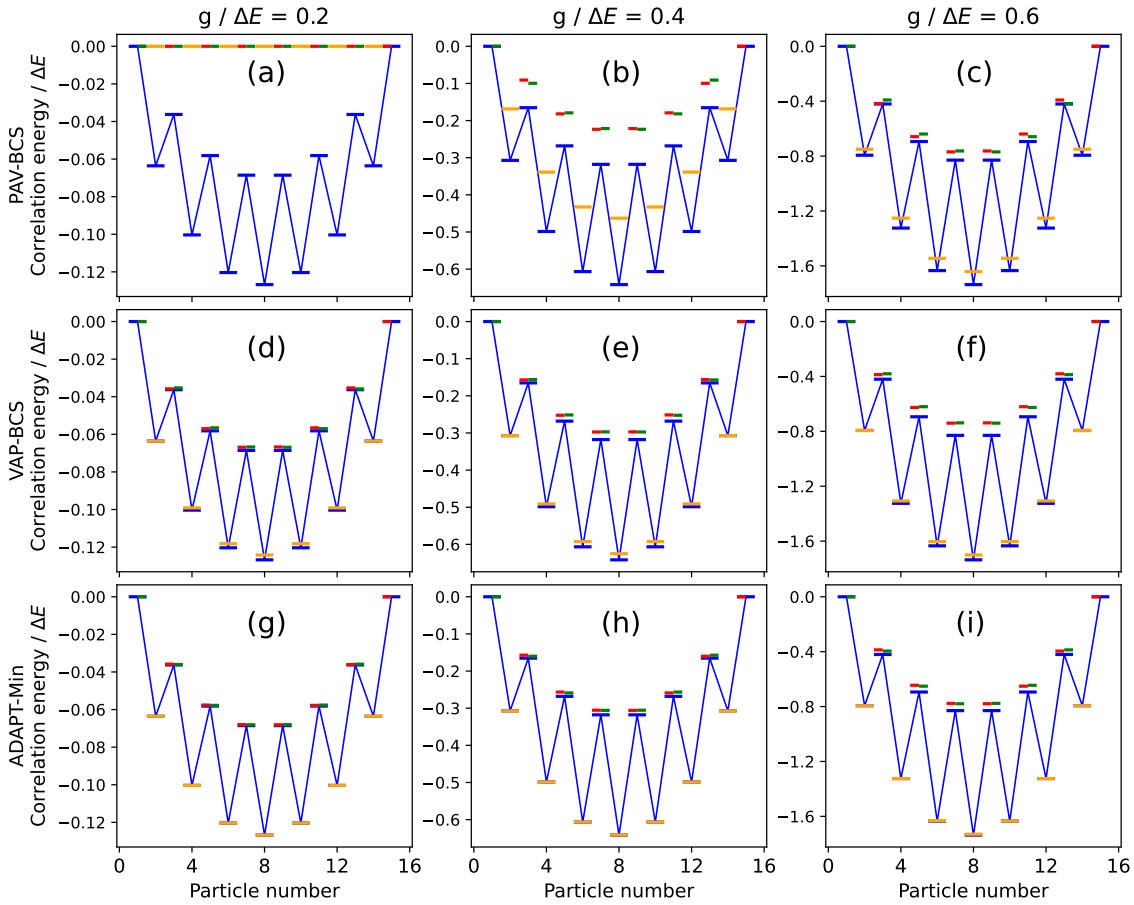


Figure 4.4: *Odd-even staggering of correlation energies obtained for $A = 1$ to $A = 15$ particles in a system of $D = 8$ doubly degenerated levels. Different columns display results for increasing coupling strengths, namely $g = 0.2$, $g = 0.4$, and $g = 0.6$. Exact results obtained by FCI are systematically shown in blue and compared with the approximated ones obtained from the ground state ansätze PAV-BCS, VAP-BCS, and ADAPT-Min (from top to bottom) calculated only for even systems. Approximate energies of even systems (in orange) are directly obtained from these ground state computations, while the odd systems ones are built using the method described in section 4.1.2 from the surrounding even systems (in red from the even system with one particle less, and in green from the one with one particle more).*

are the direct outcome of the PAV-BCS (top panels), VAP-BCS (middle panels) and ADAPT-Min (bottom panels) methods. Associated accuracies (and fidelities of the corresponding ground-state wave functions) are those reported in Fig. 3.6 of chapter 3. For odd systems, energies are computed via the eigenvalue problem (4.7), with $|\widetilde{\Psi}_0^A\rangle$ coming consistently from the three methods applied on one of the two neighbouring even systems. The two possibilities are reported in Fig. 4.4: each odd system ground energy computed from the even system with one particle less is represented in red, while each odd system ground energy computed from the even system with one particle more is represented in red.

Below the normal-to-superfluid transition, *e.g.* for $g = 0.2$, PAV-BCS identifies with the Hartree-Fock solution and is unable to account for the odd-even staggering observed in the correlation energy. As expected, the method nevertheless improves when moving towards the strong-coupling regime $g \gg g_c$, yielding reasonable results already at $g = 0.6$. Both VAP-

BCS and ADAPT-Min provide an overall good description of odd and even systems for all interaction strengths. A closer look reveals that ADAPT-Min is systematically more accurate. Note also that computing ground-state energies of odd systems from below (*i.e.* from the even system with one particle less) or from above yields very similar results, which reinforces the consistency of the present method.

The good performance of this configuration-mixing approach suggests that it might also be applied in classical computations for more traditional nuclear structure methods. In that case, by starting from a PAV-BCS or a VAP-BCS trial wave-function in the even system, one could access states in odd nuclei, which are typically harder to tackle with standard techniques. Other interesting aspects are that (i) because of the subspace diagonalization, the method not only gives the ground state but also excited states, (ii) the complexity of the set of operators $\{\Lambda_\alpha^\pm\}_\alpha$ can be increased at will either by including 2-particle–1-hole ($2p$-$1h$) and $2h$-$1p$, ... excitations or by changing the nature of QSE operators, and (iii) the input A-particle state $|\widetilde{\Psi}_0^A\rangle$ could also be modified to find an efficient balance between the complexity of the state and the complexity of the operators.

4.3.3 Evaluation of statistical error and required number of measurements

While section 4.2 addressed the general scaling properties of the expectation values given by Eq. (4.5), a relevant question concerns the number of measurements that are required in practice to simulate the Green's function up to a given target error. Because of the diagonalization step, Eq. (4.7), one cannot analytically relate a desired precision on the Green's function to errors stemming from finite numbers of N_{shots}. Instead, such a relation can be estimated numerically.

To this purpose, measurements of the expectation values (4.5) on a noiseless quantum computer have been simulated for the case of $N = 8$ particles in $D = 8$ doubly-degenerated levels and pairing strength $g = 0.6$. For each of the N_{sets} groups of commuting Pauli terms, experiments with different numbers of measurements N_{shots} have been performed and the corresponding Green's function has been reconstructed from them. For each value of N_{shots}, the standard deviation with respect to the exact solution for the first four moments of the spectral strength distribution has been determined by repeating the experiment 100 times[5]. Fig. 4.5 displays the relative standard deviation on the four first moments as a function of N_{shots}. One observes that it decreases as $1/\sqrt{N_{shots}}$ for all curves, reaching values around $10\ \%$ for $N_{shots} \approx 200$. In order to reach errors of the order of $1\ \%$, one needs instead to increase the number of measurements to $N_{shots} \approx 10^4$.

Tests with different numbers of particles and levels have been performed, and showed a similar behaviour. From these tests restricted to small systems, it seems that N_{shots} increases linearly with D. If this dependence is confirmed, with the linear dependence of N_{sets} with D obtained in section 4.2, the total number of required measurements $N_{meas} = N_{sets} \times N_{shots}$ scales quadratically with D (for this application to pairing Hamiltonian).

[5] In some experiments, the error on the overlaps (4.5a) can be such that the overlap matrices are not positive definite and thus the generalised eigenvalue problem (4.7) cannot be solved. These pathological cases have been excluded from the present analysis.

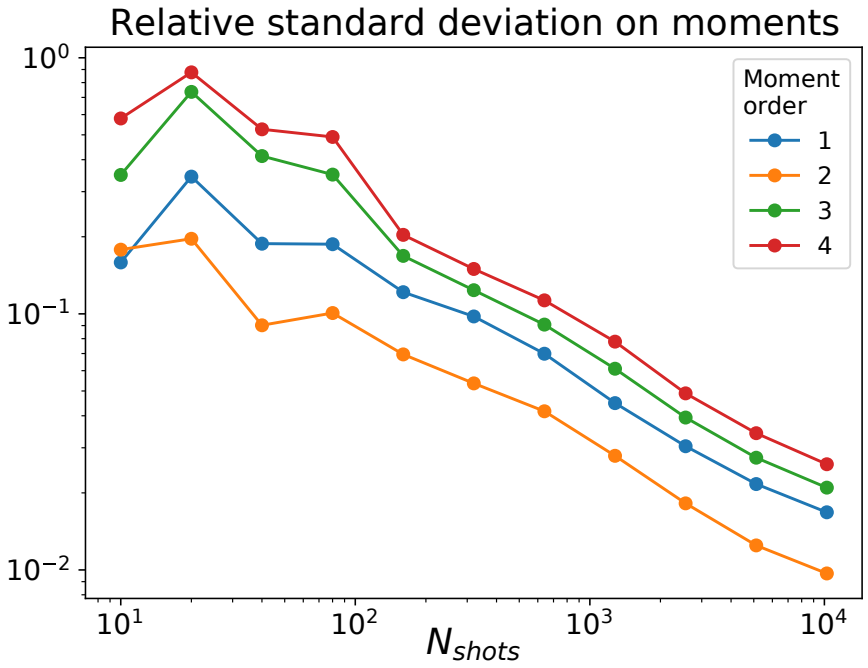


Figure 4.5: *Relative standard deviation (standard deviation divided by mean value) on the first moments of the computed Green's function* (4.25) *of a system with* $N = 8$ *particles in* $D = 8$ *doubly-degenerated levels and pairing strength* $g = 0.6$*, computed from a quantum simulation with several finite values of* N_{shots}*. The Pauli terms whose expectation values are required to build the Green's functions are grouped into* $N_{sets} = 2D + 1$ *fully commuting sets as explained in section 4.2.3. For several values of* N_{shots}*,* N_{shots} *noiseless quantum measurements are simulated to sample the measurement distributions in the basis corresponding to each of these groups. From these* $N_{sets} \times N_{shots}$ *measurements, the Green's function and the first moments of its spectral strength distribution are computed. This procedure is repeated* 100 *times in order to estimate the standard deviation and mean value of the resulting moments.*

4.4 Conclusion

This chapter has presented an end-to-end strategy based on a hybrid quantum-classical algorithm to obtain Green's functions. This method has been applied to small superfluid systems, with a quantitative study of the required number of quantum evaluations. In particular, due to (i) the symmetries of the pairing Hamiltonian, (ii) the low-weight of the corresponding Pauli strings, and (iii) the simple choice for the QSE operators $\{\Lambda_\alpha^\pm\}_\alpha$ made here, only $2D + 1$ different measurement bases need to be sampled to obtain the whole Green's function, where D is the system size.

The method described here takes as an input an ansatz wavefunction approximating the ground state. The results obtained using as such starting point the ansätze PAV-BCS, VAP-BCS, and ADAPT-Min, have been compared here. It is observed that the most accurate ansätze in terms of energy and fidelity of the ground state are also the more accurate for the reproduction of the Green's function. Calculations starting with VAP-BCS and ADAPT-Min ansätze succeed in reproducing the first moments of the Green's functions up to a few percent in relative error. Moreover, these calculations performed for even systems provide approximate eigenenergies of the neighbouring odd systems, that are usually more difficult to deal with.

Nevertheless, one has to keep in mind that these simulations were performed in the limit of a perfect sampling of the measurement distributions, *i.e.* an infinite number of measurements in each measurement basis. Section 4.3.3 shows that the number of measurements required increases as $1/\varepsilon^2$ where ε is the target precision. Furthermore, this study was made with noiseless simulations. One should expect an increase of the required number of measurements, together with the necessity of error-mitigation techniques, when considering a more realistic quantum computer.

This work can be regarded as a proof of principle in view of future applications that are relevant to nuclear physics. One can anticipate that the extension of the current approach to realistic nuclear Hamiltonians will introduce several additional challenges. First, the simplifications discussed in section 4.2 may not occur with a more general Hamiltonian, hence a significant increase of the number of measurements is to be expected. Second, realistic interactions generally produce stronger fragmentation of the spectral strength as well as collective excitations (*e.g.* deformation, pairing vibrations, clustering phenomena). As discussed above, this may require larger operator sets to get an approximate ground state with the ADAPT-VQE-based algorithms, together with enlarged QSE subspaces to approach the Green's function. In particular, in future applications one may envisage the use of QSE operators that effectively account for such collective modes as an alternative to independent multi-particle multi-hole excitations.

Chapter 5

Analog quantum computing with neutral atoms

So far, quantum computing has been addressed without considering the hardware. The algorithms discussed in chapters 2, 3, and 4 were described as a discrete succession of 1- and 2-qubit gates. However, one has to keep in mind that these gates are made from continuous operations that depend on the hardware, such as laser pulses whose values of duration, intensity, and frequency are fixed for each gate implementation. In particular, 2-qubit gates involve interaction between qubits which can be realized via various processes. Gates constitute a convenient abstraction: one can assemble them to design an algorithm without thinking about the underlying technology. The resulting algorithm is therefore independent of the hardware. To run it, a given quantum computer will translate each gate into the corresponding operations allowed by its own hardware, but the knowledge about this is not required for the programmer. This convenient way to consider quantum computing is called the digital paradigm.

Digital quantum computing requires a device for which gates can be implemented with a limited error rate, *i.e.* an error rate low enough to allow for efficient error correction. However, despite current progress, today's quantum computers remain still rather limited in terms of accuracy and number of qubits. Among the wide variety of quantum technologies developed to realize a convenient quantum computer, some are not adapted to the digital paradigm but are still promising for specific applications. To design a quantum algorithm for those, one has to think about the hardware and adapt to it. Instead of realizing a discrete succession of gates, one can consider instead the continuous evolution of the qubit state realised by the hardware, and tune some parameters to fit this evolution with the desired application. This is the analog paradigm.

After some general considerations on analog quantum computing in section 5.1, this chapter introduces in section 5.2 a specific type of hardware that is well-suited within this computing paradigm: the neutral atom quantum computer. In view of addressing variational algorithms adapted to this hardware in the following chapter, a discussion is made in section 5.3 about the challenges raised by this application.

5.1 Analog quantum computing

Within the analog paradigm, one has to consider the evolution Hamiltonian $H_R(t)$ that determines the evolution of the qubit state $|\Psi(t)\rangle$ as

$$|\Psi(t)\rangle = \mathcal{T}\Big[\exp\Big(-\frac{i}{\hbar}\int_0^\tau H_R(t)dt\Big)\Big]|\Psi(0)\rangle. \tag{5.1}$$

This Hamiltonian, called "resource Hamiltonian", is imposed by the hardware in the form of $H_R(t) = H_R(\alpha(t), \beta(t), ...)$ where $\alpha(t), \beta(t), ...$ are some time-dependent tunable parameters. An analog quantum algorithm can be understood as a choice for these parameters and their evolution in time. As schematically depicted in Fig. 5.1, this differs from a digital algorithm which can be decomposed into well-defined gates. Indeed, contrary to digital quantum algorithm, decomposing the evolution operator in Eq. (5.1) into 1- and 2-qubit gates might be difficult and not suited to the hardware. On the one hand, this usually makes difficult or even impossible the implementation of a given unitary, limiting the range of applications of analog quantum computing. On the other hand, since it is a low-level computing scheme, *i.e.* it is closer to a direct manipulation of qubits and their interactions, analog quantum computing allows to efficiently take into account the constraints of the hardware in order to save resources, reduce the computation time, and limit the accumulation of errors.

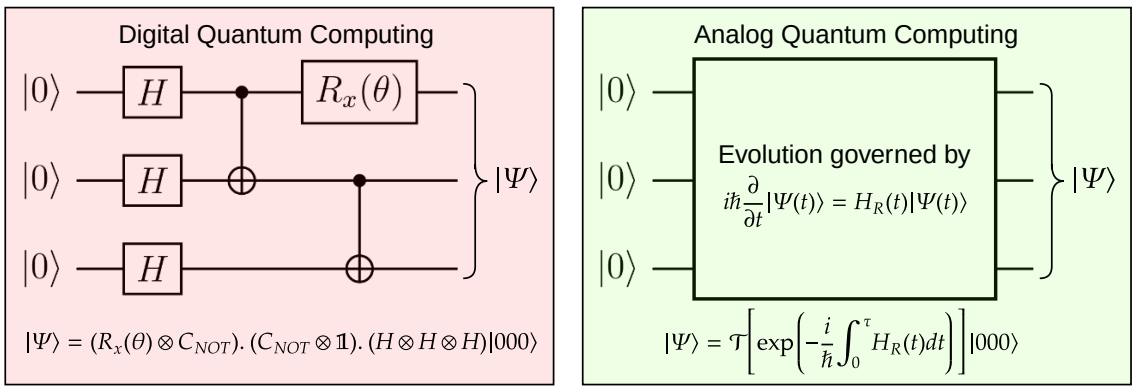


Figure 5.1: *Schematic comparison between digital and analog quantum computing. In both cases, a 3-qubit state $|\Psi\rangle$ (expressed below) is prepared by a unitary operator applied on the initial state $|000\rangle$. In the digital case, this unitary can be expressed as a product of 1- and 2-qubit unitaries, while in the analog case it is determined by the Schrödinger equation obtained with the resource Hamiltonian $H_R(t)$.*

Adiabatic evolution [95] is a typical algorithm for which the analog paradigm is well-suited. The goal of this algorithm is to find the ground state of a Hamiltonian H. To achieve it, one considers a Hamiltonian H_0 for which the ground state $|\Psi_0\rangle$ is easy to prepare. One needs to find suitable continuous functions $\alpha, \beta, ...$ defined between a starting time t_0 and a final time t_f for which $H_R(\alpha(t_0), \beta(t_0), ...) = H_0$ and $H_R(\alpha(t_f), \beta(t_f), ...) = H$. According to the adiabatic theorem [96, 97], if the qubit state is prepared in $|\Psi_0\rangle$ and the variations of $\alpha, \beta, ...$ are slow enough (see [95] for precisions), the qubit state remains in the ground state of the Hamiltonian all along the evolution, and in particular it reaches the ground state of H at time t_f. Analog quantum computing is natural for this algorithm because the adiabatic evolution is directly realized by the hardware. However, this cannot be performed if

for any accessible parameters $\alpha, \beta, ...$, $H_R(\alpha, \beta, ...) \neq H$. A given technology can be used for adiabatic evolution only on systems whose Hamiltonian H can be mapped to the resource Hamiltonian H_R. For other systems, the use of analog quantum computing is more challenging but still possible. The next chapter address such a use with variational algorithms.

5.2 Neutral atom quantum computer

Trapped neutral atoms controlled by lasers provide a promising quantum hardware for analog quantum computing. They are currently developed by several companies such as Quera [98] or Pasqal [67, 99]. In particular, within the French HQI project, Pasqal has delivered such a quantum computer, called Ruby, to the French research center CEA and installed it at the TGCC computing center. This section briefly describes the main ingredients of a neutral atom quantum computer. First some of their interesting features are evoked to motivate the focus made here on this technology. Then, a few technical information is given to explain how the atoms are prepared for the computation and how their state is measured. Finally, the computation itself is described, within the analog paradigm. More information can be found in [67, 100–103].

5.2.1 Why neutral atoms

Neutral atoms can encode qubits. They can be placed in an array of optical traps to enable controlled evolution driven by laser and multi-qubit interactions, in order to form a quantum computer. This device presents interesting features that make it promising for quantum computation. Let us evoke some of them.

- Atoms provide identical qubits without any fabrication defect.
- The required setup (described in the following) can work at room temperature since only the atoms have to be cooled down. Hence no need for a power-consuming cryogenic cooling.
- Atoms can be arranged differently for each run: no need to modify the whole setup to change the qubit connectivity.
- Current devices are able to trap hundreds of atoms. Progress is ongoing [104] to generate more optical traps and arrange atoms in them, allowing to scale the number of qubits.

Some details about the setup and protocol usually adopted for neutral atom quantum computers are given in the following.

5.2.2 Register preparation and measurement

The qubits are encoded in two electronic states of neutral atoms, typically Rubidium or Strontium, chosen according to the convenience of their electronic structure for laser cooling, trapping, and excitation [103]. Several choices can be taken for these electronic states, resulting in different 2-qubit interactions, as explained in the following section. To form the register, these atoms are trapped into an array of optical tweezers [105] generated by a modulated laser beam [106]. This can be realized, for instance, by the optical setup described in Fig. 5.2.

The preparation of the register is made in several steps. First, the atoms are cooled down inside a vacuum chamber using laser cooling. This makes them fall into the optical traps. The parameters of the setup have been adjusted so that the energy of two atoms in the same trap is sufficient to make one of them escape, resulting in a situation where each trap is occupied by at most one atom. Then, a fluorescence picture of the atoms is taken by a camera, revealing their positions. To place them according to the instructions, they are moved from a trap to another by mobile optical tweezers. Next, a second picture is taken to check that the register is ready for the computation. If the atom placement corresponds to the instructions, the computation starts. It consists in sending suitable laser pulses on the atoms in order to drive their evolution. When it is finished, a final picture is taken to detect the state of the atoms *i.e.* measure the qubits. The whole process takes ≈ 200 ms with current technology[1]. It is dominated by the register preparation and measurement, while the computation time is negligible (usually a few microseconds).

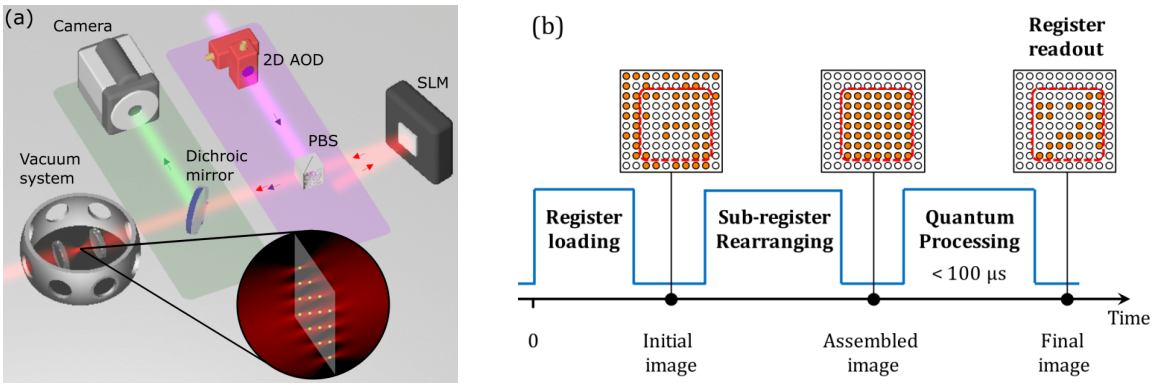


Figure 5.2: *(a) Main components of the neutral atom quantum computer described in [67]. The trapping laser beam, in red, is focused inside a vacuum chamber. Before this focus, it is reflected by a Spacial Light Modulator (SLM) which locally modifies its phase. As a result, instead of one spot in the focus plane, there are many spots arranged in a geometry related to the Fourier transform of the phase pattern induced by the SLM [106]. Each of them attracts the atoms (due to Lorentz force on dipoles), resulting in optical traps (optical tweezers [105]). To place the atoms at will in these traps, auxiliary optical tweezers are generated by a secondary beam, in purple, controlled by a 2D acousto-optic laser beam deflector (2D AOD), and superimposed on the trapping beam using a Polarizing Beam Splitter (PBS). The fluorescence of the trapped atoms, in green, is separated from the other beams by a dichroic mirror and imaged on a camera. (b) Computation cycle, as described in the text. Both figures are taken from [67].*

5.2.3 Quantum computation

The quantum computation consists in evolving the N-qubit state according to the interaction with laser pulses, and the interaction between themselves. Let us first consider a qubit encoded in two levels $|g\rangle$ and $|e\rangle$ of an atom, with their energy difference $\hbar\omega_0$ and a dipole moment $\vec{d}_{eg} = \langle e|q\vec{r}|g\rangle$. To describe its evolution induced by the field $\vec{E} = \vec{E}_0 \cos(\omega t + \phi)$ of a laser pulse, one can consider the corresponding Rabi frequency Ω and detuning δ

[1]This duration is very long compared to other quantum computing devices. It is an important limitation of current neutral atom quantum computers.

defined by

$$\hbar\Omega = \vec{d}_{eg} \cdot \vec{E}_0 \qquad \text{and} \qquad \delta = \omega - \omega_0 \, . \tag{5.2}$$

These two quantities can be controlled and evolved in time by shaping the amplitude E_0 and frequency ω of the laser pulse. Moreover, the phase ϕ is fixed for a given laser pulse but can be changed between two pulses (only the phase differences between pulses matter, due to $U(1)$ symmetry). The resulting qubit evolution is determined by the following Hamiltonian [98], called driving Hamiltonian since this it the part that can be controlled during the computation

$$H_{\text{drive}} = \frac{\hbar}{2} \sum_{i=1}^{N} \Omega_i(t) \Big(\cos(\phi_i) X_i - \sin(\phi_i) Y_i \Big) - \hbar \sum_{i=1}^{N} \delta_i(t) \hat{n}_i \, . \tag{5.3}$$

The parameters $\Omega_i(t), \delta_i(t), \phi_i$ can be different for each qubit $i \in \{1, ..., N\}$ since one can *a priori* send different pulses to individual qubits (local addressing). However, it is in practice easier to send the same series of pulses to every qubits (global addressing). In this case the driving Hamiltonian write

$$H_{\text{drive}} = \frac{\hbar}{2} \Omega(t) \Big(\cos(\phi) \sum_{i=1}^{N} X_i - \sin(\phi) \sum_{i=1}^{N} Y_i \Big) - \hbar \delta(t) \sum_{i=1}^{N} \hat{n}_i \, . \tag{5.4}$$

With H_{drive} only, the qubits remains in a product state, *i.e.* each qubit evolve independently of the others. As already evoked in section 2.3 in the context of digital quantum computing, entanglement is required to design quantum algorithm with an advantage compared to classical algorithms. This is obtained by an interaction between qubits, enabled by the promotion to a Rydberg state (a state where an electron has a high principal quantum number, typically $50 \lesssim n \lesssim 100$). Indeed, in such a state, atoms have an electric dipole moment that is several orders of magnitude larger than in the ground state. As a result, they can interact even when they are placed several μm apart. This interaction can take different forms depending on the electronic states used to define the qubits. In particular, the two following modes are usually considered for analog quantum computing[2]:

- **In XY mode**, the qubit states $|0\rangle$ and $|1\rangle$ are encoded into two dipole-coupled Rydberg states such as $|nS\rangle$ and $|nP\rangle$[3]. At first order, the dipole-dipole interaction between two such qubits separated by a distance r takes the form of an exchange term whose strength scales with r as $1/r^3$ [67, 102]. The resulting Hamiltonian writes as

$$H_{\text{XY}} = \sum_{i<j} \frac{C_3}{2 r_{ij}^3} (X_i X_j + Y_i Y_j) \, , \tag{5.5}$$

  where the coefficient C_3 depends on the chosen Rydberg states.

[2] For digital quantum computing, the qubit is encoded in two hyperfine states of the ground multiplet so that they are isolated from their neighbours, allowing for long coherence time. 1-qubit gates use microwave pulses while 2-qubit gates uses temporary promotion to a Rydberg state to enable interaction.

[3] Several electronic states lie in each $|nL\rangle$ multiplet (hyperfine structure). The degeneracy can be lifted by the coupling with the nuclear spin or a magnetic field. This gives some choice for the qubit states, which can be taken according to technical convenience such as the availability of lasers delivering frequencies associated to the transition $|0\rangle \leftrightarrow |1\rangle$.

- **In Ising mode**, the qubit state $|0\rangle$ is encoded into a state of the ground multiplet, while the qubit state $|1\rangle$ is encoded into a Rydberg state. As a consequence, two qubits interact only when they are both in the $|1\rangle$ state. Since this is the same Rydberg state, they are not dipole-coupled at first order. The second order dipole-dipole interaction leads to an energy shift of the $|11\rangle$ state of $\frac{C_6}{r^6}$ [67, 102], where the coefficient C_6 also depends on the chosen Rydberg state. This interaction produces the so-called Rydberg blockade effect: when two atoms are close enough, the excitation laser driving the ground-Rydberg transition cannot put both of them simultaneously in the Rydberg state. The corresponding Hamiltonian writes

$$H_{\text{Ising}} = \sum_{i<j} \frac{C_6}{r_{ij}^6} \hat{n}_i \hat{n}_j \ . \tag{5.6}$$

Combining the laser-qubit and qubit-qubit interactions, the evolution of the N-qubit state can be described by the resource Hamiltonian

$$H_R = H_{\text{drive}} + H_{\text{inter}} \ , \tag{5.7}$$

where H_{inter} is either H_{Ising} or H_{XY}, depending on the mode. Importantly, H_{drive} is determined by the parameters of the laser pulses, which can be controlled all along the computation. This is different for H_{inter}, which is determined by the relative positions of the atoms. While some neutral atom quantum computers are developed (in a digital spirit) with the ability to move the atoms during the computation [107, 108], this requires complex control hardware and induces delays. For platforms focusing in the analog paradigm, such as the one developed by Pasqal, the atom positions are fixed at the beginning of the computation, resulting in a constant interaction term H_{inter} [99].

5.3 Analog variational algorithm with neutral atoms - challenges

One of the ultimate uses of analog quantum computing consists in directly mapping a physical (or mathematical) problem to qubits by equalizing the resource Hamiltonian to the Hamiltonian of the target problem [109–111]. This allows to apply procedures such as, for instance, adiabatic evolution [95], or to realize, with a qubit system, phase transitions induced by theoretical models [109]. However, analog systems can only reproduce specific types of Hamiltonians. This restricts the applications of analog quantum computing with direct mapping to a limited class of problems, even though there exist techniques to extend this class, *e.g.* the slave spin method for Hubbard model [112].

One can wonder if analog quantum computing can be used in a more general way, for problems encoded on a Hamiltonian that cannot be realized by the hardware. This has been, for instance, addressed for a trapped-ion-based quantum computer [113], and some algorithms have been proposed and evaluated to address chemistry problems in [114] with neutral atoms. Focusing on neutral-atom-based quantum computers, this section explains why this task is more complicated than with digital quantum computing, and identifies crucial obstacles that was encountered during this work. The next chapter will present some ideas to overcome or diminish these obstacles.

5.3.1 Impossibility to stop the interaction

In digital quantum computation, single- and multi-qubit gates act sequentially. This means that qubits are not interacting when 1-qubit gates are applied. Conversely, when they are put in interaction to perform a multi-qubit gate, they are not disrupted by the application of 1-qubit gates. Things are different with analog neutral atom quantum computers, since the interaction is fixed and cannot be switched off during all the computation. This results in a much more complex evolution. Indeed, $[H_{\text{drive}}, H_{\text{inter}}] \neq 0$ so one cannot consider independently the 1-qubit evolution induced by H_{drive} and the multi-qubit evolution induced by H_{inter}. For instance with a constant pulse, the resulting evolution $e^{-\frac{i}{\hbar}(H_{\text{drive}}+H_{\text{inter}})t}$ is different from the evolution $e^{-\frac{i}{\hbar}H_{\text{drive}}t}e^{-\frac{i}{\hbar}H_{\text{inter}}t}$ allowed in digital quantum computing.

In particular, this raises an issue concerning the evaluation of observables. As explained in section 2.4.2, to measure observables that are not diagonal in the basis of bitstring states (*i.e.* observables whose decomposition into Pauli strings contains strings with X's or Y's), a basis rotation has to be performed. But the qubit-qubit interaction perturbs such basis rotations, leading to wrong results if this interaction cannot be neglected. This issue will be addressed in section 6.2.3.

5.3.2 A complex evolution

The non-trivial evolution of the qubit state involved by the unstoppable interaction raises also challenges for the state preparation in variational algorithms. With digital quantum computing, the ansatz wavefunction is made of operators providing some insight on how the Hilbert space is explored. For instance, it is not difficult to see that the one-qubit excitations operators (3.3) successively applied to a bitstring state $|1...10...0\rangle$ allow to reach every normalized combination of bitstring states with real coefficients and the same Hamming weight (appendix D gives an explicit procedure to reach a given such state). With analog quantum computing this is more difficult: instead of being decomposed into well-defined 1- or 2-qubit unitaries, the evolution appears as a whole N-qubit unitary from which an explicit form cannot be determined in general. As a result, it is not easy to guess which kind of laser pulses could be adjusted to drive the qubits to the ground state. Even knowing if this target state is reachable is a difficult problem.

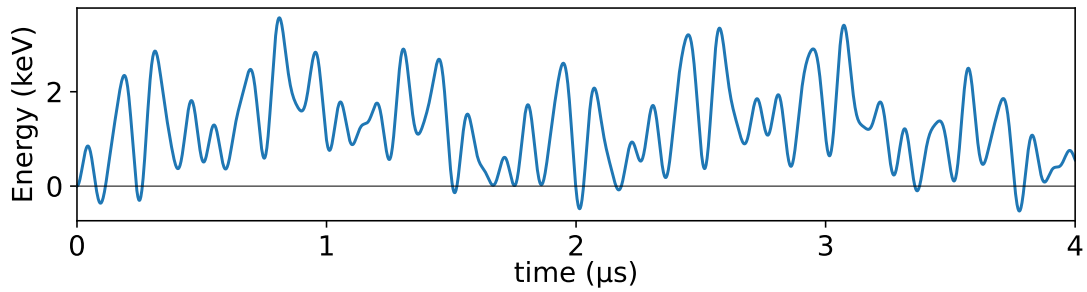


Figure 5.3: *Simulated evolution of the deuteron energy (described by the deuteron Hamiltonian (2.64) with $M = 3$ levels) of a state encoded on 3 atoms placed as a triangle with edge lengths $5\ \mu m, 5.5\ \mu m, 7.5\ \mu m$, in XY mode, and under a global $4\ \mu s$ laser pulse with constant parameters $\Omega = 0.8\ rad/\mu s,\ \delta = -3\ rad/\mu s,\ \phi = 0\ rad$. The simulation has been performed with the software Pulser [99]. It reveals a high number of local minima that complicates the minimisation of the energy towards the ground energy (-2.046 MeV for this system).*

Moreover, the energy landscapes explored when varying $t, \Omega(t), \delta(t), \phi(t), r_{ij}$ can be irregular and present many local minima, as illustrated in Fig. 5.3. This complicates even more the use of a variational method to find the ground state energy. A better understanding of this landscape is required to help locating the global minimum or restrict to a relevant part of the Hilbert space.

This could be solved if one had an analytical expression of the evolved state as a function of the parameters $t, \Omega_i(t), \delta_i(t), \phi_i, r_{ij}$, but this seems hopeless in the general case. Let us consider, for instance, the simple case of a constant global pulse on two qubits that interact within the Ising mode. The corresponding resource Hamiltonian takes the form

$$\begin{aligned}\frac{1}{\hbar}H_R &= \frac{\Omega}{2}\Big(\cos(\phi)(X_1+X_2)+\sin(\phi)(Y_1+Y_2)\Big)-\delta(\hat{n}_1+\hat{n}_2)+\gamma\hat{n}_1\hat{n}_2\\ &= \begin{pmatrix} 0 & \frac{\Omega}{\sqrt{2}}e^{-i\phi} & 0 & 0\\ \frac{\Omega}{\sqrt{2}}e^{i\phi} & -\delta & \frac{\Omega}{\sqrt{2}}e^{-i\phi} & 0\\ 0 & \frac{\Omega}{\sqrt{2}}e^{i\phi} & \gamma-2\delta & 0\\ 0 & 0 & 0 & -\delta\end{pmatrix},\end{aligned} \tag{5.8}$$

where Ω, δ, ϕ are the parameters of the pulse, and $\gamma = \frac{C_6}{\hbar r^6}$ characterizes the interaction between the two atoms placed with a relative distance r. The matrix is given in the 2-qubit basis $\{|00\rangle, \frac{|01\rangle+|10\rangle}{\sqrt{2}}, |11\rangle, \frac{|01\rangle-|10\rangle}{\sqrt{2}}\}$ showing that the symmetric and antisymmetric spaces are decoupled. This is not surprising since the Hamiltonian is invariant under the exchange of the two qubits (under a global pulse, the two qubits feel the same laser-atom interaction, and since they are just two they also feel the same atom-atom interaction). One can derive the resulting interaction by diagonalizing the 3×3 upper block. While this derivation is straightforward in the cases $\gamma = 0$ (as expected since in absence of interaction the qubits evolve independently) or $\Omega = 0$, it becomes heavy in the general case[4]. One can then imagine how difficult it can be to have some insight about the corresponding evolution with three or more qubits.

[4]Let us focus on the 3×3 submatrix in the symmetric subspace. If $\Omega \neq 0$ it can be written as

$$\begin{pmatrix} 0 & \frac{\Omega}{\sqrt{2}}e^{-i\phi} & 0\\ \frac{\Omega}{\sqrt{2}}e^{i\phi} & -\delta & \frac{\Omega}{\sqrt{2}}e^{-i\phi}\\ 0 & \frac{\Omega}{\sqrt{2}}e^{i\phi} & \gamma-2\delta\end{pmatrix} = \frac{\gamma-3\delta}{2}\mathbb{1}+\frac{\Omega}{\sqrt{2}}\begin{pmatrix} e^{i\phi} & 0 & 0\\ 0 & 1 & 0\\ 0 & 0 & e^{-i\phi}\end{pmatrix}\begin{pmatrix} 0 & 1 & 0\\ 1 & x & 1\\ 0 & 1 & -x\end{pmatrix}\begin{pmatrix} e^{-i\phi} & 0 & 0\\ 0 & 1 & 0\\ 0 & 0 & e^{i\phi}\end{pmatrix} \tag{5.9}$$

where $x = \frac{\delta-\gamma}{\Omega\sqrt{2}}$. To get the corresponding evolution operator, one can diagonalize the matrix M_x in the middle. Its characteristic polynomial $X^3-(x^2+2)X-x$ has no rational root in the general case. Using Cardan method, one finds it has 3 real roots that can be expressed as

$$\text{for } k\in\{0,1,2\},\ \ \lambda_k = 2\sqrt{\frac{x^2+2}{3}}\cos\left(\frac{1}{3}\arccos\Big(\frac{x}{2}\big(\frac{3}{x^2+2}\big)^{\frac{3}{2}}\Big)+\frac{2k\pi}{3}\right). \tag{5.10}$$

Some extra calculation (solving the linear systems $M_xV_k = \lambda_kV_k$ for to $k\in\{0,1,2\}$ to get the eigenvectors V_0, V_1, V_2) gives the orthogonal matrix $P = (p_{ij})_{ij}$ that diagonalizes M_x, allowing to express the matrix elements of the evolution operator $U = (u_{ij})_{ij}$ as

$$u_{ij} = e^{-i\frac{\gamma-3\delta}{2}t}\Big(p_{i0}p_{j0}e^{-i\frac{\Omega}{\sqrt{2}}\lambda_0 t}+p_{i1}p_{j1}e^{-i\frac{\Omega}{\sqrt{2}}\lambda_1 t}+p_{i2}p_{j2}e^{-i\frac{\Omega}{\sqrt{2}}\lambda_2 t}\Big). \tag{5.11}$$

5.3.3 Relative phases in the amplitudes of the evolved state

Another inconvenient issue of analog quantum computing concerns the evolution of the complex phases in the amplitudes of the wavefunction. A system that is symmetric under time reversal has eigenstates with real amplitudes, up to a global phase[5] [115]. It is therefore convenient to look for the ground state by staying in the subspace with real amplitudes. This can be done easily in digital quantum computing by composing operators such as (3.3) or (3.7). However, in general the evolution induced by the resource Hamiltonian does not conserve the phase on the amplitudes of the qubit state. This is discussed in particular in section 6.1.2. As a consequence, the space explored with an analog evolution can be unnecessary bigger than in the digital case with application of gates with real coefficients, leading to a more difficult optimisation.

5.3.4 Constraints on the atom relative distances

As explained in section 5.2.3, the interaction between qubits is determined by their relative positions. Considering interactions (5.5) or (5.6), one might want to tune adequately the relative distances r_{ij}. However, one has to keep in mind that these distances are not independent when the number of qubits is $N \geq 5$, due to the fact that qubits lie in a 3-dimensional space[6]. Actually, in current devices, qubits are placed in the same plane, so even with 4 qubits the relative distances $r_{01}, r_{12}, r_{23}, r_{30}, r_{02}, r_{13}$ are not independent. The number of free parameters determining the relative position of $N \geq 2$ qubits in a plane is[7] $2N-3$.

To illustrate why this can be troublesome, let us consider the pairing Hamiltonian (2.63), which can be written as

$$\sum_{k=1}^{N} 2\varepsilon_k \hat{n}_k - \frac{g}{2} \sum_{k<l} \sum (X_k X_l + Y_k Y_l) \, . \tag{5.12}$$

To find its ground state adiabatically, one needs to realize it with the resource Hamiltonian. This can be performed in XY mode using a pulse with Rabi frequency $\Omega = 0$ and detunings $\hbar\delta_k = 2\varepsilon_k$, provided that one can place the N qubits with the same relative distances $r_{ij} = (\frac{C_3}{g})^{1/3}$, *i.e.* on the vertices of the regular N-simplex. As depicted in Fig. 5.4, the only possibilities are $N = 2$, $N = 3$ (placed as an equilateral triangle), and $N = 4$ (placed as a regular tetrahedron) if the device allows for 3-dimensional placement. For $N \geq 5$, the pairing Hamiltonian with constant coupling g cannot be reproduced with the resource Hamiltonian.

5.3.5 Ruby's hardware limitations

Finally, current hardware presents many technical constraints. Let us mention some of them concerning the Ruby machine. First, only global laser pulses can be performed,

[5] In case of degeneracy, one can combine the degenerated eigenstates to get eigenstates with real amplitudes.

[6] Indeed, the placement of $N \geq 3$ qubits in the 3-dimensional space is determined to $3N-6$ degrees of freedom, while there are $\frac{N(N-1)}{2}$ relative distances r_{ij}. Therefore, if $N \geq 3$, the latter can be fixed independently if and only if $3N-6 \geq \frac{N(N-1)}{2}$ *i.e.* $N \in \{3, 4\}$. Since this is also possible with $N = 2$ qubits, the cases where the relative distances are not independent are $N \geq 5$.

[7] Two coordinates for each atom determine their relative distances with 3 redundancies: the two coordinates of the center of mass and the global orientation.

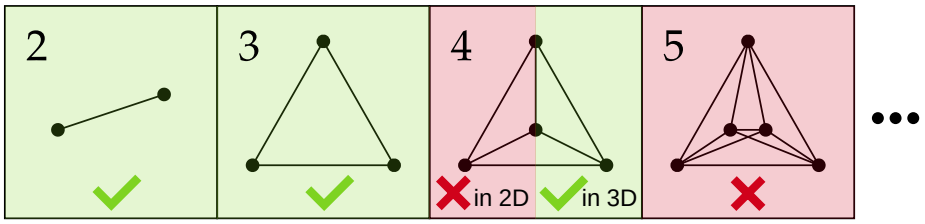


Figure 5.4: *The placement of N atoms in the register with the same relative distances is only possible for $N = 2$, $N = 3$, and eventually $N = 4$ if the device allows for 3-dimensional placement.*

i.e. qubits undergo the same laser-atom interactions. Therefore, qubits are driven by Hamiltonian (5.4) instead of the more general Hamiltonian (5.3). Two important consequences have to be considered.

1. This may restrict the accessible space of N-qubit states. If a variational algorithm is envisaged, it is important to know if this restricted space contains the target state. A particular situation happens with $N = 2$ qubits, where they also experience the same atom-atom interaction (which is determined by their relative distance). Since the resource Hamiltonian is symmetric under the exchange of the two atoms, starting from the state $|00\rangle$ they cannot escape from the symmetric space span$\left(\{|00\rangle, \frac{|01\rangle+|10\rangle}{\sqrt{2}}, |11\rangle\}\right)$, as in the example given in Eq. (5.8). Hence, one has to check that the target state belongs to this subspace. This will be discussed in section 6.2.1.

2. The unavailability of local pulses complicates the evaluation of observables from measurements. For example the 2-qubit Pauli string XZ cannot be evaluated by using the basis rotation $U_x \otimes \mathbb{1}$ as proposed in section 2.4.2, because this operation requires a local pulse on the first qubit. This will also be addressed in section 6.2.1.

Another important limitation is that only the Ising mode is currently available. Combined with the previous constraint, the resource Hamiltonian takes the form

$$H_R(t) = \frac{\hbar}{2}\Omega(t)\Big(\cos(\phi)\sum_{i=1}^{N} X_i - \sin(\phi)\sum_{i=1}^{N} Y_i\Big) - \hbar\delta(t)\sum_{i=1}^{N}\hat{n}_i + \sum_{i<j}\frac{C_6}{r_{ij}^6}\hat{n}_i\hat{n}_j \,. \tag{5.13}$$

Several other technical constraints have to be taken into account, such as

- the response time of the lasers for variations of $\Omega(t)$ and $\delta(t)$ (smooth variations have to be preferred so that the hardware can follow more closely the instructions),
- the decoherence time of the qubits,
- the maximal values allowed by the hardware for $\Omega(t)$ and $\delta(t)$,
- the actualisation time to change the phase ϕ between two pulses,
- the register constraints, such as a minimal distance between the optical traps.

The company Pasqal provides a model of typical physical device in their software *Pulser*, called "AnalogDevice", for which the specifications and limitations can be accessed via the command `AnalogDevice.print_specs()`. Finally, different sources of noise affect the performances of the computation. Some details about them can be found in [116].

5.4 Conclusion

This chapter introduced neutral atom quantum computers within the analog paradigm. Its basic ingredients have been described: encoding of the qubits on electronic levels of neutral atoms, trapping of these atoms with optical tweezers, multi-qubit interactions determined by their relative positions, single-qubit evolutions controlled by laser pulses, and measurement. These computing systems present some advantages for a use with specific methods such as adiabatic evolution. Typical applications include simulation of physical many-body systems [109, 110] or some graph optimisation problems [111] by taking advantage of the Rydberg Blockade effect.

Using analog neutral atom quantum computers for variational algorithms is challenging, and several obstacles have been identified in section 5.3. These obstacles complicate in particular the exploration of the Hilbert space towards the ground state, and the energy evaluation from measurements. They are addressed in the following chapter, which presents some methods to tackle them.

Moreover, each of the constraints evoked potentially reduces the expressivity of the device, *i.e.* reduces the set $\mathcal{S}$ of all N-qubit states that can be reached from the initial state $|0...0\rangle$, with all possible choices of the parameters $t, \Omega(t), \delta(t), \phi, r_{ij}$. In general, this set is not easy to characterize, and it is difficult to know if it contains the target state (and if not, how far is this state from $\mathcal{S}$). This question can be answered for applications to small systems as in section 6.1.2. Concerning bigger or more general systems, is may be an important point to consider for future work.

Chapter 6

Analog variational ground-state energy estimation with a constrained atom-based quantum computer

To design applications relevant to nuclear physics using a variational procedure on an analog neutral atom quantum computer, the constraints detailed in previous chapter have to be taken into account. However, some of these constraints are specific to current machines, such as Ruby, and they could potentially be lifted with other platforms in a near future. Hence, different sets of constraints can be considered for applications, leading to distinct methods and strategies. Here, two scenarios are investigated. Section 6.1 considers a quantum computer not available yet but still realistic for near future applications, with the XY mode and the local detunings generated by local modulation of a global laser pulse. In section 6.2, the current constraints of Ruby are taken into account to design a protocol adapted to its hardware, and in particular its resource Hamiltonian given in Eq. (5.13).

6.1 XY mode and local detunings

6.1.1 General method

A wide class of many-body problems are described by Hamiltonians that conserve the number of particles. This is the case for instance of the pairing and deuteron Hamiltonians presented in section 1.3. For such systems, it can be convenient to look for the ground state by only exploring the subspace of the total Fock space with a given particle number. For the qubit space, this corresponds (with the usual Jordan-Wigner fermion-to-qubit mapping) to a subspace of the N-qubit space with a given fixed Hamming weight. However, the analog neutral atom quantum computers described in section 5.2 do not conserve the Hamming weight in general, due to the term

$$\frac{\hbar}{2}\sum_{i=1}^{N}\Omega_i(t)\Big(\cos(\phi_i)X_i - \sin(\phi_i)Y_i\Big) \tag{6.1}$$

in the driving Hamiltonian (5.3). In both the Ising and XY modes, the resource Hamiltonian (5.7) conserves the Hamming weight if and only if for any $i \in \{1, ..., N\}, \Omega_i = 0$.

In this case, the resource Hamiltonian in Ising mode $H_R^{(\text{Ising})}$ is diagonal in the basis made of the bitstring states $\{|\vec{b}\rangle\}_{\vec{b}\in\{0,1\}^N}$. Therefore, under such a resource Hamiltonian, a given initial state $|\Psi_0\rangle$ written as a linear combination of the bitstring states as $|\Psi_0\rangle = \sum_{\vec{b}} c_{\vec{b}}|\vec{b}\rangle$, is evolved as

$$|\Psi(t)\rangle = \sum_{\vec{b}} c_{\vec{b}} e^{i\theta_{\vec{b}}t}|\vec{b}\rangle, \tag{6.2}$$

where the $\theta_{\vec{b}}$ are the diagonal coefficients of $H_R^{(\text{Ising})}$ in the basis $\{|\vec{b}\rangle\}_{\vec{b}\in\{0,1\}^N}$. As a result, the amplitudes of this state in this basis have a constant modulus. Then, in order to obtain the ground state of a given system, one has to start with an initial state having the same moduli, *i.e.* to already know a part of the solution. This invalidates the use of the Ising mode, and the XY mode will be used here instead. As already evoked, while the XY mode is not available on the Ruby machine, it can be in principle realized with neutral atoms [67, 102]. For this reason, it is considered here anticipating its implementation for a future quantum computer.

In XY mode and with $\Omega_i = 0$ for all i, the resource Hamiltonian takes the form

$$H_R = -\hbar \sum_{i=1}^{N} \delta_i(t)\hat{n}_i + \sum_{i<j} \frac{C_3}{2r_{ij}^3}(X_iX_j + Y_iY_j). \tag{6.3}$$

Its use for the exploration of a given Hamming weight subspace raises two issues. First, as explained in section 5.3.5, the local pulses are not available on Ruby. Then, if a Hamming-weight-preserving Hamiltonian is used, the state evolution is restricted to the space with the Hamming weight of the initial state, which is 0 since the initial state is $|0...0\rangle$. These two obstacles can be overcome using two technical tools described in the *Pulser* documentation [117]: the SLM mask and the Detuning Map Modulator (DMM).

The SLM mask uses a Spacial Light Modulator (SLM) to locally detune specific qubits away from resonance. Its effect is to hide some qubits during a pulse, *i.e.* prevent them to interact with the pulse. In particular, hiding qubits $K+1, ..., N$ allows to apply a resonant π-pulse (a pulse with zero detuning and Rabi frequency $\Omega(t)$ such that $\int \Omega(t)dt = \pi$ rad) only on qubits $1, ..., K$ in order to prepare the state $|1...10...0\rangle$ with Hamming weight K[1].

The DMM is an additional global laser pulse that can be added, with no amplitude (*i.e.* $\Omega = 0$) and a detuning $-\delta_{\text{DMM}}(t)$. This detuning can be locally modulated for each qubit, resulting in the addition to the driving Hamiltonian of a term $-\hbar\sum_i \epsilon_i\delta_{\text{DMM}}(t)\hat{n}_i$ where the modulation coefficients ϵ_i can be individually set to values between 0 and 1. Adjusting them with the values of the detunings $-\delta(t)$ and $-\delta_{\text{DMM}}(t)$ from the main pulse and the DMM pulse is then equivalent to choosing local detunings $\delta_1(t), ..., \delta_N(t)$ as

$$-\hbar\sum_i \Big(\delta(t) + \epsilon_i\delta_{\text{DMM}}(t)\Big)\hat{n}_i := -\hbar\sum_i \delta_i(t)\hat{n}_i\,. \tag{6.4}$$

[1] Actually, the interaction between qubits acts during this π-pulse, and therefore perturbs it. As a consequence, the state prepared $|\Psi_0\rangle$ is not exactly $|1...10...0\rangle$. This effect is quantified in appendix F.1 for 2 qubits. However, this is not an issue and one can consider only the resulting state $|\Psi_0'\rangle$ projected in the right Hamming-weight subspace. Indeed, the other component is not coupled with $|\Psi_0'\rangle$ by the detunings and the XY interactions, and the measurement outcomes in the wrong Hamming-weight subspace can be filtered out. The method described in the present section can be easily adapted with $|\Psi_0'\rangle$ instead of $|1...10...0\rangle$. Hence this effect can be neglected here.

Using these two tools, one can proceed as follows to find the ground state of a given K-particle system. First, the SLM mask is used to prepare the qubits in the state $|1...10...0\rangle$ with Hamming weight K, as described below. Then, the state is evolved with the Hamiltonian (6.3) whose local detunings are enabled by the DMM. These two steps are repeated several times with different values of the positions $\{r_{ij}\}_{ij}$, local detunings $\{\delta_i(t)\}_i$, and duration τ of the pulse, so that these parameters are optimised with a variational algorithm to reach the ground state. The evaluation of the energy from measurements is not evoked in the present section, but it will be discussed in section 6.2.

6.1.2 Justification of the procedure for two qubits

One can wonder if there exists a suitable choice of the parameters $\{r_{ij}\}_{ij}$, $\{\delta_i(t)\}_i$, and τ such that the state evolved under the corresponding resource Hamiltonian (6.3) reaches the ground state. As evoked in the conclusion of chapter 5, this is, in general, a difficult question. However, in the 2-qubit case, a positive answer can be given.

To justify it, let us consider the resource Hamiltonian (6.3) with 2 qubits and constant local detunings δ_1 and δ_2. This Hamiltonian and the corresponding matrix in the usual basis $\{|00\rangle, |01\rangle, |10\rangle, |11\rangle\}$ write as

$$\frac{1}{\hbar}H_R = -\delta_1\hat{n}_1 - \delta_2\hat{n}_2 + \frac{\gamma}{2}(X_1X_2 + Y_1Y_2) = \begin{pmatrix} 0 & 0 & 0 & 0 \\ 0 & -\delta_2 & \gamma & 0 \\ 0 & \gamma & -\delta_1 & 0 \\ 0 & 0 & 0 & -\delta_1 - \delta_2 \end{pmatrix}, \tag{6.5}$$

where $\gamma = \frac{C_3}{\hbar r_{12}^3}$. Using $\Delta = \frac{\delta_1+\delta_2}{2}$, $\delta = \frac{\delta_1-\delta_2}{2}$, and $\Gamma = \sqrt{\delta^2+\gamma^2}$. The 2×2 bloc corresponding to the subspace generated by $|01\rangle$ and $|10\rangle$ can be rewritten and diagonalized as

$$\begin{pmatrix} -\delta_2 & \gamma \\ \gamma & -\delta_1 \end{pmatrix} = -\Delta\mathbb{1} + \begin{pmatrix} \delta & \gamma \\ \gamma & -\delta \end{pmatrix} = -\Delta\mathbb{1} + \begin{pmatrix} c & -s \\ s & c \end{pmatrix}\begin{pmatrix} \Gamma & 0 \\ 0 & -\Gamma \end{pmatrix}\begin{pmatrix} c & s \\ -s & c \end{pmatrix}, \tag{6.6}$$

where $c = \sqrt{\frac{\Gamma+\delta}{2\Gamma}}$ and $s = \sqrt{\frac{\Gamma-\delta}{2\Gamma}}$. Hence the evolution operator reads as

$$e^{-i\frac{t}{\hbar}H_R} = e^{i\Delta t}\begin{pmatrix} e^{-i\Delta t} & 0 & 0 & 0 \\ 0 & \cos(\Gamma t) + i\frac{\delta}{\Gamma}\sin(\Gamma t) & -i\frac{\gamma}{\Gamma}\sin(\Gamma t) & 0 \\ 0 & -i\frac{\gamma}{\Gamma}\sin(\Gamma t) & \cos(\Gamma t) - i\frac{\delta}{\Gamma}\sin(\Gamma t) & 0 \\ 0 & 0 & 0 & e^{i\Delta t} \end{pmatrix}. \tag{6.7}$$

As expected, the subspaces with fixed Hamming weight are preserved. With the initial state $|10\rangle$ (prepared using the SLM mask as described in previous section), the evolved state writes, up to the irrelevant global phase $e^{-i\Delta t}$, as

$$e^{-i\frac{t}{\hbar}H_R}|10\rangle = -i\frac{\gamma}{\Gamma}\sin(\Gamma t)|01\rangle + \Big(\cos(\Gamma t) - i\frac{\delta}{\Gamma}\sin(\Gamma t)\Big)|10\rangle. \tag{6.8}$$

This state has, in general, a non-zero relative phase between its amplitudes. As detailed in section 5.3.3, this can be problematic when the target state has real amplitudes up to a global phase, as the ground state of a time-reversal-symmetric Hamiltonian.

However, in the present simple case for which an analytical expression of the evolved state is available, this issue can be overcome. The two amplitudes in Eq. (6.8) are real up to a global phase (*i.e.* equal up to a real factor) if and only if $\gamma = 0$ or $\Gamma t = k\frac{\pi}{2}$ with $k \in \mathbb{Z}$. The no-coupling case $\gamma = 0$ implies $e^{-i\frac{t}{\hbar}H_R}|10\rangle = e^{i\delta_1 t}|10\rangle$ which is not, in general, the target state. The other possibility, $\Gamma t = k\frac{\pi}{2}$ with $k \in \mathbb{Z}$, can be decomposed into two cases according to

the parity of k. An even k yields the state $e^{-i\frac{t}{\hbar}H_R}|10\rangle = e^{i\Delta t}|10\rangle$ which, again, is not useful. A more interesting state is obtained for k odd:

$$e^{-i\frac{t}{\hbar}H_R}|10\rangle = -ie^{-i\Delta t}\Big(\frac{\gamma}{\Gamma}|01\rangle + \frac{\delta}{\Gamma}|10\rangle\Big) = -ie^{-i\Delta t}\Big(\frac{1}{\sqrt{1+x^2}}|01\rangle + \frac{x}{\sqrt{1+x^2}}|10\rangle\Big) \tag{6.9}$$

where $x = \delta/\gamma$. This parameter can be set to any real value by carefully choosing the distance r_{12} (which determines γ) between the two qubits and/or the detuning difference $\delta_1 - \delta_2$ (which determines δ). Therefore, any target state $|\Psi\rangle = a|01\rangle + b|10\rangle$ with real amplitudes a, b can be obtained up to a global phase, by adjusting r_{12} and/or $\delta_1 - \delta_2$ so that

$$\frac{b}{a} = x = \frac{(\delta_1 - \delta_2)\hbar r_{12}^3}{2C_3}. \tag{6.10}$$

6.1.3 Application to the deuteron

The method described in section 6.1.1 is first applied to the determination of the ground-state energy of the deuteron Hamiltonian (2.64) on N qubits. Since the system is fully encoded into the subspace with Hamming weight 1, the ground state have to be looked for in this subspace. First, the state $|10...0\rangle$ is prepared using the SLM mask. Then, the system is evolved under the resource Hamiltonian (6.3). Restricted to the subspace with Hamming weight 1, and taken here with constant local detunings $\delta_1, ..., \delta_N$, this Hamiltonian writes in the basis $\{|100...00\rangle, |010...00\rangle, ..., |000...01\rangle\}$ as

$$\frac{1}{\hbar}H_R = \begin{pmatrix} -\delta_1 & \gamma_{12} & \gamma_{13} & \dots & \gamma_{1N} \\ \gamma_{12} & -\delta_2 & \gamma_{23} & \dots & \gamma_{2N} \\ \gamma_{13} & \gamma_{23} & -\delta_3 & \dots & \gamma_{3N} \\ \vdots & \vdots & \vdots & \ddots & \vdots \\ \gamma_{1N} & \gamma_{2N} & \gamma_{3N} & \dots & -\delta_N \end{pmatrix}. \tag{6.11}$$

Actually, only the relative values between the local detunings matter. This can be realized by rewriting the above Hamiltonian as $\frac{1}{\hbar}H_R = -\delta\mathbb{1} + \frac{1}{\hbar}H'_R$ with

$$\frac{1}{\hbar}H'_R = \begin{pmatrix} \delta - \delta_1 & \gamma_{12} & \gamma_{13} & \dots & \gamma_{1N} \\ \gamma_{12} & \delta - \delta_2 & \gamma_{23} & \dots & \gamma_{2N} \\ \gamma_{13} & \gamma_{23} & \delta - \delta_3 & \dots & \gamma_{3N} \\ \vdots & \vdots & \vdots & \ddots & \vdots \\ \gamma_{1N} & \gamma_{2N} & \gamma_{3N} & \dots & \delta - \delta_N \end{pmatrix}, \tag{6.12}$$

where δ can be anything (for example $\delta = \delta_N$). Indeed, $e^{-i\frac{1}{\hbar}H_R t} = e^{-i\delta t}e^{-i\frac{1}{\hbar}H' t}$, so the evolution operators $e^{-i\frac{1}{\hbar}Ht}$ and $e^{-i\frac{1}{\hbar}H' t}$ only differ by an irrelevant global phase. Therefore, in the following, one can set $\delta_N = 0$ without loss of generality. The relative detunings, together with the relative distances remain to be optimised to find the ground state. Here the atoms are considered to be placed in a plane, so the $\frac{N(N-1)}{2}$ relative distances are determined by $2N-3$ positional parameters, as explained in section 5.3.4. With the $N-1$ relative detunings, $3N-4$ parameters can therefore be optimised. Multiplying them all by a given constant is equivalent to change the pulse duration τ, so this optimisation can be performed with a fixed value[2] of τ.

[2] Actually, it may be useful to carefully choose the pulse duration to adapt to hardware constraints, such as the maximum values of the detunings or the response time of the laser evoked in section 5.3.5. This will be addressed in section 6.2.3.

This method has been applied (with a simulation of a neutral atom device) to the case $N = 2$ detailed in section 6.1.2. The minimisation[3] of the energy obtained at $\tau = 200$ ns has been performed on the parameters r_{12} and δ_1 (δ_2 is fixed to 0) with initial values $r_{12} = 10\ \mu m$ and $\delta_1 = 0$ rad/μs. This procedure succeeds in reaching the ground state with parameters values $r_{12} = 11.72\ \mu m$ and $\delta_1 = 15.02$ rad/μs. One can check that these values satisfy Eq. (6.10) where a, b are the ground-state amplitudes obtained with an exact diagonalisation. The resulting evolutions of the amplitudes of the qubit state together with the corresponding deuteron energy are presented in Fig. 6.1. This confirms that the ground state is reached periodically as derived in section 6.1.2. The amplitudes, represented on panels (b-d), reveal the evolution of the state from $|00\rangle$ to $|10\rangle$ driven by the π-pulse with the SLM mask hiding the second qubit, followed by the periodic oscillation in the Hamming-weight-1 subspace between $|10\rangle$ and the ground state, driven by the optimised constant pulse.

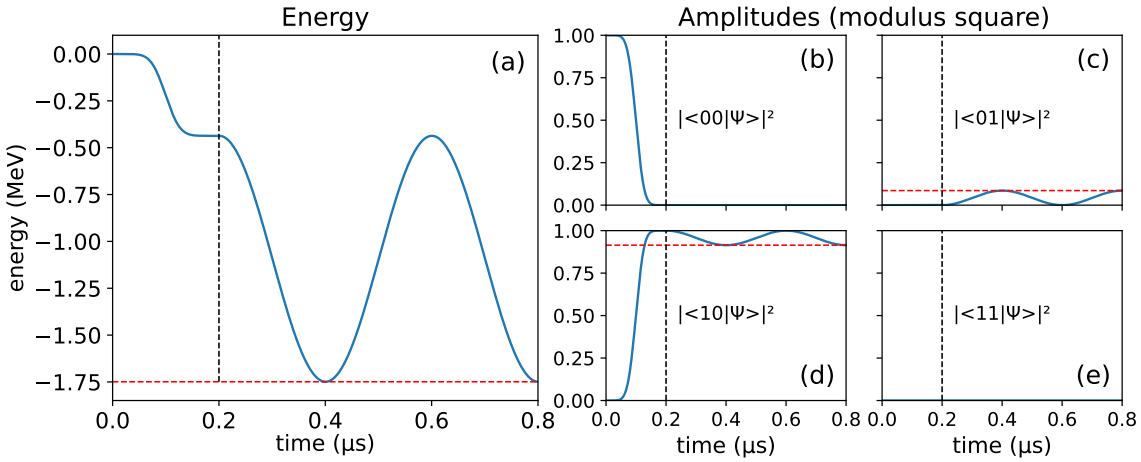


Figure 6.1: *Simulated evolution of the deuteron energy (a) and absolute amplitudes squared (b-e) of a state encoded on 2 atoms placed with a relative distance $r_{12} = 11.72\ \mu m$, and evolved in XY mode under two pulses. First, a global 200 ns π-pulse is applied with the SLM mask hiding the second qubit, in order to prepare the state $|10\rangle$. Then, a 600 ns laser pulse with a zero Rabi frequency and a constant local detuning $\delta_1 = 15.02$ rad/μs is applied to evolve the state to the ground state. Exact ground-state energy and amplitudes are represented by the red dashed lines. The vertical black dashed lines separate the two pulses. The values of r_{12} and δ_1 have been optimised in order to reach the ground state 200 ns after the beginning of the second pulse.*

The optimisation yields similar results with $N > 2$ qubits. Restricting the configurations of atoms to a 1-dimensional chain does not prevent the ground state to be reached. This reduces the number of parameters to optimise to $2N-2$ ($N-1$ local detunings $\{\delta_i\}_{1\leq i\leq N-1}$ and $N-1$ distances $\{r_{i,i+1}\}_{1\leq i\leq N-1}$ between successive atoms). Starting with initial values $\delta_1 = ... = \delta_{N-1} = 0$ rad/μs and $r_{1,2} = ... = r_{N-1,N} = 10\ \mu$m, optimisations realized for

[3]For the simulations reported here, the BFGS algorithm, already used in chapters 3 and 4, has been employed again (let us note that such a gradient-based optimisation algorithm may not be the more adequate for application to noisy hardware). The library *Pulser*, developed by Pasqal to simulate and use their neutral atom quantum computers, is not adapted for gradient-based optimisations: some parameters such as time or positions are discretized and therefore cannot be varied continuously. Hence, functions computing the evolved qubit state from the resource Hamiltonian have been directly written in python for this work. This allowed to reduce the computation to the relevant subspaces to optimise the simulation.

$2 \leq N \leq 10$ atoms find the ground state with a relative error in energy below 10^{-4}. The resulting energy evolutions are illustrated in Fig. 6.2, where only the curves corresponding to $N \in \{2, 4, 6, 8, 10\}$ have been plotted for clarity. The optimised local detunings and atom distances obtained for each $N \in \{2, ..., 10\}$ are reported in Fig. 6.3.

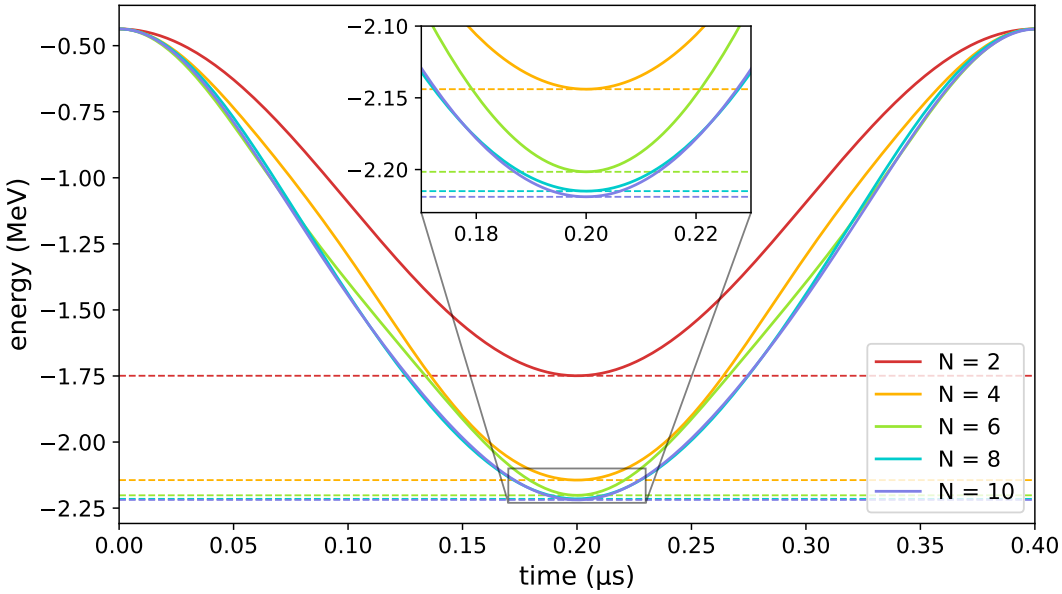


Figure 6.2: *Simulated evolution of the deuteron energy realized with parameters optimised to reach the exact ground state energy at $t = 0.2\ \mu m$, as explained in the text. The energy curves obtained with $N \in \{2, 4, 6, 8, 10\}$ qubits, encoding the deuteron Hamiltonian (1.31) with truncation order N, are represented. In each case, the exact ground state energy (dashed line) is reached. As expected, a convergence of this ground energy is observed when N increases, as underlined by the inset. The preparation of the initial state $|\Psi_0\rangle = |10...0\rangle$ is not represented.*

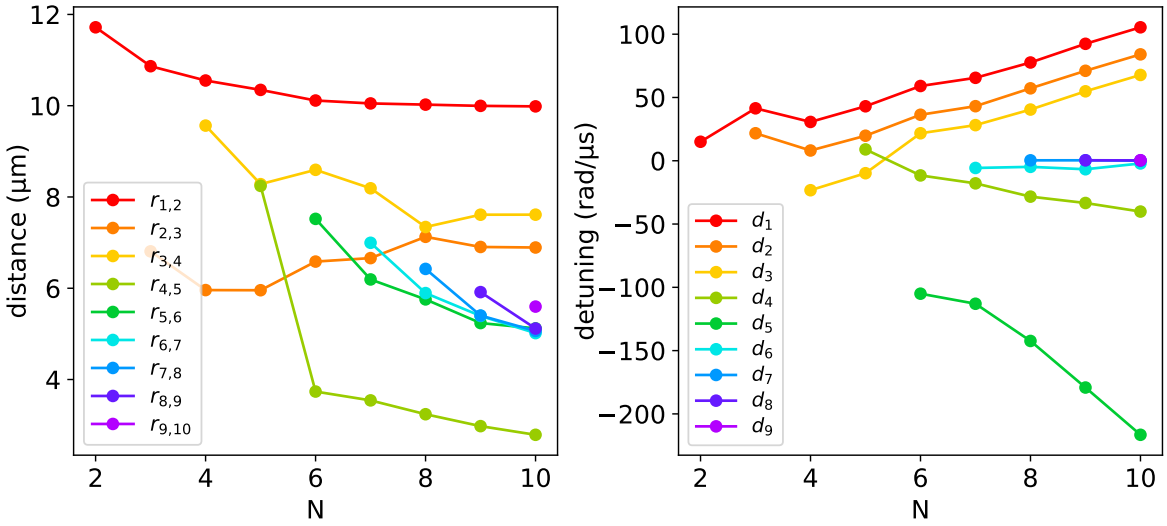


Figure 6.3: *Atom distances (left) and local detunings (right) for which the procedure described in the text reaches the ground state of the deuteron Hamiltonian (2.64). For each qubit number $N \in \{2, ..., 10\}$, the corresponding distances $r_{1,2}, ..., r_{N-1,N}$ and detunings $\delta_1, ..., \delta_{N-1}$ are represented.*

The values taken by these parameters have to be considered with the real hardware constraints. In particular, some $r_{i,i+1}$ may be smaller than the minimal distance between atoms allowed by the device, and some detunings δ_i may be higher than the maximum possible detunings. Since the evolution operator is unchanged when scaling the duration of the pulse τ, the detunings δ_i, and the distances r_{ij} respectively by a factor λ, $\frac{1}{\lambda}$, and $\lambda^{1/3}$, the duration of the pulse can be extended to decrease the detunings and increase the distances. However, this extension may be limited by other constraints such as the coherence time of the qubits. Therefore, future experimental realisation of this procedure on real hardware may require some caution on the choice of the pulse duration.

To obtain a set of parameters compatible with the hardware constraints, it may be also relevant to have a better understanding of the energy landscape. There may be some redundancies among the parameters, and identifying them would allow to both reduce the number of parameters to optimise and adapt to the hardware constraints. Moreover, the presence of several global minima (several sets of parameters leading to the ground state) could give more freedom on the optimisation. Some other atom configurations (rings, lattices, ...) can also be considered to find the more adequate ones.

The simulations realized for this work suggest that, with this procedure, the deuteron ground state can be reached for any N. However, N qubits are used to search this ground state in the N-dimensional subspace with Hamming weight 1. This can be done with a classical computer at the same cost. Therefore, this application does not present any potential for a quantum advantage. The present procedure have to be tested with applications requiring the exploration of bigger subspaces, such as the Hamming-weight-K subspace with $K \sim N/2$. To this end, in the following section, the present methodology is applied to the pairing Hamiltonian.

6.1.4 Application to the pairing Hamiltonian

The procedure described in previous sections is now applied to the pairing Hamiltonian given in Eq. (2.63). In the qubit subspaces with Hamming weight 1 or $N-1$, encoding pairing Hamiltonian with 1 or $N-1$ pair(s) in N doubly-degenerated levels, the optimisations succeed in converging to the ground state, as for the deuteron Hamiltonian. This becomes more challenging when considering Hamming-weight-K subspaces with $2 \leq K \leq N-2$. The energy landscape presents multiple local minima in which the optimisation can fall.

The placement of the atoms into a linear chain configuration, which was successful with the deuteron, was first tested again here. All energy minima found by testing different initial sets of bond lengths and detunings failed to converge to the ground state. An example is given in Fig. 6.4 for the pairing system with 3 pairs in 6 levels and coupling constant $g = 0.6$ (encoded in the Hamming-weight-3 subspace of the 6-qubit space), where the minimal energy obtained after optimisation is clearly above the exact ground energy. This energy error can be substantially reduced when relaxing the constraint on atom placement, but still remains. Relative error in energy obtained with and without the atoms constrained into a linear chain are reported in table 6.1.

Different approaches have been tested to improve the result, such as adding a second constant pulse with different values of the local detunings, testing several sets of initial parameters, ... However the ground state remains out of reach. Since local minima have been found in the energy landscape, it is not clear whether the best minima found are global or

(D, N_p)	Atom positions as a linear chain		Free atom positions	
	$\vec{\delta_0} = (0, ..., 0)$	$\vec{\delta_0} = 2\lambda_{lim}\vec{V}$	$\vec{\delta_0} = (0, ..., 0)$	$\vec{\delta_0} = 2\lambda_{lim}\vec{V}$
$(4, 2)$	0.032	0.024	0.0013	0.0021
$(5, 2)$	0.045	0.045	0.0059	0.0020
$(6, 2)$	0.072	0.056	0.0075	0.0088
$(6, 3)$	0.186	0.092	0.016	0.0067

Table 6.1: *Relative error on the ground energy (as defined in Eq. (3.9)) obtained from a minimisation of the energy at $t = 200$ ns, for different pairing systems (D, N_p) of N_p pairs in D doubly-degenerated levels, with coupling constant $g = 0.6$. The results reported in the two first columns have been obtained with atoms placed as a linear chain, initialized with a constant bond length $r = 12\ \mu m$, and the optimisation has been performed on the $D - 1$ bond lengths and the $D - 1$ relative detunings. The results reported in the two last columns have been obtained with atoms only constrained to be in the plane, initialized with various positions, and the optimisation has been made on $2D-3$ relative coordinates (cartesian coordinates (x_i, y_i) of the D atoms, with x_0, y_0, y_1 fixed to 0) and the $D - 1$ relative detunings. In this case the results are very sensitive to the initial positions (revealing the presence of many local minima), so among the various initial positions tested, only the lowest resulting errors have been kept. Two configurations of initial detunings $\vec{\delta_0}$ have been tested: $\vec{\delta_0} = (0, ..., 0)$, and $\vec{\delta_0} = 2\lambda_{lim}\vec{V}$ where λ_{lim} and $\vec{V}$ are defined in Eqs. (6.15) and (6.16).*

not. As evoked in section 5.4, a better understanding of the set of all N-qubit states that can be reached with this method is required. In particular, it would be interesting to know if the ground state belongs to this set, and if not, what is the best ground-state energy approximation that can be obtained.

To avoid local minima of the energy landscape which correspond to significant energy errors, it is important to conveniently choose the initial set of parameters $\mathcal{P} = \{\delta_i\}_i \cup \{r_{ij}\}_{ij}$ before the optimisation. In particular, the tests realized for this work revealed that a lot of such initial sets involve an evolution towards states having an energy higher than the initial state $|\Psi_0\rangle = |1...10...0\rangle$. An example is given in Fig. 6.4 (a) where the initial set of parameters induces an evolution towards high energy states (orange curve). To facilitate the optimisation (reduce the number of required evaluations and avoid the local minima with the largest energies), it is convenient to initiate it with a set $\mathcal{P}$ that lowers the energy, at least at short times. To this purpose, let us consider the energy curve $E(t) = \langle\Psi(t)|H|\Psi(t)\rangle$ associated to a given set $\mathcal{P}$, where H is the pairing Hamiltonian and $|\Psi(t)\rangle$ is the state evolved (according to (5.1) in the case of a constant Hamiltonian) by the resource Hamiltonian H_R defined by $\mathcal{P}$. To determine whether the energy is initially increasing or decreasing, the first derivatives of the energy at $t = 0$ can be computed from

$$\begin{aligned}
&\frac{d}{dt}\Big(E(t)\Big)|_{t=0} = i\langle\Psi_0|[\hat{H}_R, \hat{H}]|\Psi_0\rangle, \\
&\frac{d^2}{dt^2}\Big(E(t)\Big)|_{t=0} = -\langle\Psi_0|\big[\hat{H}_R, [\hat{H}_R, \hat{H}]\big]|\Psi_0\rangle, \\
&\qquad\qquad ...
\end{aligned} \tag{6.13}$$

A calculation detailed in appendix E indicates that the first derivative is zero, but the

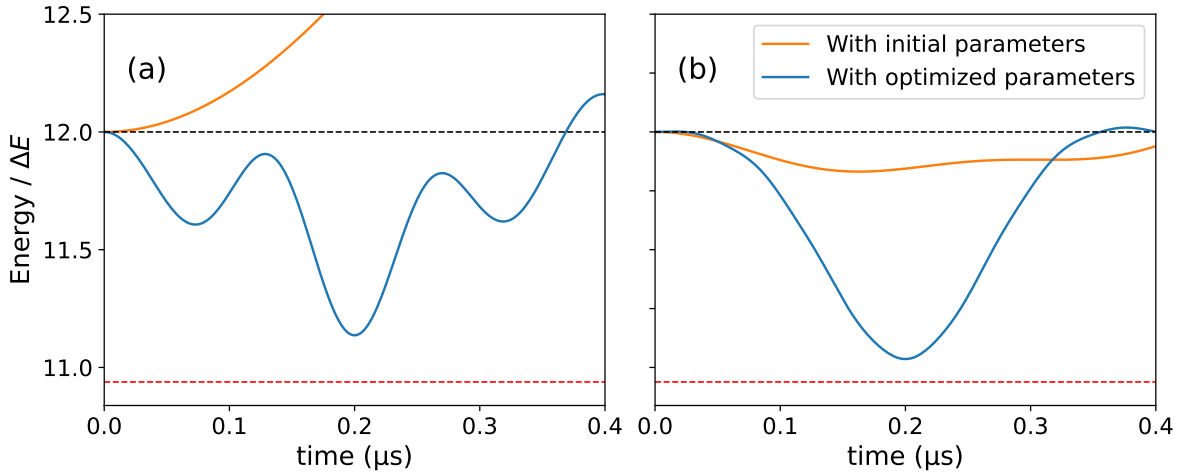


Figure 6.4: *Evolution of the energy (given in units of the energy level spacing ΔE defined in section 1.3.1) obtained for the pairing Hamiltonian with 3 pairs in 6 energy levels and coupling constant $g = 0.6$, with a 6-qubit state initialised to $|\Psi_0\rangle = |111000\rangle$ and evolved under the resource Hamiltonian (6.3) with constant detunings. (a) The evolution obtained with atom placed as a linear chain of bond length $12\ \mu m$ and detunings $\vec{\delta_0} = (0, ..., 0)$ (orange curve) is compared to the evolution obtained after the optimisation of the bond lengths and detunings to reduce the energy at $t = 0.2\ \mu s$. (b) Same, but with the initial set of detunings $\vec{\delta_0} = 2\lambda_{lim}\vec{V}$ where λ_{lim} and $\vec{V}$ are defined in Eqs. (6.15) and (6.16). The black and red dashed lines correspond respectively to the energy of the initial state $|\Psi_0\rangle$ and the exact ground state energy.*

second one is not in general, and depends on $\mathcal{P}$. In particular, the detunings and positions can be chosen so that this second derivative is negative, in order to have an energy curve which goes down for small t. Considering the interaction parameters $\gamma_{ij} = \frac{C_3}{\hbar r_{ij}^3}$ instead of the atom distances r_{ij}, this condition can be written

$$\vec{\delta} \cdot \vec{V} \geq F(\{\gamma_{ij}\}_{ij}), \tag{6.14}$$

where

$$\begin{aligned}
&\vec{\delta} = \Big(\delta_1, ..., \delta_N\Big), \\
&\vec{V} = \Big(-\sum_{j>p}\gamma_{1j},\ ...,\ -\sum_{j>p}\gamma_{pj},\ \sum_{i\leq p}\gamma_{i,p+1},\ ...,\ \sum_{i\leq p}\gamma_{iN}\Big), \\
&F(\{\gamma_{ij}\}_{ij}) = \sum_{i\leq p}\sum_{j>p}\gamma_{ij}\Big(2\gamma_{ij}\frac{\epsilon_j - \epsilon_i}{g} - \sum_{\substack{k\leq p\\ k\neq i}}\gamma_{jk} - \sum_{\substack{k>p\\ k\neq j}}\gamma_{ik}\Big) \\
&\qquad + \sum_{i<j\leq p}\sum_{k>p}\gamma_{ij}(\gamma_{ik}+\gamma_{jk}) + \sum_{p<i<j}\sum_{k\leq p}\gamma_{ij}(\gamma_{ik}+\gamma_{jk}).
\end{aligned} \tag{6.15}$$

These expressions are established in appendix E. A convenient way to satisfy the condition (6.14) is to choose

$$\vec{\delta} = \lambda\vec{V}, \qquad \text{with} \qquad \lambda \geq \lambda_{lim} := F(\{\gamma_{ij}\}_{ij})/\vec{V}^2. \tag{6.16}$$

Some results obtained with initial detunings $\vec{\delta_0} = 2\lambda_{lim}\vec{V}$ are reported in table 6.1 and Fig. 6.4 (b), where they are compared to optimised energies obtained with initial detunings

$\vec{\delta_0} = (0, ..., 0)$. The former choice of initial detunings allows in general to find a lowest energy minima than the latter. However, the ground state remains inaccessible despite the various initial positions tested. Further investigations would be needed to determine if the ground state can be reached with this method (and a convenient choice of initial set of parameters $\mathcal{P}$) or not.

6.1.5 Limitations of the method

While this method presents the advantage of exploring the N-qubit space with a fixed Hamming weight K, the preparation of the exact ground state seems impossible as soon as $2 \leq K \leq N-2$. This can be partially understood by comparing the number of parameters $u_{N,K}$ that is required to fully explore the space of N-qubit states with Hamming weight K and real amplitudes[4], and the maximum number of parameters v_N that can be varied with the present method. As determined in section 6.1.3[5], $v_N = 3N - 4$, whereas due to normalisation, $u_{N,K} = \binom{N}{K} - 1$. Hence, for N and K large enough, $v_N \ll u_{N,K}$ so only a small subspace of the relevant space can be explored. However, in the cases $(N, K) = (4, 2)$, $(N, K) = (5, 2)$, or $(N, K) = (6, 2)$ reported in table 6.1, the ground state is not exactly reached whereas $v_N \geq u_{N,K}$. This may suggest that some redundancy exists between these parameters. It is also possible that the ground state can be reached but is difficult to find due to the various local minima.

The success of the present method for the exploration of the Hamming-weight-1 subspace has to be put into perspective with the fact that using N qubits to explore a N-dimensional space does not present any quantum advantage. However, the quantum advantage can be retrieved by using an alternative encoding, as explained in the following section.

Another important limitation of this method is that it cannot be applied on the current Ruby device. Indeed, the Ising mode, the SLM mask and the DMM are not implemented yet on Ruby. However, these features are accessible in *Pulser*, and should be available in future machines. Last but not least, a relevant point that has not been discussed here concerns the evaluation of the energy. As explained in sections 5.3.1 and 5.3.5, this is more challenging than in digital quantum computing due to the impossibility to stop the interaction and the restriction to global pulses. The following section present some ideas to leverage these obstacles.

[4]The ground state of a time-reversal symmetric Hamiltonian has real amplitudes, up to a global phase.

[5]This number has been determined in the case $K = 1$, but it can be generalised to any K. Indeed, the number of parameters determining the atom relative distances (in the plane) is $2N - 3$ and does not depend on K. Moreover, the resource Hamiltonian (6.3) can be written, for any $\delta(t)$, as

$$H_R = -\hbar\delta(t)\sum_{i=1}^{N}\hat{n}_i - \hbar\sum_{i=1}^{N}\big(\delta_i(t) - \delta(t)\big)\hat{n}_i + \sum_{i<j}\frac{C_3}{2r_{ij}^3}(X_iX_j + Y_iY_j). \tag{6.17}$$

Since, in the Hamming-weight-K subspace, $\sum_{i=1}^{N}\hat{n}_i = K\mathbb{1}$, the first term of this resource Hamiltonian only impacts the global phase of the evolved state. Therefore, this term can be forgotten, resulting in a resource Hamiltonian that depends on $N-1$ relative detunings instead of N detunings (for instance, the choice $\delta(t) = \delta_N(t)$ shows that the last detuning can be set to 0).

6.2 Ising mode and alternative encoding

This section explains how an alternative encoding of a physical system on atoms can solve several issues raised in section 5.3, and not settled with the previous approach (section 6.1). Using Ising mode with only global pulses, a procedure is proposed to encode in 2 qubits the deuteron Hamiltonian (1.31) with truncation order $M = 3$, reach its ground state with a well-suited pulse, and evaluate the corresponding energy using adequate global basis rotations. These basis rotations cannot be performed exactly due to the qubit interaction. Some techniques are given and discussed to mitigate this effect and the resulting error is calculated via simulations. The statistical error involved by the finite number of measurements is also estimated.

6.2.1 Benefits of an alternative encoding

So far, to find the ground state of a many-body system represented on N one-body states, the Fock space has been mapped to the N-qubit space with the Jordan-Wigner mapping $\mathrm{JW}[.]$. Actually, this can be generalised by composing the JW transformation with a map Λ from the N-qubit space to the n-qubit space, where n is an integer eventually distinct of N. This results in a more general fermion-to-qubit mapping $\Lambda \circ \mathrm{JW}[.]$. A convenient choice for Λ has several advantages that are presented here.

Reducing the number of qubits

When the target state is known to be in a well-identified subspace of the qubit space, there is an opportunity for reducing the number of qubits. For instance, the pairing and deuteron Hamiltonians have a block-diagonal structure in the Fock space due to the fact that they conserve the number of particles (or pairs). With the Jordan-Wigner mapping, the K-particle subspace (of dimension $\binom{N}{K}$) is mapped to the Hamming-weight-K subspace (of same dimension) of the N-qubit space. Instead, a mapping Λ can be chosen so that the K-particle subspace is mapped into the n-qubit space with $\binom{N}{K} \leq 2^n < 2^N$, reducing the number of qubits.

Moreover, as evoked at the end of section 6.1.3, using N qubits to target a state in the N-dimensional subspace with Hamming weight 1 cannot provide any quantum advantage. To solve this issue, this space can be mapped into the 2^n-dimensional n-qubit space $\mathcal{H}_n$, where n is an integer satisfying $N \leq 2^n$. If N is not too small compared to 2^n, for instance by choosing the integer n such that $2^{n-1} < N \leq 2^n$, the number of qubits can be exponentially reduced. An elementary example concerns the deuteron Hamiltonians (1.31) with truncation order $M = 3$ and $M = 4$, denoted respectively H_3 and H_4 in the following. Their spaces of interest, *i.e.* the Hamming-weight-1 subspaces $\mathrm{span}(\{|100\rangle, |010\rangle, |001\rangle\})$ and $\mathrm{span}(\{|1000\rangle, |0100\rangle, |0010\rangle, |0001\rangle\})$ respectively, can be mapped into the 2-qubit space $\mathcal{H}_2$. This mapping can be made in several ways, and this freedom allows to solve several other issues such as those related to the restriction to global pulses evoked in section 5.3.5.

Mapping the relevant physical space into the accessible qubit space

One of these issues concerns the reduction of the accessible space. If the space of qubit states that can be reached with the device restricted to global pulse (and more gen-

erally with other constraints) is well characterized, the space of the problem (*i.e.* the space in which the target state is searched) can be mapped into this restricted qubit space. In this way the target state is accessible. In the 2-qubit case, the restriction to global pulses results in a reduction of the accessible 2-qubit space to the symmetric space $\mathcal{S}_2(\mathcal{H}_2) = \text{span}(\{|00\rangle, \frac{1}{2}(|01\rangle + |10\rangle), |11\rangle\})$, as explained in section 5.3.5. As a consequence, it is not convenient to encode H_4 on two qubits, because some information is needed to choose a mapping such that the mapped ground state lie in $\mathcal{S}_2(\mathcal{H}_2)$. This is not a problem with H_3, whose space of interest $\text{span}(\{|100\rangle, |010\rangle, |001\rangle\})$ can be fully encoded into $\mathcal{S}_2(\mathcal{H}_2)$.

Mapping the Hamiltonian to a measurable qubit observable

Another issue involved by the restriction to global pulses concerns the measurements. As explained in section 5.3.5, some Pauli strings cannot be obtained with the procedure given in section 2.4.2, which requires to perform local basis rotations. Here some clarifications are given about the observables that can be evaluated with basis rotations restricted to global pulses. Moreover, as evoked in section 5.3.1, the atom-atom interaction cannot be stopped while these basis rotations are performed. Since this interaction depends on the atom relative distances, it is difficult to design a basis rotation which explicitly take it into account. Here it is supposed that this interaction can be neglected. Section 6.2.3 will present some techniques to reduce its effect and make this assumption more realistic.

As explained in section 2.4, an observable O is evaluated by decomposing it as

$$O = \sum_k a_k U_k^\dagger O_k U_k \,, \tag{6.18}$$

where $\forall k$, $a_k \in \mathbb{R}$, U_k is a basis rotation (a unitary operator), and O_k is an observable that is diagonal in the bitstring basis. With only global pulses and no interaction, any possible basis rotation take the form $U^{\otimes N} = U \otimes ... \otimes U$ where U is a 1-qubit basis rotation. Therefore, observables that can be evaluated in this scenario are the ones which can be decomposed as in Eq. (6.18) with this restriction on the U_k. Moreover, every O_k of Eq. (6.18) can be decomposed into Pauli strings of the form $Z^{a_1} \otimes ... \otimes Z^{a_N}$ with $a_1, ..., a_N \in \{0, 1\}$ (*i.e.* tensor products of Z's and $\mathbb{1}$'s), so the only observables that can be evaluated are combinations of observables of the form

$$(U^\dagger)^{\otimes N}\big(Z^{a_1} \otimes ... \otimes Z^{a_N}\big)U^{\otimes N} = W^{a_1} \otimes ... \otimes W^{a_N}, \tag{6.19}$$

where $W = U^\dagger Z U$. This motivates the choice of a transformation Λ which maps the Hamiltonian of interest to such a measurable observable.

For instance with two qubits, using the unitaries U_x and U_y defined in section 2.2.3,

- $\mathbb{1}\mathbb{1}, Z\mathbb{1}, \mathbb{1}Z, ZZ$ can be evaluated without any basis rotation,
- $X\mathbb{1}, \mathbb{1}X, XX$ can be evaluated with the basis rotation $U_x \otimes U_x$,
- $X\mathbb{1}, \mathbb{1}Y, YY$ can be evaluated with the basis rotation $U_y \otimes U_y$.

Other observables can be evaluated, such as $XZ + ZX$. Indeed, with $U = e^{i\frac{\pi}{8}Y}$, one gets $UZU = \frac{1}{\sqrt{2}}(Z + X)$, so $U^{\otimes 2}(Z \otimes Z)U^{\otimes 2} = \frac{1}{2}(ZZ + XZ + ZX + XX)$. Since ZZ and XX can already be evaluated, the expectation value of $XZ + ZX$ can be obtained. However, combinations $aXZ + bZX$ with $a \neq b$ cannot be evaluated, as justified in appendix F.2.

As shown in section 2.1, Pauli strings form a basis of the space of observables. With a slight basis change, any 2-qubit observable O can be decomposed as

$$\begin{aligned} O = &\alpha_0 \mathbb{1}\mathbb{1} + \alpha_1 Z\mathbb{1} + \alpha_2 \mathbb{1}Z + \alpha_3 ZZ + \beta_1 X\mathbb{1} + \beta_2 \mathbb{1}X + \beta_3 XX + \gamma_1 Y\mathbb{1} + \gamma_2 \mathbb{1}Y + \gamma_3 YY \\ &+ \mu_1(XY + YX) + \mu_2(YZ + ZY) + \mu_3(ZX + XZ) \\ &+ \nu_1(XY - YX) + \nu_2(YZ - ZY) + \nu_3(ZX - XZ). \end{aligned} \tag{6.20}$$

It as been argued that $(ZX + XZ)$ can be evaluated while $(ZX - XZ)$ cannot. Similarly, $(XY + YX)$ and $(YZ + ZY)$ can be evaluated while $(XY - YX)$ and $(YZ - ZY)$ cannot. Hence, the 2-qubit observables that can be evaluated are the ones with $\nu_1 = \nu_2 = \nu_3 = 0$ in the above decomposition.

Therefore, a map Λ from the space of interest span$(\{|100\rangle, |010\rangle, |001\rangle\})$ of the deuteron Hamiltonian H_3 to the 2-qubit symmetric space span$(\{|00\rangle, \frac{1}{2}(|01\rangle + |10\rangle), |11\rangle\})$, for which $\Lambda H_3 \Lambda^\dagger$ respects the above property, is required. This can be achieved with

$$\Lambda : \begin{cases} |100\rangle \;\rightarrow\; \frac{1}{\sqrt{2}}(|01\rangle + |10\rangle) \\ |010\rangle \;\rightarrow\; \frac{1}{\sqrt{2}}(|00\rangle + |11\rangle) \\ |001\rangle \;\rightarrow\; \frac{1}{\sqrt{2}}(|00\rangle - |11\rangle) \end{cases} . \tag{6.21}$$

Indeed, with $u_0 = \frac{3}{4} - \frac{|V_0|}{\hbar\omega}$ and $\forall k \in \{1, 2, 3\}, u_k = k + \frac{3}{4}$ and $v_k = -\frac{1}{2}\sqrt{k\left(k + \frac{1}{2}\right)}$, Eq. (2.64) for $M = 3$ can be written as

$$\frac{1}{\hbar\omega} H_3 = u_0 \hat{n}_0 + u_1 \hat{n}_1 + u_2 \hat{n}_2 + \frac{1}{2} v_1 \Big(X_0 X_1 + Y_0 Y_1\Big) + \frac{1}{2} v_2 \Big(X_1 X_2 + Y_1 Y_2\Big). \tag{6.22}$$

Therefore it is mapped by Λ to[6]

$$\begin{aligned} \frac{1}{\hbar\omega} \Lambda H_3 \Lambda^\dagger = &\frac{u_0 + u_1 + u_2}{4} \mathbb{1}\mathbb{1} + \frac{-u_0 + u_1 + u_2}{4} ZZ + \frac{v_2}{2}(Z\mathbb{1} + \mathbb{1}Z) + \frac{v_1}{2}(X\mathbb{1} + \mathbb{1}X) \\ &+ \frac{u_0 + u_1 - u_2}{4} XX + \frac{u_0 - u_1 + u_2}{4} YY, \end{aligned} \tag{6.25}$$

which can be evaluated since it respects the above characterisation.

To sum up, with the transformation Λ defined in Eq. (6.21), the deuteron Hamiltonian H_3 is mapped from the 3-qubit space to the symmetric subspace of the 2-qubit space, from

[6] This derivation can be made using the matrix forms of H_3 and Λ obtained with the bases $\{|100\rangle, |010\rangle, |001\rangle\}$ and $\{|00\rangle, |01\rangle, |10\rangle, |11\rangle\}$:

$$\frac{1}{\hbar\omega} H_3 = \begin{pmatrix} u_0 & v_1 & 0 \\ v_1 & u_1 & v_2 \\ 0 & v_2 & u_2 \end{pmatrix} \qquad \text{and} \qquad \Lambda = \frac{1}{\sqrt{2}} \begin{pmatrix} 0 & 1 & 1 \\ 1 & 0 & 0 \\ 1 & 0 & 0 \\ 0 & 1 & -1 \end{pmatrix}. \tag{6.23}$$

This leads to

$$\begin{aligned} \frac{1}{\hbar\omega} \Lambda H_3 \Lambda^\dagger &= \frac{1}{2} \begin{pmatrix} 0 & 1 & 1 \\ 1 & 0 & 0 \\ 1 & 0 & 0 \\ 0 & 1 & -1 \end{pmatrix} \begin{pmatrix} u_0 & v_1 & 0 \\ v_1 & u_1 & v_2 \\ 0 & v_2 & u_2 \end{pmatrix} \begin{pmatrix} 0 & 1 & 1 & 0 \\ 1 & 0 & 0 & 1 \\ 1 & 0 & 0 & -1 \end{pmatrix} = \frac{1}{2} \begin{pmatrix} u_1 + u_2 + 2v_2 & v_1 & v_1 & u_1 - u_2 \\ v_1 & u_0 & u_0 & v_1 \\ v_1 & u_0 & u_0 & v_1 \\ u_1 - u_2 & v_1 & v_1 & u_1 + u_2 - 2v_2 \end{pmatrix} \\ &= \frac{u_1 + u_2}{4}(\mathbb{1}\mathbb{1} + ZZ) + \frac{v_2}{2}(Z\mathbb{1} + \mathbb{1}Z) + \frac{u_1 - u_2}{2}(XX - YY) + \frac{u_0}{2}(\mathbb{1}\mathbb{1} - ZZ + XX + YY) + \frac{v_1}{2}(X\mathbb{1} + \mathbb{1}X). \end{aligned} \tag{6.24}$$

Hence the expression of Eq. (6.25).

which a qubit state evolved by a resource Hamiltonian restricted to global pulses cannot escape. Section 6.2.2 shows that the ground state of H_3 can be prepared with a well-adjusted pulse. Moreover, the expectation value of the resulting mapped Hamiltonian can be obtained from measurements, even though the restriction to global pulses limits the number of observables that can be evaluated. While the effect of the 2-qubit interaction has been neglected here, section 6.2.3 will evaluate this effect and present techniques to reduce it.

6.2.2 A convenient pulse

The resource Hamiltonian for 2 qubits, in Ising mode, and restricted to global pulses writes as

$$\frac{1}{\hbar}H_R(t) = \frac{\Omega(t)}{2}\Big(\cos(\phi)(X_1+X_2) - \sin(\phi)(Y_1+Y_2)\Big) - \delta(t)(\hat{n}_1+\hat{n}_2) + \frac{C_6}{\hbar r^6}\hat{n}_1\hat{n}_2\,, \quad (6.26)$$

where r is the relative distance between the two qubits. To reach the ground state of the mapped deuteron Hamiltonian $\Lambda H_3 \Lambda^\dagger$, the 2-qubit state is evolved under this resource Hamiltonian, starting from $|00\rangle$. The Rabi frequency and detuning are first considered constant here, and denoted Ω and δ. The parameters Ω, δ, ϕ, r are optimised in order to minimise the energy at a given time t_0. The energy is computed from Eq. (6.25) and from the simulated amplitudes of the qubit state.

Starting with initial values of the parameters

$$r = 10\ \mu m, \quad \Omega = 1\ \text{rad}/\mu s, \quad \delta = 0\ \text{rad}/\mu s, \quad \phi = 0\ \text{rad}, \quad (6.27)$$

the optimisation succeeds in reaching the ground state (with a relative error $\approx 10^{-10}$ in energy) at a time fixed to $t_0 = 1\ \mu$s. The corresponding energy and amplitudes evolution are represented in Fig. 6.5 (a).

Pulses with constant Rabi frequency require sharp variations when the pulse starts and stops (from 0 to Ω at the beginning and from Ω to 0 at the end at the end). However, the response time of the hardware limits such sharp variations, so that the pulse realized in practice differs from this ideal situation, as illustrated in Fig. 6.6. To reduce the difference between the command and the pulse effectively realized by the device, it is preferable to use pulse waveforms that are easier to follow for the hardware. *Pulser* provides a convenient waveform for that: the Blackman waveform. With the latter, the Rabi frequency evolves as $\Omega(t) = \Omega_{\text{max}} f(t/\tau)$, where Ω_{max} is its maximum value, τ is the duration of the pulse, and f is the Blackman window function defined as

$$f : x \to \frac{1}{2}\big(1-\cos(2\pi x)\big) - \frac{\alpha}{2}\big(1-\cos(4\pi x)\big), \quad (6.28)$$

with $\alpha = 0.16$. The corresponding waveform is represented in Fig. 6.6 (b). The area under this function,

$$\mathcal{A} = \int_0^1 f(x)dx = \frac{1-\alpha}{2} = 0.42, \quad (6.29)$$

will be useful in the following.

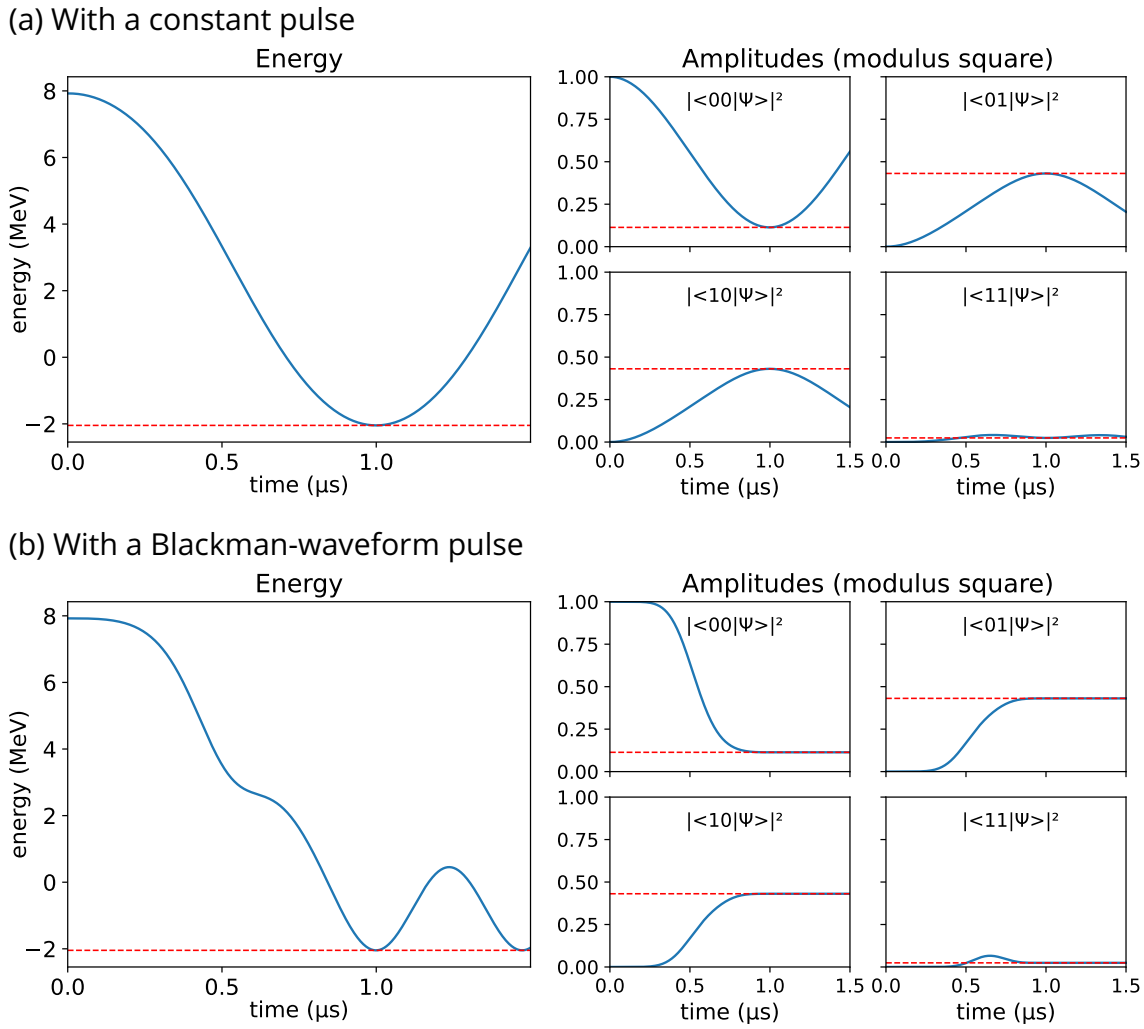


Figure 6.5: *Simulated evolution of the deuteron energy and amplitudes (modulus square) of a state encoded on 2 atoms as explained in the text, and evolved under the resource Hamiltonian (6.26). (a) Using a constant pulse, and parameter values* $r = 7.42\ \mu m$, $\Omega = 2.15\ rad/\mu s$, $\delta = -1.39\ rad/\mu s$, $\phi = 3.15\ rad$. *(b) Using a* $1\ \mu s$ *Blackman-waveform pulse, and parameter values* $r = 6.35\ \mu m$, $\widetilde{\Omega} = 1.85\ rad/\mu s$, $\widetilde{\delta} = 0.33\ rad/\mu s$, $\phi = 0.88\ rad$. *These parameters have been optimised in order to reach the ground state at* $t_0 = 1\ \mu s$. *Exact ground-state energy and amplitudes are represented by the red dashed lines. In (a), the constant pulse is not stopped after* $t = 1\ \mu s$, *hence the energy and amplitudes evolution continues. In (b),* Ω *and* δ *remain equal to* 0 *after the application of the Blackman-waveform pulse. Since only the qubit-qubit Ising interaction is active, only the phase of the* $\langle 11|\Psi\rangle$ *component evolves after* $t = 1\ \mu s$, *while the modulus of the amplitudes stay constant.*

With this waveform f for both Rabi frequency and detuning, *i.e.* $\Omega(t) = \Omega_{\text{max}} f(t/\tau)$ and $\delta(t) = \delta_{\text{max}} f(t/\tau)$, the resource Hamiltonian (6.26) can be written as

$$H_R(t) = \widetilde{H}_R \frac{f(t/\tau)}{\mathcal{A}} + \frac{C_6}{r^6}\hat{n}_1\hat{n}_2\,, \tag{6.30}$$

$$\text{with} \quad \frac{1}{\hbar}\widetilde{H}_R = \frac{\widetilde{\Omega}}{2}\Big(\cos(\phi)(X_1 + X_2) - \sin(\phi)(Y_1 + Y_2)\Big) - \widetilde{\delta}(\hat{n}_1 + \hat{n}_2),$$

where $\widetilde{\Omega} = \mathcal{A}\Omega_{\text{max}}$ and $\widetilde{\delta} = \mathcal{A}\delta_{\text{max}}$ are the average Rabi frequency and detuning along the

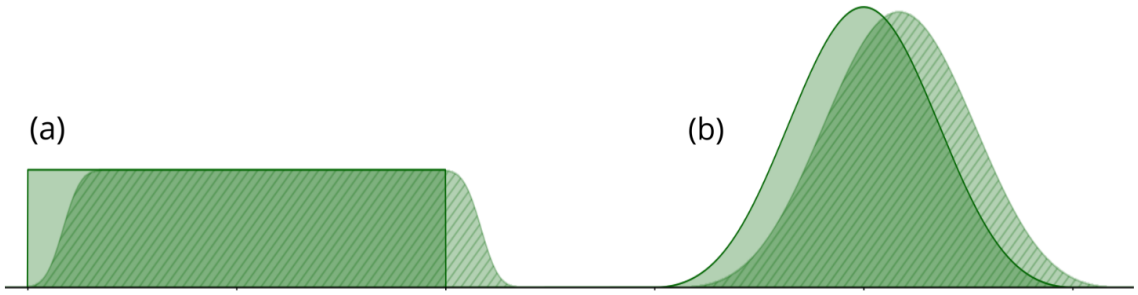


Figure 6.6: *Constant waveform (a) and Blackman waveform (b) with the same duration and area. The command (plain area) is compared to the waveform effectively realized by the hardware (hatched area). The latter has been simulated with Pulser from the modulation bandwidth of the device 'AnalogDevice' which models Pasqal's physical devices. The difference between the command and the realization is larger for the constant than for the Blackman for which the waveform, while delayed, is fairly reproduced.*

pulse. This expression highlights the fact that when the interaction can be neglected, the evolution operator does not depend on the waveform and is the same than with a constant pulse of Rabi frequency $\widetilde{\Omega}$ and detuning $\widetilde{\delta}$. Indeed, without the interaction term, for all t and t' $H_R(t)$ and $H_R(t')$ are proportional, so they commute. Therefore, the time ordering can be removed in the evolution operator, leading to

$$U(\tau) = \mathcal{T}\Big[\exp\Big(-\frac{i}{\hbar}\int_0^\tau H_R(t)dt\Big)\Big] = \exp\Big(-\frac{i}{\hbar}\widetilde{H}_R\int_0^\tau \frac{f(t/\tau)}{\mathcal{A}}dt\Big) = \exp\Big(-\frac{i}{\hbar}\widetilde{H}_R\tau\Big). \quad (6.31)$$

The evolution of two qubits under such a Blackman-waveform pulse of duration $\tau = 1\ \mu$s has been simulated. The parameters $r, \widetilde{\Omega}, \widetilde{\delta}, \phi$ have been optimised in the same way as with the constant pulse, in order to minimise the ground energy at $t = \tau$. Contrary to the previous minimisation with a constant pulse, the set of initial parameters $(r, \widetilde{\Omega}, \widetilde{\delta}, \phi) = (10\ \mu m, 1\ \text{rad}/\mu s, 0\ \text{rad}/\mu s, 0\ \text{rad})$ leads to a local minima. After testing different such sets, the set $(8\ \mu m, 1\ \text{rad}/\mu s, 0\ \text{rad}/\mu s, 0\ \text{rad})$ has been found to converge to the ground energy (still with a relative error $\approx 10^{-10}$). The corresponding energy and amplitudes evolution are represented in Fig. 6.5 (b).

This opens the possibility to prepare the ground state of the deuteron Hamiltonian H_3 with the Ruby quantum computer. However, to measure the corresponding energy with this device, the effect of the interaction during the required basis rotations has to be taken into account. This issue is addressed in the following.

6.2.3 Reducing the effect of interaction for measurements

As explicited in Eq. (6.25), the measurement of the deuteron energy requires the evaluation of observables $\mathbb{1}\mathbb{1}, Z\mathbb{1}, \mathbb{1}Z, ZZ$, which can be done by directly measuring the state obtained at the previous step, and the observables $X\mathbb{1}, \mathbb{1}X, XX, YY$ for which a basis rotation is needed before the measurement: $U_x \otimes U_x$ for $X\mathbb{1}, \mathbb{1}X, XX$ and $U_y \otimes U_y$ for YY. Using

the general expressions Eq. (2.13) and Eq. (2.14), these two basis rotations can be written as

$$\begin{aligned} U_x \otimes U_x &= e^{i\theta\left(\text{cotan}(\theta)Y_1 \pm \sqrt{\frac{1-\text{cotan}(\theta)^2}{2}}(X_1+Z_1)\right)} \otimes e^{i\theta\left(\text{cotan}(\theta)Y_2 \pm \sqrt{\frac{1-\text{cotan}(\theta)^2}{2}}(X_2+Z_2)\right)} \\ &= e^{i\theta\left(\text{cotan}(\theta)(Y_1+Y_2) \pm \sqrt{\frac{1-\text{cotan}(\theta)^2}{2}}(X_1+X_2+Z_1+Z_2)\right)}, \\ U_y \otimes U_y &= e^{i\theta\left(-\text{cotan}(\theta)(X_1+X_2) \mp \sqrt{\frac{1-\text{cotan}(\theta)^2}{2}}(Y_1+Y_2+Z_1+Z_2)\right)}. \end{aligned} \tag{6.32}$$

If the interaction $\frac{C_6}{r^6}\hat{n}_1\hat{n}_2$ could be stopped, these basis rotations might be realized (up to an irrelevant global phase) from a global constant pulse with duration τ_r and suitable Rabi frequency Ω and δ as

$$e^{-i\left(\frac{\Omega\tau_r}{2}\cos(\phi)(X_1+X_2) - \frac{\Omega\tau_r}{2}\sin(\phi)(Y_1+Y_2) - \frac{\delta\tau_r}{2}(Z_1+Z_2)\right)}. \tag{6.33}$$

As discussed previously (see Eq. (6.31)), this evolution operator is the same when the pulse is not constant, provided that $\Omega(t)$ and $\delta(t)$ evolve according to the same waveform. In this case, $\Omega\tau_r$ and $\delta\tau_r$ can be replaced in the above expression by the areas corresponding to their respective evolution, *i.e.*

$$\mathcal{A}_\Omega = \int_0^{\tau_r} \Omega(t)dt \qquad \text{and} \qquad \mathcal{A}_\delta = \int_0^{\tau_r} \delta(t)dt\,. \tag{6.34}$$

Hence, the realisation of the basis rotations $U_x \otimes U_x$ and $U_y \otimes U_y$ as explicited in Eq. (6.32), with pulse (6.33), could be satisfied with respectively

$$\begin{pmatrix} \mathcal{A}_\Omega\cos(\phi) \\ \mathcal{A}_\Omega\sin(\phi) \\ \mathcal{A}_\delta \end{pmatrix} = \begin{pmatrix} \mp\theta\sqrt{2-2c(\theta)^2} \\ 2\theta c(\theta) \\ \pm\theta\sqrt{2-2c(\theta)^2} \end{pmatrix} \quad \text{and} \quad \begin{pmatrix} \mathcal{A}_\Omega\cos(\phi) \\ \mathcal{A}_\Omega\sin(\phi) \\ \mathcal{A}_\delta \end{pmatrix} = \begin{pmatrix} 2\theta c(\theta) \\ \mp\theta\sqrt{2-2c(\theta)^2} \\ \mp\theta\sqrt{2-2c(\theta)^2} \end{pmatrix} \tag{6.35}$$

where the shorter notation $c(\theta) = \text{cotan}(\theta)$ has been used for clarity. As explained in section 2.2.3, θ can be any angle verifying $\cos(2\theta) \leq 0$. Its choice will be further discussed in the following.

However, the interaction $\frac{C_6}{r^6}\hat{n}_1\hat{n}_2$ between the qubits cannot be stopped when a basis rotation is performed. As a result, when the parameters of the pulse are fixed as in Eq. (6.35) to perform $U_x \otimes U_x$ or $U_y \otimes U_y$, the latter are not exactly reproduced. The strategy adopted here is to reduce this effect by performing the basis rotation in a short time compared to the time scale of the interaction. Two levers can be used for this.

The first one consists in reducing the interaction by increasing the qubit relative distance r. However, r cannot be changed from the beginning of the computation, so increasing it requires to change also the parameters of the pulse used to find the ground state. A first possibility is to find another combination of parameters $r, \widetilde{\Omega}, \widetilde{\delta}, \phi$ which allows to get the ground state at the chosen value of τ, with the largest possible value of r. During this work, no such combination was found with a larger r than the one reported on Fig. 6.5 (b). A second possibility, used here, is to scale all the parameters with τ according to

$$(r, \widetilde{\Omega}, \widetilde{\delta}, \phi, \tau) \to (\lambda^{\frac{1}{6}}r, \frac{1}{\lambda}\widetilde{\Omega}, \frac{1}{\lambda}\widetilde{\delta}, \phi, \lambda\tau). \tag{6.36}$$

Indeed, such scaling does not change the evolution operator. Therefore, the longer is the pulse duration τ, the larger the relative distance r can be. However, this approach is limited by the decoherence time of the qubits, which restricts the total duration of the pulse, and therefore the values of λ that can be used in practice in the above scaling.

The second lever consists in performing the basis rotation with a short pulse. The completeness of this rotation depends on the area of the pulse, so reducing its duration τ_r involves increasing the corresponding Rabi frequency Ω and detuning δ. However, these are limited by the corresponding maximum values allowed by the hardware Ω_{lim} and δ_{lim}. For the Rabi frequency, with a Blackman waveform $\Omega(t) = \Omega_{\text{max}} f(t/\tau)$, the maximum value Ω_{max} is related to the area $\mathcal{A}_\Omega$ and duration τ_r of this waveform by

$$\mathcal{A}_\Omega = \int_0^{\tau_r} \Omega(t)dt = \Omega_{\text{max}}\, \tau_r \int_0^1 f(x)dx = \Omega_{\text{max}}\, \tau_r\, \mathcal{A} = 0.42\, \tau_r\, \Omega_{\text{max}}\,, \tag{6.37}$$

where the area $\mathcal{A}$ under the Blackman window function, defined in Eq. (6.29), has been used. Hence, the Rabi frequency remains lower than Ω_{lim} if and only if $\Omega_{\text{max}} \leq \Omega_{\text{lim}}$, *i.e.* $\tau_r \geq \tau_{\Omega,\text{lim}}$ with

$$\tau_{\Omega,\text{lim}} := \frac{\mathcal{A}_\Omega}{0.42\, \Omega_{\text{lim}}}. \tag{6.38}$$

Similarly, the maximum value of the detuning δ_{lim} compatible with the hardware imposes the limit duration

$$\tau_{\delta,\text{lim}} := \frac{\mathcal{A}_\delta}{0.42\, \delta_{\text{lim}}}. \tag{6.39}$$

As a result, the reduction of the pulse duration τ_r is limited by $\tau_r \geq \max(\tau_{\Omega,\text{lim}}, \tau_{\delta,\text{lim}})$.

This limit can be improved by minimising $\mathcal{A}_\Omega$ and $\mathcal{A}_\delta$. Indeed, the bases rotations $U_x \otimes U_x$ and $U_y \otimes U_y$ can be performed in several ways (illustrated in Fig. 2.2) which are determined by the choice of the angle θ in Eq. (6.35) (with the restriction $\cos(2\theta) \leq 0$). For each of these two basis rotations,

$$\mathcal{A}_\Omega^2 = \Big(\mp\theta\sqrt{2-2c(\theta)^2}\Big)^2 + \Big(2\theta c(\theta)\Big)^2 = 2\theta^2(1+\text{cotan}(\theta)^2) = \frac{2\theta^2}{\sin(\theta)^2}. \tag{6.40}$$

Since $\Omega \geq 0$, this results in $\mathcal{A}_\Omega = \frac{\sqrt{2}}{|\text{sinc}(\theta)|}$ where sinc is the sinus cardinal function. The value of θ minimising $\mathcal{A}_\Omega$ while $\cos(2\theta) \leq 0$ is therefore $\theta = \pm\frac{\pi}{4}$, with $\mathcal{A}_\Omega = \frac{\pi}{2}$. This value also minimises $\mathcal{A}_\delta$ with $\mathcal{A}_\delta = 0$. Using Eq. (6.32), $\theta = \pm\frac{\pi}{4}$ corresponds to the basis rotations

$$U_x \otimes U_x = e^{i\frac{\pi}{4}(Y_1+Y_2)} \quad \text{and} \quad U_y \otimes U_y = e^{-i\frac{\pi}{4}(X_1+X_2)}, \tag{6.41}$$

which are realized, according to Eq. (6.35), with the respective sets of parameters

$$(\mathcal{A}_\Omega, \mathcal{A}_\delta, \phi) = (\frac{\pi}{2}, 0, \frac{\pi}{2}) \quad \text{and} \quad (\mathcal{A}_\Omega, \mathcal{A}_\delta, \phi) = (\frac{\pi}{2}, 0, 0). \tag{6.42}$$

Thereby, with the two pulses determined by these parameters, the basis rotations required to evaluate the observables $X\mathbb{1}, \mathbb{1}X, XX$, and YY can be performed in a minimal time, in order to reduce the error induced by the interaction. This allows to evaluate, with a neutral atom quantum computer restricted to global pulses, the energy of the ground state of H_3, prepared with the pulse described in section 6.2.2. The following section presents a simulation of this procedure, and evaluates the error due to the interaction.

6.2.4 Application to the AnalogDevice

The preparation of the ground state of H_3 and the evaluation of its energy, as explained above, has been simulated for the *AnalogDevice*, the model provided by *Pulser* to simulate Pasqal's physical devices with their constraints. According to the specifications of the

AnalogDevice, $\Omega_{\text{lim}} = 12.57$ rad/μs. Hence, using Eq. (6.38) with $\mathcal{A}_\Omega = \frac{\pi}{2}$, the duration of the pulse is limited by the minimal value $\tau_{\Omega,\text{lim}} = 298$ ns.

Another important parameter to take into account is the actualisation time of the phase ϕ. Indeed, the basis rotation pulse cannot directly follow the pulse preparing the ground state, because the phase has to be actualised between the two pulses. A delay is required, but during this delay the 2-qubit interaction evolves the system away from the prepared ground state. To solve this issue, instead of optimising the first pulse, of duration τ, in order to minimise the energy reached at $t = \tau$, the optimisation is made on the energy at $t = \tau + \tau_a$ where τ_a is larger than the actualisation time for ϕ. The choice of τ and τ_a has to be a compromise between the requirement for a long evolution (to allow for a larger r and then reduce the interaction, as argued previously), and a total duration $\tau + \tau_a + \tau_r$ small enough to limit decoherence.

Fixing these durations to $\tau = 4\ \mu s$, $\tau_a = 1\ \mu s$, and $\tau_r = 300$ ns, the minimisation of the energy at $t = 5\ \mu s$ allowed to reach the ground state (with a relative error in energy $\approx 10^{-12}$) with the parameters values $8.43\ \mu m$, $\widetilde{\Omega} = 0.46$ rad/μs, $\widetilde{\delta} = -0.20$ rad/μs, and $\phi = 2.20$ rad, for the Blackman-waveform pulse. The resulting evolution of the energy and the amplitudes is shown in Fig. 6.7. Combining the results of the measurements in the three different bases, the deuteron ground energy has been evaluated to -1.876 MeV, which corresponds to $8\ \%$ in relative error. Table 6.2 details the expectation values and relative errors for operators that have to be evaluated to reconstruct the energy of H_3 according to Eq. (6.25). This shows that the interaction during the basis rotation pulse $e^{i\frac{\pi}{4}(Y_1+Y_2)}$ involves limited errors for expectation values of observables $X\mathbb{1}, \mathbb{1}X, XX$, while during the basis rotation pulse $e^{-i\frac{\pi}{4}(X_1+X_2)}$ it results in $11\ \%$ in relative error on the expectation value of YY.

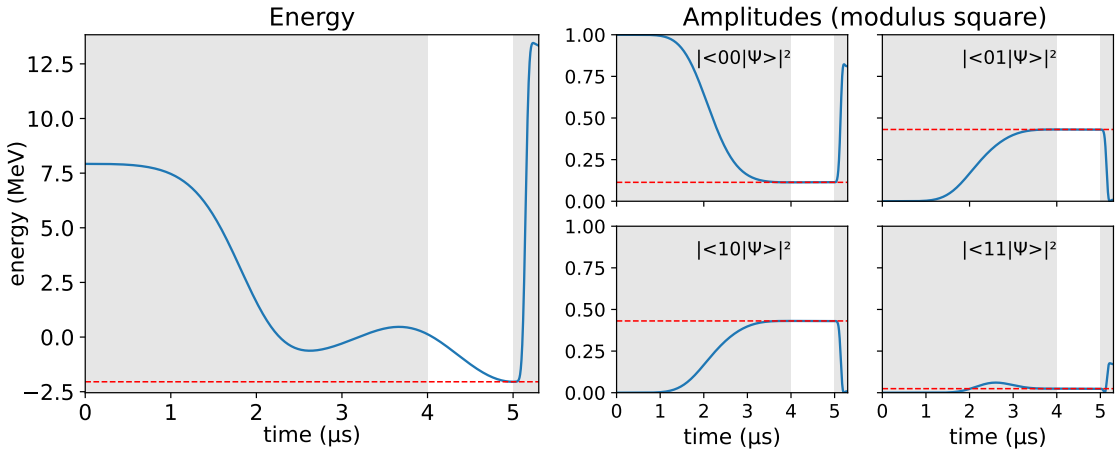


Figure 6.7: *Simulated evolution of the deuteron energy and amplitudes (modulus square) of a state encoded as explained in the text on 2 atoms separated by $r = 8.43\ \mu m$, and evolved under two Blackman-waveform pulses. The first one has a duration $\tau = 4\ \mu s$ and parameters $\widetilde{\Omega} = 0.46$ rad/μs, $\widetilde{\delta} = 0.20$ rad/μs, $\phi = 2.20$ rad. These parameters have been optimised in order to reach the ground state at $t = 5\ \mu s$. The second pulses is the 300-ns basis rotation $U_x \otimes U_x = e^{i\frac{\pi}{4}(Y_1+Y_2)}$ used to measure the observables $X\mathbb{1}$, $\mathbb{1}X$, XX. The shaded areas represent the application of the two pulses. Exact ground energy and amplitudes are represented by the red dashed lines.*

Taking into account the modulation bandwidth of the laser pulses (the pulse effectively realized by the hardware instead of the command), the relative error on the ground state

Observable	Exact expect. value	Computed expect. value		Relative error (%)	
		Ideal	Modulated	Ideal	Modulated
$Z\mathbb{1}$	0.089	0.089	0.089	0	-0.1
$\mathbb{1}Z$	0.089	0.089	0.089	0	-0.1
ZZ	-0.724	-0.724	-0.725	0	-0.04
$X\mathbb{1}$	0.647	0.639	0.641	1.2	0.9
$\mathbb{1}X$	0.647	0.639	0.641	1.2	0.9
XX	0.967	0.965	0.966	0.2	0.2
YY	0.757	0.838	0.851	-10.6	-12.4
H_3	-2.046 MeV	-1.876 MeV	-1.866 MeV	8.3	9.1

Table 6.2: *Expectation values of the observables which are evaluated to reconstruct the energy of H_3. The exact values (left), are compared with the ones computed from simulation of the protocol described in the text (middle), with ideal pulses following the command, and taking into account the modulation due to the response time of the hardware. This comparison is quantified by the relative error (right). The errors are due to the interaction during the basis rotations (hence, no error is obtained for observables $Z\mathbb{1}, \mathbb{1}Z, ZZ$ which do not require a basis rotation).*

energy grows from 8 % to 9 %. Therefore, the modulation has a limited effect, within this protocol, compared to the interaction during the basis rotation pulse $e^{i\frac{\pi}{4}(Y_1+Y_2)}$. Moreover, the effect of modulation may be reduced. Indeed, it can be separated into two contribution: the modulation of the pulse preparing the ground state, and the modulation of the basis rotation pulse. The former is due to the fact that the parameters have been optimised in a simulation where this modulation have been neglected: with a more realistic simulation or a computation on real hardware, this contribution would cancel. The latter contribution may be reduced by starting the basis rotation pulse a bit sooner, in order to compensate the delay due to the modulation.

The statistical error due to the finite number of measurement have also been estimated. As explained in section 2.4.3, to evaluate the variance V on the estimation of the energy, the Eq. (6.25) can be written as $\Lambda H_3 \Lambda^\dagger = H_3^X + H_3^Y + H_3^Z$ where H_3^Z is evaluated from the measurements performed directly after the preparation of the ground state, H_3^X is evaluated from the measurements performed after the basis rotation $U_x \otimes U_x$, and H_3^Y is evaluated from the measurements performed after the basis rotation $U_y \otimes U_y$. The three associated variances can be exactly evaluated from Eq. (2.27), using the ground state obtained from exact diagonalisation, and summed to get V. With N_{shots} measurements performed in each of the three cases, this results in the standard deviation

$$\sigma = \frac{2.77 E_{\text{exact}}}{\sqrt{N_{shots}}}\,, \tag{6.43}$$

where E_{exact} is the exact ground state energy. This standard deviation has been verified with simulations.

6.2.5 Influence of the duration and the choice of basis rotations

The error induced by the interaction during the basis rotations depends on the duration τ_r of the latter, and on the choice made to realize them, *i.e.* the choice of θ in Eq. (6.32). The relative energy error is plotted with respect to τ_r in Fig. 6.8, for three different choices of the basis rotations U_x and U_y, namely

$$\begin{aligned} &\text{Protocol 1:} \quad U_x = e^{i\frac{\pi}{4}Y}, && U_y = e^{-i\frac{\pi}{4}X}, \\ &\text{Protocol 2:} \quad U_x = e^{i\frac{\pi}{4}Y}, && U_y = e^{-i\frac{\pi}{3\sqrt{3}}(X+Y+Z)}, \\ &\text{Protocol 3:} \quad U_x = e^{i\frac{\pi}{2\sqrt{2}}(X+Z)}, && U_y = e^{-i\frac{\pi}{3\sqrt{3}}(X+Y+Z)}. \end{aligned} \tag{6.44}$$

This figure reveals that for $\tau_r \lesssim 1\ \mu s$, the error increases quasi-linearly with τ_r. This can be used to extrapolate the value of the energy in the limit $\tau_r \to 0$, from evaluations performed with different values of τ_r above its lower bound. For $\tau_r \gtrsim 1\ \mu s$, the error evolves differently with τ_r and sometimes decreases. There are even some durations for which the error cancels. This can motivate further investigations to know if these error cancellations can be predicted and exploited to obtain a more accurate result.

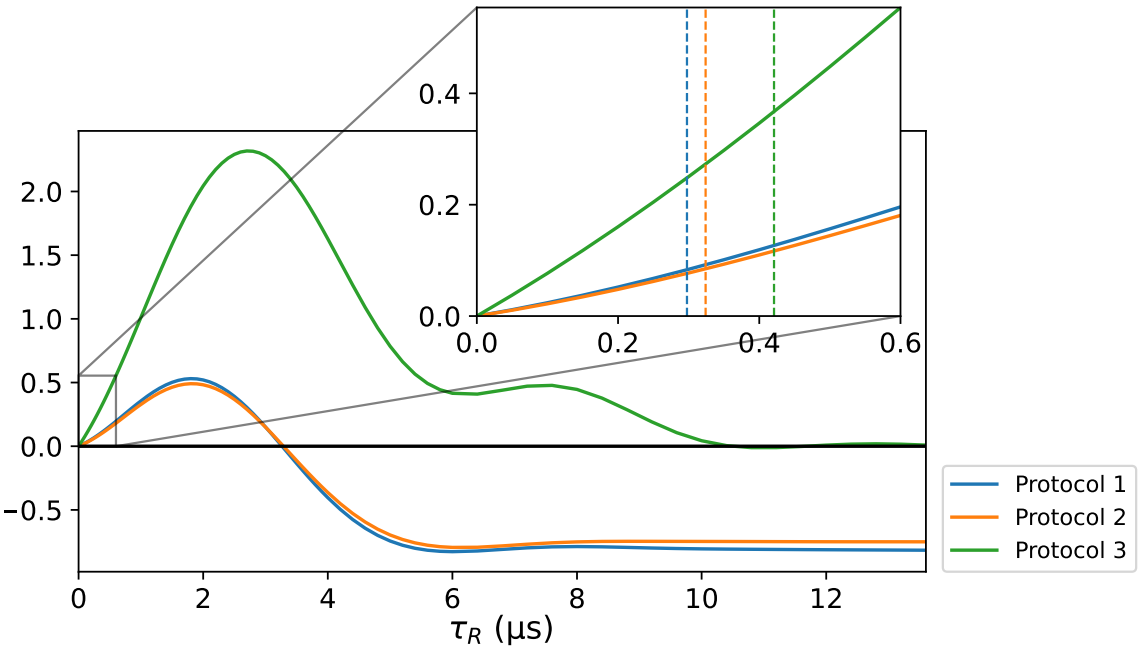


Figure 6.8: *Relative error on the deuteron energy computed with the method explained in the text, with respect to the duration τ_R of the basis rotation pulse. The three measurement protocols defined in Eq. (6.44) are represented in different colors. In the inset, the lower bounds on τ_R, imposed by the hardware, are represented by the dashed vertical bars for each of the three protocols.*

Moreover, since the three protocols have different values of $\mathcal{A}_\Omega$[7], they present different values of the lower bound on τ_r imposed by the maximum Rabi frequency. These lower

[7]Since $\mathcal{A}_\Omega$ is always larger than $\mathcal{A}_\delta$ according to Eq. (6.35) and δ_{lim} is 10 times larger than Ω_{lim} according to the specifications of the AnalogDevice, $\max(\tau_{\Omega,\text{lim}}, \tau_{\delta,\text{lim}}) = \tau_{\Omega,\text{lim}}$, so it is not required to care about the detuning for the determination of the lower bound on τ_r.

bounds are represented in the inset of Fig. 6.8 by vertical lines. Protocol 1 minimises the error because it minimises $\mathcal{A}_\Omega$, so it allows the smallest possible basis duration τ_r. However, for a given τ_r, this protocol does not provide the minimal energy error. Indeed, the energy error obtained with protocol 2 is slightly smaller. Here again, a better understanding about the effect of the interaction on the basis rotations is needed to know if the basis rotations can be chosen in a more suitable way that according to the minimisation of τ_r.

Another feature to notice is the convergence of the error to a given value as τ_r increases. In particular, the relative error obtained for the protocol 3 is converging to $0.9\,\%$: a long basis rotation involves a smaller error that the shortest possible one. While this phenomenon may depend on the state that is measured, if it could be understood and predicted, it may help reducing the error induced by the interaction during the basis rotations.

6.3 Conclusion

This chapter addresses the variational estimation of the ground-state energy of many-body systems with an analog neutral atom quantum computer. This application raises various challenges, and the objective of the work reported in this chapter is to address them in order to make such application feasible with a real hardware.

The method described in section 6.1 has been developed for an eventual future device working in the XY mode and equipped with the SLM mask and the DMM. It allows to explore a space with a fixed Hamming weight K using this device. While it succeeds in reaching the ground state of systems encoded in the Hamming-weight-1 subspace of the N-qubit space (a situation where there is no quantum advantage), the optimisation of the energy becomes more difficult for $2 \leq K \leq N-2$, due to the presence of various local minima. This requires further work to determine if a more guided optimisation can be performed, with *e.g.* convenient choices of the initial parameters.

In section 6.2, an alternative method is described to efficiently use the Ruby machine. Several techniques are presented to overcome or limit the obstacles raised in section 5.3. An alternative encoding to the usual Jordan-Wigner fermion-to-qubit mapping have been proposed to reduce the number of qubits, map the physical space of the many-body problem of interest into the accessible qubit space, and map the corresponding Hamiltonian to a measurable qubit observable. This have been applied to encode in two qubits the deuteron Hamiltonian (1.31) with truncation order $M = 3$. A laser pulse has been optimised to prepare its ground state, taking into account hardware constraints. A strategy has been proposed to evaluate the corresponding energy with basis rotation pulses while reducing the error involved by the qubit-qubit interaction.

The resulting procedure has been simulated, and two sources of error have been estimated: the error induced by the interaction during the basis rotation pulses, and the statistical error due to the finite number of measurements. While some work is required to select a more frugal and noise-resilient classical algorithm for the optimisation of the parameters, the optimised procedure presented in Fig. 6.7 is ready to be tested on real hardware with the Ruby quantum computer. This application is underway. If successful, it could pave the way for its generalisation to bigger systems.

General conclusion

This thesis has addressed the application of quantum computing algorithms to the nuclear many-body problem. Quantum computers constitute indeed a promising approach to this problem, due to their ability to efficiently encode a many-body state on interacting qubits, and evaluate the corresponding energy from measurements. The focus has been made here on variational hybrid algorithms, which combine quantum computing to a classical optimisation algorithm. Both digital and analog quantum computing approaches have been considered.

The **first chapter** has introduced some elements of nuclear physics that are relevant in following chapters. After a brief presentation of many-body physics, a quick overview of nuclear theory has been given to clarify the context of this thesis. In particular, the one-body Green's functions, as used within the self-consistent Green's function *ab-initio* method, have been defined in view of their use in chapter 4. Two models, meaningful for nuclear theory, have then been presented in order to test the methods developed in the following chapters: the pairing model and a simple model for the deuteron.

The **second chapter** has presented the basic notions of digital quantum computing that are required to understand the rest of the thesis, such as qubits, operations that can be performed on them, representation of the latter with quantum circuits, evaluation of observables from measurements, and quantum algorithms. The application of quantum computing to many-body problems has been explained, with the encoding of many-body states into qubits, and the corresponding mapping of many-body observables to qubit observables. The resulting expressions for the Hamiltonians of the two models presented in the previous chapter have been established in order to prepare the applications made in the following chapters.

The **third chapter** has addressed variational algorithms dedicated to the preparation of the ground state of many-body systems, and the evaluation of the corresponding energies. The VQE algorithm has been presented, as well as its improved version ADAPT-VQE. The latter has been introduced in a generalised form compared to the original one, and four versions have been defined. They have been benchmarked with their application to the pairing model in a noiseless simulation, and compared to projected BCS ansätze. This application showed that these ADAPT-VQE variants can efficiently prepare an ansatz wavefunction approximating the ground state with a high fidelity, while adjusting a limited number of parameters. To conclude on their potential to overcome classical algorithms, further investigations are needed to determine how this number of parameters scales with the dimension of the many-body problem of interest, and how resilient to noise these algorithms are. In any case, the compactness of the ansatz wavefunctions prepared by ADAPT-VQE-based algorithms limits the depth of the corresponding quantum circuits, making them advantageous for a use in other quantum algorithms, such as the one described in chapter 4.

Indeed, the resulting ansatz wavefunction, approximating the ground state of the many-body system of interest, has been used in the **fourth chapter** as an input for a quantum-classical hybrid method dedicated to the computation of the Green's functions defined in chapter 1. The procedure uses this ansatz encoded on qubits to efficiently evaluate expectation values within the quantum subspace expansion technique. An associated eigenvalue problem yields the building blocks needed to construct the spectral representation of the Green's function. Here again, the pairing model has been used to benchmark the method. Simulations were made from ansatz wavefunctions obtained via several methods, confirming that the ansatz which approximates the more accurately the ground state also yields the more accurate approximation of the Green's function. It has also been shown that this method provides, as a byproduct, the eigenenergies of odd systems from a computation on even systems. A quantitative study of the required number of quantum measurements has been realized, in order to determine how this number scales with the target precision and the size of the pairing problem. Simplifications induced by the pairing model allow to reduce this number of measurement, but for a more general problem, such as a realistic nuclear Hamiltonian, more quantum measurements would be required. A crucial point for such application to realistic models concerns the choice of quantum subspace expansion operators, which should include higher excitations and collective modes.

In chapters 3 and 4, simulations have been performed so that they reproduced a perfect digital quantum computer. However, current devices are subject to noise, resulting in the decoherence of qubit states, imperfect operations, and therefore an alteration of the measurement statistics. To tackle this issue, the analog quantum computing paradigm appears to be a promising approach. While limited in the range of problems that it can address, it has the potential to reduce the accumulation of errors that current hardware involves with the digital approach. The neutral atom quantum computers are particularly suited for the analog approach. In the second part of this thesis, the possibility to use them with variational algorithms has been explored.

After a short introduction to analog quantum computing, the **fifth chapter** has described the basic ingredients of neutral atom quantum computers. The resource Hamiltonian, determining the evolution of the qubit state, has been depicted with two ways of encoding the latter in neutral atoms: Ising and XY modes. Then, details have been given about the various challenges identified during this work for the realisation of variational algorithm with these devices, focusing especially on Ruby, a neutral atom quantum computer delivered at the TGCC center by the quantum hardware company Pasqal.

The **sixth chapter** has presented several techniques developed to overcome or limit these obstacles and constraints. First it has explained how a subspace of the qubit space with a fixed Hamming weight can be explored using a neutral atom quantum computer in the XY mode, equipped with the SLM mask and the detuning map modulator. This has been applied to a model for the deuteron and to the pairing model. Simulations showed that ground states of systems modelled in the Hamming-weight-1 subspace can be reached, but the question remains open for systems in higher Hamming weight subspaces. Indeed, in the latter case, the energy landscape present various local minima which makes the optimisation challenging. More investigation is required to determine whether, given a number of qubits and a Hamming weight, the ground state is reachable or not. This question is crucial since no quantum advantage can be expected when modelling systems in the Hamming-weight-1 subspace. Moreover, if the XY mode, the SLM mask, and the DMM are available

for simulations on Pulser, they are not implemented yet on current devices. The method elaborated here has been made in anticipation of eventual future neutral atom quantum processors.

In a second part of this last chapter, the current limitations of the Ruby device have been taken into account, such as the restriction to the Ising mode with global pulses or the hardware modulation bandwidth. An alternative encoding to the usual Jordan-Wigner fermion-to-qubit mapping has been introduced to reduce the number of qubits, map the relevant physical space to the qubit accessible space, and map the Hamiltonian to a qubit observable that can be measured despite the restriction to global pulses. To realize a first test, this strategy has been applied to a model of the deuteron in a 3-dimensional space, encoded in two qubits. The parameters of a laser pulse have been optimised to reach the ground state, with a waveform adapted to the hardware. Several techniques have been set up to reduce the effect of the interaction occurring during the basis rotations performed to evaluate the energy. The remaining error induced by this effect, and the statistical error due to the finite number of measurements have been evaluated.

The effect of noise still remains to be quantified. It may affect in particular the optimisation step, for which a classical optimisation algorithm more frugal and resilient to noise than the one used here in simulation has to be selected. Therefore, a first application to real hardware is planned with the parameters already optimised in a simulation. If the device succeeds in reaching the ground state and evaluate its energy with a limited error compared to the simulation presented here, this would constitute a first proof of principle before a computation including the simulation step, and a generalisation for larger and more realistic many-body systems. While interacting with the current Ruby device is a challenging process, which requires patience and perseverance, one can hope that this application will be performed in a near future.

Appendix A

Some extra elements of many-body physics

This appendix gives some justifications to statements made in section 1.1, namely the fact that Slater determinants form an orthonormal basis, the fact that the Fock space as defined in Eq. (1.6) is a Hilbert space, and the characterisation (1.8) of annihilation operators.

A.1 Slater determinants form an orthonormal basis

Let us denote the one-body states in the M-dimensional Hilbert space $\mathcal{H}$ as $\beta_1, ..., \beta_M$ and consider the set of Slater determinants

$$\mathcal{F}_N = \{|\beta_{k_1}, \beta_{k_2}, ..., \beta_{k_N}\rangle / 1 \leq k_1 < k_2 < ... < k_N \leq M\}. \tag{A.1}$$

Here it is shown that, as claimed in section 1.1.2, $\mathcal{F}$ forms an orthonormal basis of $\mathcal{A}_N(\mathcal{H}_N)$.

Consider two Slater determinants $|\beta_{p_1}, ..., \beta_{p_N}\rangle$ and $|\beta_{q_1}, ..., \beta_{q_N}\rangle$ in $\mathcal{F}_N$. To compute their scalar product, they can be decomposed using Eq. (1.5) as

$$\begin{aligned}
\langle \beta_{p_1}, ..., \beta_{p_N} | \beta_{q_1}, ..., \beta_{q_N} \rangle &= \frac{1}{N!} \Big(\sum_{\sigma \in \mathscr{S}_N} \varepsilon(\sigma) \langle \beta_{p_{\sigma(1)}}| \otimes ... \otimes \langle \beta_{p_{\sigma(N)}}| \Big) \Big(\sum_{\sigma' \in \mathscr{S}_N} \varepsilon(\sigma') |\beta_{q_{\sigma'(1)}}\rangle \otimes ... \otimes |\beta_{q_{\sigma'(N)}}\rangle \Big) \\
&= \frac{1}{N!} \sum_{\sigma, \sigma' \in \mathscr{S}_N} \sum \varepsilon(\sigma) \varepsilon(\sigma') \langle \beta_{p_{\sigma(1)}} | \beta_{q_{\sigma'(1)}} \rangle ... \langle \beta_{p_{\sigma(N)}} | \beta_{q_{\sigma'(N)}} \rangle \\
&= \frac{1}{N!} \sum_{\sigma, \sigma' \in \mathscr{S}_N} \sum \varepsilon(\sigma\sigma') \, \delta_{p_{\sigma(1)}, q_{\sigma'(1)}} ... \, \delta_{p_{\sigma(N)}, q_{\sigma'(N)}} \\
&= \sum_{\sigma \in \mathscr{S}_N} \varepsilon(\sigma) \, \delta_{p_{\sigma(1)}, q_1} ... \, \delta_{p_{\sigma(N)}, q_N} \, ,
\end{aligned} \tag{A.2}$$

where the orthonormality of $\{|\beta_k\rangle\}_{1 \leq k \leq M}$ has been used to obtain the second-to-last line, and the change of variable $\sigma \to \sigma\sigma'$ has been performed to obtain the last line, using the identity $\delta_{p_{\sigma(\sigma'(i))}, q_{\sigma'(i)}} = \delta_{p_{\sigma(i)}, q_i}$. Since $p_1 < ... < p_N$ and $q_1 < ... < q_N$, one gets

$$\langle \beta_{p_1}, ..., \beta_{p_N} | \beta_{q_1}, ..., \beta_{q_N} \rangle = \begin{cases} 1 & \text{if } \; p_1 = q_1, ..., p_N = q_N \\ 0 & \text{otherwise} \end{cases} , \tag{A.3}$$

which proves that $\mathcal{F}_N$ is orthonormal.

Moreover, $\mathcal{B}_N = \{|\beta_{k_1}\rangle \otimes |\beta_{k_2}\rangle \otimes ... \otimes |\beta_{k_N}\rangle\}_{k_1,k_2,...,k_N}$ is a basis of $\mathcal{H}_N$, so every element of $\mathcal{H}_N$ writes as a combination of such $|\beta_{k_1}\rangle \otimes |\beta_{k_2}\rangle \otimes ... \otimes |\beta_{k_N}\rangle$. Then, every element of $\mathcal{A}_N(\mathcal{H}_N)$ is a combination of states of the form $\mathcal{A}_N\big(|\beta_{k_1}\rangle \otimes |\beta_{k_2}\rangle \otimes ... \otimes |\beta_{k_N}\rangle\big) = |\beta_{k_1}, \beta_{k_2}, ..., \beta_{k_N}\rangle$, which, up to some minus signs, are elements of $\mathcal{F}_N$. Hence, $\mathcal{F}_N$ generates $\mathcal{A}_N(\mathcal{H}_N)$. Since it has been shown above that it is also orthonormal (therefore linearly independent), one can conclude it is an orthonormal basis of $\mathcal{A}_N(\mathcal{H}_N)$.

A.2 The Fock space as a Hilbert space

In section 1.1.3, the Fock space has been defined as the direct sum

$$F(\mathcal{H}) = \mathbb{C} \oplus \mathcal{H}_1 \oplus \mathcal{A}_2(\mathcal{H}_2) \oplus ... \oplus \mathcal{A}_M(\mathcal{H}_M). \tag{A.4}$$

To become a Hilbert space, it is naturally equipped with the scalar product defined in the following way. Given two states $|\Psi\rangle, |\Phi\rangle \in F(\mathcal{H})$, written as a combination of states with $0, 1, 2, ..., M$ particles as

$$\begin{aligned} |\Psi\rangle &= \sum_{N=0}^{M} u_N |\Psi_N\rangle, \\ |\Phi\rangle &= \sum_{N=0}^{M} v_N |\Phi_N\rangle, \end{aligned} \tag{A.5}$$

their scalar product is defined as

$$\langle\Phi|\Psi\rangle = \sum_{N=0}^{M} v_N^* u_N \langle\Phi_N|\Psi_N\rangle, \tag{A.6}$$

where for any N, $\langle\Phi_N|\Psi_N\rangle$ is the scalar product on $\mathcal{H}_N$ (and then on $\mathcal{A}_N(\mathcal{H}_N)$). Therefore, Slater determinants with different numbers of particles are orthogonal. Then the Slater determinants in $\mathcal{F}_0, \mathcal{F}_1, \mathcal{F}_2, ..., \mathcal{F}_M$ can be joined together to form a convenient orthonormal basis of $F(\mathcal{H})$ as

$$\mathcal{F} = \bigcup_{N=0}^{M} \mathcal{F}_N. \tag{A.7}$$

A.3 On the annihilation operator

In section 1.1.3, the creation operator $a_\beta^\dagger$ has been defined by its action on Slater determinants as

$$a_\beta^\dagger |\alpha_1, ..., \alpha_N\rangle = |\beta, \alpha_1, ..., \alpha_N\rangle, \tag{A.8}$$

and the annihilation operator a_β has been defined as its Hermitian conjugate. It is convenient to explicit its action on every element of the orthonormal basis $\mathcal{F}$ of the Fock space, defined in Eq. (A.7). Such characterisation is made in Eq. (1.8) and justified here.

Consider a N-particle Slater determinant $|S_N\rangle = |\alpha_1, ..., \alpha_N\rangle \in \mathcal{F}_N$. To explicit $a_\beta|S_N\rangle$, one can determine its decomposition in the orthonormal basis $\mathcal{F}$ by considering the scalar

product with elements $|S\rangle \in \mathcal{F}$. If one finds such $|S\rangle$ satisfying $\langle S|a_\beta|S_N\rangle = 1$, one can conclude $a_\beta|S_N\rangle = |S\rangle$. If for any $|S\rangle \in \mathcal{F}$, $\langle S|a_\beta|S_N\rangle = 0$, it means that $a_\beta|S_N\rangle = 0$ (the zero element of $F(\mathcal{H})$).

- Consider first the case $\beta = \alpha_1$. One has

$$\begin{aligned}\langle \alpha_2, ..., \alpha_N|a_\beta|\alpha_1, \alpha_2, ..., \alpha_N\rangle &= \langle \alpha_1, \alpha_2, ..., \alpha_N|a_\beta^\dagger|\alpha_2, ..., \alpha_N\rangle^* \\ &= \langle \alpha_1, \alpha_2, ..., \alpha_N|\alpha_1, \alpha_2, ..., \alpha_N\rangle^* \\ &= 1. \end{aligned} \tag{A.9}$$

  Therefore, $a_\beta|\alpha_1, \alpha_2, ..., \alpha_N\rangle = |\alpha_2, ..., \alpha_N\rangle$.

- The case $\beta = \alpha_i$ for some $i \in \{1, ..., N\}$ is similar if one first uses

$$|\alpha_1, ..., \alpha_{i-1}\alpha_i, \alpha_{i+1}, ..., \alpha_N\rangle = (-1)^{i-1}|\alpha_i, \alpha_1, ..., \alpha_{i-1}\alpha_{i+1}, ..., \alpha_N\rangle. \tag{A.10}$$

  This explains the signs in Eq. (1.8).

- Suppose now that $\beta \notin \{\alpha_1, ..., \alpha_N\}$. Then for any $|S\rangle \in \mathcal{F}$,

$$\langle S|a_\beta|\alpha_1, \alpha_2, ..., \alpha_N\rangle = \langle \alpha_1, \alpha_2, ..., \alpha_N|a_\beta^\dagger|S\rangle^* = 0. \tag{A.11}$$

  Indeed, if the one-body state β is occupied in $|S\rangle$, then $a_\beta^\dagger|S\rangle = 0$, otherwise $a_\beta^\dagger|S\rangle$ is a Slater determinant where β is occupied, so it is orthogonal to $|\alpha_1, \alpha_2, ..., \alpha_N\rangle$.

Finally, Eq. (1.8) is recovered.

Appendix B

General expression of a unitary mapping Z to X or Y

Let us consider a unitary operator U. As explained in section 2.2.2, it can be written as $U = e^{i\theta G}$ where $G = aX + bY + cZ$ with $a, b, c \in \mathbb{R}$ and $a^2 + b^2 + c^2 = 1$. This last point implies $G^2 = \mathbb{1}$, and then $U = \cos(\theta)\mathbb{1} + i\sin(\theta)G$. Therefore, U transforms operator Z into

$$\begin{aligned} U^\dagger Z U &= \big(\cos(\theta)\mathbb{1} - i\sin(\theta)G\big) Z \big(\cos(\theta)\mathbb{1} + i\sin(\theta)G\big) \\ &= \cos(\theta)^2 Z + \sin(\theta)^2 GZG + i\cos(\theta)\sin(\theta)[Z, G] \\ &= \cos(\theta)^2 Z + \sin(\theta)^2 \times \Big((2c^2-1)Z + 2c(aX+bY)\Big) + i\cos(\theta)\sin(\theta)\times 2i(aY-bX) \\ &= \big(ac(1-\cos(2\theta)) + b\sin(2\theta)\big)X \\ &+ \big(bc(1-\cos(2\theta)) - a\sin(2\theta)\big)Y \\ &+ \big(c^2(1-\cos(2\theta)) + \cos(2\theta)\big)Z\,. \end{aligned} \tag{B.1}$$

Let us now suppose that U implements a basis change from the Z basis to the X basis, *i.e.* $X = U^\dagger Z U$. Using previous expression, one sees that this constrains the parameters a, b, c, θ to satisfy the following three equations

$$\begin{cases} 1 = ac(1-\cos(2\theta)) + b\sin(2\theta) \\ 0 = bc(1-\cos(2\theta)) - a\sin(2\theta) \\ 0 = c^2(1-\cos(2\theta)) + \cos(2\theta) \end{cases}. \tag{B.2}$$

The solutions respecting the normalization $a^2 + b^2 + c^2 = 1$ write as

$$b = \text{cotan}(\theta) \quad \text{and} \quad a = c = \pm\sqrt{\frac{1-b^2}{2}}\,, \tag{B.3}$$

where θ is an angle verifying $\cos(2\theta) \leq 0$. Then G writes as

$$G = \text{cotan}(\theta)Y \pm \sqrt{\frac{1-\text{cotan}(\theta)^2}{2}}(X+Z)\,. \tag{B.4}$$

Let us consider now that U implements a basis change from the Z basis to the Y basis, *i.e.* $Y = U^\dagger Z U$. This yields the system of equations obtained from Eqs. (B.2) with the transformation $(a, b, c) \to (-b, -a, -c)$. Hence, its solution is also given by Eqs. (B.3) up to this transformation, leading to

$$G = -\text{cotan}(\theta)X \mp \sqrt{\frac{1-\text{cotan}(\theta)^2}{2}}(Y+Z)\,, \tag{B.5}$$

where θ is an angle verifying $\cos(2\theta) \leq 0$.

Appendix C

Some derivations required for the algorithms presented in section 3.2

C.1 Decomposition into Pauli strings of the commutators in Eq. (3.5)

To evaluate the energy derivatives of Eq. (3.5), one needs first to decompose into Pauli strings the commutators $[H, G_{\alpha\beta}]$ (for $\alpha \neq \beta$), where H is the pairing Hamiltonian (2.63), and $G_{\alpha\beta}$ the qubit excitation operators (3.3). Let us recall that they write as

$$H = \sum_{k=1}^{D} \varepsilon_k (\mathbb{1} - Z_k) - \frac{g}{2} \sum_{k<l} \sum (X_k X_l + Y_k Y_l), \tag{C.1}$$

$$G_{\alpha\beta} = \frac{1}{2}(X_\alpha Y_\beta - Y_\alpha X_\beta). \tag{C.2}$$

Let us denote $A_{kl} = \frac{1}{2}(X_k X_l + Y_k Y_l)$. $[H, G_{\alpha\beta}]$ can be decomposed into a combination of commutators $[Z_\alpha, G_{\alpha\beta}]$, $[Z_\beta, G_{\alpha\beta}]$, and $[A_{kl}, G_{\alpha\beta}]$ for any possible values of k and l such that $k < l$. Using the commutation relations of Pauli operators (see Eq.(2.2)), the first two give

$$[Z_\alpha, G_{\alpha\beta}] = \frac{1}{2}\Big([Z_\alpha, X_\alpha]Y_\beta - [Z_\alpha, Y_\alpha]X_\beta\Big) = \frac{1}{2}\Big(2iY_\alpha Y_\beta + 2iX_\alpha X_\beta\Big) = 2iA_{\alpha\beta}\ , \tag{C.3}$$

$$[Z_\beta, G_{\alpha\beta}] = -[Z_\beta, G_{\beta\alpha}] = -2iA_{\beta\alpha} = -2iA_{\alpha\beta}\ . \tag{C.4}$$

To avoid confusion on the computation of $[A_{kl}, G_{\alpha\beta}]$ for all possible values of k and l, let us associate to the commutators the following diagrams

$$\left(\begin{array}{cc} k & l \\ \alpha & \beta \end{array} \right) = [A_{kl}, G_{\alpha\beta}], \tag{C.5}$$

where each vertex corresponds to an index, and two vertices are connected by a line when the corresponding indices are equal. Since $k < l$ and $\alpha \neq \beta$, these pairs of indices are never linked in the corresponding diagrams. The index labels are dropped in the following for

clarity. These diagrams can help to enumerate all the cases as

$$\begin{aligned}
&\left(\begin{smallmatrix}\bullet & \bullet\\ \bullet & \bullet\end{smallmatrix}\right) = [A_{k\beta}, G_{\alpha\beta}] = iA_{k\alpha}Z_\beta, && \left(\begin{smallmatrix}\bullet & \bullet\\ \bullet & \bullet\end{smallmatrix}\right) = [A_{kl}, G_{\alpha\beta}] = 0,\\
&\left(\begin{smallmatrix}\bullet & \bullet\\ \bullet & \bullet\end{smallmatrix}\right) = [A_{\alpha l}, G_{\alpha\beta}] = -iA_{l\beta}Z_\alpha, && \left(\begin{smallmatrix}\bullet & \bullet\\ \bullet & \bullet\end{smallmatrix}\right) = [A_{\alpha\beta}, G_{\alpha\beta}] = i(Z_\beta - Z_\alpha) \ \text{(only appears if } \alpha<\beta),\\
&\left(\begin{smallmatrix}\bullet & \bullet\\ \bullet & \bullet\end{smallmatrix}\right) = [A_{k\alpha}, G_{\alpha\beta}] = -iA_{k\beta}Z_\alpha, && \left(\begin{smallmatrix}\bullet & \bullet\\ \bullet & \bullet\end{smallmatrix}\right) = [A_{\beta\alpha}, G_{\alpha\beta}] = i(Z_\beta - Z_\alpha) \ \text{(only appears if } \beta<\alpha),\\
&\left(\begin{smallmatrix}\bullet & \bullet\\ \bullet & \bullet\end{smallmatrix}\right) = [A_{\beta l}, G_{\alpha\beta}] = iA_{l\alpha}Z_\beta. &&
\end{aligned} \tag{C.6}$$

Note that the four cases of the first column can be deduced from each other using $A_{kl} = A_{lk}$, $G_{\alpha\beta} = -G_{\beta\alpha}$, and relabelling of indices. Moreover, if one considers the matrices of $A_{\alpha\beta}$, $G_{\alpha\beta}$, and $\frac{1}{2}(Z_\alpha - Z_\beta)$ in the usual 2-qubit basis, one can realize that they are also representations of the Pauli operators, therefore the cases $\left(\begin{smallmatrix}\bullet & \bullet\\ \bullet & \bullet\end{smallmatrix}\right)$ and $\left(\begin{smallmatrix}\bullet & \bullet\\ \bullet & \bullet\end{smallmatrix}\right)$ can be deduced from the Pauli relation $[X, Y] = 2iZ$.

One then has all the required pieces to compute $[H, G_{\alpha\beta}]$ as

$$\begin{aligned}
[H, G_{\alpha\beta}] &= -\varepsilon_\alpha[Z_\alpha, G_{\alpha\beta}] - \varepsilon_\beta[Z_\beta, G_{\alpha\beta}] - g(\left(\begin{smallmatrix}\bullet & \bullet\\ \bullet & \bullet\end{smallmatrix}\right) \text{ if } \alpha<\beta \text{ or } \left(\begin{smallmatrix}\bullet & \bullet\\ \bullet & \bullet\end{smallmatrix}\right) \text{ if } \beta<\alpha)\\
&\qquad - g\left(\sum_{\substack{k<\beta\\ k\neq\alpha}}\left(\begin{smallmatrix}\bullet & \bullet\\ \bullet & \bullet\end{smallmatrix}\right) + \sum_{\substack{l>\beta\\ l\neq\alpha}}\left(\begin{smallmatrix}\bullet & \bullet\\ \bullet & \bullet\end{smallmatrix}\right) + \sum_{\substack{l>\alpha\\ l\neq\beta}}\left(\begin{smallmatrix}\bullet & \bullet\\ \bullet & \bullet\end{smallmatrix}\right) + \sum_{\substack{k<\alpha\\ k\neq\beta}}\left(\begin{smallmatrix}\bullet & \bullet\\ \bullet & \bullet\end{smallmatrix}\right)\right)\\
&= i(\varepsilon_\beta - \varepsilon_\alpha)A_{\alpha\beta} - ig(Z_\beta - Z_\alpha) - ig\left(\sum_{\substack{k<\beta\\ k\neq\alpha}}A_{k\alpha}Z_\beta + \sum_{\substack{l>\beta\\ l\neq\alpha}}A_{l\alpha}Z_\beta - \sum_{\substack{l>\alpha\\ l\neq\beta}}A_{l\beta}Z_\alpha - \sum_{\substack{k<\alpha\\ k\neq\beta}}A_{k\beta}Z_\alpha\right)\\
&= i(\varepsilon_\beta - \varepsilon_\alpha)A_{\alpha\beta} - ig(Z_\beta - Z_\alpha) - ig\sum_{k\neq\alpha,\beta}\Big(A_{k\alpha}Z_\beta - A_{k\beta}Z_\alpha\Big)\\
&= i(\varepsilon_\beta - \varepsilon_\alpha)(X_\alpha X_\beta + Y_\alpha Y_\beta) - ig(Z_\beta - Z_\alpha) - ig\sum_{k\neq\alpha,\beta}\Big(X_kX_\alpha Z_\beta + Y_kY_\alpha Z_\beta - X_kX_\beta Z_\alpha - Y_kY_\beta Z_\alpha\Big).
\end{aligned} \tag{C.7}$$

The resulting $4(D-1)$ Pauli terms can be grouped into 5 fully commuting sets as for instance

$$\{X_kX_\alpha Z_\beta\}_k \cup \{Z_\beta\},\ \ \{Y_kY_\alpha Z_\beta\}_k,\ \ \{X_kX_\beta Z_\alpha\}_k \cup \{Z_\alpha\},\ \ \{Y_kY_\beta Z_\alpha\}_k,\ \ \{X_\alpha X_\beta, Y_\alpha Y_\beta\}. \tag{C.8}$$

Therefore, measurements in only 5 different bases are required to evaluate $\left(\frac{dE_n^{\alpha\beta}(\theta)}{d\theta}\right)_{\theta=0}$.

C.2 Justification of Eq. (3.6)

The qubit excitation operators $G_{ij} = \frac{1}{2}(X_iY_j - Y_iX_j)$, considered in this work satisfy the property $G_{ij}^3 = G_{ij}$. Here, it is shows that this property is sufficient to obtain Eq. (3.6).

Let G be an operator satisfying $G^3 = G$. Then, for $p \in \mathbb{N}$,

$$G^p = \begin{cases} \mathbb{1} & \text{if } p = 0\\ G & \text{if } p \text{ is odd}\\ G^2 & \text{if } p \text{ is even} \neq 0 \end{cases}. \tag{C.9}$$

This allows to write, for any angle θ,

$$e^{i\theta G} = \sum_{p=0}^{\infty} \frac{(i\theta G)^p}{p!} = \mathbb{1} + \sum_{p=1}^{\infty} \frac{(-1)^p \theta^{2p}}{(2p)!} G^2 + i \sum_{p=0}^{\infty} \frac{(-1)^p \theta^{2p+1}}{(2p+1)!} G$$
$$= \mathbb{1} + (\cos(\theta) - 1) G^2 + i \sin(\theta) G \,. \tag{C.10}$$

By inserting this expression in $E(\theta) = \langle\psi| e^{-i\theta G} H e^{i\theta G} |\psi\rangle$, developing all terms and exploiting some trigonometric identities, one can finally write $E(\theta)$ in the form of Eq. (3.6) as

$$E(\theta) = C_0 + C_1 \cos(\theta + \gamma_1) + C_2 \cos(2\theta + \gamma_2) \,. \tag{C.11}$$

C.3 Determination of the parameters in Eq. (3.6)

The five parameters $(C_0, C_1, C_2, \gamma_1, \gamma_2)$ introduced in Eq. (3.6) can be determined from five evaluations of $E(\theta)$. As an example, let us consider

$$\begin{aligned}
E(0) &= C_0 + C_1 \cos(\gamma_1) + C_2 \cos(\gamma_2), \\
E(\pi/2) &= C_0 - C_1 \sin(\gamma_1) - C_2 \cos(\gamma_2), \\
E(\pi) &= C_0 - C_1 \cos(\gamma_1) + C_2 \cos(\gamma_2), \\
E(3\pi/2) &= C_0 + C_1 \sin(\gamma_1) - C_2 \cos(\gamma_2), \\
E(\pi/4) &= C_0 + C_1 \cos(\pi/4 + \gamma_1) - C_2 \sin(\gamma_2).
\end{aligned} \tag{C.12}$$

In this case, C_0, C_1, γ_1 can be retrieved from

$$\begin{aligned}
C_0 &= \frac{1}{4}\Big(E(0) + E(\pi/2) + E(\pi) + E(3\pi/2)\Big), \\
C_1 \cos(\gamma_1) &= \frac{1}{2}\Big(E(0) - E(\pi)\Big), \\
C_1 \sin(\gamma_1) &= \frac{1}{2}\Big(E(3\pi/2) - E(\pi/2)\Big).
\end{aligned} \tag{C.13}$$

Subsequently, C_2 and γ_2 can be deduced from

$$\begin{aligned}
C_2 \cos(\gamma_2) &= \frac{1}{2}\Big(E(0) + E(\pi)\Big) - C_0, \\
C_2 \sin(\gamma_2) &= C_0 + C_1 \cos(\pi/4 + \gamma_1) - E(\pi/4).
\end{aligned} \tag{C.14}$$

This allows to fully determine the function $\theta \mapsto E(\theta)$ and, more specifically, to find its global minimum. In the presence of noise, more evaluations can be performed to fit $E(\theta)$.

Appendix D

A procedure for the exact preparation of a given state

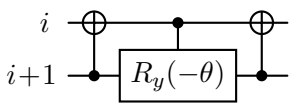
Let us consider a given N-qubit state $|\Psi\rangle$ belonging to the subspace generated by the $n = \binom{N}{k}$ bitstrings of Hamming weight k, denoted $|\phi_1\rangle, ..., |\phi_n\rangle$ here. $|\Psi\rangle$ can then be decomposed as

$$|\Psi\rangle = \sum_{m=1}^{n} c_m |\phi_m\rangle. \tag{D.1}$$

For simplicity, the c_i coefficients are supposed to be real in the following, but this can be adapted to the case where there are complex numbers. Then, $|\Psi\rangle$ is fully determined by $n-1$ parameters (dimension of the subspace considered, minus 1 for the normalization).

This appendix describes a procedure to build a quantum circuit exactly preparing $|\Psi\rangle$. It starts with the state $|1...10...0\rangle$ made from the initial state $|0...0\rangle$ by applying X gates on the k first qubits. Then it assembles a minimal number (hence $n-1$) of 2-qubit rotations $Q_i(\theta)$ controlled by other qubits, in order to build a N-qubit unitary U such that $|\Psi\rangle = U|1...10...0\rangle$. For $i \in \{1, ..., N-1\}$, the rotation $Q_i(\theta)$ acts on qubits i and $i+1$ and can be represented as

$$Q_i(\theta) = \begin{pmatrix} 1 & 0 & 0 & 0 \\ 0 & \cos(\theta) & -\sin(\theta) & 0 \\ 0 & \sin(\theta) & \cos(\theta) & 0 \\ 0 & 0 & 0 & 1 \end{pmatrix}_{i,i+1} =$$



. (D.2)

Defining a rooted tree To set up the quantum circuit corresponding to $|\Psi\rangle$, one first builds a rooted tree whose vertices are the $\binom{N}{k}$ states $|\phi_i\rangle$. The root is $|\phi_0\rangle = |1...10...0\rangle$. Then, the successors of each state $|\phi_i\rangle$ are the states $|\phi_j\rangle$ obtained with one excitation, *i.e.* the transformation of a '10' in the bitstring into a '01'. These excitations occur between neighbouring qubits, and it will be realized by the $Q_i(\theta)$ defined in Eq. (D.2). This results in an oriented graph but not a rooted tree : some vertices have several parents. One has to select only one parent of each vertex, and remove the other edges, in order to turn it into a rooted tree. Some examples are represented in Fig. D.1.

Building the circuit This rooted tree determines the placement of the controlled 2-qubit rotations. After having placed the k X gates in order to prepare the state $|\phi_0\rangle = |1...10...0\rangle$, one can consider the corresponding vertex on the tree, which is the root. The first edge links

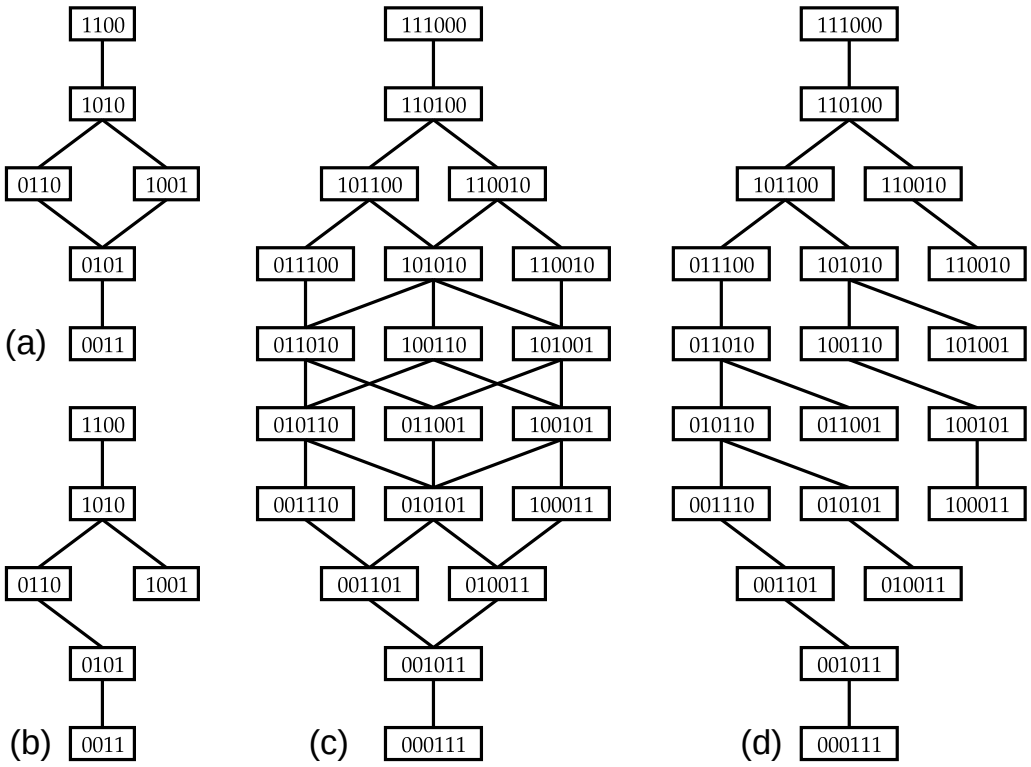
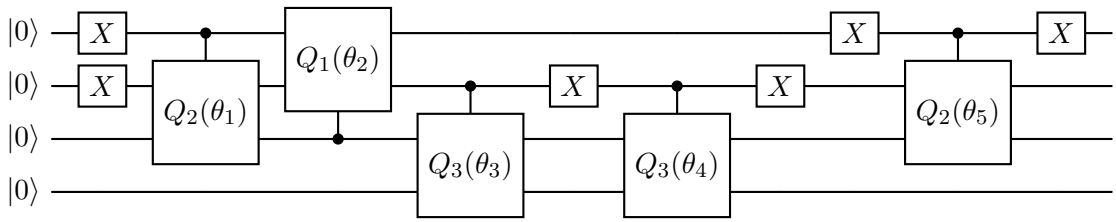


Figure D.1: *Examples of graphs (a,c) and rooted trees (b,d) corresponding to $N = 4, k = 2$ (a,b) and $N = 6, k = 3$ (c,d), used in the procedure described in the text. The graphs and trees are oriented from top to bottom.*

$|1...1100...0\rangle$ to $|1...1010...0\rangle$ so it corresponds to an excitation between qubits k and $k + 1$. Therefore, one can place a rotation $Q_k(\theta_1)$, where θ_1 will be determined later.

Similarly, for each edge of the rooted tree, there is a corresponding excitation between two qubits i and $i + 1$, hence a rotation $Q_i(\theta_m)$ to be placed on the quantum circuit. The placing order has to respect the partial order defined by the rooted tree. The purpose of this constraint is to easily determine the value of each angle, which is done in the following. There is an extra constraint for that: rotations have to be controlled by other qubits. More precisely, given a rotation $Q_i(\theta_m)$ corresponding to an edge on the tree between two vertices $|b_1...b_{i-1}10b_{i+2}...b_N\rangle$ and $|b_1...b_{i-1}01b_{i+2}...b_N\rangle$, one has to ensure that it will not affect another component $|b'_1...b'_{i-1}10b'_{i+2}...b'_N\rangle$ of the wavefunction. To this end, one can control $Q_i(\theta_m)$ by all other qubits except one, since the latter is fully determined by the others (because the Hamming weight is k). For each control qubit j, if $b_j = 0$, an X gate has to be placed before and after the control. An example with 4 qubits and a Hamming weight of 2, corresponding to the rooted tree (b) of Fig. D.1, is given below.



Fixing rotation angles The last step consists in fixing the angles. First, let us see how the amplitudes $c_1, ...c_n$ of the state $|\Psi\rangle$ generated by the circuit described in the previous step write as a function of the angles $\theta_1, ..., \theta_{n-1}$. By construction, $|\Psi\rangle$ is a combination of all the bitstring states $|\phi_m\rangle$ corresponding to the vertices of the rooted tree. Moreover, for each edge $|\phi_p\rangle \to |\phi_q\rangle$ of the tree, there is a rotation $Q_i(\theta_m)$ which assigns

- a $\sin(\theta_m)$ to the amplitudes associated to $|\phi_q\rangle$ and all its successors on the tree,
- a $\cos(\theta_m)$ to the amplitude(s) associated to $|\phi_p\rangle$ and eventually (if $|\phi_p\rangle$ has several direct successors) all its successors that are not $|\phi_q\rangle$ or the successors of the latter.

For instance, in the case $N = 4, k = 2$, one can follow this procedure with the rooted tree of Fig. D.1 (b) to get the following amplitudes

$$\begin{cases} c_1 = \cos(\theta_1) \\ c_2 = \sin(\theta_1)\cos(\theta_2)\cos(\theta_3) \\ c_3 = \sin(\theta_1)\sin(\theta_2)\cos(\theta_4) \\ c_4 = \sin(\theta_1)\cos(\theta_2)\sin(\theta_3) \\ c_5 = \sin(\theta_1)\sin(\theta_2)\sin(\theta_4)\cos(\theta_5) \\ c_6 = \sin(\theta_1)\sin(\theta_2)\sin(\theta_4)\sin(\theta_5) \end{cases} . \tag{D.3}$$

The resulting system of equations $\mathcal{S}$ can be solved easily to get the angles $\theta_1, ..., \theta_{n-1}$ as a function of the amplitudes $c_1, ...c_n$. One can use again the rooted tree to determine the angles one by one, starting from the root.

Let us consider a vertex $|\phi_p\rangle$ for which the angles corresponding to every previous edges on the tree have been fixed. Then, two situations can happen.

- If $|\phi_p\rangle$ has only one direct successor, one can fix the angle θ_m corresponding to the edge between $|\phi_p\rangle$ and its successor. In the system $\mathcal{S}$, there is an equation $c_p = \sin(\theta_1)...\sin(\theta_j)\cos(\theta_m)$ (where c_p is the amplitude associated to $|\phi_p\rangle$ in $|\Psi\rangle$) for which every angle $\theta_1...\theta_j$ has previously been fixed, so that θ_m can be determined. Then one can continue with the successor of $|\phi_p\rangle$.
- If $|\phi_p\rangle$ has several direct successors, one can choose one of them $|\phi_q\rangle$ and sum the squares of the equations corresponding to other branches (*i.e.* the successors of $|\phi_p\rangle$ that are neither $|\phi_q\rangle$ nor the successors of the latter). With the relation $\cos(\theta)^2 + \sin(\theta)^2 = 1$, simplifications occur so that one gets an equation with only one undetermined angle (the one corresponding to the edge between $|\phi_p\rangle$ and $|\phi_q\rangle$), which can then be determined. Then, one can continue with the successor(s) of $|\phi_q\rangle$ and the other successor(s) of $|\phi_p\rangle$.

Actually, at each step, one has to fix θ according to an equation of the form $\cos(\theta) = X$ or $\sin(\theta) = X$. This leads to two solutions to determine this angle: $\theta = \pm\arccos(X)$ in the first case, or $\theta = \arcsin(X)$ or $\pi - \arcsin(X)$ in the second. This ambiguity results in a sign which can be fixed using the equations corresponding to the vertices at the end of the branches.

For example, in the case $N = 4, k = 2$, the procedure is the following.

- The vertex $|1100\rangle$ (the root of the tree) has one successor $|1010\rangle$. Their edge corresponds to the angle θ_1 which can be fixed using the first equation of the system (D.3).
- The vertex $|1010\rangle$ has two successors. To determine the angle associated to the edge between $|1010\rangle$ and $|0110\rangle$, one sums the squares of the second and fourth equations in (D.3), leading to $c_2^2 + c_4^2 = \sin(\theta_1)^2\cos(\theta_2)^2$. Since θ_1 is already determined, θ_2 can be fixed.

- Before continuing with $|0110\rangle$, one can fix the angle θ_3 on the other branch, using the second equation of (D.3).
- The vertex $|0110\rangle$ has one successor $|0101\rangle$. The corresponding angle θ_4 can be fixed using the third equation of (D.3).
- Finally, the vertex $|0101\rangle$ has one successor $|0011\rangle$, and the corresponding angle θ_5 can be fixed using the fifth equation of (D.3).

This procedure has the advantage to be easily automatized. Moreover, it uses rotations between neighbouring qubits. However, these rotations come with controls by other qubits, that require chains of interactions involving nearly all the qubits. The qubit state obtained with this method encodes the exact state $|\Psi\rangle$. This procedure can only be used for small systems because it requires $\binom{N}{k} - 1$ parameters, which could be intractable with large values of N. With bigger systems, approximate ansätze such as the ones obtained by the methods described in chapter 3 should be preferred.

Appendix E

Calculation of the energy curve derivatives (6.13)

This appendix details the calculation of the energy curve derivatives (6.13) and establishes expression (6.14). To this purpose, commutators $[H_R, H]$ and $\big[H_R, [H_R, H]\big]$ between the resource Hamiltonian H_R and the pairing Hamiltonian H are explicited.

Preliminaries To simplify the derivation, let us define the operators

$$A_{ij} = \frac{1}{2}(X_iX_j + Y_iY_j),$$
$$B_{ij} = \frac{i}{2}(X_iY_j - Y_iX_j). \tag{E.1}$$

Together with the operators $\{Z_i\}_i$, they form a set that is stable under the action of the commutator. Their commutation relations are summarized in Tables E.1. Since they de-

	$[Z_k, A_{ij}]$	$[Z_k, B_{ij}]$
	0	0
	$-2B_{ij}$	$-2A_{ij}$
	$2B_{ij}$	$2A_{ij}$

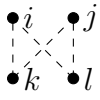
	$[A_{ij}, A_{kl}]$	$[A_{ij}, B_{kl}]$	$[B_{ij}, B_{kl}]$
	0	0	0
	Z_iB_{jl}	Z_iA_{jl}	Z_iB_{jl}
	Z_jB_{ik}	$-Z_jA_{ik}$	Z_jB_{ik}
	Z_iB_{jk}	$-Z_iA_{jk}$	$-Z_iB_{jk}$
	Z_jB_{il}	Z_jA_{il}	$-Z_jB_{il}$
	0	$Z_i - Z_j$	0
	0	$Z_j - Z_i$	0

Table E.1: *Some commutators with 3 indices (left) and 4 indices (right) that are used for the derivation of $[H_R, H]$ and $\big[H_R, [H_R, H]\big]$. The diagrams represent the different cases for the equality of indices, as explained in the text.*

pend on the equalities between indices, different index configurations have to be considered for each commutator. These configurations are indicated by diagrams, already used in appendix C.1, whose vertices represent indices which are connected when they are equal. These commutation relations are used for the derivation of $[H_R, H]$ and $\big[H_R, [H_R, H]\big]$, because the resource and pairing Hamiltonians can be written as a linear combination of the operators $\{Z_i\}_i$ and $\{A_{ij}\}_{ij}$ as

$$H_R = -\sum_{k=1}^{N} \delta_k \hat{n}_k + \sum\sum_{k<l} \gamma_{kl} A_{kl} \,, \tag{E.2}$$

$$H = \sum_{k=1}^{N} 2\epsilon_k \hat{n}_k - g \sum\sum_{k<l} \hat{A}_{kl} \,. \tag{E.3}$$

First derivative Using $\hat{n}_k = \frac{1}{2}(\mathbb{1} - Z)$, the commutator $[H_R, H]$ can be explicited as

$$\begin{aligned}
[H_R, H] &= \Big[-\sum_{i=1}^{N} \delta_i \hat{n}_i + \sum\sum_{i<j} \gamma_{ij} A_{ij} \,, \sum_{k=1}^{N} 2\epsilon_k \hat{n}_k - g \sum\sum_{k<l} A_{kl} \Big] \\
&= 0 + g \sum_{i=1}^{N} \sum\sum_{k<l} \delta_i [\hat{n}_i, A_{kl}] + \sum_{k=1}^{N} \sum\sum_{i<j} 2\epsilon_k \gamma_{ij} [A_{ij}, \hat{n}_k] \\
&\qquad - g \sum\sum_{i<j} \sum\sum_{k<l} \gamma_{ij} [A_{ij}, A_{kl}] \\
&= \sum_{k=1}^{N} \sum\sum_{i<j} (\epsilon_k \gamma_{ij} - \frac{g}{2} \delta_k) [Z_k, A_{ij}] - g \sum\sum_{i<j} \sum\sum_{k<l} \gamma_{ij} [A_{ij}, A_{kl}] \\
&= \sum\sum_{i<j} \Big(2(\epsilon_j - \epsilon_i)\gamma_{ij} - g(\delta_j - \delta_i) \Big) B_{ij} \\
&\qquad - g \sum\sum_{i<j} \gamma_{ij} \Big(\sum_{l>i} Z_i B_{jl} + \sum_{k<j} Z_j B_{ik} + \sum_{k<i} Z_i B_{jk} + \sum_{l>j} Z_j B_{il} \Big) \\
&= \sum\sum_{i<j} \Big(2(\epsilon_j - \epsilon_i)\gamma_{ij} - g(\delta_j - \delta_i) \Big) B_{ij} - g \sum\sum_{i<j} \gamma_{ij} \Big(Z_i \sum_{k \neq i} B_{jk} + Z_j \sum_{k \neq j} B_{ik} \Big) \\
&= \sum\sum_{i<j} \Big(\Delta_{ij} B_{ij} - g \gamma_{ij} \sum_{k \neq i,j} (Z_i B_{jk} + Z_j B_{ik}) \Big),
\end{aligned} \tag{E.4}$$

where $\Delta_{ij} = 2(\epsilon_j - \epsilon_i)\gamma_{ij} - g(\delta_j - \delta_i)$. A combination of operators of the form B or ZB is obtained. Since the expectation values of such operators on the state $|1...10...0\rangle$ are zero, $\frac{d}{dt}\big(E(t)\big)|_{t=0} = 0$.

Second derivative In the same way, many terms of $\big[H_R, [H_R, H]\big]$ have a zero expectation value on the state $|1...10...0\rangle$, so they can be ignored. The terms that give non-zero expectation values are the terms Z_i, Z_iZ_j, ... with only Z's factors, once simplified. They come from $[A_{ij}, B_{ij}] = Z_i - Z_j$ and $[A_{ij}, B_{ji}] = Z_j - Z_i$ (see Tables E.1). One should also care about the commutators $[A_{ij}, Z_m B_{kl}]$, but when $i, j \neq m$ or $i, j \neq k, l$ they reduce respectively to $Z_m[A_{ij}, B_{kl}]$ or $[A_{ij}, Z_m]B_{kl}$, and the other cases are, up to permutations of the indices, $[A_{ij}, Z_i B_{jk}] = A_{ik}$. All the other terms, which have a zero expectation values on $|1...10...0\rangle$, can be grouped into some operators denoted $\hat{\Omega}_1$ and $\hat{\Omega}_2$ here, which are not

explicited. This allows to simplify the expression of the second-order commutator as

$$\begin{aligned}\Big[H_R,[H_R,H]\Big] &= \sum_{i<j}\sum\Big(\Delta_{ij}[H_R,B_{ij}] - g\gamma_{ij}\sum_{k\neq i,j}[H_R,(Z_iB_{jk}+Z_jB_{ik})]\Big)\\ &= \hat{\Omega}_1 + \sum_{i<j}\sum\Big(\Delta_{ij}\sum_{p<q}\sum\gamma_{pq}[A_{pq},B_{ij}] - g\gamma_{ij}\sum_{k\neq i,j}\sum_{p<q}\sum\gamma_{pq}[A_{pq},(Z_iB_{jk}+Z_jB_{ik})]\Big)\\ &= \hat{\Omega}_2 + \sum_{i<j}\sum\gamma_{ij}\Big(\Delta_{ij}(Z_i-Z_j) - g\sum_{k\neq i,j}\big(Z_i\gamma_{jk}(Z_j-Z_k)+Z_j\gamma_{ik}(Z_i-Z_k)\big)\Big). \end{aligned} \tag{E.5}$$

To obtain $\frac{d^2}{dt^2}\Big(E(t)\Big)|_{t=0}$, the expectation value of this commutator on the initial state $|1...10...0\rangle$ has to be computed. The Hamming weight of this state is denoted p here, in order to write $\langle 1...10...0|Z_q|1...10...0\rangle = s_{qp}$ where s_{qp} is -1 if $q \leq p$ and 1 else. Therefore,

$$\begin{aligned}\frac{d^2}{dt^2}\Big(E(t)\Big)|_{t=0} &= -\sum_{i<j}\sum\gamma_{ij}\Big(\Delta_{ij}(s_{ip}-s_{jp}) - g\sum_{k\neq i,j}\big(s_{ip}\gamma_{jk}(s_{jp}-s_{kp})+s_{jp}\gamma_{ik}(s_{ip}-s_{kp})\big)\Big)\\ &= 2\sum_{i\leq p}\sum_{j>p}\gamma_{ij}\Delta_{ij} + g\sum_{i<j}\sum\gamma_{ij}\sum_{k\neq i,j}u_{ijkp}, \end{aligned} \tag{E.6}$$

where $u_{ijkp} = s_{ip}(s_{jp}-s_{kp})\gamma_{jk}+s_{jp}(s_{ip}-s_{kp})\gamma_{ik}$. This quantity can be written more explicitly by considering separately the 3 possible cases for the comparison of p with i and j.

- If $i<j\leq p$, then $s_{ip}=s_{jp}=-1$. Hence $u_{ijkp}=0$ if $k\leq p$, and $u_{ijkp}=2(\gamma_{ik}+\gamma_{jk})$ else. Therefore,
$$\sum_{k\neq i,j}u_{ijkp} = 2\sum_{k>p}(\gamma_{ik}+\gamma_{jk}). \tag{E.7}$$
- If $p<i<j$, one gets in the same way
$$\sum_{k\neq i,j}u_{ijkp} = 2\sum_{k\leq p}(\gamma_{ik}+\gamma_{jk}). \tag{E.8}$$
- Finally, if $i\leq p<j$,
$$\sum_{k\neq i,j}u_{ijkp} = -2\Big(\sum_{\substack{k\leq p\\ k\neq i}}\gamma_{jk}+\sum_{\substack{k>p\\ k\neq j}}\gamma_{ik}\Big). \tag{E.9}$$

Therefore, the second derivative of the energy curve writes as

$$\begin{aligned}\frac{d^2}{dt^2}\Big(E(t)\Big)|_{t=0} = 2\sum_{i\leq p}\sum_{j>p}\gamma_{ij}\Big(\Delta_{ij} - g\Big(\sum_{\substack{k\leq p\\ k\neq i}}\gamma_{jk}+\sum_{\substack{k>p\\ k\neq j}}\gamma_{ik}\Big)\Big)\\ + 2g\sum_{i<j\leq p}\sum\gamma_{ij}\sum_{k>p}(\gamma_{ik}+\gamma_{jk}) + 2g\sum_{p<i<j}\sum\gamma_{ij}\sum_{k\leq p}(\gamma_{ik}+\gamma_{jk}). \end{aligned} \tag{E.10}$$

Inequality (6.14) The detunings are hidden in the term $\Delta_{ij} = 2(\epsilon_j-\epsilon_i)\gamma_{ij} - g(\delta_j-\delta_i)$. The condition $\frac{d^2}{dt^2}\Big(E(t)\Big)|_{t=0}\leq 0$ can then be written as

$$\sum_{i\leq p}\sum_{j>p}\gamma_{ij}(\delta_j-\delta_i) \geq F(\{\gamma_{ij}\}_{ij}), \tag{E.11}$$

where

$$F(\{\gamma_{ij}\}_{ij}) = \sum_{i\leq p}\sum_{j>p}\gamma_{ij}\Big(2\gamma_{ij}\frac{\epsilon_j-\epsilon_i}{g} - \sum_{\substack{k\leq p\\k\neq i}}\gamma_{jk} - \sum_{\substack{k>p\\k\neq j}}\gamma_{ik}\Big) + \sum_{i<j\leq p}\sum\gamma_{ij}\sum_{k>p}(\gamma_{ik}+\gamma_{jk}) + \sum_{p<i<j}\sum\gamma_{ij}\sum_{k\leq p}(\gamma_{ik}+\gamma_{jk}). \tag{E.12}$$

Defining the vectors

$$\vec{\delta} = \Big(\delta_1, ..., \delta_N\Big), \tag{E.13}$$

$$\vec{V} = \Big(-\sum_{j>p}\gamma_{1j},\ ...,\ -\sum_{j>p}\gamma_{pj},\ \sum_{i\leq p}\gamma_{i,p+1},\ ...,\ \sum_{i\leq p}\gamma_{iN}\Big), \tag{E.14}$$

this condition can be rewritten as

$$\vec{\delta}\cdot\vec{V} \geq F(\{\gamma_{ij}\}_{ij}). \tag{E.15}$$

Appendix F

Some other derivations required in chapter 6

F.1 Effect of qubit-qubit interaction during the state preparation with SLM mask in the 2-qubit case

During the π-pulse used with SLM mask in section 6.1 in order to prepare a state with a given Hamming weight, the qubit-qubit interaction distorts the pulse. As a result, the probability to measure the system in the selected Hamming-weight subspace does not exactly reach 1. This effect has been neglected in section 6.1, but it can be evaluated in a simple case (2 qubits and a constant pulse) with a straightforward derivation. This derivation is detailed here in order to determine the probability to get the system in the Hamming-weight-1 subspace when using the SLM mask to prepare the state $|10\rangle$ from the state $|00\rangle$.

Let us consider two qubits initially in the state $|00\rangle$ and evolved under a constant pulse with Rabi frequency Ω, no detuning, and the SLM mask hiding the second qubit. In absence of interaction, the resource Hamiltonian and the corresponding evolved state write as

$$\frac{1}{\hbar}H_R = \frac{\Omega}{2}X_1\ , \qquad |\Psi(t)\rangle = e^{-i\frac{\Omega t}{2}X_1}|00\rangle = \cos\Big(\frac{\Omega t}{2}\Big)|00\rangle - i\sin\Big(\frac{\Omega t}{2}\Big)|10\rangle. \tag{F.1}$$

Therefore, the state $|10\rangle$ is reached when Ωt is an integer multiple of π. Taking into account the qubit-qubit interaction in the XY mode, a term $\frac{C_3}{2\hbar r^3}(X_1X_2 + Y_1Y_2)$ has to be added, where r is the distance between the two atoms. The resulting resource Hamiltonian, and the corresponding matrix in the basis $\{|00\rangle, |01\rangle, |10\rangle, |11\rangle\}$, can be written as

$$\frac{1}{\hbar}H_R = \frac{\Omega}{2}\Big(X_1 + a(X_1X_2 + Y_1Y_2)\Big) = \frac{\Omega}{2}\begin{pmatrix} 0 & 0 & 1 & 0 \\ 0 & 0 & 2a & 1 \\ 1 & 2a & 0 & 0 \\ 0 & 1 & 0 & 0 \end{pmatrix}, \tag{F.2}$$

where $a = \frac{C_3}{\Omega\hbar r^3}$. Its characteristic polynomial $X^4 - 2(1+2a^2)X^2 + 1$ (up to the factor $\frac{\Omega}{2}$) is biquadratic, hence this operator can be diagonalized without the emergence of huge expressions that usually appear with the resolution of a general quartic equation. The corresponding roots are, in ascending order, $-\lambda_+, \lambda_-, -\lambda_-, \lambda_+$, where

$$\lambda_\pm = a \pm \sqrt{1+a^2}. \tag{F.3}$$

Thereby, the diagonalization of Hamiltonian (F.2) leads to $\frac{1}{\hbar}H_R = \frac{\Omega}{2}PDP^T$ with

$$D = \begin{pmatrix} -\lambda_+ & 0 & 0 & 0 \\ 0 & \lambda_- & 0 & 0 \\ 0 & 0 & -\lambda_- & 0 \\ 0 & 0 & 0 & \lambda_+ \end{pmatrix} \quad \text{and} \quad P = \begin{pmatrix} -u_+ & u_- & -u_- & u_+ \\ -\lambda_+ u_+ & \lambda_- u_- & -\lambda_- u_- & \lambda_+ u_+ \\ \lambda_+ u_+ & \lambda_- u_- & \lambda_- u_- & \lambda_+ u_+ \\ u_+ & u_- & u_- & u_+ \end{pmatrix}, \tag{F.4}$$

where $u_\pm = 1/\sqrt{2+2\lambda_\pm}$.

This allows to compute the evolution operator as $e^{-i\frac{t}{\hbar}H_R} = Pe^{-i\frac{\Omega t}{2}D}P^T$. Performing the matrix product and arranging the resulting coefficients leads to

$$e^{-i\frac{t}{\hbar}H_R} = \begin{pmatrix} cC + \frac{a}{\sqrt{1+a^2}}sS & -\frac{1}{\sqrt{1+a^2}}sS & -\frac{i}{\sqrt{1+a^2}}cS & -i\big(sC - \frac{a}{\sqrt{1+a^2}}cS\big) \\ -\frac{1}{\sqrt{1+a^2}}sS & cC - \frac{a}{\sqrt{1+a^2}}sS & -i\big(sC + \frac{a}{\sqrt{1+a^2}}cS\big) & -\frac{i}{\sqrt{1+a^2}}cS \\ -\frac{i}{\sqrt{1+a^2}}cS & -i\big(sC + \frac{a}{\sqrt{1+a^2}}cS\big) & cC - \frac{a}{\sqrt{1+a^2}}sS & -\frac{1}{\sqrt{1+a^2}}sS \\ -i\big(sC - \frac{a}{\sqrt{1+a^2}}cS\big) & -\frac{i}{\sqrt{1+a^2}}cS & -\frac{1}{\sqrt{1+a^2}}sS & cC + \frac{a}{\sqrt{1+a^2}}sS \end{pmatrix}, \tag{F.5}$$

where the notations $C = \cos\big(\sqrt{1+a^2}\frac{\Omega t}{2}\big)$, $S = \sin\big(\sqrt{1+a^2}\frac{\Omega t}{2}\big)$, $c = \cos\big(a\frac{\Omega t}{2}\big)$, $s = \sin\big(a\frac{\Omega t}{2}\big)$ have been used for clarity. Hence, the 2-qubit state evolves as

$$e^{-i\frac{t}{\hbar}H_R}|00\rangle = \big(cC + \tfrac{a}{\sqrt{1+a^2}}sS\big)|00\rangle - \tfrac{1}{\sqrt{1+a^2}}S\big(s|01\rangle - ic|10\rangle\big) - i\big(sC - \tfrac{a}{\sqrt{1+a^2}}cS\big)|11\rangle. \tag{F.6}$$

One can check that, with $a = 0$, the expression of Eq. (F.1) is recovered as expected. For a general value of a, the probability to measure the qubits in the hamming-weight-1 subspace at a given time t writes as

$$p_{01} + p_{10} = \frac{1}{1+a^2}S^2 = \frac{1}{1+a^2}\sin\Big(\sqrt{1+a^2}\frac{\Omega t}{2}\Big)^2. \tag{F.7}$$

This is represented as a function of $\Omega t/\pi$ in Fig. F.1. The maximal value of this probability is $\frac{1}{1+a^2}$, reached when Ωt is an odd multiple of $\frac{\pi}{\sqrt{1+a^2}}$.

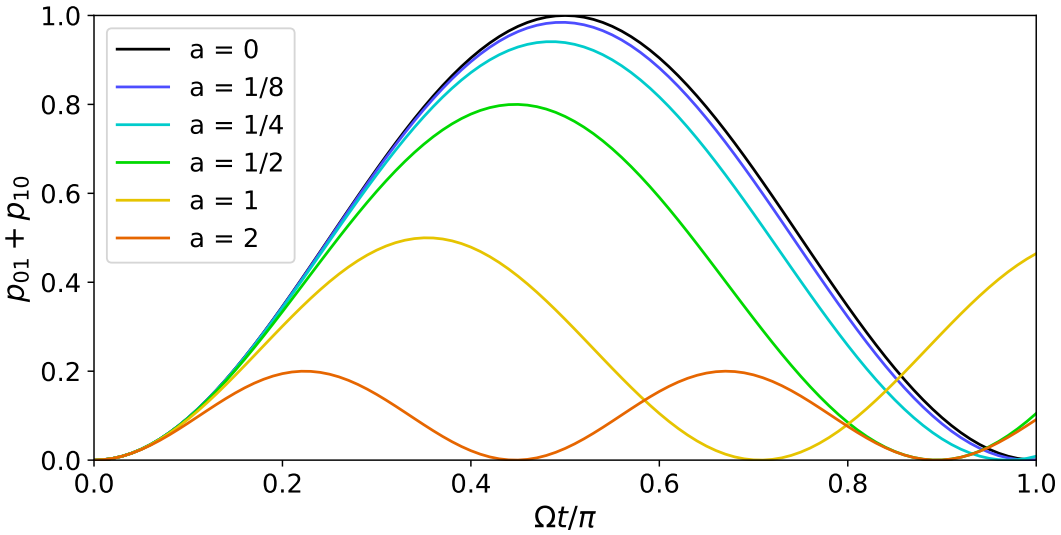


Figure F.1: *Evolution of the probability $p_{01} + p_{10}$ to measure the two qubits in the Hamming-weight-1 subspace, with the method described in the text. This probability, expressed in Eq. (F.7), is represented here as a function of $\Omega t/\pi$, for several values of the quotient $a = \frac{C_3}{\Omega\hbar r^3}$.*

Therefore, the 2-qubit state cannot be exactly prepared in the subspace with Hamming weight 1 using this method, when $a \neq 0$. With $C_3/\hbar = 3700\ \mu m^3/\mu s$ (value used for the *MockDevice* in Pulser), and the typical values $r = 10\ \mu m$ and $\Omega = \frac{\pi}{0.2\ \mu s}$ (for a π-pulse with 200 ns duration) used in section 6.1, one gets $a \approx 1/4$, which corresponds to $\frac{1}{1+a^2} \approx 0.94$. The resulting 6 % of undesired measurements outcomes with the wrong Hamming weight (00 or 11) can simply be filtered out, so that this effect is not an issue.

F.2 Impossibility to evaluate some observables with global basis rotations

In section 6.2.1, it has been claimed that an observable of the form $aXZ + bZX$ with $a \neq b$ cannot be evaluated when the basis rotations are performed by global pulses, *i.e.* are of the form $U \otimes U$ where U is a given 1-qubit unitary. This claim is justified here.

If $a \neq b$, then

$$XZ = \frac{1}{a-b}\big(aXZ + bZX\big) - \frac{b}{a-b}\big(XZ + ZX\big). \tag{F.8}$$

Hence, since $XZ+ZX$ can be evaluated, it is sufficient to show that XZ cannot be evaluated. Let us suppose this is actually the case, and get a contradiction. In this case, $XZ = X \otimes Z$ can be obtained from a combination of observables $O_1, ..., O_m \in \{\mathbb{1}\otimes\mathbb{1}, Z\otimes\mathbb{1}, \mathbb{1}\otimes Z, Z\otimes Z\}$ on which are performed some basis rotations $U_1 \otimes U_1, ..., U_m \otimes U_m$. This provides coefficients $\alpha_1, ..., \alpha_m$ such that

$$X \otimes Z = \sum_{i=1}^{m} \alpha_i (U_i \otimes U_i)^\dagger O_i (U_i \otimes U_i). \tag{F.9}$$

With the subsets of indices $\mathcal{S}_{00}, \mathcal{S}_{10}, \mathcal{S}_{01}, \mathcal{S}_{11}$ defined by $\mathcal{S}_{ab} = \{i \in \{1, ..., m\} / O_i = Z^a \otimes Z^b\}$, and using $U_i^\dagger \mathbb{1} U_i = \mathbb{1}$, this can be rewritten as

$$X\otimes Z = \sum_{i\in\mathcal{S}_{00}} \alpha_i \mathbb{1}\otimes\mathbb{1} + \sum_{i\in\mathcal{S}_{10}} \alpha_i U_i^\dagger Z U_i \otimes \mathbb{1} + \sum_{i\in\mathcal{S}_{01}} \alpha_i \mathbb{1}\otimes U_i^\dagger Z U_i + \sum_{i\in\mathcal{S}_{11}} \alpha_i U_i^\dagger Z U_i \otimes U_i^\dagger Z U_i\,. \tag{F.10}$$

Let us decompose the 1-qubit observable $U_i^\dagger Z U_i$ in the Pauli basis as $U_i^\dagger Z U_i = a\mathbb{1} + bX + cY + dZ$. Since $\mathrm{Tr}(U_i^\dagger Z U_i) = \mathrm{Tr}(Z) = 0$, and X, Y, Z are also traceless, the trace of this decomposition gives $a = 0$. Hence, the fourth term in Eq. (F.10) is a combination of Pauli strings with no $\mathbb{1}$'s. Since the Pauli strings composing the three first terms all contain $\mathbb{1}$'s and Pauli strings are linearly independent, these three terms cancel, resulting in

$$X \otimes Z = \sum_{i\in\mathcal{S}_{11}} \alpha_i U_i^\dagger Z U_i \otimes U_i^\dagger Z U_i\,. \tag{F.11}$$

Here is the contradiction: the right part of this equation is symmetric with respect to the exchange of the two qubits, while the left part is not.

Appendix G

Synthèse en français

De nombreux systèmes physiques peuvent être décrits comme des ensembles de particules en interaction, soumises à des effets quantiques. C'est le cas, par exemple, d'électrons dans les solides, atomes, ou molécules, de spins dans des systèmes magnétiques, ... et également des nucléons dans un noyau atomique, ce qui constitue la motivation de cette thèse. Leur description est connue sous le nom de problème à N corps. La résolution exacte de ce dernier se heurte à la croissance exponentielle des ressources de calcul nécessaires avec le nombre de degrés de liberté considérés, limitant les connaissances sur ces systèmes.

Parmi les développements menés pour aborder ce problème et repousser les limites actuelles, le calcul quantique représente une piste prometteuse. En utilisant les propriétés de systèmes quantiques pour réaliser des tâches de calcul spécifiques, celui-ci a le potentiel de dépasser le calcul classique pour de nombreuses applications, comme la factorisation, la recherche de données, l'optimisation, ou la simulation de systèmes à N corps. Cette thèse explore l'application du calcul quantique au problème à N corps nucléaire. Elle se focalise en particulier sur les algorithmes quantiques variationnels, des algorithmes hybrides classique-quantique plus résilients face aux erreurs que leurs homologues purement quantiques, ce qui les rend particulièrement intéressants pour aborder le problème à N corps avec les plateformes quantiques actuellement disponibles. Les approches digitales et analogiques sont toutes deux considérées dans cette thèse.

Les deux premiers chapitres introduisent les notions nécessaires à la compréhension de cette thèse, de son contexte, et de ses objectifs. Le **premier** présente le problème à N corps nucléaire. Il donne quelques bases de formalisme sur le problème à N corps, ainsi qu'une rapide vue d'ensemble de la description théorique des systèmes nucléaire. Les fonctions de Green, qui sont utilisées dans la suite, sont introduites et définies dans le contexte des méthodes ab initio de fonctions de Green auto-cohérentes. Ce chapitre s'achève avec la présentation de deux modèles d'intérêt pour la physique nucléaire, le modèle de pairing (modèle de Richardson) et un modèle simple du deutéron, en vue de leur utilisation comme modèles tests pour les méthodes développées dans les chapitres suivants.

Le **second chapitre** introduit les briques élémentaires du calcul quantique digital : qubits, opérations unitaires, circuits quantique, mesure. Deux exemples d'algorithmes quantiques sont décrits pour illustrer le potentiel avantage des ordinateurs quantiques sur les ordinateurs classiques pour certaines tâches spécifiques. Ensuite, la stratégie utilisée dans la suite pour encoder le problème à N corps sur des qubits est introduite et appliquée aux deux modèles présentés dans le chapitre précédent.

Cette stratégie est combinée dans le **troisième chapitre** avec des algorithmes quantiques variationnels afin d'approcher de l'état fondamental d'un système à N corps. Plusieurs procédures, basées sur la méthode Adaptive Derivative-Assembled Pseudo-Trotter ansatz Variational Quantum Eigensolver (ADAPT-VQE), sont définies. Leurs performances sont testées et comparées en simulation sur le modèle de pairing. Les états fondamentaux approchés ainsi obtenus et encodés sur des qubits, sont utilisés dans le **quatrième chapitre** comme base d'une méthode hybride classique-quantique dédiée au calcul des fonctions de Green. Là encore, cette procédure est simulée et évaluée avec le modèle de pairing. Une analyse quantitative du nombre de mesures quantiques à effectuer est détaillée.

Ces résultats ont été obtenus sur des émulateurs d'ordinateurs quantiques digitaux supposés parfaits, sans bruit. Cependant, les ordinateurs quantiques actuels sont bruités, ce qui limite leurs performances. Une grande variété de technologies quantiques est développée pour attaquer ce problème, et parmi elles, certaines sont plus adaptées à l'approche analogique. C'est le cas en particulier des ordinateurs quantiques à atomes neutres. Une telle machine, nommée Ruby, a récemment été livrée au *Commissariat à l'énergie atomique et aux énergies alternatives* (CEA) par l'entreprise Pasqal. La deuxième partie de cette thèse explore la possibilité de l'appliquer au problème à N corps nucléaire.

La machine Ruby est naturellement adaptée pour étudier les systèmes physiques décrits par un Hamiltonien qu'elle peut réaliser. C'est le cas par exemple pour le modèle d'Ising, mais cela ne s'applique pas à la grande diversité des systèmes en physique nucléaire. Les méthodes variationnelles ont été choisies ici parce qu'elles ne nécessitent pas de réaliser le Hamiltonien du système étudié sur la machine. Après quelques précisions sur l'approche analogique, le **cinquième chapitre** présente la technologie des atomes neutres en se focalisant sur Ruby, puis il détaille les différents obstacles et limitations identifiés lors de cette thèse pour son utilisation avec des procédures variationnelles.

Plusieurs méthodes sont présentées dans le **sixième chapitre** pour contourner ces difficultés. Deux scénarios ont été étudiés, l'un considérant la machine Ruby dans son état actuel, l'autre considérant une amélioration de celle-ci plausible dans un futur proche. Ce scénario futuriste est tout d'abord examiné pour mettre en place une procédure variationnelle qui prend en compte la fixation du nombre de particules, en restreignant l'exploration de l'espace des états de qubits à un sous-espace de poids de Hamming fixé. La méthode obtenue est simulée, montrant que si elle converge bien lorsque le poids de Hamming vaut 1 (un cas pour lequel il n'y a pas d'avantage quantique), l'état fondamental semble inatteignable dans le cas général. Une autre approche est utilisée dans le scénario correspondant à la machine Ruby actuelle : un encodage alternatif du système étudié sur des qubits permet de résoudre plusieurs difficultés relevées dans le chapitre précédent. En commençant par un cas simple du deutéron encodé sur deux qubits, un protocole est mis en place pour calculer son état fondamental, prêt à être testé sur la machine Ruby actuelle.

Bibliography

[1] HQI contributors. *HQI website*. url: https://www.hqi.fr/ (visited on 08/03/2026).

[2] Pasqal contributors. *Pasqal website*. url: https://www.pasqal.com/fr/ (visited on 08/03/2026).

[3] CEA DAM. *TGCC - Très Grand Centre de Calcul du CEA*. url: https://www-hpc.cea.fr/en/TGCC.html (visited on 07/07/2026).

[4] Harper R. Grimsley et al. "An adaptive variational algorithm for exact molecular simulations on a quantum computer". In: *Nature Communications* 10.1 (2019). doi: 10.1038/s41467-019-10988-2.

[5] J. C. Slater. "The Theory of Complex Spectra". In: *Phys. Rev.* 34 (1929), pp. 1293–1322. doi: 10.1103/PhysRev.34.1293.

[6] G. C. Wick. "The Evaluation of the Collision Matrix". In: *Phys. Rev.* 80 (1950), pp. 268–272. doi: 10.1103/PhysRev.80.268.

[7] Brookhaven National Laboratory. *National Nuclear Data Center*. url: https://www.nndc.bnl.gov/nudat3/ (visited on 05/20/2026).

[8] Vittorio Somà. "From the liquid drop model to lattice QCD". In: *The European Physical Journal Plus* 133 (2018), p. 434. doi: 10.1140/epjp/i2018-12244-2.

[9] Peter Schuck Peter Ring. *The Nuclear Many-Body Problem*. Springer Berlin, Heidelberg, 2004.

[10] G. Gamow. "Mass defect curve and nuclear constitution". In: *Proceedings of the Royal Society of London. Series A, Containing Papers of a Mathematical and Physical Character* 126.803 (1930), pp. 632–644. doi: 10.1098/rspa.1930.0032.

[11] C. F. v. Weizsäcker. "Zur Theorie der Kernmassen". In: *Zeitschrift für Physik* 96 (1935), pp. 431–458. doi: 10.1007/BF01337700.

[12] Maria Goeppert-Mayer. "On Closed Shells in Nuclei. II". In: *Phys. Rev.* 75 (1949), pp. 1969–1970. doi: 10.1103/PhysRev.75.1969.

[13] Otto Haxel, J. Hans D. Jensen, and Hans E. Suess. "On the "Magic Numbers" in Nuclear Structure". In: *Phys. Rev.* 75 (1949), p. 1766. doi: 10.1103/PhysRev.75.1766.2.

[14] E. Caurier et al. "The shell model as a unified view of nuclear structure". In: *Rev. Mod. Phys.* 77 (2005), pp. 427–488. doi: 10.1103/RevModPhys.77.427.

[15] S.K. Bogner, R.J. Furnstahl, and A. Schwenk. “From low-momentum interactions to nuclear structure”. In: *Progress in Particle and Nuclear Physics* 65.1 (2010), pp. 94–147. doi: https://doi.org/10.1016/j.ppnp.2010.03.001.

[16] Heiko Hergert. “A Guided Tour of ab initio Nuclear Many-Body Theory”. In: *Frontiers in Physics* Volume 8 (2020). doi: 10.3389/fphy.2020.00379.

[17] A. Ekström et al. “What is ab initio in nuclear theory?” In: *Frontiers in Physics* Volume 11 (2023). doi: 10.3389/fphy.2023.1129094.

[18] Pierre Arthuis. “Bogoliubov Many-Body Perturbation Theory for Nuclei: Systematic Generation and Evaluation of Diagrams and First ab initio Calculations”. https://theses.hal.science/tel-01992165. Theses. *Université Paris-Saclay*, (2018).

[19] K. Tsukiyama, S. K. Bogner, and A. Schwenk. “In-Medium Similarity Renormalization Group For Nuclei”. In: *Phys. Rev. Lett.* 106 (2011), p. 222502. doi: 10.1103/PhysRevLett.106.222502.

[20] H. Hergert et al. “The In-Medium Similarity Renormalization Group: A novel ab initio method for nuclei”. In: *Physics Reports* 621 (2016). Memorial Volume in Honor of Gerald E. Brown, pp. 165–222. doi: 10.1016/j.physrep.2015.12.007.

[21] K. Kowalski et al. “Coupled Cluster Calculations of Ground and Excited States of Nuclei”. In: *Phys. Rev. Lett.* 92 (2004), p. 132501. doi: 10.1103/PhysRevLett.92.132501.

[22] G Hagen et al. “Coupled-cluster computations of atomic nuclei”. In: *Reports on Progress in Physics* 77.9 (2014). doi: 10.1088/0034-4885/77/9/096302.

[23] W.H. Dickhoff and C. Barbieri. “Self-consistent Green’s function method for nuclei and nuclear matter”. In: *Progress in Particle and Nuclear Physics* 52.2 (2004), pp. 377–496. doi: 10.1016/j.ppnp.2004.02.038.

[24] T. Duguet et al. “Ab initio calculation of the potential bubble nucleus ^{34}Si”. In: *Phys. Rev. C* 95 (2017), p. 034319. doi: 10.1103/PhysRevC.95.034319.

[25] Arnau Rios. “Green’s Function Techniques for Infinite Nuclear Systems”. In: *Frontiers in Physics* Volume 8 (2020). doi: 10.3389/fphy.2020.00387.

[26] Baishan Hu et al. “Ab initio predictions link the neutron skin of ^{208}Pb to nuclear forces”. In: *Nature Phys.* 18.10 (2022), pp. 1196–1200. doi: 10.1038/s41567-022-01715-8.

[27] Francesca Bonaiti, Gaute Hagen, and Thomas Papenbrock. “Structure of the doubly magic nuclei ^{208}Pb and ^{266}Pb from ab initio computations”. (2025). arXiv: 2508.14217 [nucl-th].

[28] S. K. Bogner et al. “Nonperturbative Shell-Model Interactions from the In-Medium Similarity Renormalization Group”. In: *Phys. Rev. Lett.* 113 (2014), p. 142501. doi: 10.1103/PhysRevLett.113.142501.

[29] G. R. Jansen et al. “Ab Initio Coupled-Cluster Effective Interactions for the Shell Model: Application to Neutron-Rich Oxygen and Carbon Isotopes”. In: *Phys. Rev. Lett.* 113 (2014), p. 142502. doi: 10.1103/PhysRevLett.113.142502.

[30] Michael Bender, Paul-Henri Heenen, and Paul-Gerhard Reinhard. “Self-consistent mean-field models for nuclear structure”. In: *Rev. Mod. Phys.* 75 (2003), pp. 121–180. doi: 10.1103/RevModPhys.75.121.

[31] George Green. “An Essay on the Application of mathematical Analysis to the theories of Electricity and Magnetism”. (1828). arXiv: 0807.0088 [physics.hist-ph].

[32] Vittorio Somà. “Self-Consistent Green’s Function Theory for Atomic Nuclei”. In: *Frontiers in Physics* Volume 8 (2020). doi: 10.3389/fphy.2020.00340.

[33] J. Bardeen, L. N. Cooper, and J. R. Schrieffer. “Microscopic Theory of Superconductivity”. In: *Phys. Rev.* 106 (1957), pp. 162–164. doi: 10.1103/PhysRev.106.162.

[34] R.W. Richardson and N. Sherman. “Pairing models of Pb206, Pb204 and Pb202”. In: *Nuclear Physics* 52 (1964), pp. 253–268. doi: 10.1016/0029-5582(64)90690-X.

[35] D. M. Brink and R. A. Broglia. *Nuclear Superfluidity: Pairing in Finite Systems*. Cambridge University Press, 2005.

[36] V. Zelevinsky and A. Volya. “Nuclear pairing: New perspectives”. In: *Physics of Atomic Nuclei* 66 (2003), pp. 1781–1801. doi: 10.1134/1.1619492.

[37] T Duguet. “Symmetry broken and restored coupled-cluster theory: I. Rotational symmetry and angular momentum”. In: *Journal of Physics G: Nuclear and Particle Physics* 42.2 (2014), p. 025107. doi: 10.1088/0954-3899/42/2/025107.

[38] T Duguet and A Signoracci. “Symmetry broken and restored coupled-cluster theory: II. Global gauge symmetry and particle number”. In: *Journal of Physics G: Nuclear and Particle Physics* 44.1 (2016), p. 015103. doi: 10.1088/0954-3899/44/1/015103.

[39] V Somà, T Duguet, and C Barbieri. “Gorkov self-consistent Green’s function calculations of semi-magic nuclei”. In: *Journal of Physics: Conference Series* 321.1 (2011), p. 012039. doi: 10.1088/1742-6596/321/1/012039.

[40] Thomas M. Henderson et al. “Quasiparticle coupled cluster theory for pairing interactions”. In: *Phys. Rev. C* 89 (2014), p. 054305. doi: 10.1103/PhysRevC.89.054305.

[41] Y. Qiu et al. “Particle-number projected Bogoliubov-coupled-cluster theory: Application to the pairing Hamiltonian”. In: *Phys. Rev. C* 99 (2019), p. 044301. doi: 10.1103/PhysRevC.99.044301.

[42] J A Sheikh et al. “Symmetry restoration in mean-field approaches”. In: *Journal of Physics G: Nuclear and Particle Physics* 48.12 (2021), p. 123001. doi: 10.1088/1361-6471/ac288a.

[43] Edgar Andres Ruiz Guzman. “Symmetry breaking and restoration for many-body problems treated on quantum computers”. Theses. *Université Paris-Saclay*, (2023). arXiv: 2310.17996 [quant-ph].

[44] E. F. Dumitrescu et al. “Cloud Quantum Computing of an Atomic Nucleus”. In: *Phys. Rev. Lett.* 120 (2018), p. 210501. doi: 10.1103/PhysRevLett.120.210501.

[45] Michael A. Nielsen and Isaac L. Chuang. *Quantum Computation and Quantum Information: 10th Anniversary Edition*. Cambridge University Press, 2010.

[46] Thomas Ayral et al. “Quantum computing with and for many-body physics”. In: *The European Physical Journal A* 59 (2023). doi: 10.1140/epja/s10050-023-01141-1.

[47] Richard Jozsa and Noah Linden. “On the role of entanglement in quantum-computational speed-up”. In: *Proceedings of the Royal Society of London. Series A: Mathematical, Physical and Engineering Sciences* 459.2036 (2003), pp. 2011–2032. doi: 10.1098/rspa.2002.1097.

[48] Daniel Gottesman. “The Heisenberg Representation of Quantum Computers”. (1998). arXiv: quant-ph/9807006 [quant-ph].

[49] Adriano Barenco et al. “Elementary gates for quantum computation”. In: *Phys. Rev. A* 52 (1995), pp. 3457–3467. doi: 10.1103/PhysRevA.52.3457.

[50] A. Yu. Kitaev. “Quantum computations: algorithms and error correction”. In: *Russian Math. Surveys* 52 (1997), pp. 1191–1249. doi: 10.1070/RM1997v052n06ABEH002155.

[51] Christopher M. Dawson and Michael Nielsen. “The Solovay-Kitaev algorithm”. In: *Quantum Information and Computation* 6 (2006), pp. 81–95. doi: 10.26421/QIC6.1-6.

[52] Hsin-Yuan Huang, Richard Kueng, and John Preskill. “Predicting many properties of a quantum system from very few measurements”. In: *Nature Physics* 16 (2020), pp. 1050–1057. doi: 10.1038/s41567-020-0932-7.

[53] Hsin-Yuan Huang, Richard Kueng, and John Preskill. “Efficient Estimation of Pauli Observables by Derandomization”. In: *Phys. Rev. Lett.* 127 (2021), p. 030503. doi: 10.1103/PhysRevLett.127.030503.

[54] Peter W. Shor. “Polynomial-Time Algorithms for Prime Factorization and Discrete Logarithms on a Quantum Computer”. In: *SIAM Journal on Computing* 26.5 (1997), pp. 1484–1509. doi: 10.1137/S0097539795293172.

[55] A. Yu. Kitaev. “Quantum measurements and the Abelian Stabilizer Problem”. (1995). arXiv: quant-ph/9511026 [quant-ph].

[56] H. F. Trotter. “On the Product of Semi-Groups of Operators”. In: *Proceedings of the American Mathematical Society* 10.4 (1959), pp. 545–551. doi: 10.2307/2033649.

[57] Richard P. Feynman. “Simulating physics with computers”. In: *International Journal of Theoretical Physics* 21 (1982), pp. 467–488. doi: 10.1007/BF02650179.

[58] Nicolas P. D. Sawaya et al. “Resource-efficient digital quantum simulation of d-level systems for photonic, vibrational, and spin-s Hamiltonians”. In: *npj Quantum Information* 6.49 (2020). doi: 10.1038/s41534-020-0278-0.

[59] P. Jordan and E. Wigner. “Über das Paulische Äquivalenzverbot”. In: *Zeitschrift für Physik* 47 (1928), pp. 631–635. doi: 10.1007/BF01331938.

[60] Vincent E. Elfving et al. “Simulating quantum chemistry in the seniority-zero space on qubit-based quantum computers”. In: *Phys. Rev. A* 103 (2021), p. 032605. doi: 10.1103/PhysRevA.103.032605.

[61] Sergey B. Bravyi and Alexei Yu. Kitaev. “Fermionic Quantum Computation”. In: *Annals of Physics* 298 (2002), pp. 210–226. doi: 10.1006/aphy.2002.6254.

[62] Isaac Hobday, Paul D. Stevenson, and James Benstead. “Quantum computing calculations for nuclear structure and nuclear data”. In: *Quantum Technologies 2022*. Ed. by Eleni Diamanti et al. Vol. 12133. International Society for Optics and Photonics. SPIE, 2022, 121330J. doi: 10.1117/12.2632782.

[63] Thomas Ayral et al. “Topical issue on quantum computing in low-energy nuclear theory”. In: *The European Physical Journal A* 61 (2025). doi: 10.1140/epja/s10050-025-01575-9.

[64] A. Pérez-Obiol et al. “Nuclear shell-model simulation in digital quantum computers”. In: *Scientific Reports* 13 (2023). doi: 10.1038/s41598-023-39263-7.

[65] Alessandro Roggero et al. “Quantum computing for neutrino-nucleus scattering”. In: *Phys. Rev. D* 101 (2020). doi: 10.1103/PhysRevD.101.074038.

[66] I. Stetcu, A. Baroni, and J. Carlson. “Variational approaches to constructing the many-body nuclear ground state for quantum computing”. In: *Phys. Rev. C* 105 (2022), p. 064308. doi: 10.1103/PhysRevC.105.064308.

[67] L. Henriet et al. “Quantum computing with neutral atoms”. In: *Quantum* 4 (2020), p. 327. doi: 10.22331/q-2020-09-21-327. eprint: 2006.12326.

[68] Samuel Aychet-Claisse et al. “Quantum simulations of Green’s functions for small superfluid systems”. In: *Phys. Rev. C* 113 (2026), p. 044324. doi: 10.1103/bw5d-d4d6.

[69] Alberto Peruzzo et al. “A variational eigenvalue solver on a photonic quantum processor”. In: *Nature Communications* 5 (2014). doi: 10.1038/ncomms5213.

[70] Sam McArdle et al. “Quantum computational chemistry”. In: *Rev. Mod. Phys.* 92 (2020), p. 015003. doi: 10.1103/RevModPhys.92.015003.

[71] Jonathan Romero et al. “Strategies for quantum computing molecular energies using the unitary coupled cluster ansatz”. (2018). arXiv: 1701.02691 [quant-ph].

[72] Dave Wecker, Matthew B. Hastings, and Matthias Troyer. “Progress towards practical quantum variational algorithms”. In: *Phys. Rev. A* 92 (2015), p. 042303. doi: 10.1103/PhysRevA.92.042303.

[73] Martín Larocca et al. “Barren plateaus in variational quantum computing”. In: *Nature Reviews Physics* 7 (2025), pp. 174–189. doi: 10.1038/s42254-025-00813-9.

[74] Maria Schuld et al. “Evaluating analytic gradients on quantum hardware”. In: *Physical Review A* 99 (2019). doi: 10.1103/physreva.99.032331.

[75] César Feniou et al. “Greedy gradient-free adaptive variational quantum algorithms on a noisy intermediate scale quantum computer”. In: *Scientific Reports* 15 (2025). doi: 10.1038/s41598-025-99962-1.

[76] Bryan T. Gard et al. “Efficient symmetry-preserving state preparation circuits for the variational quantum eigensolver algorithm”. In: *npj Quantum Information* 6 (2020). doi: 10.1038/s41534-019-0240-1.

[77] Farrokh Vatan and Colin Williams. “Optimal quantum circuits for general two-qubit gates”. In: *Phys. Rev. A* 69 (2004), p. 032315. doi: 10.1103/PhysRevA.69.032315.

[78] Manuel Hagelueken et al. “Exponential Scaling Barriers for Variational Quantum Eigensolvers”. (2026). arXiv: 2603.13073 [quant-ph].

[79] Qiskit contributors. “Qiskit: An open-source framework for quantum computing”. (2019). doi: 10.5281/zenodo.2562111.

[80] Jing Zhang, Denis Lacroix, and Yann Beaujeault-Taudière. “Neutron-proton pairing correlations described on quantum computers”. In: *Phys. Rev. C* 110 (2024), p. 064320. doi: 10.1103/PhysRevC.110.064320.

[81] Diksha Dhawan, Dominika Zgid, and Mario Motta. “Quantum Algorithm for Imaginary-Time Green’s Functions”. In: *J. Chem. Theory Comput.* 20 (2024), pp. 4629–4638. doi: 10.1021/acs.jctc.4c00241.

[82] Edgar Andres Ruiz Guzman and Denis Lacroix. “Calculation of generating function in many-body systems with quantum computers: technical challenges and use in hybrid quantum-classical methods”. (2021). arXiv: 2104.08181 [quant-ph].

[83] Jarrod R. McClean et al. “Hybrid quantum-classical hierarchy for mitigation of decoherence and determination of excited states”. In: *Phys. Rev. A* 95 (2017), p. 042308. doi: 10.1103/PhysRevA.95.042308.

[84] Jarrod R. McClean et al. “Decoding quantum errors with subspace expansions”. In: *Nature Communications* 11.1 (2020). doi: 10.1038/s41467-020-14341-w.

[85] Tyler Takeshita et al. “Increasing the Representation Accuracy of Quantum Simulations of Chemistry without Extra Quantum Resources”. In: *Phys. Rev. X* 10 (2020), p. 011004. doi: 10.1103/PhysRevX.10.011004.

[86] Nobuyuki Yoshioka et al. “Variational quantum simulation for periodic materials”. In: *Phys. Rev. Res.* 4 (2022), p. 013052. doi: 10.1103/PhysRevResearch.4.013052.

[87] Francois Jamet, Abhishek Agarwal, and Ivan Rungger. “Quantum subspace expansion algorithm for Green’s functions”. (2022). arXiv: 2205.00094 [quant-ph].

[88] Chukwudubem Umeano et al. “Quantum subspace expansion approach for simulating dynamical response functions of Kitaev spin liquids”. In: *Phys. Rev. Mater.* 9 (2025), p. 034401. doi: 10.1103/PhysRevMaterials.9.034401.

[89] B. Gauthier et al. “Occupation-number quantum-subspace-expansion approach to computing the single-particle Green function: An opportunity for noise filtering”. In: *Phys. Rev. A* 110 (2024), p. 032624. doi: 10.1103/PhysRevA.110.032624.

[90] Edgar Andres Ruiz Guzman and Denis Lacroix. “Accessing ground-state and excited-state energies in a many-body system after symmetry restoration using quantum computers”. In: *Phys. Rev. C* 105 (2022), p. 024324. doi: 10.1103/PhysRevC.105.024324.

[91] Yann Beaujeault-Taudière and Denis Lacroix. “Solving the Lipkin model using quantum computers with two qubits only with a hybrid quantum-classical technique based on the generator coordinate method”. In: *Phys. Rev. C* 109 (2024), p. 024327. doi: 10.1103/PhysRevC.109.024327.

[92] Manqoba Q. Hlatshwayo et al. “Simulating excited states of the Lipkin model on a quantum computer”. In: *Phys. Rev. C* 106 (2022), p. 024319. doi: 10.1103/PhysRevC.106.024319.

[93] Manqoba Q. Hlatshwayo, John Novak, and Elena Litvinova. “Quantum benefit of the quantum equation of motion for the strongly coupled many-body problem”. In: *Phys. Rev. C* 109 (2024), p. 014306. doi: 10.1103/PhysRevC.109.014306.

[94] T. Duguet et al. “Nonobservable nature of the nuclear shell structure: Meaning, illustrations, and consequences”. In: *Phys. Rev. C* 92 (2015), p. 034313. doi: 10.1103/PhysRevC.92.034313.

[95] Tameem Albash and Daniel A. Lidar. “Adiabatic quantum computation”. In: *Rev. Mod. Phys.* 90 (2018), p. 015002. doi: 10.1103/RevModPhys.90.015002.

[96] T. Kato. “On the Adiabatic Theorem of Quantum Mechanics”. In: *J. Phys. Soc. Jpn.* 5.6 (1950), pp. 435–439. doi: 10.1143/JPSJ.5.435.

[97] M. Born and V. Fock. “Beweis des Adiabatensatzes”. In: *Zeitschrift für Physik* 51 (1928), pp. 165–180. doi: 10.1007/BF01343193.

[98] Jonathan Wurtz et al. “Aquila: QuEra’s 256-qubit neutral-atom quantum computer”. (2023). arXiv: 2306.11727 [quant-ph].

[99] Henrique Silvério et al. “Pulser: An open-source package for the design of pulse sequences in programmable neutral-atom arrays”. In: *Quantum* 6 (2022), p. 629. doi: 10.22331/q-2022-01-24-629.

[100] M Saffman. “Quantum computing with atomic qubits and Rydberg interactions: progress and challenges”. In: *Journal of Physics B: Atomic, Molecular and Optical Physics* 49.20 (2016), p. 202001. doi: 10.1088/0953-4075/49/20/202001.

[101] Antoine Browaeys and Thierry Lahaye. “Many-body physics with individually controlled Rydberg atoms”. In: *Nature Physics* 16.2 (2020), pp. 132–142. doi: 10.1038/s41567-019-0733-z.

[102] Xiaoling Wu et al. “A concise review of Rydberg atom based quantum computation and quantum simulation”. In: *Chinese Physics B* 30.2 (2021), p. 020305. doi: 10.1088/1674-1056/abd76f.

[103] Karen Wintersperger et al. “Neutral atom quantum computing hardware: performance and end-user perspective”. In: *EPJ Quantum Technology* 10.1 (2023). doi: 10.1140/epjqt/s40507-023-00190-1.

[104] Grégoire Pichard et al. “Rearrangement of individual atoms in a 2000-site optical-tweezer array at cryogenic temperatures”. In: *Physical Review Applied* 22.2 (2024). doi: 10.1103/physrevapplied.22.024073.

[105] Nicolas Schlosser et al. “Sub-poissonian loading of single atoms in a microscopic dipole trap”. In: *Nature* 411 (2001), pp. 1024–1027. doi: 10.1038/35082512.

[106] F. Nogrette et al. “Single-Atom Trapping in Holographic 2D Arrays of Microtraps with Arbitrary Geometries”. In: *Phys. Rev. X* 4 (2014), p. 021034. doi: 10.1103/PhysRevX.4.021034.

[107] Dolev Bluvstein et al. “A quantum processor based on coherent transport of entangled atom arrays”. In: *Nature* 604 (2022), pp. 451–456. doi: 10.1038/s41586-022-04592-6.

[108] Ohad Lib et al. “Velocity-Enabled Quantum Computing with Neutral Atoms”. (2026). arXiv: 2603.15561 [quant-ph].

[109] Vincent Lienhard et al. “Observing the Space- and Time-Dependent Growth of Correlations in Dynamically Tuned Synthetic Ising Models with Antiferromagnetic Interactions”. In: *Phys. Rev. X* 8 (2018), p. 021070. doi: 10.1103/PhysRevX.8.021070.

[110] Sylvain de Léséleuc et al. “Observation of a symmetry-protected topological phase of interacting bosons with Rydberg atoms”. In: *Science* 365.6455 (2019), pp. 775–780. doi: 10.1126/science.aav9105.

[111] Hannes Pichler et al. “Quantum Optimization for Maximum Independent Set Using Rydberg Atom Arrays”. (2018). arXiv: 1808.10816 [quant-ph].

[112] Antoine Michel et al. “Hubbard physics with Rydberg atoms: Using a quantum spin simulator to simulate strong fermionic correlations”. In: *Phys. Rev. B* 109 (2024), p. 174409. doi: 10.1103/PhysRevB.109.174409.

[113] C. Kokail et al. “Self-verifying variational quantum simulation of lattice models”. In: *Nature* 569 (2019), pp. 355–360. doi: 10.1038/s41586-019-1177-4.

[114] Antoine Michel et al. “Blueprint for a digital-analog variational quantum eigensolver using Rydberg atom arrays”. In: *Phys. Rev. A* 107 (2023), p. 042602. doi: 10.1103/PhysRevA.107.042602.

[115] Senthil Todadri. “Consequences of Time Reversal Symmetry”. MIT OpenCourseWare, 8.321, Quantum theory I, Lecture 23, section 23.1 (2017), https://ocw.mit.edu/courses/8-321-quantum-theory-i-fall-2017/25761cfb449c1432477eb7f782dc275c_MIT8_321F17_lec23.pdf (visited on 08/03/2026).

[116] Harold Erbin et al. “Many-body Quantum Score: a scalable benchmark for digital and analog quantum processors and first test on a commercial neutral atom device”. (2026). arXiv: 2601.03461 [quant-ph].

[117] Pasqal contributors. *Pulser documentation*. url: https://docs.pasqal.com/pulser/ (visited on 07/17/2026).